Analytische Näherungsverfahren zur Beschreibung der nuklearen Spin-Dephasierung

Dissertation zur Erlangung des
naturwissenschaftlichen Doktorgrades
der Bayerischen Julius-Maximilians-Universität
Würzburg

vorgelegt von

Priv.Doz.Dr. med. Dipl.Phys.Wolfgang Rudolf Bauer

2002

Eingereicht am: 2002
bei der Fakultät für Physik und Astronomie

1. Gutachter:	Prof. Dr. A. Haase
2. Gutachter:	Priv.Doz. Dr. G. Reents

der Dissertation

1. Prüfer:	Prof. W.A. Haase
2. Prüfer:	Priv.Doz. Dr. G. Reents

Tag der mündlichen Prüfung: 9.12.2002
Doktorurkunde ausgehändigt am:

Inhaltsverzeichnis

Kapitel 1

Einleitung

1.1 Grundlagen und Anwendung der Kernspinrelaxation in biologischen Geweben

Die Kernspinresonanz- oder NMR- (*nuclear magnetic resonance*) Bildgebung hat inzwischen ihren festen Stellenwert in der biomedizinischen Grundlagenforschung und Anwendung. Das Grundprinzip ist vereinfacht dargestellt, daß die Magnetisierung von Kernspins, die sich in einem äußeren Magnetfeld befinden, zunächst aus ihrem Gleichgewichtszustand gebracht wird, und danach deren Relaxation, also Rückkehr zum Gleichgewichtszustand, ortsaufgelöst beobachtet wird. Die Signalintensität und damit der Bildkontrast sind eine Funktion der Kernspindichte und der Relaxationszeiten. Bei der am häufigsten verwendeten ^{1}H-Bildgebung ist die Kernspindichte der Wasserkonzentration proportional. Diese ist, die fetthaltigen Gewebe wie z.B. Hirn oder Knochenmark ausgenommen, in fast allen Geweben gleich. Folglich wird dort der Kontrast im wesentlichen durch die Relaxationszeiten bestimmt. Zwei Relaxationsprozesse werden unterschieden: 1. die Spin-Gitter oder longitudinale Relaxation der parallel zum äußeren Feld orientierten Komponente der Kernmagnetisierung; und 2. die transversale Relaxation des zum äußeren Feld senkrecht orientierten Anteils der Kernmagnetisierung. .

Bei der longitudinalen Relaxation, deren Zeitkonstante mit T_1 bezeichnet wird, klappen antiparallel zum äußeren Magnetfeld orientierte Spins in die energetisch tiefer liegende parallele Orientierung um. Dieses Umklappen der Spinorientierung wird durch Störfelder induziert, die zusätzlich zum äußeren Magnetfeld einwirken. Beim Umklappen findet ein Energieaustausch zwischen dem Spin und dessen Umgebung statt. Wie aus der quantenmechanischen Störtheorie bekannt ist, wird dieser Austausch der Energie ΔE dabei fast nur durch Störfeldfluktuationen innerhalb eines schmalen Frequenzbandes um die Resonanzfrequenz $\omega_0 = \Delta E/\hbar$ vermittelt.

Bei der transversalen Relaxation wird ein reversibler und ein irreversibler Anteil unterschieden. Die Zeitkonstante der gesamten transversalen Relaxation wird mit T_2^*, die des irreversiblen Anteils mit T_2 bezeichnet. Zur transversalen Relaxation trägt zum einen ein Mechanismus wie bei der longitudinalen Relaxation (nicht säkularer Anteil der transversalen Relaxation) bei, jedoch spielt dieser bei NMR Experimenten in biologischen Systemen meist keine wesentliche Rolle. Ein wesentlich wichtigerer Mechanismus für die transversale Relaxation ist die Dephasierung. Diese entsteht durch Modulationen der Spinphase, durch parallel zum äußeren Feld einwirkende Störfelder (säkularer Anteil der transversalen Relaxation). Zur Dephasierung trägt das gesamte Frequenzband der Störfeldfluktuationen bei. Das erklärt auch, warum T_2^*

bzw. T_2 meist wesentlich kürzer ist als T_1.

Für die biomedizinische Forschung ist vor allem interessant, wie physiologische, morphologische und biophysikalische Parametern die Dynamik und Stärke der Störfelder, und damit die Relaxationszeiten beeinflussen. Durch Auswahl eines geeigneten NMR Experimentes ist man dann in der Lage, über die Relaxation biologisch interessante Größen zu messen. Eine wichtige Klasse von Prozessen, die zur Spin-Dephasierung führen, sind die diffusionsvermittelten Phasenmodulationen von Spins in einem inhomogenen Magnetfeld. So kann nach geeigneter Schaltung eines externen Feldgradienten über die Dephasierung der in diesem Gradienten diffundierenden Spins deren Diffusionkoeffizient gemessen werden. Weitere wichtige Anwendungen der Spin-Dephasierung nutzen den BOLD (*blood oxygenation level dependent*) Effekt [1]aus, der auf der paramagnetischen Eigenschaft von dem im Intravasalraum befindlichen desoxygenierten Hämoglobin beruht. Zum einen beschleunigt Desoxyhämoglobin als ,,natürliches” NMR-Kontrastmittel die transversale Relaxation der Spins im Intravasalraum. Zum anderen führt der in einem äußeren Magnetfeld entstehende Suszeptibilitätssprung zwischen Intra- und Extravasalraum zu einem perivaskulären Magnetfeld, was auch die Dephasierung der extravaskulären Spins. beschleunigt. Unter physiologischen Bedingungen ist der Anteil des Desoxyhämoglobins im arteriellen System sehr gering, d.h. für den BOLD Effekt sind im wesentlichen die Kapillaren und Venen von Bedeutung. Anwendung hat der BOLD Effekt in der funktionellen Bildgebung des Gehirns gefunden [2]. Hier wird ausgenutzt, daß nach Aktivierung von Hirnarealen deren Durchblutung kurzzeitig überproportional zur Zunahme des Sauerstoffbedarfs ansteigt. Der intrakapilläre/

-venöse Oxygenierungsgrad des Hämoglobins steigt bzw. die Desoxyhämoglobinkonzentration sinkt und damit wird die Dephasierung schwächer, was durch Änderungen der Signalintensität sichtbar gemacht werden kann.

Verhältnismäßig neu ist die Untersuchung des BOLD Effektes in der humanen kardialen NMR Bildgebung. So konnte von unserer Arbeitsgruppe nach Gabe eines die Durchblutung steigernden Medikamentes eine Verlängerung der transversalen Relaxations beobachtet werden [3]. Bei Patienten mit einem verengten Herzkranzgefäß wurde basal als auch nach Steigerung der Durchblutung in dem assoziierten Herzmuskelgewebe eine Beschleunigung der transversalen Relaxation gefunden.

Um die Dephasierung quantitativ zu verstehen und ggf. anzuwenden sind Modelle nötig, welche die Dephasierung als Funktion morphologischer, physiologischer und biophysikalischer Parametern beschreiben. Speziell beim BOLD Effekt kann man diese in Parameter unterteilen, die das perivaskuläre Feld festlegen wie

- die Gefäßarchitektur, also u.a. die Dichte der einzelner Gefäßtypen und deren Raumorientierung,
- der funktionelle Gefäßzustand, der sich im Gefäßdiameter widerspiegelt
- die intravasale Oxygenierung, die aus der Durchblutung und dem Sauerstoffverbrauch resultiert

und Parameter, welche die Fluktuationsdynamik der Phasenmodulationen bestimmen, wie

- der Diffusionskoeffizient

- Dimensionen von Barrieren, welche die Diffusion einschränken, wie Zellmembranen, Gefäßwände
- Austauschraten zwischen Wasserkompartimenten mit unterschiedlichen instrinsischen Relaxationseigenschaften, also z.B. zwischen gebundenem und freiem Wasser.

Natürlich wird man in die Modelle nicht alle Parameter aufnehmen können, sondern sich in der speziellen Situation auf die relevanten beschränken. So kann z.B. u.U. die Gefäßgeometrie vereinfacht werden, oder bei den Fluktuationsparametern wird eine mittlere Situation im Sinne eines *mean field* Ansatzes angenommen. Meistens wird die eingeschränkte Diffusion im Extra- und Intrazellularraum und die Diffusion über die Zellmembran durch eine mittlere Diffusionsdynamik im Gewebe ersetzt.

Quantitative bzw. analytisch lösbare Modelle für die Spin Dephasierung existieren meist jedoch nur für die Grenzfälle der Fluktuationsdynamik. Dieses ist der im nächsten Kapitel beschriebene *motional narrowing* Grenzfall, bei einer sehr schnellen Fluktuationsdynamik, sowie der *static dephasing* Grenzfall, bei sehr langsamen Störfeldfluktuationen. Ein Nachteil dieser Ansätze ist, daß sie auf einer Störentwicklung in der Fluktuationsdynamik bzw. im Betrag der Störfelder basieren und jeweils bei Extrapolation zum anderen Dynamikbereich hin divergieren. Daher sind beide Ansätze im intermediären Dynamikbereich nicht anwendbar.

Modelle, die über den ganzen dynamischen Bereich der Störfeldfluktuationen analytische Resultate liefern, sind das Anderson-Weiss Modell [5], oder die Dephasierung bei freier Diffusion in einem linearen Magnetfeld [6]. Das Anderson-Weiss Modell setzt eine Gauß-verteilte Fluktuationsdynamik und damit notwendigerweise eine Gaußverteilung der Störfelder voraus, die nur in speziellen Fällen vorhanden ist. Soll das zweite Modell auf die diffusionsvermittelte Dephasierung in einem inhomogenen Magnetfeld $B(x)$ angewendet werden, so muß die Diffusionstrecke l, die innerhalb der Relaxation zurückgelegt wird, im Bereich der Linearapproximation des Feldes liegen $B(x+l) \approx B(x) + l\partial_x B(x)$. Folglich, muß entweder die Variation des Feldgradienten, oder aber die Diffusionslänge hinreichend klein sein $l \cdot \partial_x^2 B(x) \ll \partial_x B(x)$.

Häufig ist in der realen Situation keiner der Grenzfälle der Fluktuationsdynamik vorhanden, noch sind die oben genannten analytischen Verfahren anwendbar. Beispielsweise ist dies bei der Beschreibung des BOLD Effektes in der Kapillarregion der Fall [7]. Meist versagen selbst numerische Verfahren, so daß die Dephasierung nur simuliert werden kann [8]. Das Ziel dieser Arbeit war es, analytische Näherungsverfahren zu entwickeln, welche die Dephasierung durch stochastische Störfeldfluktuationen über deren gesamten dynamischen Bereich beschreiben. Entscheidend ist, daß die vorgestellte Technik kein Verfahren aus der Störtheorie ist, d.h. es wird weder eine Entwicklung in der Fluktuationsdynamik noch in dem Betrag der Störfelder durchgeführt. Stattdessen wird die Dynamik der Störfeldfluktuation systematisch durch einen einfacheren stochastischen Prozess angenähert. Die Ergebnisse wurden zum einen mit Simulationen der Spin-Dephasierung in Gewebemodellen bzw. mit NMR-Meßergebnissen aus eigenen Experimenten bzw. aus der Literatur verglichen. Weiterhin wurde die Techniken auf analytisch oder numerisch lösbare Modelle (Paradigmen) angewendet und validiert.

Die Arbeit ist wie folgt strukturiert: Zunächst wird im Kapitel *Theorie* *der Spin-Dephasierung* der Stand der Forschung dargestellt. Die Näherungsmethoden für extrem schnelle (*motional narrowing*) und extrem langsame (*static dephasing*) Störfeldflukutationen, sowie das Anderson-Weiss Modell werden vorgestellt. Beim Anderson-Weiss Modell wird erstmals herausgearbeitet, bei welcher Klasse von Störfeldfluktuationen dieses überhaupt anwendbar ist, was weder in der Orginalarbeit [5] noch in den Folgearbeiten zu finden ist. Das Kapitel *Theorie* stellt im Kontext die Theorie der *strong collision* Approximation sowie deren Erweiterung vor. Im Folgekapitel *Anwendungen* wird zunächst die *strong collision* Näherung auf Simulations- und reale BOLD NMR-Experimente angewendet. Danach wird deren Erweiterung am Anderson-Weiss Modell, sowie für die Beschreibung der ,,Dephasierung durch eingeschränkte Diffusion in einem linearen Magnetfeld" getestet. Da beide Modelle analytisch oder zumindest einfach numerisch lösbar sind, kann dort die Güte des Näherungsverfahren überprüft werden.

Kapitel 2

Theorie der Spin-Dephasierung

Das magnetische Dipolmoment eines transversal in der x-y Ebene polarisierten Kernspins μ_s, der unter Einfluß senkrecht dazu stehender fluktuierender Störfelder steht, wird durch die Gleichung

$$\partial_t \mu_s(t) = \mathrm{i}\,\omega(t)\;\mu_s(t) \tag{2.1}$$

beschrieben, wobei das Dipomoment polar dargestellt ist, $\mu_s = \mu_{s,x} - \mathrm{i}\;\mu_{s,y}$ ist, und $\omega(t)$ die Larmorfrequenz des Störfeldes bezeichnet. Da die Larmorfrequenz des äußeren Feldes ω_0 nur den Phasenfaktor $e^{\mathrm{i}\omega_0 t}$ beiträgt, wurde sie wegnormiert. Die Lösung von Gl. 2.1 ist

$$\mu_s(t) = \mu_s(0)\;\exp\left(\mathrm{i}\int_0^t d\xi\;\omega(\xi)\right)\;. \tag{2.2}$$

Betrachtet man ein Ensemble von Spins, dann ist deren gesamte Magnetisierung M dem Mittelwert der einzelnen Dipolmomente proportional

$$\begin{aligned} M(t) &= N\;\langle\mu_s(t)\rangle \\ &= M(0)\;\langle e^{\mathrm{i}\,\phi(t)}\rangle\;, \end{aligned} \tag{2.3}$$

wobei $\langle\rangle$ die Ensemble-Mittelung symbolisiert, N steht für die Spindichte und $\phi(t)$ ist der Phasenwinkel

$$\phi(t) = \int_0^t d\xi\ \omega(\xi)\ . \tag{2.4}$$

2.1 Der *motional narrowing* Grenzfall

Analytische Lösungen existieren in Fülle für den Grenzfall sehr kleiner und schnell fluktuierender Störfelder. Die Ableitung ist in jedem NMR Lehrbuch zu finden (z.B. [9]) und ebenso die Beispiele (Relaxation durch: - Spin-Spin Wechselwirkung, - Dipolfelder mit unterschiedlicher räumlicher Anordnung, etc.[10]). Die Grundidee ist die einer Störentwicklung von $M(t)$ in Gl. 2.3 in ω

$$\begin{aligned} M(t+\delta t) - M(t) &= M(t) \int_t^{t+\delta t} d\eta\ \mathrm{i}\langle\omega(\eta)\rangle + \\ & M(t)\ \mathrm{i}^2 \int_t^{t+\delta t} d\eta \int_t^{\eta} d\xi \langle\omega(\eta)\omega(\xi)\rangle + \dots\ . \end{aligned} \tag{2.5}$$

Der Mittelwert der Störfeldfluktuationen $\langle\omega(\eta)\rangle$ läßt sich immer auf 0 normieren, weshalb der entsprechende Term in Gl. (2.5) verschwindet. Für stationäre stochastische Prozesse ist die zeitliche 2-Punkt Korrelationsfunktion der Störfelder

$$C_2(\eta, \xi) = \langle\omega(\eta)\omega(\xi)\rangle \tag{2.6}$$

unabhängig vom Ausgangszeitpunkt ξ, d.h. sie ist nur durch die Zeitdifferenz $\eta - \xi$ bestimmt. Damit läßt sich nach Variablentransformation $\eta' = \eta - \xi$ und $\xi' = \eta + \xi$ das Doppelintegral in Gl. (2.5) umformen in

$$\int_t^{t+\delta t} d\eta \int_t^{\eta} d\xi\ \langle\omega(\eta)\omega(\xi)\rangle = 1/2 \int_0^{\delta t} d\eta'\ C_2(\eta') \int_{t+\eta'}^{t+2\delta t-\eta'} d\xi'$$

$$= \int_0^{\delta t} d\eta' \, C_2(\eta')(\delta t - \eta') \, . \tag{2.7}$$

Bei sehr schnell fluktuierenden, schwachen Störfeldern kann man δt so wählen, daß es zum einen groß gegenüber der Korrelationszeit der Störfelder ist [1]

$$\begin{aligned} \delta t \gg \tau \quad &:= \int_0^\infty dt \, \frac{C_2(t) - C_2(\infty)}{C_2(0) - C_2(\infty)} \\ &= \int_0^\infty dt \, C_2(t)/C_2(0) \, . \end{aligned} \tag{2.8}$$

Zum anderen soll δt aber noch klein genug sein, so daß die Änderung der Magnetisierung gering bleibt, und die Beziehung

$$M(t + \delta t) - M(t) = \dot{M}(t) \, \delta t \tag{2.9}$$

erfüllt ist. Damit läßt sich Gl. (2.5) mit Gl. (2.7) umformen in

$$\dot{M}(t) = -\tau \langle \omega^2 \rangle \, M(t) + \delta t^{-1} \int_0^{\delta t} d\eta' \, \eta' c_2(\eta') \;\; M(t) \, , \tag{2.10}$$

mit $\langle \omega^2 \rangle = C_2(0)$ als der Varianz der Störfeldfluktuationen. Nimmt man, wie es häufig getan wird, an, dass die 2-Punkt Korrelationsfunktion einfach exponentiell abfällt [9], d.h. $C_2(t) \sim e^{-t/\tau}$, dann ist das Integral in Gl. (2.10) von der Größordnung $\tau/\delta t$ gegenüber dem ersten Term, d.h. vernachlässigbar klein, und man erhält schließlich

$$\dot{M}(t) = -\tau \langle \omega^2 \rangle \, M(t) \, . \tag{2.11}$$

---

[1] wir setzen hier die stochastische Unabhängigkeit der Störfelder für $t \rightarrow \infty$ aus ($C_2(\infty) = \langle \omega \rangle^2$), was meist erfüllt ist. Da der Mittelwert auf Null normiert ist, gilt dann $C_2(\infty) = 0$

Foglich fällt $M(t)$ monoexponentiell mit der Relaxationsrate

$$\frac{1}{T_2} = \tau \langle \omega^2 \rangle \tag{2.12}$$

ab. Der Bereich der Korrelationszeit in dem die Gleichungen (2.11), (2.12) gültig sind, wird als *motional narrowing* Grenzfall bezeichnet. Der Begriff resultiert daraus, daß mit immer schneller werdenden Bewegungen der Kernspins (*motion*) die Korrelationszeiten τ immer kürzer werden. Die Relaxationszeit wird entsprechend Gl. (2.12) immer länger, d.h. die Resonanzbreite der Dephasierung wird immer enger. Eine wesentlich allgemeinere Herleitung der Beziehung zwischen Dephasierung und der Korrelation der Störfelder, die auch Korrelationszeiten höherer Ordnung berücksichtigt, findet man im Appendix der Orginalarbeit [17].

2.2 Der *static dephasing* Grenzfall

Beim *static dephasing* Grenzfall verbleibt ein transveral polarisierte Spin an seiner Position x, d.h. er steht konstant unter dem Einfluss desselben lokalen Magnetfeldes mit der Frequenz $\omega(x)$. Damit gilt für die Phase eines Spins

$$\phi(x,t) = \omega(x)\, t \tag{2.13}$$

und die Gesamtmagnetisierung (s.Gl. 2.3) ist dann einfach der Summe über die Phasenfaktoren $e^{\mathrm{i}\omega(x)t}$ proportional,

$$\begin{aligned} M(t) &= N\, \langle e^{\mathrm{i}\omega(x)t} \rangle \\ &= N\, V^{-1} \int_V dx\, e^{\mathrm{i}\omega(x)t} \end{aligned} \tag{2.14}$$

wobei V das magnetisierte Volumen ist. Yablonski und Haake [12] untersuchten diesen Grenzfall für verschiedene Anordnungen von Zylindern und

Kugeln im Raum, die mit einer para- oder ferromagnetischen Substanz gefüllt waren. Anwendbar ist die *static dephasing* Näherung dann, wenn die Magnetfeldamplitude, die ein diffundierender Spin während der Relaxation ,,sieht", klein gegenüber dem Magnetfeld selber ist. Diese Voraussetzung trifft bei der BOLD-Bildgebung dann zu, wenn z.B. wie im Gehirn das paramagnetische Desoxyhämoglobin hauptsächlich in größeren Gefäßen (Venen) lokalisiert ist. Im Herzmuskel ist diese Voraussetzung allerdings nicht erfüllt. Hier findet sich das Desoxyhämoglobin fast ausschließlich in den Kapillaren. Die Querschnitte dieser parallel verlaufenden Gefäße sind regelmäßig im Abstand von $\approx 19\mu$m angeordnet, d.h. das perikapilläre Magnetfeld ist in dieser Distanz ungefähr periodisch. Bei einer Relaxationszeit von $T_2^* > 30$ ms und einem Diffusionskoeffizienten von $D = 1\mu\mathrm{m}^2/\mathrm{ms}$ diffundiert ein Spin während der Relaxation $t > 2\ T_2^*$ eine Distanz von $\sqrt{Dt} > 7\ \mu$m, d.h. er ,,sieht" fast die gesamte Variation des perikapillären Feldes, was eine Anwendung des *static dephasing* Ansatzes ausschließt.

Kiselev und Posse [13] erweiterten den *static dephasing* Ansatz. Sie ließen Diffusion in einem Zeitbereich zu, in dem die Diffusionslänge l so klein ist, daß Feldänderungen linear approximiert werden können,

$$\omega(x_0 + l) \approx \omega(x_0) + \partial_x \omega(x_0)\ l\ . \tag{2.15}$$

Es ist offensichtlich, daß obige Näherung für nichtlineare Felder im allgemeinen nur dann gilt, wenn man die Spin Dephasierung in einem hinreichend kurzen Zeitfenster bezogen auf die Relaxation betrachtet. Ist das das Beobachtungszeitfenster in der Größordnung der Relaxationszeit und folglich $l \approx \sqrt{DT_2^*}$, dann ist die Bedingung (2.15) für nichtlineare Felder nur dann erfüllt, wenn entweder die Diffusion hinreichend gering, oder aber die Relaxation sehr schnell ist.

2.3 Das Anderson-Weiss Modell

Ein sehr wichtiges Modell, das analytische Lösungen der Dephasierung liefert, ist das Anderson-Weiss Modell [5, 11]. Ausgangspunkt ist die Annahme einer stationären Gauß-verteilten Stärke der Störfelder, d.h. die Wahrscheinlichkeitsdichte der Störfeldfrequenzen ω hat die Form

$$p_0(\omega) = \frac{1}{\sqrt{2\pi\varsigma^2}}\, e^{-\frac{\omega^2}{2\varsigma^2}} \ , \tag{2.16}$$

wobei ς^2 die Varianz der Verteilung ist. Anderson und Weiss gingen nun davon aus, daß wenn die stochastischen Variablen $\omega(t)$ zu allen Zeitpunkten t entsprechend Gl. 2.16 Gauß-verteilt sind, daß dann auch jede Linearkombination dieser Variablen Gauß-verteilt ist. Insbesondere sollte dies auf den Phasenwinkel $\phi(t) = \int_0^t d\xi\ \omega(\xi)$ zutreffen, wobei der Integralausdruck als Spezialfall einer Linearkombination zu sehen ist. Setzt man diese Behauptung voraus, so erhält man mit $\langle\phi^2\rangle$ als der Varianz der Phasenwinkelverteilung für die Magnetisierung nach Gl. 2.3

$$\begin{aligned} M(t) &= \int_{-\infty}^{\infty} d\phi\ \frac{1}{\sqrt{2\pi\langle\phi^2(t)\rangle}}\ \exp\left(\frac{-\phi^2(t)}{2\langle\phi^2(t)\rangle}\right) e^{\mathrm{i}\phi(t)} \\ &= \exp(-\langle\phi^2(t)\rangle/2) \ , \end{aligned} \tag{2.17}$$

wobei wir ohne Beschränkung der Allgemeinheit die initiale Magnetisierung auf $M(0) = 1$ normiert haben. Die Varianz wird durch die 2-Punktkorrelationsfunktion 2.6 bestimmt

$$\langle\phi^2(t)\rangle = \int_0^t \int_0^t d\eta d\xi\ \langle\omega(\eta)\omega(\xi)\rangle$$

$$= \quad 2\langle\omega^2\rangle \int_0^t (t-\eta)\, C_2(\eta)\ . \tag{2.18}$$

Problematisch ist, daß Anderson und Weiss als bewiesen annahmen, daß die Gaußverteilung des Phasenwinkels ϕ automatisch bei einer Gaußverteilung der Störfelder ω gegeben ist. Auch andere Autoren [11] übernahmen diese Schlußfolgerung, d.h. in der Literatur wird für die Anwendung des Anderson-Weiss Modells nur eine stationäre Gaußverteilung der Störfelder vorausgesetzt.

Diese Bedingung allein ist jedoch nicht ausreichend. Wir wollen im folgenden herausarbeiten, daß zusätzlich die Stöfeldfluktuationen bestimmte Kriterien erfüllen müssen, damit der Phasenwinkel Gauß-verteilt, und somit das Anderson-Weiss Modell anwendbar ist. Einfachkeitshalber setzen wir voraus, daß sich die Störfelddynamik durch einen stationären Markov Prozess beschreiben läßt. Übergänge zwischen zwei Störfeldrealisationen sind dann nur vom Ausgangszustand und nicht von den weiter in der Vergangenheit zurück liegenden Zuständen abhängig. Weiterhin sind die Übergansraten zeitunabhängig. Statt zu prüfen, welche Dynamiken ein Gauß-verteilter Phasenwinkel zuläßt, testen wir den schwächeren Fall, nämlich wir setzen $\omega' = \omega(t) + \omega(t+\Delta t)$ (Δt klein) als Gauß-verteilt voraus [2]. Wir werden in einem zweiten Schritt zeigen, daß die daraus hergeleitete stochastische Dynamik der Störfelder umgekehrt auch hinreichend für eine Gaußverteilung des Phasenwinkels ist.

Wir gehen davon aus, daß ein stochastisches Gleichgewicht herrscht, dessen Wahrscheinlichkeitsdichte $p_0(\omega)$ durch Gl. 82.16 gegeben ist. Bezeichnet

---

[2] Offensichtlich ist bei einem Gauß-verteilten Phasenwinkel für kleine Δt immer auch ω' Gauß-verteilt, denn $\omega' \approx \phi(\Delta t)/\Delta t$

$g(\omega')$ die Gaußverteilung der Variablen ω', dann erfüllt diese die Gleichung

$$g(\omega') = \int_{-\infty}^{\infty} d\omega \; P(\omega' - \omega, \omega; \Delta t) \; , \tag{2.19}$$

wobei $P(\sigma, \omega; \Delta t)$ die Wahrscheinlichkeitsdichte ist, daß das Störfeld zum Zeitpunkt t den Wert ω und zum Zeitpunkt $t + \Delta t$ den Wert σ hat. Aufgrund der Stationarität hängt P nur von der Zeitdifferenz Δt ab. Da wir vom Gleichgewichstzustand $p_0(\omega)$ ausgehen, ist

$$P(\sigma, \omega; 0) = \delta(\sigma - \omega) \; p_0(\omega) \; . \tag{2.20}$$

Für sehr kurze Zeiten Δt ist $P(\sigma, \omega, \Delta t)$ dem Wahrscheinlichkeitsstrom $j_{\omega \to \sigma}$ vom Störfeldzustand mit der Frequenz ω zu dem mit der Frequenz σ proportional

$$P(\sigma, \omega, \Delta t) \approx j_{\omega \to \sigma} \; \Delta t \; . \tag{2.21}$$

Im stochastischen Gleichgewicht gilt das Prinzip der detaillierten Bilanz, d.h. die Anzahl der Übergänge $\omega \to \sigma$ in der Zeit Δt ist gleich der $\sigma \to \omega$, also

$$\begin{aligned} j_{\omega \to \sigma} &= j_{\sigma \to \omega} \; \text{ und damit} \\ P(\omega, \sigma; \Delta t) &= P(\sigma, \omega; \Delta t) \end{aligned} \tag{2.22}$$

Technisch einfacher ist es jetzt, mit den Fouriertransformierten der Wahrscheinlichkeitsdichten zu rechnen. Anwendung auf Gl. (2.19) zeigt

$$\tilde{g}(\zeta) = \sqrt{2\pi} \; \tilde{P}(\zeta, \zeta; \Delta t) \; , \tag{2.23}$$

wobei $\tilde{P}(\zeta_1, \zeta_2; \Delta t)$ die Fouriertransformatierte von P in den zwei Variablen (σ, ω) ist. Entsprechend Gl. (2.20) ist

$$\tilde{P}(\zeta_1, \zeta_2; 0) = \frac{1}{2\sqrt{2\pi}} \; \tilde{p}_0\Big(\frac{\zeta_1 + \zeta_2}{2}\Big) \; . \tag{2.24}$$

Schreiben wir nun

$$\tilde{P}(\zeta_1,\zeta_2;\Delta t) = \exp\Big(f_0(\zeta_1,\zeta_2) + f_1(\zeta_1,\zeta_2;\Delta t)\Big)\,, \tag{2.25}$$

wobei f_0, f_1 Potenzreihen in ζ_1 und ζ_2 sind. Wir legen $f_1(\zeta_1,\zeta_2;0) = 0$ fest. Dann folgt aus Gl. (2.24), daß $f_0(\zeta_1,\zeta_2) \sim (\zeta_1+\zeta_2)^2$. Aus der Symmetrie von P unter Variablenvertauschung (Gl. (2.22)), folgt die der Fouriertransformierten $\tilde{P}$ in den Variablen ζ_1,ζ_2 und damit die von f_0+f_1. Da f_0 symmetrisch ist, muß auch f_1 symmetrisch sein. Zusätzlich gilt entprechend Gl. (2.23) und der Tatsache, daß $\tilde{g}(\zeta)$ eine Gaußverteilung ist, daß $f_1(\zeta,\zeta;\Delta t)$ eine quadratische Form in ζ ist. Da $f_1(\zeta_1,\zeta_2;\Delta t)$ symmetrisch unter der Varibalenvertauschung $(\zeta_1,\zeta_2) \to (\zeta_2,\zeta_1)$ ist, ist $f_1(\zeta,\zeta;\Delta t)$ nur dann eine quadratische Form in ζ, wenn $f_1(\zeta_1,\zeta_2,\Delta t)$ auch eine quadratische Form in ζ_1 und ζ_2 ist.

Die letzte Schlußfolgerung ist entscheidend: damit ist $\tilde{P}(\zeta_1,\zeta_2;\Delta t)$ und somit auch $P(\sigma,\omega;\Delta t)$ eine Gaußfunktion [3]. Führen wir nun die Greensfunktion $G(\sigma|\omega;\Delta t)$ ein, d.h. die bedingte Wahrscheinlichkeitsdichte, daß wenn ursprünglich die Störfeldrealisation mit der Frequenz ω vorgelegen hat, nach der Zeit Δt eine Realisation mit der Frequenz σ vorliegt. Dann ist

$$P(\sigma,\omega;\Delta t) = G(\sigma|\omega;\Delta t)\; p_0(\omega) \tag{2.26}$$

Da $p_0(\omega)$ und $P(\sigma,\omega;\Delta t)$ Gaußfunktionen sind, muß auch die Greensfunktion eine Gaußfunktion sein. Wir haben also gezeigt, daß wenn $\omega(t)+\omega(t+\Delta t)$ Gauß-verteilt ist, dann ist auch die Greensfunktion $G(\sigma|\omega;\Delta t)$ eine Gaußfunktion.

---

[3] eine Gaußfunktion in den Variablen x,y wird allgemein als $\exp(Q(x,y))$ definiert, wobei $Q(x,y) = A\ x^2 + B\ y^2 + C\ xy + D \quad A,B < 0$ eine quadratische Form in beiden Variablen ist

Umgekehrt ist die Wahrscheinlichkeitsdichte für den Phasenwinkel $\phi(t)$ wie folgt zu bestimmen: bei hinreichend kleinem Δt kann man den Winkel als $\phi = \sum_{i=0}^{n} \omega(i\ \Delta t)\Delta t$ schreiben. Die Wahrscheinlichkeitsdichte für einen Winkel ist dann durch

$$\begin{aligned}\rho(\phi) &= \int\limits_{-\infty}^{\infty} \cdots \int\limits_{-\infty}^{\infty} d\omega_n \cdots d\omega_0 \\ &\quad G(\omega_n|\omega_{n-1};\Delta t) \cdots G(\omega_1|\omega_0;\Delta t)\ p_0(\omega_0)\ \delta(\phi - \Delta t \sum_{i=0}^{n} \omega_i) \qquad (2.27)\end{aligned}$$

gegeben. Offensichtlich handelt es sich um eine verkettete Faltung von Gaußfunktionen, d.h. $\rho(\phi)$ ist selber wieder eine Gaußfunktion. Wir haben also folgend Äquivalenz gezeigt: eine Gaußverteilung des Phasenwinkels liegt genau dann vor, wenn die Greensfunktion $G(\sigma|\omega;\Delta t)$, also die Übergangswahrscheinlichkeitdichte zwischen zwei Störfeldrealisationen mit Frequenzen $\omega \rightarrow \sigma$ eine Gaußverteilung ist.

Anderson und Weiss nannten als einzige Voraussetzung für die Anwendbarkeit ihres Modelles eine Gauß-förmige Gleichgewichtsverteilung in den Störfeldfrequenzen $p_0(\omega)$. Wie oben dargestellt, ist diese Voraussetzung nicht ausreichend. Das Modell ist nur bei einer speziellen Klasse von Störfelfluktuationen anwendbar: nämlich genau dann, wenn die Übergangswahrscheinlichkeitsdichte (Greensfunktion) zwischen zwei Störfeldzuständen eine Gaußkurve in den Frequenzen dieser Felder ist. Das impliziert automatisch eine Gauß-verteilung des Gleichgewichtszustands, denn $p_0(\omega) = \lim_{t\to\infty} G(\omega|0,t)$. Der umgekehrte Schluß ist jedoch nicht richtig, denn es existieren Prozesse wie die in der Orginalarbeit [17]) vorgestellten *strong collision* Prozesse und deren Erweiterungen, die zwar eine Gauß-förmige Gleichgewichtsverteilung haben, jedoch keine Gauß-förmige Greensfunktion.

Kapitel 3

Theorie

In diesem Kapitel wird die Theorie der Orginalarbeiten [7, 15, 16, 17] (s. Anlage) im Gesamtzusammenhang dargestellt. Das Ziel ist es, die Dephasierung bei einer gegebenen stochastischen Dynamik von Störfeldfluktuationen näherungsweise zu berechnen. Dies wird erreicht, indem die ursprüngliche Dynamik systematisch durch eine weniger komplexe Dynamik zu ersetzt wird, wobei spezifische Eigenschaften der ursprünglichen Dynamik beibehalten werden. Aufgrund der speziellen Struktur der reduzierten Störfelddynamik, wird die Berechnung der durch sie induzierten Dephasierung erheblich vereinfacht.

3.1 Formelle Beschreibung der reversiblen und irreversiblen Dephasierung

Für die Entwicklung der Näherungsverfahren der Spin-Dephasierung sind Formalismen notwendig, die in diesem Abschnitt eingeführt werden.

Transversal polarisierte Kernspins präzedieren im äußeren Magnetfeld und unter dem Einfluß von flukutierenden Störfeldern mit Frequenzen ω_i, wobei i eine diskrete oder kontinuierliche Variable sein darf. Die stochastische Dynamik soll ein stationärer Markov Prozeß sein, wobei die Übergangsraten zwischen Zuständen $i \to j$ mit r_{ji} bezeichnet werden. Diese werden in der Ratenmatrix $\mathbf{R} = (r_{ji})$ als Generator des Prozesses zusammengefaßt. Die Eigenwerte l von $\mathbf{R}$ erfüllen $l \leq 0$, wobei der Eigenwert $l = 0$ zum Gleichgewichtszustand gehört. Die normalisierten linken und rechten Eigenzustände von $\mathbf{R}$ werden mit $\langle l|$ bzw. $|l\rangle$ bezeichnet, und sie erfüllen die Orthonormalbedingung $\langle l'|l\rangle = \delta_{l'l}$.

Die Zeitentwicklung der Quermagnetisierung von den Spins, die unter dem Einfluß des Störfeldes j stehen (polare Notation $m_j = m_{j\,x} - \mathrm{i} m_{j\,y}$), ergibt sich als lineare Superposition der stochastischen Übergangs- und Präzessionsdynamik $\partial_t m_j(t) = \sum_i r_{ji}\, m_i(t) + \mathrm{i}\, \omega_j\, m_j(t)$. Die Präzession im externen Feld wurde weggeeicht, da sie nur den Phasenfaktor $e^{\mathrm{i}(B_0/\gamma)\,t}$ (B_0 Flußdichte des äußeren Feldes, γ gyromagnetische Konstante) liefert. Faßt man die Störfeldfrequenzen in einer Diagonalmatrix $\mathbf{\Omega} = (\delta_{ji}\ \omega_i)$ zusammen, dann erhält man eine verallgemeinerte Bloch-Torrey Gleichung für die Magnetisierung $|m\rangle = (m_j)$

$$\partial_t |m(t)\rangle \ = (\mathbf{R} + \mathrm{i}\, \mathbf{\Omega})\ |m(t)\rangle\ . \tag{3.1}$$

Von Torrey wurden in der Orginalarbeit nur Diffusionsprozesse betrachtet [6], d.h. $\mathbf{R} = \nabla D(x) \nabla$ und $\mathbf{\Omega} = \omega(x)$, wobei $D(x)$ der lokale Diffusionskoeffizient und $\omega(x)$ die lokale Präzessionsfrequenz ist. Die ursprüngliche Bloch-Torrey Gleichung stellt sich somit als Spezialfall von Gl. (3.1) dar, nämlich

$$\partial_t m(x,t) = (\nabla D(x) \nabla + \mathrm{i}\, \omega(x))\ m(x,t)\ . \tag{3.2}$$

Die initiale Magnetisierung ist meist dem Gleichgewichtszustand proportional, $|m(0)\rangle \sim |0\rangle$. Daher kann man nach Normalisierung der gesamten initalen Magnetisierung auf 1 ($\langle 0|m(0)\rangle = 1$), die Zeitentwicklung der Magnetisierung formell als

$$|m(t)\rangle = \exp[(\mathbf{R} + \mathrm{i}\mathbf{\Omega})\, t]\, |0\rangle \;, \tag{3.3}$$

schreiben. Die gesamte Magnetisierung ist dann,

$$\begin{aligned} M(t) &= \langle 0|m(t)\rangle \\ &= \langle 0|\exp\left[(\mathbf{R} + \mathrm{i}\mathbf{\Omega})\, t\right]\, |0\rangle \;. \end{aligned} \tag{3.4}$$

Die Gleichungen (3.3) und (3.4) beschreiben den freien Induktionszerfall der Magnetisierung. Dieser beinhaltet kohärente (reversible) und inkohärente (irreversible) Anteile der Spin-Dephasierung. Die inkohärente Komponente der Spin Dephasierung erhält man z.B. durch ein Spin-Echo Experiment. Dabei werden transversal polarisierte Spins durch einen 180^0 (π)-Puls nach einer Zeit $t/2$ um die x-Achse gedreht. Dadurch wird die Magnetisierung $|m(t/2)\rangle$ komplex adjungiert $|m^*(t/2)\rangle = \exp[(\mathbf{R} - \mathrm{i}\mathbf{\Omega})\; t/2]\; |0\rangle$. Diese Prozedur läßt kohärente Anteile der Dephasierung zum Zeitpunkt t (Echozeit) verschwinden, d.h. der Zerfall der Magnetisierung zum Zeitpunkt t ist nur durch den inkohärenten Anteil der Spin Dephasierung bedingt. Nach der halben Echozeit $t' > t/2$ wird die Zeitentwicklung der Magnetisierung durch

$$|m(t')\rangle = \exp[(\mathbf{R} + \mathrm{i}\,\mathbf{\Omega})(t' - t/2)]\exp[(\mathbf{R} - \mathrm{i}\mathbf{\Omega})t/2]|0\rangle \;, \tag{3.5}$$

beschrieben. Die gesamte Magnetisierung zur Echozeit t (Spin-Echo Magnetisierung) ist dann

$$\begin{aligned} M_{SE}(t) &= \langle 0|\exp[(\mathbf{R}+\mathrm{i}\,\mathbf{\Omega})t/2]\;\exp[(\mathbf{R}-\mathrm{i}\mathbf{\Omega})\;t/2]\;|0\rangle \\ &= \langle m(t/2)|m^*(t/2)\rangle\;. \end{aligned} \tag{3.6}$$

Wichtig ist, daß die Gleichung (3.6) die Spin-Echo Gesamtmagnetisierung M_{SE} in Beziehung zur Magnetisierung, die beim freien Induktionszerfall zur halben Echozeit vorhanden ist $|m(t/2)\rangle$, setzt.

3.2 Die *strong collision* (SC) Approximation und ihre Erweiterung (ESC)

Die Gleichung (3.1) bzw. ihr Spezialfall (3.2) mit denen man den Zeitverlauf der transversalen Magnetisierung bestimmt, sind nur für spezielle Fälle analytisch lösbar. Das Ziel ist es nun, den durch den Generator **R** definierten stochastischen Prozess durch einen einfacheren Prozess anzunähern, der spezifische dynamische Eigenschaften des ursprünglichen Prozesses beibehält.

3.2.1 Heuristik der *strong collision* Approximation

In vielen Fällen finden die Fluktuationen der Störfelder auf einer sehr viel kürzeren Zeitskala statt, als die durch sie induzierte Dephasierung. Quantitativ beschrieben werden diese Fluktuationen durch die Korrelationszeit (genauer: 2-Punkt Korrelationszeit)

$$\tau_2 = \int_0^\infty dt\,\frac{C_2(t)-C_2(\infty)}{C_2(0)-C_2(\infty)} \tag{3.7}$$

wobei $C_2(t)$ die 2-Punkt Korrelationsfunktion

$$\begin{aligned} C_2(t) &= \langle \omega(t)\omega(0)\rangle \\ &= \langle 0|\mathbf{\Omega}\exp(\mathbf{R}t)\mathbf{\Omega}|0\rangle \end{aligned} \tag{3.8}$$

ist. Anschaulich beschreibt die Korrelationszeit wie lange im Mittel ein Spin unter dem Einfluß einer Störfeldrealisation steht. Für den BOLD Effekt im Herzmuskel konnte von uns abgeschätzt werden, daß durch die Spindiffusion in perivaskulären Magnetfeldern eine Korrelationszeit von $\tau \leq 6$ms gegeben ist [7, 15]. Die Relaxationszeiten des freien Induktionszerfalls im Myokard liegen bei klinischen Bildgebungsgeräte (Feldstärke= 1.5 Tesla) in der Größenordnung von ≥ 30ms. Folglich ist die Relaxationszeit, die den durch den BOLD Effekt induzierten Anteil der Relaxation charakterisiert, noch größer, d.h. die Zeitskala der Dephasierung ist deutlich länger als die der Störfeldflukutationen.

Für ergodische Markovprozesse gilt, daß in einem Zeitintervall von einigen Korrelationszeiten, von einem Spin alle relevanten Störfeldrealisationen mit der Gleichgewichtswahrscheinlichkeit besucht worden sind. Ist die Korrelationszeit deutlich kleiner als die Relaxationszeit, dann hat sich die Magnetisierung in diesem Zeitintervall nur wenig verändert. Anders formuliert bedeutet das: obwohl sich die Magnetisierung nur wenig in diesem Zeitintervall geändert hat, haben alle Störfeldrealisationen proportional ihrer Gleichgewichtswahrscheinlichkeit an der Dephasierung mitgewirkt. Folglich sollte man das gleiche Resultat für die Dephasierung erhalten, wenn man einen Prozess konstruiert, bei dem die Übergangsrate zwischen zwei Störfeldzuständen $i \rightarrow j$ der Gleichgewichtswahrscheinlichkeit des Endzustands $p_{0,j}$ proportional ist. Eine solche Dynamik wird als *strong collision* Dynamik bezeichnet. Der Name *strong collision* stammt aus der statistischen Physik und charakterisiert dort Prozesse, bei denen nach einer harten Stoßwechselwirkung Anfangs- und Endzustand stochastisch unabhängig sind, und damit die Wahrscheinlichkeit durch einen Stoß in einen bestimmten Endzustand zu gelangen dessen Gleichgewichtswahrscheinlichkeit proportional ist.

Der Generator einer *strong collision* Dynamik **D** hat die Form

$$\mathbf{D} = -\lambda\,(\mathbf{id} - \mathbf{\Pi}_0) \tag{3.9}$$

mit $\mathbf{\Pi}_0 = |0\rangle\langle 0|$ als Projektionsoperator in den Eigenraum $[\ |0\rangle\ ]$ und **id** als Identitätsoperator. Der Faktor λ beschreibt als Fluktuationsparameter, wie schnell der Prozeß abläuft und wird selbstkonsistent wie folgt bestimmt: Die Korrelationszeiten (genauer 2-Punktkorrelationszeiten) des ursprünglichen stochastischen Prozesses (**R**) und von dessen *strong collision* Approximation (**D**) sollen identisch sein

$$\tau_2^{(SC)}(\lambda) = \tau_2\ . \tag{3.10}$$

Anschaulich ist das einzusehen, denn dann ist die mittlere Wirkungsdauer einer Störfeldrealisation für beide Prozesse gleich. Weiterhin ist mit der Selbstkonsistenzbedingung sichergestellt, daß beide Prozesse im *motional narrowing* Grenzfall die gleiche Relaxationszeit haben (ausführliche Herleitung auch für Korrelationszeiten höherer Ordnung s. Appendix B in Ref. [17]).

Die 2-Punkt Korrelationssfunktion für den *strong collision* Prozess erhält man durch Einsetzen des Generators **D** (Gl. (3.9)) anstelle des Generator **R** in Gl. (3.8). Wie in Ref. [7] und im allgemeineren Zusammenhang in Ref. [17] gezeigt ist diese Funktion ein einfacher exponentieller Abfall

$$C_2^{SC}(t) \sim e^{-\lambda t}\ , \tag{3.11}$$

d.h. die 2-Punkt Korrelationszeit des *strong collision* Prozesses ist

$$\tau_2^{SC} = \lambda^{-1} \, . \tag{3.12}$$

Die Selbstkonsistenzbedingung (3.10) legt dann λ als

$$\lambda = \tau_2^{-1} \tag{3.13}$$

fest.

3.2.2 Erweiterung der *strong collision* (ESC) Approximation

Der Ausgangspunkt für die Einführung der SC-Approximation war, daß die Störfeldflukutationen viel schneller sind, als die Dephasierung. Auf einer für die Dephasierung relevanten Zeitskala konnte dann die ursprüngliche Störfelddynamik durch die SC-Dynamik ersetzt werden. Daß bedeutet, daß die Übergangswahrscheinlichkeit zwischen zwei Störfeldzuständen nur vom Endzustand abhängt. Befindet man sich also nach einem Übergang in einem bestimmten Zustand, so kann man zwar angeben, wie lange man im Mittel dort bleibt (Korrelationszeit), es ist jedoch nicht möglich zu sagen, in welchem Zustand man vorher gewesen war. Nach einem Übergang sind also Anfangs- und Enzustand unkorreliert. Wenn man jetzt auch Zeitskalen zuläßt, bei denen Anfangs- und Endzustand von Störfeldern noch korreliert sind, so gelangt man zur erweiterten (*extended*) *strong collision* (ESC) Approximation.

Für die Konstruktion der ESC-Approximation zerlegt man zunächst den

Generator der Störfeldfluktuationen $\mathbf{R}$ spektral

$$\mathbf{R} = \sum_{j=0}^{\infty} l_j \, \mathbf{\Pi}_j \, , \tag{3.14}$$

wobei $l_0 = 0 > l_1 > \ldots$ die geordneten Eigenwerte von $\mathbf{R}$ sind, und $\mathbf{\Pi}_j = |j\rangle\langle j|$ ist der Projektionsoperator auf den Eigenraum $[\ |j\rangle\ ]$. Die Evolution der Störfeldfluktuationen ist dann durch $\exp(\mathbf{R}\ t) = \sum_{j=0}^{\infty} e^{l_j t}\, \mathbf{\Pi}_j$ gegeben. Es ist offensichtlich, daß die Eigenwerte niedriger Ordnung das Langzeitverhalten bestimmen, während mit zunehmender Ordnung das Kurzzeitverhalten des stochastischen Prozesses, und damit auch die Korrelation der Störfelder bestimmt wird. Schreibt man nun den Generator des SC-Prozesses (Gl. (3.9)) wie folgt,

$$\mathbf{D} = l_0 \mathbf{\Pi}_0 - \lambda \left(\mathbf{id} - \mathbf{\Pi}_0 \right) \tag{3.15}$$

(Hinweis $l_0 = 0$), dann ist offensichtlich, daß die SC-Approximation nur den Term niedrigster Ordnung der Spektralentwicklung (3.14) berücksichtigt, während der Beitrag der höheren Eigenwerte nur über die Selbstkonsistenzbedingung (3.10) in dem Parameter λ zusammengefaß wird. Eine natürliche Weiterentwicklung wäre, in Gl. (3.15) auch höhere Eigenwerte l_i zu berücksichtigen. Dieser Weg und dessen Nachteile sind in Ref.[17] zu finden. Wir stellen gleich einen noch allgemeineren Ansatz vor, indem wir den Generator der erweiterten *strong collision* Approximation $n-$ter Ordnung (ESC$_n$) definieren als

$$\mathbf{D} = -\sum_{j=1}^{n} \lambda_j \, \mathbf{\Pi}_j \ - \lambda (\mathbf{id} - \mathbf{\Pi}) \, , \tag{3.16}$$

wobei $\mathbf{\Pi} = \sum_{j=0}^{n} \mathbf{\Pi}_j$. Es ist offensichtlich, daß die *strong collision* Näherung der ESC$_0$-Näherung entspricht. Die Fluktuationsparameter λ_j, $j = 1, \ldots, n$ sind im allgemeinen keine Eigenwerte von $\mathbf{R}$ mehr, sondern werden, wie auch

λ, über Selbstkonsistenzbedingungen (s.u.) definiert. Weiterhin müssen die $\mathbf{\Pi}_j$ nicht notwendigerweise auf die Eigenräume von $\mathbf{R}$ projezieren, sondern im allgemeinen auf paarweise orthogonale Funktionen $|f_j\rangle$, $j = 1, \ldots, n$, mit $\langle f_i|f_j\rangle = \delta_{ij}$ und $\langle f_j|0\rangle = 0$; d.h. die Projektoren haben die Form $\mathbf{\Pi}_j = |f_j\rangle\langle f_j|$. In Ref. [17] haben wir zwei Funktionsbasen für die ESC-Approximation betrachtet: eine war durch die Eigenfunktionen gegeben, d.h. $|f_j\rangle = |j\rangle$. Die andere wurde über Polynome des Frequenzoperators Ω definiert (Ω-Basis)

$$|f_i\rangle = P_i(\mathbf{\Omega})|0\rangle \ , \tag{3.17}$$

wobei P_i eine Polynom der Ordnung i ist, dessen Koeffizienten so gewählt sind, daß die Orthonormalbedingungen erfüllt sind.

Die Fluktuationsparameter λ, λ_j, $j = 1, \ldots, n$, in Gl. (3.16) müssen über Selbstkonsistenzbedingungen bestimmt werden. Während bei der SC-Näherung die 2-Punktkorrelationsfunktion (3.8) genügte, müssen bei der ESC-Approximation auch höhere Korrelationsfunktionen betrachtet werden

$$\begin{aligned} C_m(t_{m-1}, \ldots, t_1) = & \\ & \left\langle \omega\left(\textstyle\sum_{j=1}^{m-1} t_j\right) \ldots \omega(t_2+t_1)\omega(t_1)\omega(0)\right\rangle \\ = & \ \langle 0|\mathbf{\Omega}\exp(\mathbf{R}t_{m-1})\mathbf{\Omega}\ldots\exp(\mathbf{R}t_1)\mathbf{\Omega}|0\rangle \ . \end{aligned} \tag{3.18}$$

In Ref. [17] (Abschnitt B, Appendix A) ist ausführlich beschrieben, wie aus diesen Korrelationsfunktionen höhere Korrelationszeiten bestimmt werden. Analog zur Selbstkonsistenzbedingung der SC-Approximation fordert man nun die Äquivalenz der höheren Korrelationszeiten vom ursprünglichen Prozess und von dessen ESC$_n$-Näherung. Die $n+1$ Fluktuationsparameter $\lambda, \lambda_1, \ldots, \lambda_n$ sind dann aus folgenden $n+1$ Selbstkonsistenzgleichungen zu bestimmen

$$\tau_m^{(ESC_n)}(\lambda, \lambda_1, \ldots, \lambda_n) = \tau_m \ , \tag{3.19}$$

wobei durch den Index $m = 2, ...$ die ersten $n+1$ Korrelationszeiten bezeichnet.

Die ESC-Näherung hat nun folgende Eigenschaften: die durch sie induzierte Dephasierung hat die gleiche *motional narrowing* Entwicklung $n + 1-$ter Ordnung wie der ursprüngliche Prozess (s. Appendix B in Ref. [17]). Der ESC- und der ursprüngliche Prozess bedingen weiterhin die gleiche Dephasierung im *static dephasing limit* ($\mathbf{D} \to 0, \ \mathbf{R} \to 0$). Damit interpoliert die durch den ESC-Prozeß induzierte Dephasierung die Dephasierung unter dem ursprünglichen Prozess zwischen beiden dynamischen Grenzbereichen, also im intermediären Dynamikbereich.

3.2.3 Dephasierung in der SC- und ESC-Näherung

Wir werden in diesem Abschnitt Audrücke für die Dephasierung (freier Induktionszerfall, Spin-Echo Zerfall) in der ESC$_n$-Näherung ableiten. Die SC-Näherung wird dann als Sonderfall $n = 0$ aufgeführt. Die allgemeine Herleitung der Dephasierung eines ESC$_n$-Prozesses ist ausführlich in Ref. [17], die für den SC-Prozess in der Arbeit [7] (freier Induktionszerfall) und in Ref. [15, 16] (Spin-Echo Zerfall) beschrieben.

3.2.3.1 Freier Induktionszerfall

Der freie Induktionszerfalls unter der ESC-Dynamik wird auch durch die verallgemeinerte Bloch Torrey Gleichung 3.1 beschrieben, wobei der Operator

$\mathbf{R}$ gegen $\mathbf{D}$ aus Gl. (3.16) ausgetauscht wird. Anstatt direkt den Propagator $\mathbf{U}(t) = \exp((\mathbf{D} + \mathrm{i}\mathbf{\Omega})t)$ zu berechnen, ist es einfacher, dessen Laplace-Transformierte $\hat{\mathbf{U}}(s) = (s - \mathbf{D} - \mathrm{i}\mathbf{\Omega})^{-1}$ zu bestimmen. Diese kann man wie folgt entwickeln

$$\hat{\mathbf{U}}(s) = \hat{\mathbf{U}}_0(s + \lambda) + \hat{\mathbf{U}}_0(s + \lambda)\ \mathbf{\Lambda}\ , \hat{\mathbf{U}}(s) \tag{3.20}$$

wobei $\hat{\mathbf{U}}_0(s) = (s - \mathrm{i}\mathbf{\Omega})^{-1}$ die Laplace-Transformierte im *static dephasing limit* ($\mathbf{D} = 0$) ist. Der durch die Fluktuationsparameter λ_j bestimmte Operator $\mathbf{\Lambda}$ hat die Form

$$\mathbf{\Lambda} = \sum_{j=0}^{n} (\lambda - \lambda_j)\ \mathbf{\Pi}_j\ , \tag{3.21}$$

wobei $\lambda_0 = 0$ gesetzt wurde. Die Gleichung (3.20) setzt den freien Induktionszerfall in Beziehung zu dem Zerfall der Magnetisierung im *static dephasing limit*. Betrachten wir die Operatoren in Gl. (3.20) nur innerhalb des durch den Projektionsoperators $\mathbf{\Pi} = \sum_{j=0}^{n} \mathbf{\Pi}_j$ definieren Unterraumes $\mathbf{operator}^{\Pi} := \mathbf{\Pi}\ \mathbf{operator}\ \mathbf{\Pi}$ so ist

$$\hat{\mathbf{U}}^{\Pi}(s) = \hat{\mathbf{U}}_0^{\Pi}(s + \lambda) + \hat{\mathbf{U}}_0^{\Pi}(s + \lambda)\ \mathbf{\Lambda}^{\Pi}\ \hat{\mathbf{U}}^{\Pi}(s)\ , \tag{3.22}$$

wobei die Identität $\mathbf{\Lambda} = \mathbf{\Pi}\ \mathbf{\Lambda}\ \mathbf{\Pi}$ und die Idempotenz von Projektionsoperatoren $\mathbf{\Pi} = \mathbf{\Pi}^2$ augenutzt wurden. Die Gleichung (3.22) ist von fundamentaler Bedeutung: sie zeigt, daß die in Gl. (3.20) grundsätzlich gültige Beziehung zwischen dem freien Induktionszerfall bei stochastischen Störfeldfluktuationen und dem Zerfall im *static dephasing* Grenzfall auch in dem Unterraum $[\ |0\rangle, |f_1\rangle, \ldots, |f_n\rangle\ ]$ gültig ist. Diese Eigenschaft ist spezifisch für den ESC-Prozeß bzw. dessen Generator $\mathbf{D}$. Man kann jetzt Gl. (3.22) nach der Laplace-Transformierten des Propagators auflösen

$$\hat{\mathbf{U}}^{\Pi}(s) = (\mathbf{\Pi} - \hat{\mathbf{U}}_0^{\Pi}(s + \lambda)\ \mathbf{\Lambda}^{\Pi})^{-1}\ \hat{\mathbf{U}}_0^{\Pi}(s + \lambda)\ . \tag{3.23}$$

Die Transformierte des freien Induktionszerfalls der Gesamtmagnetisierung $\hat{M}_{[n]}(s)$ ist dann durch

$$\hat{M}_{[n]}(s) = \langle 0|\, \hat{\mathbf{U}}^{\Pi}(s)\, |0\rangle \tag{3.24}$$

gegeben. Man sieht, daß aufgrund der entscheidenden Beziehung (3.22) die Berechnung des freien Induktionszerfall drastisch vereinfacht wird. Ein grundsätzlich unendlich dimensionales Problem (Gl. (3.20)) kann auf ein endlichdimensionales reduziert werden. Notwendig für die Lösung von Gl. (3.24) ist die Bestimmung des Laplace-transformierten Propagators im *static dephasing* Grenzfall innerhalb des Unterraumes $[\ |0\rangle, |f_1\rangle, \ldots, |f_n\rangle\ ]$, was grundsätzlich von der Mathematik nicht problematisch ist.

Besonders einfach wird es in der SC- (ESC$_0$)-Approximation, wo die Propagatoren nur innerhalb des 1-dimensionalen Unterraumes $[\ |0\rangle\ ]$ berechnet werden. Die Gleichungen (3.23) und (3.24) ergeben dann

$$\hat{M}_{[0]}(s) = \frac{\hat{M}_{sd}(s+\lambda)}{1 - \hat{M}_{sd}(s+\lambda)\ \lambda}\ . \tag{3.25}$$

wobei

$$\hat{M}_{sd}(s) = \langle 0|\hat{\mathbf{U}}_0(s+\lambda)|0\rangle \tag{3.26}$$

die Laplace-Transformierte des freien Induktionszerfalls im *static dephasing* Grenzfall ist.

3.2.3.2 Spin-Echo Zerfall

Für die Berechnung des Spin-Echo Zerfalls in der ESC$_n$-Näherung wird der Generator $\mathbf{D}$ in Gl. (3.6) eingesetzt und man erhält

$$\partial_t M_{SE,[n]}(t) \quad = \quad -\lambda\ M_{SE,[n]}(t) + \langle m(t/2)|\mathbf{\Lambda}|m^*(t/2)\rangle$$

$$\begin{aligned} &= -\lambda\, M_{SE,[n]}(t) + \langle 0|\mathbf{U}(t/2)\mathbf{\Lambda}\mathbf{U}^{*}(t/2)|0\rangle \\ &= -\lambda\, M_{SE,[n]}(t) + \langle 0|\mathbf{U}^{\Pi}(t/2)\mathbf{\Lambda}\mathbf{U}^{*\,\Pi}(t/2)|0\rangle\ . \end{aligned} \tag{3.27}$$

Die zeitliche Ableitung der Spin-Echo Magnetisierung ist somit eine Funktion der Spin-Echo Magnetisierung und der Projektionen des freien Induktionszerfall $\mathbf{U}^{\Pi}(t)|0\rangle$ auf den Unterraum $[\ |0\rangle, |f_1\rangle, ..., |f_n\rangle\ ]$. Die Lösung von Gl. (3.27) ist

$$M_{SE,[n]}(t) = e^{-\lambda t}\left[1 + 2\int_0^{t/2} d\xi e^{2\lambda\xi}\langle 0|\mathbf{U}^{\Pi}(\xi)\mathbf{\Lambda}\mathbf{U}^{*\Pi}(\xi)|0\rangle\right]\ . \tag{3.28}$$

3.2.4 Zeitkonstanten der Dephasierung

Der freie Induktionszerfall bzw. der Zerfall der Spin-Echo Magnetisierung werden üblicherweise durch die Zeitkonstanten T_2^* und T_2 beschrieben. Diese Konstanten bzw. Relaxationszeiten sind nicht einheitlich festgelegt. Eine übliche Definition lautet

$$\begin{aligned} 1/T_2^* &= -\ln(M(t))/t \\ 1/T_2 &= -\ln(M_{SE})/t\ , \end{aligned} \tag{3.29}$$

wobei man für die ESC$_n$-Zerfälle M gegen $M_{[n]}$ bzw. M_{SE} gegen $M_{SE,[n]}$ austauschen muß.

Eine andere Definition bestimmt die Zeitkonstanten so, daß durch sie die Zerfälle möglichst gut mit einer einfach-exponentiellen Approximation angenähert werden, $M(t) \approx e^{-t/T_2^*}$, $M_{SE} \approx e^{-t/T_2}$. Nach der *mean relaxation time approximation* Methode sind dann die Relaxationszeiten die ersten Langzeitmomente der Magnetisierungszerfälle [18],

$$T_2^* := \mu_{-1}(M) \ = \ \int_0^{\infty} dt\, M(t)$$

$$T_2 := \mu_{-1}(M_{SE}) \;=\; \int_0^\infty dt\; M_{SE}(t) \tag{3.30}$$

wobei für die ESC$_n$-Zerfälle der Index $[n]$ angehängt wird. Die so definierten Relaxationszeiten stehen in direktem Zusammenhäng mit den Laplace-Transformationen der Magnetisierungszerfälle. Speziell für die ESC-Prozesse gilt

$$\begin{aligned} T_2^* &= \hat{M}_{[n]}(0) \\ T_2 &= \hat{M}_{SE,[n]}(0)\;, \end{aligned} \tag{3.31}$$

Der Term $\hat{M}_{[n]}(0)$, der T_2^* festlegt, wird über Gl. (3.24) bestimmt. Wendet man einige Regeln für Laplace-Transformationen auf Gl. (3.27) an, dann erhält man $\hat{M}_{SE,[n]}(0)$ bzw. T_2 als

$$T_2 = \lambda^{-1} + 2\sum_{i=0}^{n}(1-\lambda_i/\lambda)\;\Theta_i\;, \tag{3.32}$$

mit

$$\begin{aligned} \Theta_0 &= \int_0^\infty dt\; |\langle 0|\mathbf{U}^\Pi(t)|0\rangle|^2 \\ &= \frac{1}{2\pi \mathrm{i}}\int_{-\mathrm{i}\infty}^{\mathrm{i}\infty} dz\; \langle 0|\hat{\mathbf{U}}^\Pi(z)|0\rangle\langle 0|\widehat{\mathbf{U}}^{*\Pi}(-z)|0\rangle \end{aligned} \tag{3.33}$$

als der Relaxationszeit des quadrierten Betrages des Induktionszerfalls $|M_{[n]}(t)|^2 = |\langle 0|\mathbf{U}(t)^\Pi|0\rangle|^2$. Die Größen

$$\begin{aligned} \Theta_i &= \int_0^\infty dt\; \langle 0|\mathbf{U}^\Pi(t)|f_i\rangle\langle f_i|\mathbf{U}^{*\Pi}|0\rangle(t)\rangle \\ &= \frac{1}{2\pi \mathrm{i}}\int_{-\mathrm{i}\infty}^{\mathrm{i}\infty} dz\; \langle 0|\hat{\mathbf{U}}^\Pi(z)|f_i\rangle\langle f_i|\widehat{\mathbf{U}}^{*\Pi}(-z)|0\rangle \end{aligned} \tag{3.34}$$

$i \geq 1$ können als mittlere Transitzeiten von Nicht-Gleichgewichtskomponenten des freien Induktionszerfalls $\langle 0|\mathbf{U}^\Pi(t)|f_i\rangle\langle f_i|\mathbf{U}^{*\Pi}|0\rangle(t)\rangle$ interpretiert werden.

Gleichung (3.32) ist von besonderer Bedeutung. Sie setzt T_2, das den inkohärenten also irreversiblen Anteil der Spin Dephasierung beschreibt, in Beziehung zur Dynamik der Störfelderfluktuationen (λ, λ_i) und zu den Zeitkonstanten des freien Induktionszerfalls (Θ_i). Diese Zeitkonstanten beschreiben die Überlagerung des kohärenten (reversiblen) und des inkohärenten (irreversiblen) Anteils der Dephasierung. Folglich kann man Gl. (3.32) als Dissipations-Fluktuations-Kohärenz Beziehung auffassen. Anzumerken ist, daß über die Gleichungen (3.33) und (3.34) die Zeitkonstanten Θ_i durch die Laplace-Transformation des freien Induktionszerfalls $\hat{\mathbf{U}}^{\Pi}(s)$ gegeben sind, wobei letztere durch die Fundamentalgleichung (3.22) bestimmt ist.

Gleichung (3.32) erlaubt asymptotische Betrachtungen für sehr langsame oder schnelle Störfeldflukutationen. Wenn ϵ ein Skalierungsparameter von $\mathbf{D}$ ist, also $\lambda,\ \lambda_i \sim \epsilon$, dann geht Gl. (3.32) im *static dephasing limit* $(\epsilon \to 0)$ über in

$$T_2 \approx \lambda^{-1} , \tag{3.35}$$

wobei wir ausnutzten, daß die Zeitkonstanten $\Theta_i(\epsilon)$ gegen endliche Grenzwerte im *static dephasing limit* gehen. Bei sehr schnellen Feldfluktuationen, also im *motional narrowing limit* $(\epsilon \to \infty)$ nutzt man aus, daß $\langle f_i|\hat{\mathbf{U}}(s)|0\rangle / \langle 0|\hat{\mathbf{U}}(s)|0\rangle \sim \epsilon^{-1}$ wie eine Potenzreihenentwicklung in ϵ zeigt, d.h. man erhält

$$T_2 \approx 2\ \Theta_0 . \tag{3.36}$$

Folglich ist bei sehr schnellen Störfeldfluktuationen die Spin-Echo Relaxationszeit poportional der Relaxationszeit des quadrierten Absolutbetrages des freien Induktionszerfalls. Das heißt vice versa, daß der freie Induktionszerfall nur irreversible Komponenten der Dephasierung hat.

Die Dissipations-Fluktuations-Kohärenz Relation (3.32) vereinfacht sich in der *strong collision* (ESC_0) Approximation zusätzlich, wenn der freie Induktionszerfall der Gesamtmagnetisierung sich durch eine einfach exponentielle Funktion beschreiben läßt, also $M_{[0]}(t) \approx e^{-t/T2^*}$. Da $\lambda = \tau_2^{-1}$ (Gl. (3.13) wird Gl. (3.32) zu

$$\begin{aligned} T_2 &= \tau_2 + 2\Theta_0 \\ &\approx \tau_2 + T_2^* \,. \end{aligned} \tag{3.37}$$

Jetzt ist direkt ersichtlich, daß im *motional narrowing limit* ($\tau \rightarrow 0$) die Relation $T_2 \approx T_2^*$ gilt, während im *static dephasing limit* ($\tau \rightarrow \infty$) in der *strong collision* Approximation $T_2 \approx \tau_2$ gilt.

Kapitel 4

Anwendungen

In diesem Kapitel wird die zuvor in dem Kapitel ,,Theorie" entwickelte Methode der *strong collision* (SC) Approximation bzw. deren Erweiterung (ESC) zur Beschreibung der Spin-Dephasierung angewendet. Insbesondere wird mit der *strong collision* Näherung der BOLD-Effekt im Herzmuskel untersucht, und die Resultate mit Simulationen und experimentellen Daten verglichen. Die ESC Approximation wird auf zwei generische Modelle der Spin-Dephasierung angewendet, das Anderson-Weiss Modell und die Dephasierung bei eingeschränkter Diffusion im einem linearen Gradienten.

4.1 Myokardialer BOLD Effekt

Die Details sind den Orginalarbeiten [7, 15, 16] zu entnehmen. Der BOLD (*blood oxygenation level dependent*) Effekt beschreibt die Abhängigkeit der transversalen Spin-Relaxation vom Oxygenierungsgrad des intravasalen Hämoglobins. Im Herzmuskel entsteht er großteils durch Spins, die in perikapillären

Magnetfeldern diffundierend, dephasieren. Die Bedeutung der Kapillaren im Vergleich zum venösen System erklärt sich daraus, daß 90% des myokardialen Blutvolumens in den Kapillaren zu finden ist [19], d.h. der überwiegende Anteil des desoxygenierten, also paramagnetischen Hämoglobins ist ebenfalls dort lokalisiert. Die Tatsache, daß der BOLD Effekt damit von der funktionellen Kapillardichte abhängt, läßt sich möglicherweise auch diagnostisch nutzen. So beobachteten wir erstmals bei Patienten mit einem verengten Kranzgefäß eine Reduktion von T_2^* im nachgeschalteten Myokard [4]. Erklärbar ist dieses Phänomen durch einen autoregulatorischen Anstieg der funktionellen Kapillardichte, und damit eine Zunahme des desoxygenierten Hämoglobins im betroffenen Myokard.

Für die Modellierung des BOLD Effektes im Myokard berücksichtigten wir nur den Gefäßtyp der Kapillare. Diese sind parallel und regelmäßig angeordnet. Daher betrachteten wir nicht das gesamte Herzmuskelgewebe, sondern nur eine zylinderförmige Kapillare (Radius R_c), die konzentrisch von einem zylinderförmigen Versorgungsgebiet umgeben ist (Radius R_s). Die Diffusion der Spins wurde auf den Raum innerhalb dieser Zylinder eingeschränkt, wobei wir ausnutzten, daß die Kapillarwand auf der Zeitskala der Dephasierung (30-50 ms) fast impermeabel ist. Die Einschränkung innerhalb des Versorgungszylinders war möglich, da wir Diffusionstrajektorien, die von dem Versorgunsgebiet einer Kapillare zu dem der benachbarten zogen, durch Trajektorien ersetzten, die am inneren Rand des ursprünglichen Gebietes reflektiert wurden. Eine weitere Vereinfachung ergab sich daraus, daß nur die extrakapillären Spins betrachtet wurden, da das Intrakapillarvolumen ($\varsigma = R_c^2/R_s^2$) weniger als 10% des Gewebevolumens ausmacht. Weil das Verhältnis von Kapillarlänge zu Interkapillarabstand sehr groß ist ($>$ 20), ist der Desoxyhämoglobin-Gradient und somit die Inhomogenität des Magnetfeldes entlang der Kapillarachse vernachlässigbar.

Zusammenfassend betrachteten wir also eine zweidimensionale Diffusion innerhalb konzentrischer Kreise mit den Radien R_c und R_s. Die Bloch-Torrey Gleichung (3.2), welche die lokale Quermagnetisierung am Punkt $x = (r, \phi)$ beschreibt, hat die Form

$$\partial_t m(x,t) = (D[\nabla^2] + \mathrm{i}\omega(x))\, m(x,t)\ , \tag{4.1}$$

wobei D der Diffusionskoeffizient und $\omega(x)$ die lokale Frequenz des perikapillären Magnetfeldes ist. Die Klammern [ ] symbolisieren, daß der Differentialoperator nur auf Funktionen angewendet wird, welche die reflektorischen Randbedingungen

$$\partial_r m(r,\phi,t) \equiv 0 \ \text{ bei } r = R_c,\ R_s \tag{4.2}$$

berücksichtigen. Nach den Gesetzen der Magnetostatik wird in einem äußeren Magnetfeld B_0 um die Kapillaren mit paramagnetischen Inhalt (Desoxyhämoglobin) ein Magnetfeld induziert, dessen lokale Frequenz

$$\omega(r,\phi) = -\delta\omega R_c^2 \cos(2\phi)/r^2\ , \tag{4.3}$$

ist, wobei

$$\delta\omega = 2\pi\gamma\Delta\chi B_0 \sin(\theta) \tag{4.4}$$

die äquatoriale Frequenzverschiebung ist. Der Parameter γ ist das gyromagnetische Verhältnis ($= 2.675 \cdot 10^8 \mathrm{rad\ s^{-1}}$), $\Delta\chi$ ist die Suszeptibilitätsdifferenz zwischen Intra- und Extrakapillarraum, und θ ist der Winkel zwischen Kapillarachse und äußerem Feld.

Die Abhängigkeit der Suszpetibilitätsdifferenz von der relativen Sauerstoffsättigung des Blutes Y wird durch

$$\Delta\chi = \Delta\chi_0\,(1 - Y)\ , \tag{4.5}$$

beschrieben, wobei $\Delta\chi_0$ der Suszeptibilitätssprung bei vollkommen desoxygeniertem ($Y = 0$)Blut ist. Da für diesen Parameter bei einem Hämatokrit von $\approx 40\%$

$$\Delta\chi = 8 \cdot 10^{-8} \tag{4.6}$$

gilt [12], ist bei klinischen Scannern (magnetische Flußdichte $B_0 \leq 2$T) die induzierte intrakapilläre Magnetisierung

$$\Delta M = \Delta\chi B_0 \sin(\theta) \tag{4.7}$$

kleiner als 1.6 mgauss und $\delta\omega = 2\pi\gamma\Delta M \leq 269$ rad s^{-1}. Nimmt man realistische Werte für den Versorgungsradius ($R_s \approx 11$ μm) und den Durchmesser einer Kapillare ($2R_c \approx 5 - 5.5$ μm), so erhält man am Rand des Versorgungsgebietes eine Präzessionsfrequenz ≤ 17 rad s^{-1}, d.h. Beiträge von Magnetfeldern benachbarter Kapillaren können vernachlässigt werden.

Der Magnetisierungszerfall, bzw. dessen Laplace-Transformierte $\hat{M}_{[0]}(s)$, hängt in der *strong collision* Näherung lt. Gl. (3.25) nur vom Fluktuationsparameter λ und der Laplace-Transformierten im *static dephasing* Grenzfall (Gl. (3.26)) ab. Diese konnte von uns (s.Ref. [7] Appendix) als

$$\hat{M}_{sd}(s) = \frac{1 + \varsigma}{\sqrt{s^2 + \delta\omega^2\varsigma^2} + \varsigma\sqrt{s^2 + \delta\omega^2}}\ , \tag{4.8}$$

bestimmt werden, wobei $\varsigma = R_c^2/R_s^2$ das relative Intrakapillarvolumen ist

[1]. Der Parameter λ ist bei einem *strong collision* Prozeß dessen inverse 2-Punkt Korrelationszeit τ^{SC} (Gl. 3.12). Die Selbstkonsistenzbedingung fordert die Äquivalenz der 2-Punkt Korrelationszeiten des *strong collision* und des ursprünglichen Prozesses (Gl. (3.10)). Die letztere wurde von uns für das Kapillarmodell [7, 15] als

$$\tau = \frac{R_c^2}{4D} \frac{\ln(\varsigma)}{\varsigma - 1} \tag{4.9}$$

bestimmt, wodurch dann der Fluktuationsparameter über

$$\lambda = \tau^{-1} \tag{4.10}$$

festgelegt ist.

Die Relaxationszeit des freien Induktionszerfalls der Gesamtmagnetisierung ergibt sich entsprechend Gl. (3.31) als (s. Refs. [7, 15])

$$\begin{aligned} T_2^* &= \hat{M}_{[0]}(0) \\ &= \frac{\tau(1+\varsigma)}{[\sqrt{1+(\varsigma\tau\delta\omega)^2}-1]+\varsigma[\sqrt{1+(\tau\delta\omega)^2}-1]} \, . \end{aligned} \tag{4.11}$$

Wenn das relative Intrakapillarvolumen, wie bei den meisten Geweben, klein ist $\varsigma \ll 1$, kann man die Relaxationszeit in Gl. (4.11) wie folgt annähern

$$T_2^* \approx \frac{\tau}{\varsigma[\sqrt{1+(\tau\delta\omega)^2}-1]} \tag{4.12}$$

Der Zerfall der Spin-Echo Magnetisierung nimmt bei der *strong collision* Näherung entsprechen Gl. (3.28) und Gl. (4.10) die Form

$$M_{SE,[0]}(t) = e^{-t/\tau}\left[1 + 2\tau^{-1}\int_0^{t/2} d\xi e^{2\xi/\tau}|M_{sd}(\xi)|^2\right] \, . \tag{4.13}$$

---

[1] in Refs. [7, 16] wird das relative intrakapilläre Blutvolumen ς auch als *RBV* bezeichnet. Wegen der Komplexität der Formeln wurde jedoch in Ref. [15] und in diesem Kapitel die kürzere Bezeichnung ς gewählt.

an, wobei diese Gleichung bereits in den Arbeiten [15, 16] abgeleitet wurde.

4.1.1 Vergleich mit Simulationen

Kennan et al. [8] simulierte die Dephasierung diffundierender Spins in perikapillären Magnetfeldern, wobei die Querschnitte der parallelen Kapillaren ein quadratisches Gitter bildeten. Die Autoren untersuchten die Abhängigkeit der Relaxationsrate $1/T_2^*$ von der induzierten intrakapillären Magnetisierung $\Delta M = \Delta\chi B_0$ und fanden ein Potenzgesetz

$$\frac{1}{T_2^*} \sim \Delta M^{\epsilon} , \tag{4.14}$$

wobei der Parameter ϵ vom Diffusionsregime (=Regime der Störfelddynamik) abhängt. Dieses wurde von der Autoren über die Diffusionszeit, in der ein Spin eine Distanz eines Kapillarradius zurückgelegt hat $\tilde{\tau} = R_c^2/D$, abgeschätzt, wobei der Zusammenhang mit der Korrelationszeit in Gl. (4.9) offensichtlich ist. Für ein langsames ($\tilde{\tau} = 6250$ ms), mittelschnelles ($\tilde{\tau} = 9.61$ ms) und schnelles ($\tilde{\tau} = 3.125$ ms) Diffusionsregime war $\epsilon = 1.1, \quad 1.49$ und 1.95. Entsprechend Gl. 4.11 ergibt unser Modell für ein sehr langsames Diffusionregime ($\tau \to \infty$), $1/T_2^* = 2\varsigma\ \delta\omega$, für ein schnelles Diffusionsregime $\tau \to 0$ das *motional narrowing* Resultat $1/T_2^* = \varsigma\tau\delta\omega^2/2$. Da $\delta\omega \sim \Delta M$, entsprechen unsere Resultate den Simulationsergebnissen. Setzt man die Parameter von Kennan et al. für das intermediäre Diffusionsregime in Gl. (4.11) ein, so fanden wir nach doppelt logarithmisch-linearer Regression $\log(1/T_2^*)$ vs. $\log(\Delta M)$ für den Exponenten in Gl. (4.14) $\epsilon = 1.61$ (s. Abb.3 in Ref.[7]), d.h. nahe dem durch Simulation gefundenen Wert.

Weiterin untersuchten Kennan et al. die Relaxationsraten des freien Induktionszerfalls $1/T_2^*$ und Spin-Echo Zerfalls $1/T_2$ in Abhängigkeit vom Diffusionskoeffizienten D. Zum Vergleich mit der *strong collision* Näherung setzten wir deren Simulationsparametern (relatives Intrakapillarvolumen ς, Kapillarradius R_c, intrakapilläre Magnetisierung ΔM) in Gl. (4.11) für die Berechnung von T_2^* bzw. in Gl. (4.13) für die Berechung von T_2 nach Gl. (3.29) ein [7, 15, 16]. Sowohl für den freien Induktionszerfall (Abbildungen 2 in Refs. [7, 15], Abb. 4 in Ref. [16]), als auch für den Spin-Echo Zerfall (Abbildungen 1 und 2 in Ref. [15], 3 und 4 in Ref. [16]) zeigte sich eine gute Übereinstimmung zwischen Simulations- und Modelldaten. Sowohl das asymptotische Verhalten ($\log(D) \to \pm\infty$), als auch der Verlauf im Intermediärbereich wurde korrekt beschrieben. Die Abbildung 2 aus Ref. [16] ist als Abb. 4.1 zu sehen.

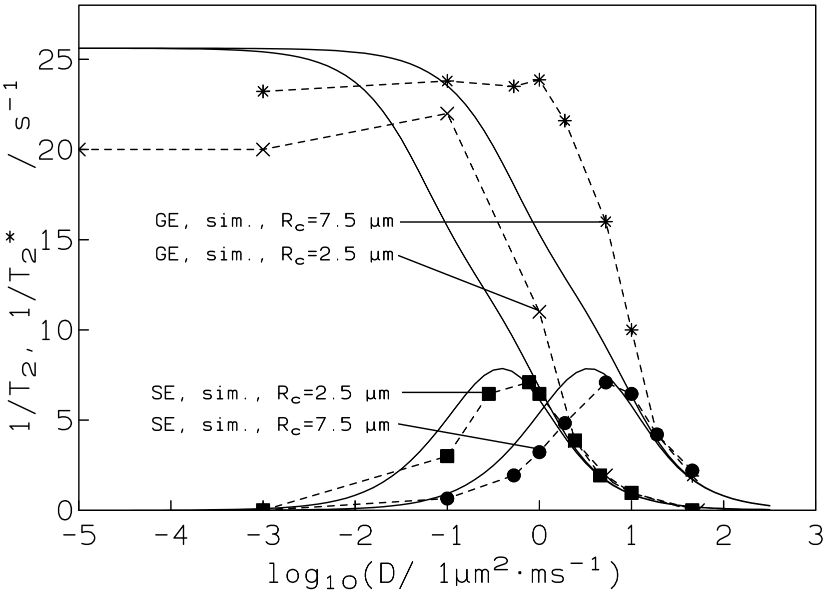

Abbildung 4.1: Relaxationsraten des freien Induktions- ($1/T_2^*$) und Spin-Echo ($1/T_2$) Zerfalls als Funktion des Diffusionskoeffizienten D. Das relative intrakapilläre Blutvolumen ist $\varsigma = 5\%$. Betrachtet werden zwei Kapillarradien: $R_c = 2.5\mu$m (x: Simulationsdaten eines Gradientenechoexperiments (GE, sim.) für den freien Induktionszerfall, Quadrat: für den Spin-Echozerfall (SE, sim.)); $R_c = 7.5\mu$m ($*$: Simulationsdaten für den freien Induktionszerfall (GE, sim.), Kreis: für den Spin-Echozerfall (SE, sim.). Die durchgezogenen Linien wurden von uns analytisch berechnet

4.1.2 Vergleich mit experimentellen Daten

4.1.2.1 Experimente am isolierten Herzen

Atalay et al. [20, 21] bestimmten in isolierten, mit Blut perfundierten Kaninchenherzen die Relaxationsraten des freien Induktionszerfall und der Spin-Echo Magnetisierung bei unterschiedlich starker Sauerstoffsättigung Y des Hämoglobins (s.a. Gl. (4.5). Durch eine hohe Kaliumkonzentration im Blut waren die Herzen kardioplegisch (nicht schlagend), weiterhin waren die Gefäße medikamentös maximal dilatiert. Diese spezielle Präparation hat folgenden Sinn: durch die maximale Dilatation der Blutgefäße hat man ein starres Gefäß- bzw. Kapillarsystem, und die funktionelle Kapillardichte entspricht der anatomischen. Dadurch ist der BOLD Effekt nur eine Funktion der intravasalen Desoxyhämoglobinkonzentration. Ein natives Gefäßsystem würde bei einer niedrigen Oxygenierung kompensatorisch dilatieren, d.h. der BOLD Effekt wäre eine komplexe Funktion der Vasomotorik und der intravasalen Desoxyhämoglobinkonzentration. Der durch die Kardioplegie stark gedrosselte Sauerstoffverbrauch führt dazu, daß wie von uns in Ref. [7] berechnet, nur ein minimaler Gradient der Oxygenierung entlang der Kapillarachse besteht. In erster Näherung ist also die intrakapilläre O_2-Sättigung des Hämoglobins identisch mit der eingestellten im Perfusat.

Atalay et al. leiteten empirische Formeln für die Abhängigkeit der Relaxationsraten vom Oxygenierungsgrad ab $(1/T_2^* = f(Y),\ 1/T_2 = g(Y))$. Zum Vergleich mit der *strong collision* Näherung bestimmten wir $\delta\omega$ als Funktion der O_2-Sättigung Y nach den Gleichungen (4.4, 4.5), wobei wir entsprechend dem Apparaturaufbau von Atalay et al. den Winkel zwischen äußerem

Magnetfeld und Kapillarachse $\theta = \pi/2$ setzten. Das relative Intrakapillarvolumen ς unter maximaler Dilatation wurde wie aus der Literatur bekannt als 10% und der Kapillarradius 2.75μm gesetzt [14]. Die Relaxationszeit des freien Induktionszerfalls wurde aus Gl. (4.11), die des Spin-Echo Zerfalls aus Gl. (4.13) für eine von Atalay et al. vorgegebene Echozeit bestimmt. Wie aus der Abbildung 4.2 bzw. den Orginalabbildungen 5 aus Refs. [7, 16] zu ersehen ist, stimmen unsere Resultate sehr gut mit den empirischen Kurven überein.

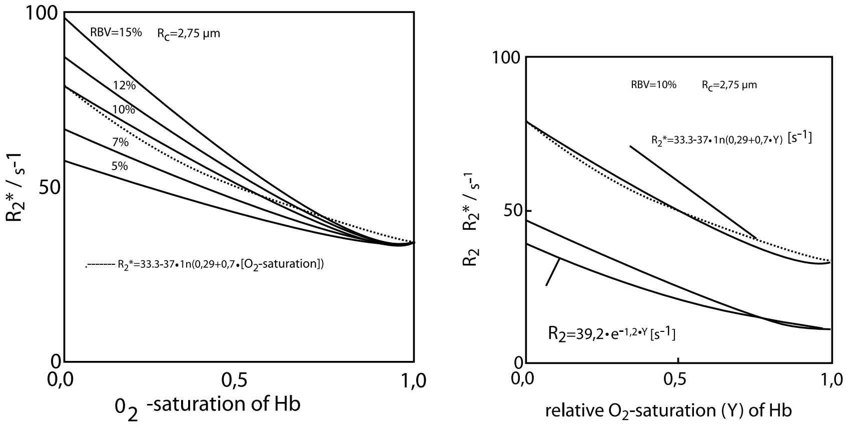

Abbildung 4.2: $R_2^* = 1/T_2^*$, $R_2 = 1/T_2$ des Herzmuskels als Funktion der Sauerstoffsättigung des Hämoglobins. Von Atalay et al. [20] wurden über Gradienten Echo (R_2^*) oder Spin-Echo (R_2) Experimente bei 4.7 Tesla an isolierten, mit Blut perfundierten Herzen empirische Gleichungen gefunden, die in den Bildern zu sehen sind. Die von uns errechneten Linien ergeben sich aus den Gleichungen (4.9,4.12) für R_2^* bzw. aus Gl. (4.13 mit $R_2 = -\ln M_{SE,[0]}(t)/t$), wobei eine Echozeit von $t = 23$ms [21] angenommen wurde. Der Diffusionskoeffizient wurde $D = 1\mu\text{m}^2/\text{ms}$ gesetzt. Da unser Modell nur den BOLD Anteil der Relaxation berücksichtigt, ist der *offset* der Modellkurven bei 100% Sauerstoffsättigung identisch mit dem der empirischen Kurven. Der Kapillarradius betrug 2.75μm. Die relativen Intrakapillarvolumina $RBV = \varsigma$ sind in den Zeichnungen eingesetzt. Der Wert $RBV = \varsigma = 10\%$ entspricht dem Literaturwert bei maximaler Dilatation.

4.1.2.2 Messungen am menschlichen Herzen

Unsere Arbeitsgruppe bestimmte die Relaxationszeit des freien Induktionszerfalls T_2^* am menschlichen Herzen mittels einer segmentierten Multigradientenecho-Sequenz, wobei 10 Bilder in der kurzen Herzachse mit Echozeiten von 6 bis 54 ms aufgenommen wurden. [3]. Mittels EKG Triggerung erfolgte die Bildaufnahme middiastolisch mit einer *inplane* Auflösung von 1.61mm ×1.17 mm. Nach manueller Segmentierung des linksventrikulären Myokards wurde aus den Relaxationskurven des freien Induktionszerfalls mittels eines Exponentialfits T_2^* mit einem Fehler $< 2\%$ bestimmt. Die T_2^* Messungen erfolgten unter Basalbedinungen und nach Gabe des Vasodilatators Dipyridamol. Da dieser Vasodilatator die Perfusion steigert, ohne die Herzarbeit zu erhöhen, führte die Hyperperfusion zu einem Anstieg der intrakapillären Oxygenierung. Dieser führte bei Messungen an 16 Probanden zu einer Verlängerung von T_2^* (Abb.4.3, diese entspricht Abb. 5 in Ref. [3]), wobei im Mittel der Basalwert von $T_2^* = 35 \pm 3$ms im linksventrikulären Myokard auf einen Spitzenwert von $T_2^* = 42 \pm 5$ms ($P < 0.05$) anstieg [3]. Unsere ausführlichen Modellrechnungen in Ref. [7] zeigten, daß bei einer physiologisch normalen basalen intrakapilläre Oxygenierung von $Y = 25 - 40\%$, ein Anstieg auf 40 - 42.6 ms zu beobachten wäre, d.h. man liegt sehr gut im beobachteten Größordnungsbereich.

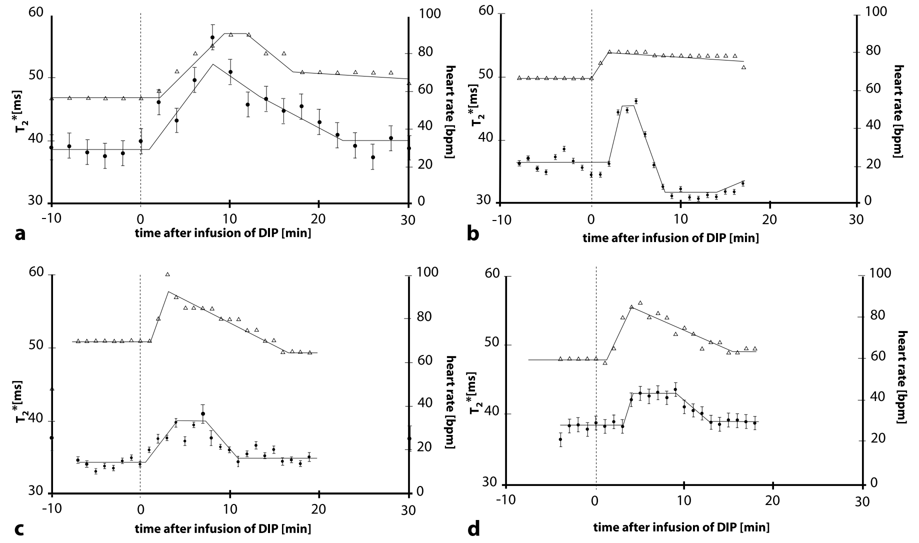

Abbildung 4.3: T_2^*- (Kreis) und Herzfrequenzverlaufskurven (Dreieck) nach Dipyridamolinfusion von 4 Probanden. Der Beginn der Dipyridamolinfusion ist mit einer gestrichelten Linie markiert. Von der Substanz wurde 0.84mg/kg Körpergewicht in 4 Minuten infundiert. Man beachte, daß sowohl der Anstieg der Herzfrequenz, als auch der von T_2^* unterschiedliche Verläufe haben kann. In der Unterabbildung b) fällt T_2^*, nach initialem Anstieg sogar unter seinen Ausgangswert.

4.2 Anwendungen der ESC-Approximation

Die Erweiterung der *strong collision* Näherung (ESC) ist ausführlich in der Orginalarbeit [17] beschrieben.

4.2.1 Das Anderson-Weiss Modell

Das Anderson-Weiss Modell [5] wurde bereits im Kapitel ,,Theorie der Spin-Dephasierung” behandelt. Für das Anderson-Weiss Modell existieren analytische Lösungen für den freien Induktionszerfall $M(t)$ und den Zerfall der Spin-Echo Magnetisierung $M_{SE}(t)$

$$\begin{aligned} M(t) &= \exp\left[-\int_0^t (t-\xi)\; c_2(\xi)\; d\xi \right] && (4.15) \\ M_{SE}(t) &= \exp\left[-4\int_0^{t/2} (t/2-\xi)\; c_2(\xi)\; d\xi \right. \\ &\qquad \left. + \int_0^t (t-\xi)\; c_2(\xi)\; d\xi \right] , && (4.16) \end{aligned}$$

wobei c_2 die Zweipunkt Korrelationsfunktion ist. Bei der Ableitung des Anderson-Weiss Modells wurde vorausgesetzt, daß die Verteilung des Phasenwinkels $\phi(t) = \int_0^t d\xi\;\; \omega(\xi)$ Gauß-förmig ist. Wie wir zeigen konnten bedeutet dies, daß die Greensfunktion, also die bedingte Wahrscheinlichkeit zwischen zwei Störfeldrealisationen $\omega_1,\;\omega_2$, ebenfalls eine Gaußfunktion in ω_1 und ω_2 ist. Wir konnten in Ref. [17] mit Verfahren aus [22] zeigen, daß dann die Wahrscheinlichkeitsdichte der Störfeldrealisationen $p(\omega, t)$ einer Fokker-Planck Gleichung genügt

$$\begin{aligned} \partial_t p(\omega, t) &= \mathbf{R}\, p(\omega, t) \\ &= \partial_\omega\; D(\omega)(\partial_\omega - F(\omega))\; p(\omega, t)\; , && (4.17) \end{aligned}$$

wobei $D(\omega)$ ein im allgemeinen von ω abhängiger Diffusionkoeffizient, und $F(\omega)$ eine Driftkraft ist. Da die Gleichgewichtsverteilung Gauß-förmig ist, muß $F(\omega) = -c \cdot \omega$ mit $c > 0$. Die generalisierte Bloch-Torrey Gleichung (3.1), welche die Dephasierung als Überlagerung der Präzessions- und der stochastischen Übergangsdynamik beschreibt, hat dann die Form

$$\partial_t m(\omega, t) = [\partial_\omega D(\omega)(\partial_\omega + c\,\omega) + \mathrm{i}\,\omega] m(\omega, t)\ . \tag{4.18}$$

Die von uns abgeleiteten Beziehungen (4.17), (4.18) sind von grundlegender Bedeutung. Sie sagen aus, daß Markov'sche Störfeldfluktuationen in ω, die den Anderson-Weiss Bedingungen genügen, äquivalent durch einen Diffusionsprozeß in ω innerhalb eines harmonischen Potentials $c\,\omega^2/2$ beschrieben werden können.

Für das weitere Prozedere ist es einfacher Gl. (4.18)durch Variablentransformation $\omega \to c^{1/2}\omega$ und $t \to c^{-1/2}t$ umzuschreiben in Gl. (4.18) to

$$\partial_t m(\omega, t) = [\partial_\omega \beta(\omega)(\partial_\omega + \omega) + \mathrm{i}\,\omega] m(\omega, t) \tag{4.19}$$

wobei wir der Einfachheit halber auch die transformierten Variablen weiter als ω und t schreiben und $\beta = c^{3/2}\ D$ als den (transformierten) Diffusionkoeffizienten bezeichnen. Dieser soll im weiteren als konstant angenommen werden.

4.2.1.1 ESC-Approximation

Der Propagator in der ESC-Approximation berechnet sich aus dem Propagator im *static dephasing limit* $\mathbf{U}_0 = \exp(\mathrm{i}\boldsymbol{\Omega}t) = [\exp(\mathrm{i}\omega t)]$, und der $\boldsymbol{\Lambda}$-Matrix aus Gl. (3.21), wobei die Operatoren entweder auf den Funktionsraum [$|0\rangle$] für die ESC$_0$ (=*strong collision* Approximation) oder [$|0\rangle$, $|f_1\rangle$]

für die ESC_1-Approximation Gl. (3.23) eingeschränkt werden. Die spezielle Struktur des stochastischen Übergangsoperators beim Anderson-Weiss Modell $\mathbf{R} = \partial_\omega \beta(\partial_\omega + \omega)$ bedingt, daß die Eigenfunktionsbasis Hermite-Polynome in ω sind, d.h. Eigenfunktions- und Ω-Basis (Gl. 3.17) sind in diesem Modell identisch. Wir setzten also im folgenden $|f_1\rangle = P_1(\mathbf{\Omega})|0\rangle = |1\rangle$

ESC_0(=*strong collision*)-Approximation Das Matrixelement des Laplace-transformierten Propagators im *static dephasing limit*, welches für die ESC_0-Näherung benötigt wird, ist

$$\langle 0|\hat{\mathbf{U}}_0(s)|0\rangle = \sqrt{\pi/2}\, e^{s^2/2} \,\mathrm{cerf}(s/\sqrt{2}) \quad , \tag{4.20}$$

wobei $\mathrm{cerf}(z) = 1 - \mathrm{erf}(z)$ die komplementäre Fehlerfunktion ist. Der Fluktuationsparameter λ, der die Selbstkonsistenzbedingung 3.10 garantiert, konnte von uns als

$$\lambda = \beta \ , \tag{4.21}$$

bestimmt werden.

ESC_1-Approximation Die Matrixelemente des Laplace-transformierten Propagators im *static dephasing limit*, die für die ESC_1-Approximation in der Ω-Basis benötigt werden sind

$$\begin{aligned} \langle 0|\hat{\mathbf{U}}_0(s)|1\rangle &= N\,\mathcal{L}[\langle 0|\exp(\mathrm{i}\mathbf{\Omega}t)\mathbf{\Omega}|0\rangle] \\ &= N\,(-\mathrm{i})\mathcal{L}[\partial_t\langle 0|\exp(\mathrm{i}\mathbf{\Omega}t)|0\rangle] \\ &= N\,\mathrm{i}(1 - s\langle 0|\hat{\mathbf{U}}_0(s)|0\rangle) \ , \end{aligned} \tag{4.22}$$

wobei N ein Normierungsfaktor mit $N^2 = \langle 0|\mathbf{\Omega}^2|0\rangle$ ist, was in unserem Fall sich zu $N = 1$ vereinfacht; $\mathcal{L}$ symbolisiert die Laplace-Transformation. Die weiteren Matrixelemente erhält man mittels elementare Regeln der Laplace-Transformation als

$$\begin{aligned} \langle 1|\hat{\mathbf{U}}_0(s)|0\rangle &= \langle 0|\hat{\mathbf{U}}_0(s)|1\rangle \\ \langle 1|\hat{\mathbf{U}}_0(s)|1\rangle &= N^2\, s\, (1 - s\, \langle 0|\hat{\mathbf{U}}_0(s)|0\rangle)\ , \end{aligned} \tag{4.23}$$

Es sollte hervorgehoben werden, daß die Gleichungen (4.22) bis (4.23) für alle ESC$_1$-Näherungen in einer Ω-Basis gelten.

Die Fluktuationsparameter der ESC$_1$-Näherung λ, λ_1 müssen die Selbstkonsistenzbedinung Gl. (3.13) erfüllen. Wir konnten diese als

$$\begin{aligned} \lambda_1 &= \beta \\ \lambda &= 2\beta\ , \end{aligned} \tag{4.24}$$

bestimmen.

4.2.1.2 Relaxation in der ESC$_0$ und ESC$_1$ -Näherung

Die Matrix $\hat{\mathbf{U}}_0^{\Pi}(s)$ und die Flukutationsparameter, die in der Λ-Matrix zusammengefaßt sind, bestimmen den Laplace-transformierten ESC-Propagator $\hat{\mathbf{U}}^{\Pi}(s)$ (Gl. (3.23)), der selber wiederum der Ausgangspunkt für alle weiteren Berechnungen ist. Man erhält nach Gl. (3.31) die Relaxationszeit T_2^*, wenn diese als erstes Langzeitmoment des freien Induktionszerfalls definiert wird (Gl. (3.24). Setzt man $\hat{\mathbf{U}}^{\Pi}(s)$ in die Gleichungen (3.33,3.34) ein, so erhält man nach Gl. (3.32) die Spin-Echo Relaxationszeit T_2, sofern diese als erstes Langzeitmoment der Spin-Echo Relaxationskurve definiert ist. Die inverse Laplace-Transformation von $\hat{\mathbf{U}}^{\Pi}(s)$ ergibt den ESC-Propagator $\mathbf{U}^{\Pi}(t)$, der erlaubt, die Spin-Echo Zerfallskurve nach Gl. (3.28)zu berechnen.

Die Relaxationszeit $T_2^* := \mu_{-1}(M)$ des Anderson-Weiss Prozesses wird gut durch die ESC_0 und ESC_1-Approximation über den gesamten dynamischen Bereich der Störfeldflukutationen (Diffusionsregime) angenähert, wie in Abb. 1 der Ref. [17] zu sehen ist. Zum *static dephasing limit* hin, nähern sich alle Kurven asymptotisch $\lim_{\beta\to 0} \mu_{-1}^{-1}(\beta) = \sqrt{2/\pi}$. Die schrittweise bessere Näherung der Spin-Echo Relaxation von der ESC_0 zur ESC_1-Approximation wird durch die Zerfallskurven der Magnetisierung (Abb. 2) und die Abhängigkeit der Relaxationsraten $1/T_2$ vom Diffusionkoeffizienten (Abbildungen 3 und 4 in Ref. [17]) deutlich. Die $1/T_2(D)$ Kurve des Anderson-Weiss Prozesses konvergiert im *motional narrowing* Grenzfall ($\tau_2(\langle 0|\mathbf{\Omega}^2|0\rangle)^{1/2} = \beta^{-1} \ll 1$) gegen die seiner ESC-Approximationen. Alle Kurven zeigen eine vergleichbare Lokalisation des Maximums. Zum *static dephasing* Grenzfall hin ($\beta \to 0$) fallen die Relaxationsraten beim Anderson-Weiss Prozeß schneller ab, als die der ESC-Prozesse.

4.2.2 Eingeschränkte Diffusion im linearen Magnetfeld

4.2.2.1 Beschreibung des Prozesses

Die Dephasierung durch eingeschränkte Diffusion im linearen Magnetfeld ist ein Modell, daß aufgrund seiner Einfachheit Einblicke in grundsätzliche Eigenschaften der diffusionsvermittelten Phasenrelaxation eröffnet. Es ist jedoch nicht nur von akademischem Interesse. In biologischen Geweben ist z.B. durch die Kompartimentisierung (Zellmembranen, Gefäßwände etc.) die Diffusion häufig eingeschränkt, und inhomogene Magnetfelder können innerhalb der Kompartimente linear approximiert werden. Während die Dephasierung frei diffundierender Spins im linearen Magnetfeld analytisch gelöst werden kann, existieren jedoch nur numerische Lösungen für die eingeschränkte Diffusion [23]. Wir werden letzteren Fall durch die *strong collision* (ESC_0) und ESC_1-Prozess annähern. Bei der ESC_1-Approximation werden zwei Funktionsbasen analysiert: die Ω-Polynom Basis, also $|f_1\rangle \sim \mathbf{\Omega}|0\rangle$ und die Eigenfunktionsbasis, also $|f_1\rangle = |1\rangle$.

Die Spins sollen in einem Intervall der Länge L in einem linearen Magnetfeld mit der Frequenz $\omega(x) = g\ x$ diffundieren. An Rand $x = \pm L/2$ werden die Spins reflektiert, also gilt dort für die Magnetisierung $\partial_x m(\pm L/2, t) \equiv 0$. Mit dem Diffusionskoeffizienten D und $\mathbf{R} = D[\partial_x^2]$ wird die Bloch Torrey Gl. (3.1) zu $\partial_t m(x,t) = (D[\partial_x^2] + \mathrm{i} g x) m(x,t)$, wobei die Klammern [ ] symbolisieren, daß der Operator ∂_x^2 nur auf Funktionen, die den Randbedingungen genügen, angewendet wird. Eine Transformation in dimensionslose Variablen $x \to x/L$ and $t \to t\ g\ L$ resultiert in

$$\partial_t m(x,t) = (\beta\ [\partial_x^2] + \mathrm{i}\ x)\ m(x,t)\ , \tag{4.25}$$

mit verschwindenden Ableitungen der Magnetisierung am Rande des Einheitsintervalls

$$\partial_x m(\pm 1/2, t) \equiv 0\ . \tag{4.26}$$

Der dimensionslose Diffusionskoeffizient ist $\beta = D/(gL^3)$. Die tranformierten Variablen werden ebenfalls als x und t bezeichnet. Wenn, wie immer angeommen, die initiale Magnetisierung der Gleichgewichtswahrscheinlichkeit proportional ist, $m(x,0) \equiv 1$, dann genügt die Laplace-Transformierte $\hat{m}(x,s)$ der lokalen Magnetisierung

$$(\beta\ [\partial_x^2] + \mathrm{i}\ x)\hat{m}(x,s) = -1\ . \tag{4.27}$$

Die Gleichungen (4.25, 4.27) wurden numerisch gelöst. Der freie Induktionszerfall der gesamten Magnetisierung ergab sich durch Integration im Einheitsintervall von $m(x,t)$. Anwendung von Gl. (3.6) auf $m(x,t)$ ergab die Spin-Echo Magnetisierung. Die Spin-Echo Relaxationszeit, definiert als das erste statistische Moment des Zerfalls, wurde über Gl. (3.30) bestimmt. Wenn T_2^* als das erste Moment des freien Induktionszerfalls definiert ist, wurde nach Bestimmung von $\hat{m}(x,s)$ aus Gl. (4.27) diese Funktion über dem Einheitsintervall integriert $\int_{-1/2}^{1/2} dx\ \hat{m}(x,s) = \hat{M}(s)$ und die Relaxationszeit als $T_2^* = \hat{M}(0) = \mu_{-1}(M)$ bestimmt.

4.2.2.2 ESC-Approximation

Die Vorgehensweise bei der ESC$_0$ und ESC$_1$-Approximation ist fast analog der beim Anderson-Weiss Modell. Allerdings sind hier Ω-Polynom und Eigenfunktionsbasis nicht identisch.

ESC$_0$-Approximation Der dem Diffusionoperator $[\partial_x^2]$ zugeordnete Gleichgewichtszustand wird im Einheitsintervall durch die Funktion

$$|0\rangle \equiv 1\ , \tag{4.28}$$

beschrieben. Daraus folgt, wie in Ref. [17] gezeigt,

$$\langle 0|\hat{\mathbf{U}}_0(s)|0\rangle = \mathrm{i}\ \ln\left(\frac{s-\mathrm{i}/2}{s+\mathrm{i}/2}\right)\ . \tag{4.29}$$

Aufgrund der Selbskonsistenzbedinunge für den *strong collision* Prozess (3.10) wird der Parameter λ bestimmt als

$$\lambda = 10\ \beta \tag{4.30}$$

Nach Einsetzen der Resultate der Gleichungen (4.29) und (4.30) in Gl. (3.23) ergibt die Laplace-Transformierte des Propagators in der ESC_0-Näherung $\langle 0|\hat{\mathbf{U}}(s)|0\rangle$ aus der T_2^*, T_2 und die Spin-Echo Zerfallskurven bestimmt wurden.

ESC_1-Approximation in der Ω-Polynom Basis: Die erste nichttriviale Basisfunktion der Ω-Polynom Basis hat die Form

$$\begin{aligned} |f_1\rangle &= \langle 0|\mathbf{\Omega}|0\rangle^{-1/2}\,\mathbf{\Omega}|0\rangle \\ &= 2\sqrt{3}\,x \end{aligned} \tag{4.31}$$

Das Matrixelement (4.29) und die Gleichungen (4.22) bis (4.23) bestimmen dann den *static dephasing* Operator $\hat{\mathbf{U}}_0(s) = (s - \mathrm{i}\,x)^{-1}$ in der $[|0\rangle, |f_1\rangle]$ Basis. Die Fluktuationsparameter λ_1, λ der ESC_1-Approximation werden über die Selbstkonsistenzbedinung (3.13) bestimmt. In Ref. [17] leiteten wir ab, daß

$$\begin{aligned} \lambda_1 &= 10\,\beta \\ \lambda &= \frac{443520}{8900}\beta \\ &\approx 49.83\,\beta \end{aligned} \tag{4.32}$$

ESC_1-Approximation in der Eigenfunktionsbasis: Die normierten Eigenfunktionen des Diffusionsoperators $[\partial_x^2]$, welche die Randbedinungen (4.26) erfüllen, sind

$$\begin{aligned} |\nu\rangle &= \sqrt{2}\,\sin(\nu\pi\,x) \text{ for } \nu = 1, 3, ... \\ &= \sqrt{2}\,\cos(\nu\pi\,x) \text{ for } \nu = 2, 4, ... \,. \end{aligned} \tag{4.33}$$

Da $[\partial_x^2]$ ein symmetrischer Operator ist, sind links- und rechtseitige Eigenfunktionen identisch. Mit $|f_1\rangle = |1\rangle$ und $z = \pi(1/2 + \mathrm{i}\, s)$ erhält man

$$\begin{aligned}\langle 0|\hat{\mathbf{U}}_0(s)|1\rangle &= \sqrt{2}(\sinh(\pi s)\mathrm{Ci}(\xi) + \mathrm{i}\cosh(\pi s)\mathrm{Si}(\xi))|_{\xi=-z^*}^{\xi=z} \\ \langle 1|\hat{\mathbf{U}}_0(s)|1\rangle &= -2\arctan(2s) - \\ &\quad (\mathrm{i}\cosh(2\pi s)\mathrm{Ci}(\xi) + \sinh(2\pi s)\mathrm{Si}(\xi))|_{\xi=-2z^*}^{\xi=2z}\end{aligned} \tag{4.34}$$

wobei Ci und Si die Integralcosinus- und Integralsinusfunktion symbolisieren. Die Fluktuationsparameter λ_1 λ wurden von uns in Ref. [17] für die Eigenfunktionsbasis bestimmt als

$$\begin{aligned}\lambda_1 &\approx 9.89\,\beta \\ \lambda &\approx 41.6\,\beta\end{aligned} \tag{4.35}$$

4.2.2.3 Spin-Dephasierung in der ESC$_0$ und ESC$_1$-Näherung

Abbildung 4 in Ref.[17] zeigt T_2^* als das erste Langzeitmoment des freien Induktionszerfalls und von dessen ESC$_0$ und ESC$_1$-Approximationen (Eigenfunktions- und Ω-Polynom Basis) in Abhängigkeit vom Diffusionskoeffizienten β. Im *static dephasing* ($\beta \rightarrow 0$) und im *motional narrowing* Grenzfall ($\tau_1\langle 0|x^2|0\rangle = 1/120\,\beta^{-1} \ll 1$) zeigen alle Kurven das gleiche asymptotische Verhalten. Im intermediären Dynamibereich wird die bessere Näherung der ESC$_1$-Kurven verglichen mit der in der ESC$_0$-Näherung offensichtlich. Die ESC$_1$-Kurven beider Funktionsbasen unterscheiden sich nicht wesentlich.

In Abbildung 5 der Ref. [17] wird der Zerfall der Spin-Echo Magnetisierung dargestellt. Im Langzeitverhalten approximieren die ESC$_1$-Kurven beider Funktionsbasen den Orginalzerfall besser als die ESC$_0$-Kurve. Das wird auch bei der Abhängigkeit der Spin-Echo Relaxationsrate $1/T_2$ von der Echozeit (Abb. 6) und vom Diffusionskoeffizienten (Abb. 6,7) deutlich. Bei kurzen Echozeiten sind die ESC_0 und ESC_1-Kurven parallel zur Kurve des Orginalprozesses. Bei längeren Echo Zeiten und kleinerem Diffusionskoeffizienten approximieren die ESC_1-Kurven deutlich besser als die ESC_0-Kurve die Kurve des Orginalprozesses. Wiederum unterscheiden sich die ESC_1-Kurven beider Funktionsbasen nicht wesentlich.

Kapitel 5

Zusammenfassung

Die Motivation für diese Arbeit war, daß bei der Kernspinresonanzbildgebung biologischer Systeme die Dynamik der Spin-Dephasierung wichtige morphologische, physiologische und pathophysiologische Informationen enthält. Als Beispiel sei die BOLD (*blood oxygenation dependence*) Bildgebung genannt. Diese kann aufgrund unterschiedlicher Dephasierung der Spins im Gehirn neuronale Aktivitätsareale und im Herzen potentiell ischämische Gebiete lokalisieren. Für ein nicht nur empirisches Verständnis der Spin-Dephasierung sind quantitative Modelle notwendig, welche die Spin-Dephasierung in Abhängigkeit von den biologisch relevanten Parametern beschreiben. Physikalisch betrachtet, erfolgt die Dephasierung durch die phasenmodulierende Wirkung stochastisch fluktuierender Störfelder. In vielen Fällen geschieht dies durch die Diffusion der Spins in einer magnetisch heterogenen Umgebung, die z.B. beim BOLD-Effekt durch das intravasale paramagnetische Desoxyhämoglobin entsteht. Obwohl man die Dephasierung oft implizit über eine partielle Differentialgleichung, wie z.B. die Bloch-Torrey Gleichung, beschreiben kann, existieren explizite Lösungen über den gesamten dynamischen Bereich der Störfeldfluktuationen nur in wenigen Fällen. Diese sind z.B. das Anderson-Weiss Modell und die Dephasierung bei freier Diffusion in einem linearen Magnetfeld.

Anders verhält es sich, wenn man nur einen Grenzbereich, d.h. entweder sehr schnelle (*motional narrowing limit*) oder extrem langsame (*static dephasing limit*) Störfeldfluktuationen betrachtet. Für den ersten Grenzfall existieren seit langem analytische Lösungen und für den zweiten auch seit kurzem. Das Problem beider Ansätze ist, daß sie auf störtheoretischen Verfahren beruhen, d.h. sie gelten nur in ihrem jeweiligen dynamischen Grenzfall und divergieren bei Extrapolation in den jeweils anderen Grenzbereich. Folglich ist das *intermediate motion regime* der stochastischen Feldfluktuationen, was in biologischen Systemen von großer Relevanz ist (z.B. bei der kardialen BOLD Bildgebung), überhaupt nicht abgedeckt. Der mathematische Hintergrund, warum das *intermediate motion regime* sich einem analytischen Ansatz entzieht, ist folgender: der Generator, der zur Dephasierung führenden Phasenmodulationen, ist zwar häufig bekannt (z.B. für diffundierende Spins der Bloch-Torrey Generator), d.h. in einem sehr (infinitesimal) kurzen Zeitintervall kann die Dephasierung analytisch beschrieben werden. Allerdings kann meist der dem Generator zugeordnete Propagator, der den Relaxationsverlauf in endlichen Zeitintervallen beschreibt, außer in wenigen Fällen, weder analytisch noch numerisch bestimmt werden.

In dieser Arbeit wurde ein neuer Ansatz zur Approximation des Propagators der Dephasierung vorgeschlagen. Anstatt je nach Grenzfall entweder die Dynamik oder lokale Frequenz des Magnetfeldes als Störung zu betrachten, wird hier versucht, die als Markov Prozeß angenommene Dynamik der Phasenmodulationen durch eine einfachere Dynamik anzunähern. Dabei soll diese einfachere Dynamik spezifische Eigenschaften der ursprünglichen beibehalten. Als Selbstkonsistenzbedingung wird gefordert, daß die Korrelationszeiten beider Prozesse bis zu einer gewissen Ordnung identisch sind. Damit besitzen beide Prozesse die gleiche *motional narrowing* Entwicklung und offensichtlich beschreiben beide asymptotisch auch ein gleiches Verhalten im *static dephasing regime*. Somit wird die ursprüngliche Dynamik von beiden Grenzbereichen kommend angenähert.

Ausgangspunkt war die *strong collision* Näherung, bei der angenommen wird, daß die Übergangsgwahrscheinlichkeit zwischen zwei stochastischen Zuständen unabhängig vom Ausgangszustand ist. Diese Näherung gilt, wenn die Spin-Dephasierung auf einer deutlich längeren Zeitskala stattfindet als die Phasenmodulationen. Bei dieser Näherung zerfallen alle stochastischen Besetzungszustände senkrecht zum Gleichgewichtszustand mit demselben Exponentialfaktor. Folgerichtig wurde eine *extended strong collision* (ESC) Näherung so definiert, daß Besetzungszustände einer endlichen Funktionen-Basis mit unterschiedlichen Exponentialfaktoren zerfallen dürfen, Zustände senkrecht zu dieser Basis jedoch mit einem identischen Faktor. Ein interessantes Ergebnis ist, daß sich in dieser Näherung der Propagator der Spin-Dephasierung direkt durch den Propagator im static dephasing Grenzfall darstellen läßt. Damit wird die Berechnung der Spin Dephasierung aus folgenden Gründen erheblich vereinfacht: 1. der Propagator ist im *static dephasing* Grenzfall häufig sehr einfach zu bestimmen, da er nur einen mittleren Phasenfaktor darstellt; 2. Die Bestimmung der ESC Propagators erfolgt abgeschlossen in dem von der endlichen Basis aufgespannten Vektorraum, d.h. man hat ,,nur" ein endlich dimensionales Problem zu lösen. Die Besetzungszustände der Basis können z.B. durch die Eigenzustände des Generators der zu nähernden Dynamik oder aber auch durch Polynome der lokalen Frequenzen gegeben sein.

Anwendung fand die *strong collision* Approximation für die Beschreibung der Spin Dephasierung im Herzmuskel. Die stochastischen Phasenmodulationen werden hierbei durch die Diffusion der Spins in perikapillären Feldgradienten, wie sie durch den BOLD Effekt hervorgerufen werden, induziert. Es konnten einfache Relationen zwischen Relaxationszeiten, Diffusionskonstanten, Kapillardichte und Oxygenierungsgrad abgeleitet werden. Ein Vergleich mit Simulationen bestätigte die Güte der Approximation. Weiterhin konnten experimentelle Daten für die kardiale BOLD Bildgebung am isolierten Herzen und am Menschen vorhergesagt werden.

Die erweiterte strong collision (ESC) Approximation wurde für zwei generische Modelle der Spin Dephasierung (Anderson-Weiss Modell, eingeschränkte Diffusion im linearen Magnetfeld) untersucht. Der Grund für die Modellauswahl war, daß sich beim Anderson- Weiss Modell die Dephasierung analytisch, und bei der Diffusion im linearen Magnetfeld zumindest einfach numerisch bestimmen läßt, was für die Validierung der ESC Methode wichtig war. Beim Anderson-Weiss Modell mußte zunächst der Generator der stochastischen Phasenmodulationen gefunden werden, was soweit bekannt, in dieser Arbeit zum ersten mal gelang. Für beide Modelle konnte die Güte der ESC Approximation von Relaxationszeiten (T_2^*, T_2) und von Spin-Echo Zerfallskurven demonstriert werden

Kapitel 6

Anlagen

6.1 Theoretische Orginalarbeiten

- W.R. Bauer, W. Nadler, M. Bock, L.R. Schad, C. Wacker, A. Hartlep, G. Ertl: *Theory of the BOLD effect in the capillary region: an analytical approach for the determination of* T_2^* *in the capillary network of myocardium*; Magn. Res. Med. **41** (1999), 51. [7]

- W.R. Bauer, W. Nadler, M. Bock, L.R. Schad, C. Wacker, A. Hartlep, G. Ertl: *Theory of coherent and incoherent nuclear spin dephasing in the heart*; Phys. Rev. Letters, **83(20)** (1999), 4215.[15]

- W.R. Bauer, W. Nadler, M. Bock, L.R. Schad, C. Wacker, A. Hartlep, G. Ertl *The relationship between the BOLD-induced* T_2 *and* T_2^**: a theoretical approach for the vasculature of myocardium*, Magn. Res. Med. **42** (1999), 1004. [16]

- W.R. Bauer, W. Nadler *Spin dephasing in the extended strong collision *approximation* Phys. Rev. E, **65 (6-1)**, 066123-1. [17]

6.2 Experimentelle Arbeiten

- Wacker CM, Bock M, Hartlep AW, Beck G, van Kaick G, Ertl G, Bauer WR, Schad L. *Changes in myocardial oxygenation and perfusion under pharmacological stress with dipyridamole. Assessment using* T_2^* *and* T_1 *measurements.* Magn. Res. Med. **41** (1999), 686. [3]
- Wacker CM, Bock M, Hartlep AW, Bauer WR, van Kaick G, Pfleger S, Ertl G, Schad L. *BOLD-MRI in ten patients with coronary artery disease: evidence for imaging of capillary recruitment in myocardium supplied by the stenotic artery.* Mag*ma **8** (1999), 48. [4]

Literaturverzeichnis

[1] S. Ogawa, T.-M. Lee, A.R. Kay, D.W. Tank, Proc. Natl. Acad. Sci. USA **87** (1990), 9868.

[2] J. Belliveau et al., Science **254** (1991), 716.

[3] C.M. Wacker et al., Magn. Res. Med. **41(4)**, (1999), 686

[4] C.M. Wacker et al. , Mag*ma **8** (1999) 48.

[5] P.W. Anderson, P.R. Weiss, Rev. Modern Physics **25(1)** (1953), 269.

[6] H.C. Torrey, Phys. Rev. **104** (1956), 563.

[7] W.R. Bauer et al. , Magn. Res. Med. **41** (1999), 51.

[8] R.P. Kennan, J. Zhong, J.C. Gore, Magn. Res. Med. **31** (1994), 9.

[9] A. Abragham, *The Principles of Nuclear Magnetism*, Oxford University Press, 1961

[10] J. McConnell, *The theory of nuclear magnetic relaxation in liquids*, Cambridge University Press 1987

[11] P.T. Callaghan, Principles of Nuclear Magnetic Resonance Microscopy (Clarendon, Oxford, 1991), p. 371. P.T. Callaghan, J. Stepisnik, Phys. Rev. Letters **75** (1995), 4532

[12] D.A. Yablonski, E.M. Haake, Magn. Res. Med. **32** (1994), 749.

[13] V.G. Kiselev, S. Posse, Phys. Rev. Lett. **81(25)** (1998), 5696.

[14] J.B. Bassingthwaigthe et al., Microvasc. Res. **7** (1974), 229

Res.

[15] W.R. Bauer et al., Phys. Rev. Letters, **83(20)** (1999), 4215.

[16] W.R. Bauer et al. , Magn. Res. Med. **42** (1999), 1004.

[17] W.R. Bauer, W. Nadler, Phys. Rev. E, **65 (6-1)**, 066123-1.

[18] W. Nadler, K. Schulten, J. Chem. Phys. **82** (1985), 151.

[19] S. Kaul, A.R. Jayaweera, Circulation **96** (1997) 719.

[20] M.K. Atalay et al., Magn. Res. Med. **189** (1993), 759.

[21] M.K. Atalay et al., Magn. Res. Med. **34** (1995), 623.

[22] C. W. Gardiner, *Handbook of Stochastic Methods*, (Springer, Berlin 1983).

[23] A. Duh, A. Mohorič, J. Stepišnik, in *Proceedings of the 15-th European Experimental NMR Conference* (University of Leipzig 2000), p. 1

Magnetic Resonance in Medicine 41:51–62 (1999)

Theory of the BOLD Effect in the Capillary Region: An Analytical Approach for the Determination of T_2^* in the Capillary Network of Myocardium

Wolfgang R. Bauer,[1]* Walter Nadler,[2] Michael Bock,[3] Lothar R. Schad,[3] Christian Wacker,[2] Andreas Hartlep,[3] and Georg Ertl[1]

This article presents an analytical approach for the quantification of the blood oxygen level dependent (BOLD) effect in the capillary region. The capillary geometry of myocardium is considered. The relaxation rate R_2^* is determined as a function of the capillary radius R_c, the intracapillary volume fraction RBV, and the diffusion coefficient D. When the intracapillary volume fraction is small, the approximation $R_2^* = \text{RBV} \cdot \tau^{-1} \cdot (\sqrt{1 + (\tau\delta\omega)^2} - 1)$ is valid, with the correlation time $\tau = (R_c^2/4D) \cdot (|\ln \text{RBV}|/(1 - \text{RBV}))$. The predictions of this model agree well with numerical simulations and experimental data of others and with data recently measured by our group. Magn Reson Med 41:51–62, 1999. © 1999 Wiley-Liss, Inc.

Key words: BOLD effect; capillary; myocardium; transverse relaxation

INTRODUCTION

The BOLD (blood oxygen level dependent) effect in tissue results from the paramagnetic deoxyhemoglobin in capillaries and venous vessels. In addition to its application in functional imaging of the brain (1), the BOLD effect has been observed in cardiac imaging (2–5). This application bears a great potential for the diagnosis of ischemic heart disease. However, a quantitative model that considers parameters of myocardial microcirculation is a prerequisite. Although it is not a problem to understand the BOLD effect qualitatively, its quantitative analysis is very complex and demands further evaluation. The acceleration of the transverse relaxation depends on the concentration of deoxyhemoglobin in the vessels and the geometry of the vessel network. Yablonski and Haake (6) studied some geometries of cylindrical vessels filled with a (para)magnetic substance and determined the dephasing of spins induced by the inhomogeneous magnetic field in such vessel networks. In their work, the authors considered the spins as stationary (static dephasing regime), i.e., the diffusion of spins during relaxation was neglected. This approximation is justified as long as the amplitude of the field fluctuations that a diffusing nuclear spin ‘‘sees’’ during relaxation is much smaller than the magnitude of this inhomogeneous field.

This theory, however, does not describe the BOLD effect in myocardium, at least when clinical imaging systems (<2 T) are used, for the following reason: concerning the myocardial blood volume, the dominating vessels are the capillaries with a volume fraction of more than 90% of the intramyocardial blood volume (7). The capillaries are arranged parallel with an intercapillary distance of about 19 μm, i.e., one can assume a kind of periodicity of the BOLD-related inhomogeneous field after this distance. Typical relaxation times of transverse magnetization in these low-field systems are in the range of $T_2^* = 30$–40 ms. Thus, the diffusion distance during relaxation ($t > 2 \times T_2^*$) is $\sqrt{tD} > 7$ μm (diffusion coefficient $D = 1\ \mu\text{m}^2/\text{ms}$), i.e., taking into account the intercapillary distance a nuclear spin ‘‘sees’’ nearly the whole variation of the inhomogeneous field. Hence, the field fluctuations due to diffusion are in the range of the magnitude of the inhomogeneous field, which excludes the application of the theory of Yablonski and Haake.

Another analytical approach to determine transverse relaxation exists as long as the *motional narrowing* condition is valid. This condition states that the product of correlation time and the magnitude of the field fluctuations has to be significantly smaller than 1. When this condition is fulfilled, the relaxation rate is simply

$$R_2^* = \tau \cdot \langle \omega^2 \rangle$$

where τ is the correlation time and $\langle \omega^2 \rangle$ the variance of the precession frequency of the inhomogeneous field. Although this approach can be widely used in other fields (8), it is not appropriate for the description of the BOLD effect in the capillary system. A crude approximation that provides the magnitude of the correlation time is given by the diffusion time $\tau = R_c^2/\text{D}$, where $R_c \approx 2.5$ μm and is the capillary radius and $D = 1\ \mu\text{m}^2/\text{ms}$ and is the diffusion constant. The equatorial field around a capillary in a low-field system (e.g., 1.25 T) may be estimated to be in the range of 1 mgauss, i.e., the frequency is $\delta\omega = 168$ rad s^{-1} (6). Hence, the product $\tau \cdot \delta\omega \approx 1$ does not fulfill the motional narrowing condition.

Since there is no sufficient theory of the BOLD effect in the capillary region, and since in at least some tissues such as myocardium the capillary fraction clearly dominates, our intention was to develop an analytical approach to determine the transverse relaxation rate as a function of the capillary/tissue geometry and the intracapillary BOLD-related magnetization. In this study, we will only focus on the decay of the transverse magnetization, which, for example, can be observed in gradient echo sequences, i.e.

---

[1] Medizinische Universitätsklinik Mannheim/Heidelberg.

[2] HLRZ c/o Forschungszentrum Jülich, Jülich.

[3] Department of Biophysics, German Cancer Research Center, Heidelberg, Germany.

Grant sponsor: Deutsche Gesellschaft für Kardiologie; Grant sponsor: Forschungsfonds des Klinikums Mannheim/Heidelberg; Grant Number: Project 42; Grant sponsor: Sonderforschungsbereich 355 “Pathophysiologie der Herzinsuffizienz;” Grant sponsor: Graduiertenkolleg “NMR”; Grant number: HA 1232/8-1.

*Correspondence to: Dr. W. R. Bauer, II. Medizinische Klinik, Klinikum Mannheim/Universität Heidelberg, Theodor-Kutzer Ufer 1-3, 68167 Mannheim, Germany.

Received 28 November 1997; revised 23 March 1998; accepted 1 June1998.

© 1999 Wiley-Liss, Inc.

this decay is due to reversible and irreversible dephasing of transverse polarized spins. The article is structured as follows: we will first construct a model of the capillary system and tissue that reflects the geometry and topology in myocardium. In the mathematical analysis, we will first derive an expression of the correlation time of field fluctuations that nuclear spins are subjected to while diffusing in our tissue model. Thereafter, we will demonstrate that we can replace the exact time evolution of transverse magnetization determined by the Bloch-Torrey equation (9) by a *strong collision* approximation. In contrast to other approaches, e.g., the *motional narrowing* approximation, the *strong collision* approximation is not based on any assumption of the relation of local field strength and correlation time. Instead, its application is justified when the local field fluctuations are rapid when compared with relaxation. The *strong collision* approximation leads directly to an analytical expression of the Laplace transform of the relaxation process, and this transform will provide the relaxation time. In the following section, we will compare our results with the computer simulations of Kennan et al. (10) and the experimental data of Atalay et al. (2, 3) and our own group (C. Wacker, et al., Noninvasive assessment of myocardial oxygenation and perfusion without exogeneous contrast agents using T_2^* and T_1, manuscript submitted).

TISSUE MODEL

1. The BOLD effect in tissue arises from the paramagnetic property of deoxyhemoglobin, which, confined in capillaries and venous vessels, induces a perivascular inhomogeneous magnetic field in the presence of an external magnetic field. The blood volume fraction of capillaries in myocardium is more than 90% of the whole myocardial blood volume (arterial plus capillary plus venous compartment) (7), i.e., the fraction of the venous compartment is less than 10%. This finding implies that in myocardium the volume contribution of the capillaries to the BOLD effect is clearly dominating. In our model, therefore, we will consider only this vessel type.

2. The BOLD-related transverse relaxation of spins is induced by the inhomogeneous magnetic field around vessels containing deoxyhemoglobin. Since oxygen delivery from blood to tissue takes place in capillaries, there is a gradient of deoxyhemoglobin along the capillary axis, i.e., there is also a pericapillary magnetic field gradient in this direction. In myocardium, capillaries are arranged in parallel to the muscle fibers. The intercapillary distance is ≈19 μm (11) and the length of a single capillary is more than 400 μm (11). Since the diffusion coefficient of water is about $D = 1$ μm^2/ms and typical values for T_2^* in myocardium are in the range of 35 ms, the range of the diffusion distance along the capillary axis within relaxation ($t \approx 2 - 3 \times T_2^*$) is $\sqrt{tD} \approx$ 8–10 μm, i.e., the diffusion distance is short compared with the capillary length. Due to the length of the capillary and this short diffusion distance, the contribution of diffusion in the direction of the capillary axis to relaxation is negligible when compared with that of perpendicular diffusion. Hence, we only consider diffusion of spins in the cross-sectional plane of the capillary bed.

3. We only consider two compartments in tissue: the intracapillary volume plus the capillary wall and the extracapillary tissue. Since the interstitial-intracapillary exchange rate of water protons was found to be less than 7 Hz (12), the extracapillary to intracapillary transport rate is small compared with the relaxation rate T_2^{*-1} and, therefore, is neglected. In our model, we assume, therefore, reflectory boundary conditions at the capillary wall for a diffusing nuclear spin of the interstitial space. Furthermore, we only consider the extracapillary fraction of nuclear spins, due to their dominating contribution (>90%) to overall magnetization.

4. In myocardium, the capillaries and muscle fibers form an almost regular structure. Therefore, it is reasonable to assign each capillary an area of tissue that is predominantly supplied by this capillary. According to Krogh's capillary model, this supply area is a coaxial cylinder around the capillary the radius of which is $R_s = 1/\sqrt{\pi \times \text{capillary density}}$. In our mathematical model, we restrict diffusion of spins to this area. The legitimization for this restriction and its mathematical implications for evaluation of diffusion have already been discussed in detail (13). One implication is that reflectory diffusive boundary conditions have to be assumed for the trajectories of a nuclear spin at R_s, i.e., trajectories of spins that pass from the supply area of the capillary under observation to that of the neighboring capillary are replaced by symmetric trajectories that are located within the original supply area. Together with Paragraphs 2 and 3, this implies that the diffusion space is the area between concentric circles: the inner one with the capillary radius R_c, the outer one with the supply radius R_s (Fig. 1). Within this diffusion space, we only consider the interaction of a nuclear spin with the magnetic field around the central capillary, which

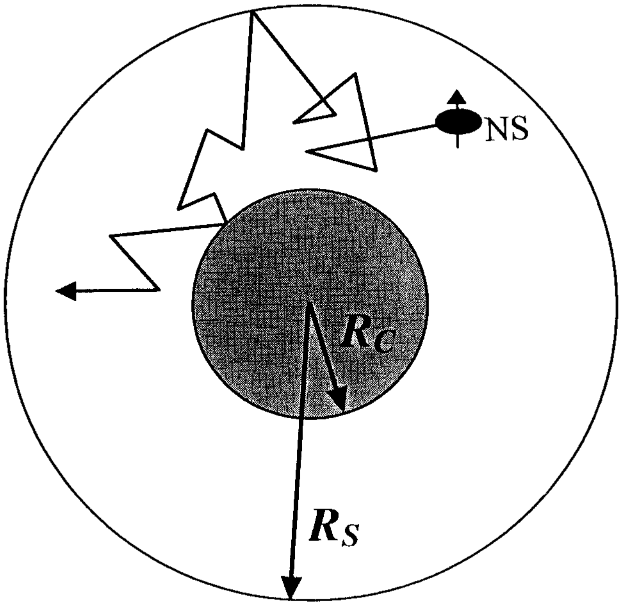

FIG. 1. Cross-sectional view of the capillary plus the coaxial surrounding supply tissue with the trajectory of a diffusing nuclear spin (NS) according to our model (see text). The radius of the capillary is denoted as R_c that of the supply area as R_s. Reflectory diffusive boundary conditions are assumed at the outer capillary wall and the periphery of the supply area.

is generated by the paramagnetic deoxyhemoglobin. According to basic magnetostatics (e.g., ref. 14) the difference of intracapillary to extracapillary magnetization in the presence of an external magnetic field B_0 is determined by (cgs units)

$$\Delta M = \Delta\chi \cdot B_0 \cdot \sin^2(\theta) \qquad [1]$$

with $\Delta\chi$ as the difference of the volume susceptibility (e.g., $\Delta\chi = 8 \cdot 10^{-8}$ for deoxygenated blood with a hematocrit of 40% (6, 10)) and the tilt angle θ between the capillary axis and the direction of the external field. The Larmor frequency around the capillary is then determined by (14)

$$\omega(r, \phi) = -\delta\omega \cdot R_c^2 \cos(2\phi)/r^2 \qquad [2]$$

with the cylindrical coordinates $x = (r, \phi)$ in the cross-sectional plane of the capillary. The term $\delta\omega$ is the characteristic equatorial shift of the radial frequency of a magnetized cylinder, i.e., $\delta\omega = |\omega(R_c, 0)|$, which according to magnetostatics is

$$\delta\omega = 2\pi\gamma \cdot \Delta M \qquad [3]$$

with γ as the gyromagnetic ratio.

MATHEMATIC ANALYSIS

Determination of the Correlation Time

When we consider the trajectories $x_j(t)$ of an ensemble of N spins, the autocorrelation function $K(t)$ of the local NMR frequencies $\omega(x)$ is determined by (We assume that the spatial average of $\omega(x)$ vanishes, which is valid for our model (see Eq. [2]). In general, this outcome can always be achieved by normalization of $\omega(x)$.)

$$K(t) = \frac{1}{N}\sum_{j=1}^{N} \omega(x_j(t)) \cdot \omega(x_j(0)) \qquad [4]$$

or when $p(x, x_0, t)$ defines the probability density to find a spin at the point x after the time t with the initial ($t = 0$) position x_0

$$K(t) = \int_V dx \int_V dx_0\, \omega(x) \cdot p(x, x_0, t) \cdot \omega(x_0) \cdot p(x_0) \qquad [5]$$

where $\int_v$ denotes the integration over the diffusion space with volume V, and $p(x_0)$ defines the probability density function of the steady state, i.e., in this case, it is identical with the spin density, which may be assumed to be homogeneous in tissue, $p(x_0) = 1/V$. Since we assume free diffusion of spins within the boundaries $R_c \leq |x| \leq R_s$, the probability $p(x, x_0, t)$ is simply the Green's function of the diffusion equation

$$\partial_t p(x, x_0, t) = D\nabla^2 p(x, x_0, t) \qquad [6]$$

i.e.,

$$p(x, x_0, t) = \exp(D\nabla^2 \cdot t)\delta(x - x_0) \qquad [7]$$

with the reflectory boundary conditions $\partial_r p(x, x_0, t) = 0$ for $|x| = R_c, R_s$. In general, the function $K(t)$ may be quite complicated; however, usually a single exponential decay is assumed, i.e.,

$$K(t) = K(0) \cdot \exp(-t/\tau) \qquad [8]$$

where τ is the correlation time. The correlation time provides an information on the time after which the fluctuations of the local fields may be considered as stochastically independent, i.e., when $t \geq 2\tau$ the probability density $p(x, x_0, t)$ satisfies the relation

$$p(x, x_0, t) \approx p(x) \qquad [9]$$

One way to approximate the correlation function by a single exponential function is given by the *mean relaxation* time approximation (15)

$$\tau = \int_0^\infty dt\, K(t)/K(0) \qquad [10]$$

and with Eqs. [5] and [7] (see Appendix).

$$\tau = \frac{1}{K(0) \cdot D \cdot V}\int_V dx\, \omega(x)\left[-\frac{1}{\nabla^2}\right]\omega(x)$$

$$= \frac{1}{2D} \cdot \frac{\ln(R_s/R_c)}{R_c^{-2} - R_s^{-2}} = -\frac{R_c^2}{4D} \cdot \frac{\ln(\mathrm{RBV})}{1 - \mathrm{RBV}} \qquad [11]$$

where $\mathrm{RBV} = R_c^2/R_s^2$ is the volume fraction of capillary space (regional blood volume).

Time Evolution of the Magnetization

In this section, we will demonstrate the most important step in the development of our model. We will replace the exact time evolution of the magnetization by an evolution based on the *strong collision* approach. The term *strong collision* derives from the original field of application of this approximation in statistical physics. When we consider diffusion of spins within an inhomogeneous magnetic field, the time evolution of the local transverse magnetization (notation in polar form, i.e., $m = m_x - im_y$) is determined by the Bloch-Torrey (9) equation

$$\partial_t m(x, t) = (D\nabla^2 + i \cdot \omega(x))m(x, t) \qquad [12]$$

which, after formal time integration, provides

$$m(x, t) = \exp[(D\nabla^2 + i \cdot \omega(x)) \cdot t]m(x, 0) \qquad [13]$$

and for the whole magnetization

$$M(t) = \frac{1}{V}\int_V dx \exp[(D\nabla^2 + i \cdot \omega(x)) \cdot t]m(x, 0) \qquad [14]$$

where $\omega(x)$ is the local precession frequency. There are only a few cases in which Eqs. [12]–[14] can be solved analytically, e.g., when $\omega(x)$ is the frequency of a linear gradient field. In general, however, only numerical calculations or computer simulations (10) may be applied to determine the time course of transverse magnetization.

When we determine the correlation time of the local field fluctuations that influence a diffusing nuclear spin, we obtain for typical values of myocardium (RBV = 5–10%, $R_c = 2.75\ \mu\mathrm{m}$, $D = 1\ \mu\mathrm{m}^2/\mathrm{ms}$) $\tau \leq 6$ ms. Typical relaxation times of the transverse magnetization in myocardium are in the range of $T_2^* = 30$–40 ms for magnets used in clinical imaging systems. Since T_2^* describes the influence of both, non-BOLD and BOLD effects on relaxation, a relaxation time describing only the BOLD effects would be even longer. Hence, the time scale on which the local fields are correlated is much smaller than the time scale of the relaxation related to the BOLD effect. This finding implies that, on the time scale of this transverse relaxation, the local fields are uncorrelated.

Strong Collision Approximation

We, therefore, make the approximation to replace the diffusion operator $D\nabla^2$ in Eqs. [12]–[14] by an operator

$$\mathbf{D} = \lambda(\mathbf{II} - \mathbf{id}) \tag{15}$$

(16, 17) where $\mathbf{II}$ denotes the projection operator onto the functional space generated by the steady state probability function $p(x)$, i.e., the application of this operator on a function $f(x)$ is

$$\mathbf{II} f(x) = p(x) \cdot \int_V dx\, f(x) \tag{16}$$

and $\mathbf{id}$ is the identity, i.e.,

$$\mathbf{id} f(x) = f(x) \tag{17}$$

The operator $\mathbf{D}$ describes the stochastic field fluctuations as a stationary Markov process with the transition rates between two distinct local field realizations $\omega(x)$, $\omega(x_0)$ as $\lambda \cdot p(x)$, i.e., the rate is independent of the initial state. An approach of this type is referred to as *random phase* or *strong collision* approximation (16, 17). Since in myocardium the water proton density is rather homogeneous, the probability density function of the steady state is simply $p(x) = 1/V$.

The Green's function $p_D(x, x_0, t)$ of this transition operator $\mathbf{D}$ is

$$\begin{aligned}
p_D(x, x_0, t) &= \exp(\mathbf{D} \cdot t)\delta(x - x_0) \\
&= \exp(-\lambda t(\mathbf{id} - \mathbf{II}))\delta(x - x_0) \\
&= \sum_{\nu=0}^{\infty} \frac{(-\lambda t)^\nu}{\nu!} (\mathbf{id} - \mathbf{II})^\nu\, \delta(x - x_0) \\
&= \left[\mathbf{id} + \sum_{\nu=1}^{\infty} \frac{(-\lambda t)^\nu}{\nu!} (\mathbf{id} - \mathbf{II})\right] \delta(x - x_0) \\
&= \left[\mathbf{II} + \mathbf{id} - \mathbf{II} + \sum_{\nu=1}^{\infty} \frac{(-\lambda t)^\nu}{\nu!} (\mathbf{id} - \mathbf{II})\right] \cdot \delta(x - x_0) \\
&= [\mathbf{II} + e^{-\lambda t}(\mathbf{id} - \mathbf{II})]\delta(x - x_0) \\
&= p(x) \cdot (1 - e^{-\lambda t}) + e^{-\lambda t}\delta(x - x_0)
\end{aligned} \tag{18}$$

where we applied the idempotency of the projection operator $(\mathbf{id} - \mathbf{II})$, i.e., $(\mathbf{id} - \mathbf{II})^\nu = (\mathbf{id} - \mathbf{II})$ for $\nu \geq 1$. The transition rate λ in the *strong collision* operator [15] is determined self consistently. We require that $\mathbf{D}$ reproduces the correlation time τ of the local field fluctuations (Eq. [11]). Since the correlation function of the field fluctuations determined by the *strong collision* Green's function p_D (Eqs. [5] and [18]) is

$$\begin{aligned}
K_D(t) &= \int_V dx \int_V dx_0\, \omega(x) \cdot p_D(x, x_0, t) \cdot \omega(x_0) \cdot p(x_0) \\
&= K_D(0) \cdot e^{-\lambda t}
\end{aligned} \tag{19}$$

the transition rate has to be set as

$$\lambda = \frac{1}{\tau} \tag{20}$$

The Eqs. [18] and [20] demonstrate that on the time scale of the evolution of magnetization ($\gg\tau$) the relation

$$p_D(x, x_0, t) \approx p(x) \tag{21}$$

holds. Comparison with Eq. [9] shows that, in this case, the Green's function of the exact diffusion process $p(x, x_0, t)$ is equivalent to the Green's function of the stochastical process determined by the operator $\mathbf{D}$ (Eq. [15]). Therefore, it is justified to rewrite Eqs. [13] and [14] as

$$m(x, t) = \exp[(\mathbf{D} + i \cdot \omega(x)) \cdot t]m(x, 0) \tag{22}$$

or for the whole magnetization

$$M(t) = \frac{1}{V}\int_V dx \exp[(\mathbf{D} + i \cdot \omega(x)) \cdot t]m(x, 0) \tag{23}$$

Determination of Relaxation Time

Instead of solving Eq. [23], it is more suitable to consider the Laplace transform of the magnetization decay, i.e.,

$$\hat{M}(s) = \int_0^\infty dt\, e^{-s \cdot t} \cdot M(t) \tag{24}$$

$$= \frac{1}{V}\int_V dx \frac{1}{s - \mathbf{D} - i \cdot \omega(x)}\, m(x, 0) \tag{25}$$

$$= \frac{1}{V}\int_V dx \frac{1}{s - \tau^{-1}(\mathbf{II} - \mathbf{id}) - i \cdot \omega(x)} \tag{26}$$

where we assume homogeneity of the initial magnetization, which had been normalized to $m(x, 0) = 1$.

It is useful to decompose $s - \mathbf{D} - i \cdot \omega(x)$ into (see Eqs. [15] and [16]) $A = (s + \tau^{-1})\mathbf{id} - i \cdot \omega(x)$ and $B = -\tau^{-1}\mathbf{II} = -\tau^{-1}.\ V^{-1}\int_V dx$ and to transform Eq. [26] according to the operator identity $1/(A + B) = 1/A - (1/A) \cdot B \cdot 1/(A + B)$, i.e.,

$$\hat{M}(s) = \underbrace{\frac{1}{V}\int_V dx \, \frac{1}{(s + \tau^{-1})\mathbf{id} - i \cdot \omega(x)}}_{= \hat{M}_0(s + \tau^{-1})}$$

$$+ \underbrace{\frac{1}{V}\int_V dx \, \frac{1}{(s + \tau^{-1})\mathbf{id} - i \cdot \omega(x)}}_{= \hat{M}_0(s + \tau^{-1})}$$

$$\cdot \tau^{-1} \cdot \underbrace{\frac{1}{V}\int_V dx \, \frac{1}{s - \mathbf{D} - i \cdot \omega(x)}}_{= \hat{M}(s)}$$

$$= \hat{M}_0(s + \tau^{-1}) + \tau^{-1}\hat{M}_0(s + \tau^{-1}) \cdot \hat{M}(s) \qquad [27]$$

where $\hat{M}_0(s)$ is the Laplace transform of the time course of magnetization that would be present in the absence of diffusion (static dephasing regime). Equation [27] straightforwardly gives the expression of the Laplace transform $\hat{M}(s)$

$$\hat{M}(s) = \frac{\hat{M}_0(s + \tau^{-1})}{1 - \tau^{-1} \cdot \hat{M}_0(s + \tau^{-1})} \qquad [28]$$

When the local frequency around the capillary is given by Eq. [2], $\hat{M}_0(s)$ has the form (see Appendix)

$$\hat{M}_0(s) = \frac{R_c^2 + R_s^2}{\sqrt{s^2 R_s^4 + \delta\omega^2 R_c^4} + R_c^2\sqrt{s^2 + \delta\omega^2}} \qquad [29]$$

and, hence,

$$\hat{M}(s) = (R_c^2 + R_s^2) \cdot \Big(\sqrt{(s + \tau^{-1})^2 R_s^4 + \delta\omega^2 R_c^4}$$

$$+ R_c^2\sqrt{(s + \tau^{-1})^2 + \delta\omega^2} - \tau^{-1}(R_c^2 + R_s^2)\Big)^{-1}$$

$$= (1 + RBV) \cdot \Big(\sqrt{(s + \tau^{-1})^2 + \delta\omega^2 RBV^2}$$

$$+ RBV\sqrt{(s + \tau^{-1})^2 + \delta\omega^2} - \tau^{-1}(1 + RBV)\Big)^{-1} \qquad [30]$$

In principle, the Laplace transform $\hat{M}(s)$ provides all information about the relaxation of magnetization. The time course could be obtained by backward transformation; however, this process is very cumbersome. We are interested in the relaxation time T_2^*, i.e., the time constant that approximates best the magnetization decay by a single exponential function

$$M(t) = e^{-t/T_2^*} \qquad [31]$$

This relaxation time can be determined according to the *mean relaxation time approximation* (15) as

$$T_2^* = \int_0^\infty dt \, M(t) \qquad [32]$$

A comparison with Eq. [24] shows that

$$T_2^* = \hat{M}(0) \qquad [33]$$

i.e., according to Eq. [30]

$$T_2^* = (1 + RBV) \cdot \Big(\sqrt{\tau^{-2} + \delta\omega^2 RBV^2}$$

$$+ RBV \cdot \sqrt{\tau^{-2} + \delta\omega^2} - \tau^{-1}(1 + RBV)\Big)^{-1}$$

$$= \tau \cdot (1 + RBV) \cdot \Big(\Big[\sqrt{1 + (\tau\delta\omega \cdot RBV)^2} - 1\Big]$$

$$+ RBV \cdot \Big[\sqrt{1 + (\tau\delta\omega)^2} - 1\Big]\Big)^{-1}, \qquad [34]$$

or when considering the rate $R_2^* = 1/T_2^*$,

$$R_2^* = \tau^{-1} \cdot \frac{1}{1 + \mathrm{RBV}} \cdot \Big(\Big[\sqrt{1 + (\tau\delta\omega \cdot \mathrm{RBV})^2} - 1\Big]$$

$$+ \mathrm{RBV} \cdot \Big[\sqrt{1 + (\tau\delta\omega)^2} - 1\Big]\Big) \qquad [35]$$

APPLICATIONS

Approximations

Although Eq. [35] may appear rather complex, it can, however, be transformed to a more suitable form for certain limiting cases.

Motional Narrowing Limit

In the motional narrowing limit ($\tau \cdot \delta\omega \ll 1$) one obtains for the relaxation rate from Eq. [35]

$$R_2^* = \tau \cdot \left(\mathrm{RBV} \cdot \frac{\delta\omega^2}{2}\right) \qquad [36]$$

Using the variance $\langle \omega(x)^2 \rangle$ of the local spin precession frequency

$$\langle \omega^2(x) \rangle := \frac{1}{V}\int_V dx \, \omega^2(x) = \mathrm{RBV} \cdot \frac{\delta\omega^2}{2} \qquad [37]$$

Equation [36] can be written as

$$R_2^* = \tau \cdot \langle \omega^2(x) \rangle \qquad [38]$$

Equation [36] is just the well-known general result for transverse relaxation rate obtained for the motional narrowing limit, i.e., our result correctly describes this.

Approximation for a Small Intracapillary Volume

In many tissues, the relative fraction of intracapillary volume satisfies the condition $\mathrm{RBV} \ll 1$. Typical correlation times in myocardium (and also in other tissues) are smaller than 6 ms (Eq. [11]). When considering the BOLD effect, characteristic equatorial radial frequencies $\delta\omega$ are (see Eq. [3], $\Delta\chi = 8 \cdot 10^{-8}$ (18)) for imaging systems $B_0 \leq$ 2T, lower than 270 rad s^{-1}, i.e., the condition

$$(\tau\delta\omega \cdot \mathrm{RBV})^2 \ll 1 \qquad [39]$$

holds. Hence, Eq. [35] leads to

$$R_2^* = \mathrm{RBV} \cdot \tau^{-1} \cdot \left(\sqrt{1 + (\tau\delta\omega)^2} - 1\right) \qquad [40]$$

Comparison with Simulations of Kennan et al.

Kennan et al. (10) performed Monte Carlo simulations of diffusing spins within a square box the length of which was assumed to be the distance between two neighboring capillaries. The cross-section of a capillary filled with a paramagnetic agent was located in the center of the box and the field around the capillary was that of Eq. [2]. Additionally, the fields of the four nearest neighbor capillaries were considered. These authors investigated the effect of the diffusion, intracapillary magnetization, and capillary diameter on the transverse relaxation rate for spin-echo and gradient echo experiments. Our analysis will only focus on the results of the latter.

R_2^* versus Diffusion Coefficient

For a realistic set of tissue parameters the dependence of relaxation rate on diffusion evaluated by simulation is shown in Fig. 2. It is evident that the curve determined from our model (Eqs. [11] and [35]) is similar to that determined from the data points of the simulation. For smaller diffusion coefficients there is a difference of ≤20% from our model curve. It has to be stated that our model was developed under the assumption that the correlation time of field fluctuations which are induced by diffusion is considerably smaller than the BOLD-related relaxation time of magnetization. This is obviously not the case for a slow diffusion regime, i.e., small diffusion coefficients. On the other hand, Fig. 2 demonstrates that the predictions of the model are also valid for this range of diffusion coefficients. However, one has to keep in mind that in the *strong collision* model the diffusion operator $D\nabla^2$ in the time evolution operator is replaced by the operator τ^{-1} $(\mathbf{II} - \mathbf{id})$ (Eq. [23]). Both operators vanish when the diffusion coefficient approaches zero. Hence, both dynamics of field fluctuations have the same asymptotic time evolution of magnetization, which is that of the *static dephasing* regime. This explains the similarity of the model curve and the curve obtained from simulation data in the range of small diffusion coefficients.

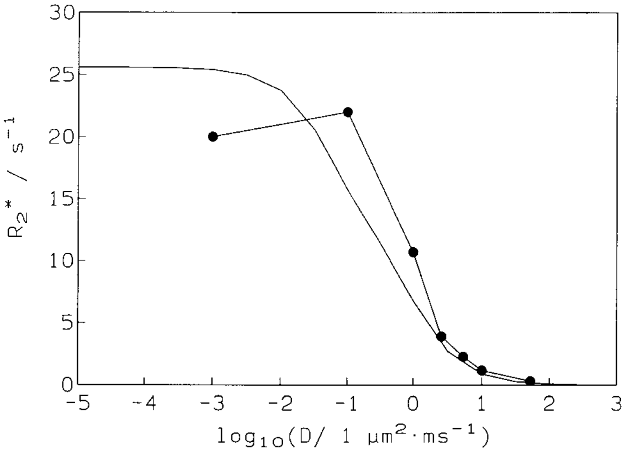

FIG. 2. Transverse relaxation rate R_2^* as a function of the tissue diffusion coefficient *D*. The circles denote data that were obtained by the computer simulation of Kennan et al. and taken from ref. (10) (see text). These authors assumed a capillary diameter of 5 µm and a volume fraction (RBV) of 5%. The difference of intracapillary extracapillary magnetization was chosen to be $\Delta M = \Delta\chi \cdot B_0 = 1.6$ mgauss, which would be present for deoxygenated blood ($\Delta\chi = 8 \cdot 10^{-8}$ for hematocrit = 40%) at $B_0 = 2$ T. The second curve denotes data obtained for these parameters from our model according to Eqs. [11] and [35]. The characteristic frequency and the dipole field are determined according to Eqs. [2] and [3] for $\Delta M = 1.6$ mgauss. Realistic diffusion coefficients in tissue are in the range of 1 µm²/ms, i.e., $\log_{10}(D/1\ \mu\mathrm{m}^2/\mathrm{ms}) \approx 0$.

R_2^* versus Intracapillary Magnetization

From their simulations Kennan et al. observed a power law for the dependence of relaxation rate on intracapillary magnetization, or more precisely, on the intracapillary extracapillary magnetization difference ΔM

$$R_2^* \sim \Delta\, M^{\Lambda} \qquad [41]$$

For a slow ($D = 10^{-3}$ μm²/ms), intermediate ($D = 0.65$ μm²/ms), and rapid ($D = 2$ μm²/ms) diffusion regime they obtained $\Lambda = 1.1$, 1.49, and 1.95 respectively, when ΔM is varied from 0.1 to 1.6 mgauss. The intracapillary volume fraction was chosen for the three regimes to be RBV = 5%, 3%, and 5% and the capillary radius $R_c = 2.5$ μm in all regimes. When considered in our model, this implies correlation times of $\tau = 4930$, 8.69, and 2.46 ms (Eq. [11]). The range of the characteristic frequency $\delta\omega$ was given by that of ΔM (Eq. [3]), i.e., it is 16.8–269 rad · s^{-1}. For the slow diffusion regime, this implies that $\tau\delta\omega \gg 1$ and Eq. [35] can be approximated by

$$R_2^* = \mathrm{RBV} \cdot 2\delta\omega \qquad [42]$$

Since $\delta\omega \sim \Delta M$ we obtain an exponent $\Lambda = 1$ in the power law Eq. [41].

For the rapid diffusion regime, the relation $\tau\delta\omega \ll 1$ holds for the lower values of the $\delta\omega(\Delta M)$-range, i.e., according to Eq. [36] we would obtain an exponent $\Lambda = 2$. For the higher values of the characteristic frequencies the relation $\tau\delta\omega \leq 0.66$ holds, i.e., when expanding Eq. [35] in a power series of $\tau\delta\omega$, one has to consider the term of the 4th order in this variable, i.e., when RBV is small

$$R_2^* = \tau^{-1} \cdot \mathrm{RBV}\ \tfrac{1}{2} \cdot \left((\tau\delta\omega)^2 - \tfrac{1}{4}(\tau\delta\omega)^4\right) \qquad [43]$$

This correction explains why Kennan et al. found an exponent somewhat smaller than 2.

For the intermediate diffusion regime, we analyzed Eq. [35] for the parameters given by Kennan et al. for a magnetization range of $\Delta M = 0.16$–5 mgauss and performed a linear regression analysis of this data (Fig. 3). The exponent fitted was $\Lambda = 1.61$, which is close to the value of 1.49 obtained from simulation experiments.

R_2^* *versus Intracapillary Blood Volume*

The authors [10] investigated the dependence of the transverse relaxation rate on the intracapillary volume fraction RBV $= R_c^2/R_s^2$ where they varied this parameter by increasing the capillary radius R_c or the intracapillary distance 2 R_s. In both cases, they found a nearly linear dependence; however, the slope in the case of variable intercapillary spacing was significantly smaller. We performed the same analysis. Similar to Kennan et al., we considered the diffusion coefficient $D = 0.65\ \mu\text{m}^2/\text{ms}$ and the intracapillary magnetization as 1.6 mgauss. Since Kennan et al. did not give the capillary radius and the relative intracapillary volume from where they started varying either the capillary radius or the intercapillary distance, we were not able to reproduce their simulations exactly. We determined the relaxation rate for a relative intracapillary volume of RBV = 5% and a capillary radius of 2.5 μm according to Eqs. [11] and [35]. Then we varied R_c or R_s. As in the simulations of Kennan et al., in both cases a nearly linear dependence was evident (Fig. 4), and the slope of the regression line was significantly higher in the case of a variable capillary radius $m = 2.41\ \text{s}^{-1}/\%$ vs. $m = 1.51\ \text{s}^{-1}/\%$.

Comparison with Experimental Data of Atalay et al.

Atalay et al. (2) performed T_2^* sensitive gradient echo imaging at 4.7 T in the isolated red cell perfused rabbit heart at various oxygenation levels of the perfusate. This perfusate contained a cardioplegic potassium concentration to minimize oxygen utilization. Additionally the perfusate contained adenosine to achieve maximal vasodilation. Together with the results presented in their second article (3), these authors found an empirical relation between the transverse relaxation rate R_2^* and the oxygen saturation of hemoglobin in the perfusate

$$R_2^* = -37 \cdot \ln(0.29 + 0.7 \cdot [\text{O}_2 - \text{saturation}])\text{s}^{-1} + 33.3\ \text{s}^{-1} \quad [44]$$

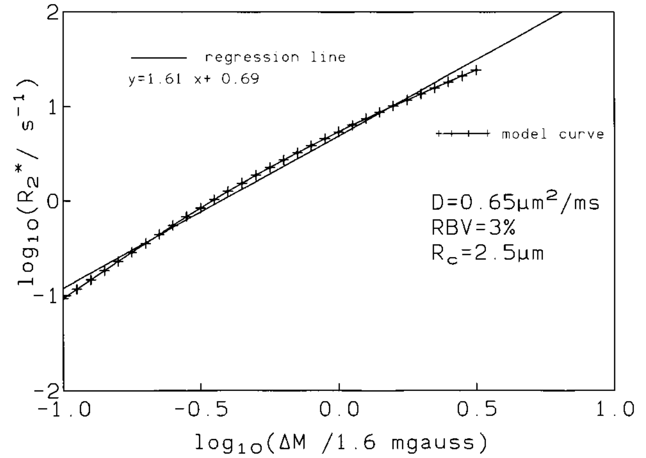

FIG. 3. Logarithm of the transverse relaxation rate as a function of the logarithm of the intracapillary extracapillary magnetization difference ΔM according to Eqs. [3] and [35]. The intracapillary volume fraction was RBV = 3%, the capillary radius was R_c = 2.5 μm, and the diffusion coefficient was D = 0.65 μm²/ms, which were the parameters of Kennan et al. in their simulation experiments for the intermediate diffusion regime. A linear regression analysis is performed. The slope of the regression line determines the exponent of the power law (see Eq. [41] and text).

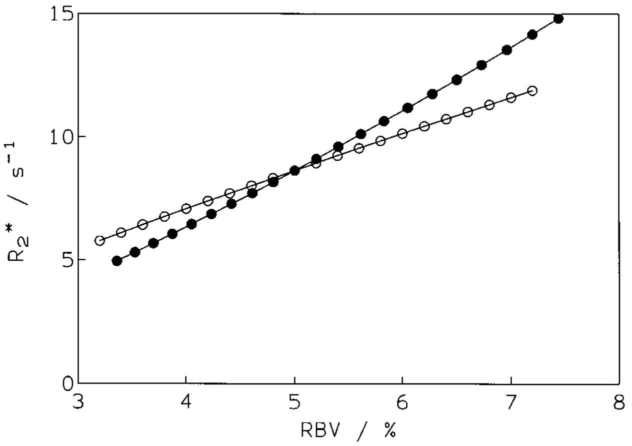

FIG. 4. Transverse relaxation rate R_2^* as a function of the relative intracapillary volume RBV obtained from Eqs. [11] and [35]. The filled circles denote data in which RBV was altered by varying the capillary radius, the open circles denote data in which the capillary radius was held constant at 2.5 μm and the intercapillary distance was varied. The diffusion coefficient was D = 0.65 μm²/ms. The starting point of both curves was an RBV = 5% and an intracapillary radius of R_c = 2.5 μm. Linear regression analysis revealed a slope of 1.53, 2.41 $\text{s}^{-1}/\%$ for the open and the filled circle curve, respectively.

According to our model, we determined R_2^* for various RBV values (5–15%) as a function of the oxygen saturation of hemoglobin (Fig. 5). We assumed a mean capillary diameter of 5.5 μm (11) (R_c = 2.75 μm) and a diffusion coefficient of 1 μm²/ms. According to Eq. [11], this method provides correlation times between $\tau = 5.96$ ms (RBV = 5%) and $\tau = 4.22$ ms (RBV = 15%). When blood is completely deoxygenated, the characteristic frequency at 4.7 T is (see Eqs. [1] and [3]) $\delta\omega = 632\ \text{rad} \cdot \text{s}^{-1}$, and, hence, $(\tau\delta\omega \cdot \text{RBV})^2 \ll 1$, i.e., the condition of Eq. [39] holds and we can approximate relaxation rate by Eq. [40].

The intracapillary oxygenation and, hence, intracapillary magnetization, which is required for the model calculations is estimated according to the following consideration. Since cardioplegic hearts were investigated, only basal oxygen consumption has to be considered, which is about $\dot{\text{MVO}}_{2,\text{basal}} = 0.02$ ml O₂/g(tissue)/min (19). The relationship between oxygen consumption, perfusion F, and arteriovenous difference of oxygen saturation ΔY is given by

$$\dot{\text{MVO}}_{2,\text{basal}} = F \cdot \Delta\text{Y} \cdot [\text{Hb}] \cdot 1.34\ \text{ml O}_2/\text{g(Hb)} \quad [45]$$

The term [Hb] denotes the concentration of hemoglobin, and the factor 1.34 ml O₂/g(Hb) is Hüfner's number. The authors did not provide data about perfusion and concentration of hemoglobin. However, they obtained a mean

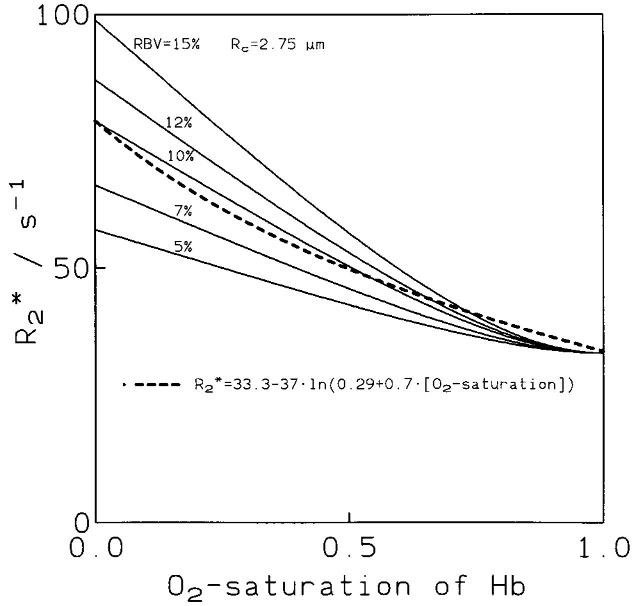

FIG. 5. Transverse relaxation rate R_2^* as a function of the oxygen saturation of hemoglobin in myocardium. The dashed curve represents the empirical curve that Atalay et al. (3) obtained from gradient echo imaging in isolated red cell perfused rabbit hearts at 4.7 T. The solid curves were obtained from our model (see Eqs. [11] and [40]), in which we assumed a capillary radius of R_c = 2.75 μm; a relative intracapillary volume of RBV = 15%, 12%, 10%, 7%, 5%; and a diffusion coefficient of $D = 1\ \mu\text{m}^2/\text{ms}$. Since the curves obtained from our model only considered the BOLD-related relaxation, they were given the offset of the empirical curve at 100% oxygen saturation.

coronary flow of 23 ml/min (3). Hence, a lower limit of the average perfusion can be estimated when the weight of a rabbit heart is assumed to be <15 g, i.e., $F > 1.5$ ml/g per min. When we assume a reasonable lower bound of hemoglobin concentration of [Hb] = 12 g/100 ml (blood), we obtain that the arteriovenous difference of oxygen saturation is

$$\Delta Y < 8.3\% \qquad [46]$$

which is considerably smaller than the arteriovenous difference of a beating heart (≈70%). This finding suggests that the gradient of the intracapillary oxygen saturation may be neglected, i.e., the intracapillary oxygenation level is almost that of the perfusate Y_p. Thus, we determined $\delta\omega$ according to Eqs. [1] and [3] for the susceptibility difference $\Delta\chi = (1 - Y_p) \cdot \Delta\chi_0$, with $\Delta\chi_0 = 8 \cdot 10^{-8}$ as the susceptibility difference for complete deoxygenated blood. Since experiments were performed in a horizontal system, the long heart axis, and, hence, the mean orientation of the capillaries was most probably perpendicular to the direction of the external field, i.e., the assumption that $\theta = \pi/2$ (Eqs. [1] and [3]) is reasonable, and the equatorial shift of the radial frequency is $\delta\omega = 2\pi\gamma \cdot (1 - Y_p)\Delta\chi_0 \cdot B_0$.

Since we can only determine the BOLD-related part of relaxation, the offset of the empirical function (Eq. [44]) at 100% oxygen saturation of hemoglobin ($R_2^*(\text{O}_2 \text{ sat.} = 1) = 33.3\ \text{s}^{-1}$) was added to our data. Figure 5 demonstrates clearly similarity between the empirical curve and the curve obtained from our model when RBV = 10%, which is a reasonable value for a dilated microvascular system (20).

Comparison with Our Own Results

We performed diastolic measurements of myocardial T_2^* in healthy volunteers ($n = 15$) in the short axis view by a segmented gradient echo sequence, which acquires 10 successive gradient echoes per excitation (TE = 6–54 ms, ΔTE = 5.4 ms). The exact description of the method, the protocol, and the results is given in detail in another article (C. Wacker, et al., manuscript submitted). In this section, only the essentials of the results are reported to demonstrate that the theory may be applied in this field. Measurements were performed before and after application of the vasodilator dipyridamol (0.56–0.84 mg/kg body weight, continuous infusion) in a 1.5 T system. In this dosage, dipyridamol has the property to increase coronary blood flow from a value at rest of $F_{\text{rest}} \approx 0.8$ ml/g per min to $F_{\text{dipyridamol}} = 4$ ml/g per min (21) with negligible effect on myocardial performance, and hence, oxygen consumption. Thus, the capillary deoxyhemoglobin concentration should decrease and the BOLD effect should become evident. The mean T_2^* we determined under resting conditions was 36 ms, and we observed an increase of about 17% after dipyridamol administration.

Under resting conditions, the oxygen pressure in the venous coronary system is about 17 Torr (22), i.e., the oxygenation of hemoglobin is about $Y_{\text{v,rest}} = 25\%$. Arterial oxygenation is almost $Y_a \approx 100\%$, and the myocardial oxygen consumption $\text{M}\dot{\text{V}}\text{O}_2$ is proportional to coronary blood flow and the arteriovenous difference of oxygenation $\Delta Y_{\text{rest}} = Y_a - Y_{\text{v,rest}}$, i.e.

$$\text{M}\dot{\text{V}}\text{O}_2 \sim F \cdot \Delta Y \qquad [47]$$

Since dipyridamol does not alter the oxygen consumption $\text{M}\dot{\text{V}}\text{O}_2$, administration of this drug reduces the arteriovenous difference to

$$\Delta Y_{\text{dipyridamol}} = \frac{F_{\text{rest}}}{F_{\text{dipyridamol}}} \cdot \Delta Y_{\text{rest}} \qquad [48]$$

$$= 15\%, \qquad [49]$$

i.e., the venous oxygenation after dipyridamol administration is $Y_{\text{v,dipyridamol}} \approx 85\%$.

As a first step to estimate the myocardial BOLD effect according to our model, we consider the intracapillary oxygenation to be Y_v. The dependence of the susceptibility difference $\Delta\chi$ on oxygenation is determined by $\Delta\chi = \Delta\chi_0 \cdot (1 - Y_v)$, with $\Delta\chi_0 = 8 \cdot 10^{-8}$ for deoxygenated blood with a hematocrit of 40%. When we take a capillary radius of 2.75 μm, an intercapillary distance of 19 μm (11), and a diffusion coefficient of $D = 1\ \mu\text{m}^2/\text{ms}$, the intracapillary volume fraction is RBV = 8.4% and the correlation time $\tau = 5.11$ ms (Eq. [11]). Insertion into Eqs. [1]–[3], and [35] gives a BOLD-related relaxation rate of $R_2^* = 4.43\ \text{s}^{-1}$ under resting conditions and $R_2^* = 0.2\ \text{s}^{-1}$ after dipyridamol application. Hence, the BOLD-related decrease of relaxation rate is $\Delta R_2^* = -4.23\ \text{s}^{-1}$. Under resting conditions, we measured a mean $T_{2,\text{rest}}^* \approx 36$ ms, i.e., $R_{2,\text{rest}}^* = 27.7\ \text{s}^{-1}$.

Thus, our calculations would predict a rate of $R^*_{2,\text{dipyridamol}} = 23.47\ \text{s}^{-1}$ after dipyridamol administration, i.e., $T^*_{2,\text{dipyridamol}} = 42.6$ ms. Similar calculations reveal for capillary oxygenation levels of Y = 30%, 35%, 40%, and 50% corresponding relaxation times of $T^*_{2,\text{dipridamol}} = 41.6$ ms, 40.8 ms, 40 ms, and 39 ms, respectively. Hence, calculations performed for a capillary oxygenation at rest in the range of 25–35% predict an increase of $T^*_{2,\text{rest}}$ by 13–18%, which is in good agreement with the increase of 17% obtained from experimental data.

It has to be stated that the considerations above are rather crude. For example, we did not consider an intracapillary gradient of oxygenation along the capillary axis. However, the determination of such a gradient in myocardium is very difficult. In the brain, for example, almost stationary conditions of perfusion and oxygen consumption suggest a stationary gradient of oxygenation in the direction of the capillary axis. In the beating heart, the contractions of myocardium lead to cyclic variations of oxygen consumption and intracapillary flow. Thus, the intracapillary oxygenation is a complex function of the phasic oxygen demand, phasic intracapillary red cell flux, and the diffusion controlled oxygen transport from hemoglobin to extracapillary tissue. Some theories (23) assume a rapid delivery of oxygen from all intracapillary red blood cells in early diastole, i.e., intracapillary oxygenation would rapidly decrease to that of the venous system in early diastole. This hypothesis would be in accordance with our calculations that predict the observed increase of T^*_2 best when the intracapillary oxygenation is close to that of the coronary venous system. However, other theories assume several heart cycles for the delivery of oxygen, which suggests the formation of a longitudinal gradient of intracapillary oxygenation (23). To our knowledge no experimental data exist of these gradients of intracapillary oxygenation in myocardium. Hence, we think that our assumption above is justified as a first step to estimate the BOLD effect in myocardium.

DISCUSSION

Based on a simple model geometry of capillary and surrounding tissue we derived an analytical expression for the transverse relaxation rate as a function of the relative capillary volume fraction, the capillary radius, the intracapillary magnetization and the diffusion coefficient. The decisive step that allowed this analytical approach was the application of the *strong collision* approach to the dynamics of spin diffusion. The predictions of the model agree well with the data obtained by simulation experiments of Kennan et al. (10) and the experimental results of Atalay et al. (2, 3) and our group (C. Wacker, et al., manuscript submitted). It has to be emphasized that our approach may also be transferred to other capillary arrangements besides that in myocardium.

Model Assumptions

We considered diffusion between coaxial cylinders, i.e., the capillary and the supply cylinder. One might argue, that we did not consider a rectangular geometry for the diffusion space as others did for their simulations (10). However, for morphometric analysis in myocardium a hexagonal arrangement of capillaries is often assumed (11, 24). The capillary supply distance (half of the mean intercapillary distance) is $R_s = 1/\sqrt{\text{capillary density} \cdot c}$ with $c = 2\sqrt{3} = 3.46$ for the hexagonal, $c = \pi$ for the cylindrical, and $c = 4$ for the rectangular model, i.e., the cylindrical model is closer to the hexagonal one than the rectangular. Furthermore, mathematical analysis is performed much easier in the cylindrical model, and the intention of our article preferred to demonstrate fundamental properties of our model rather than to reproduce morphometrical exactness.

Within the diffusion space, we only considered the interaction of a nuclear spin with the magnetic field around one capillary, i.e., **the field contribution of the neighboring capillary** was neglected. In myocardium, the intercapillary distance is about 19 μm and the capillary radius 2.75 μm (11). Hence, the contribution of a neighboring field at the periphery of the supply region field is less than 10% from its maximum, i.e., as a first step it is justified to neglect these fields.

In our model, we did not consider intravascular contributions to the BOLD effect. Boxerman et al. (25) performed Monte Carlo simulations of diffusing spins to quantitate signal changes in fMRI. The physiological and anatomical parameters they applied in their simulations were that of the brain. For an echo time of TE = 40 ms and a relative flow increase of e.g. 1.6, they obtained a BOLD-related signal change of ≈1%, which is related to the extravascular magnetization, and ≈2% when the intracapillary and extravascular components are considered. When all components that contribute to the BOLD effect are considered, i.e., extravascular, intracapillary, and intravenous magnetization, the signal change was about 3.5%. Hence, the authors state that the intravascular contribution of the BOLD effect to signal change is clearly dominating. In our model, we did not consider the intravascular or intracapillary contribution to the BOLD effect, since the anatomical and physiological situation is different in myocardium. In myocardium the intravascular volume consists mainly of the intracapillary volume (>90%) (7), whereas the volume of the venous system is less than 10% of the intravascular volume. In the brain, however, the volume fractions of both the intracapillary and intravenous system are almost the same (25). This finding suggests that the contribution of the venous system to the BOLD effect is considerable in the brain, although it may be negligible in myocardium. When we restrict our considerations to the capillary system, there are also decisive differences between both tissues: the relative volume fraction of the intracapillary space is higher in myocardium (≈8.4% (12)) than in the brain (≈2%), which implies that more extravascular spins are affected by the pericapillary magnetic field gradient in myocardium than in the brain. Another point is that the oxygen extraction within the capillary is much higher in myocardium. This finding leads to a venous oxygenation of about 25%, whereas in the brain it is 60%. Furthermore, there is phasic oxygen delivery in myocardium, i.e., there is not stationary oxygenation gradient along the capillary axis as there is in the brain. Some authors even assume that almost the whole oxygen delivery takes place in early diastole (23), i.e., the intracapillary oxygenation would rapidly decline to that of the coronary venous system during diastole. This finding suggests that the magnitude of the pericapillary magnetic field, and hence, the contribution of the extravascular relaxation enhancement to the BOLD effect is much higher in myocardium than in the brain. This finding can also be quantified as follows: a relative signal change of about 1% (TE $=$ 40 ms) due to the extravascular contribution of the BOLD effect in the brain (25) suggests an increase of the relaxation rate of $\Delta R_2^* = 0.25\ \text{s}^{-1}$, when we assume that the relative signal change is $1 - e^{-\text{TE}\cdot\Delta R_2^*} \approx \text{TE}\cdot\Delta R_2^*$. In myocardium, our model, which only considers extravascular BOLD effects, reveals reasonable increases of relaxation rate in the order of $\Delta R_2^* \approx 4\ \text{s}^{-1}$, i.e., 16 times higher than that in the brain. Therefore, we think that as a first step it is justified to consider only the extravascular magnetization and its contribution to relaxation in myocardium. Nevertheless, our model may be developed to a model that also includes the effect of intracapillary magnetization. In this case, tissue is considered as a two-compartment system, with two intrinsic relaxation rates: the intracapillary and the extravascular relaxation rate, of which the latter is determined according to our model. In another context, we recently derived an analytical expression that provides the relaxation rate of such a two-compartment system as a function of the intracapillary and extravascular relaxation rate, and the exchange rate between both compartments (26). The application of this complex model will be one of our future aims.

In our model, capillaries are considered as cylinders filled with blood. Blood inside the capillaries is assumed to be a homogeneous magnetic substance, and the pericapillary magnetic field is determined according to principles of magnetostatics. This assumption is valid in larger vessels; however, in capillaries the situation is different. The cross-section of a capillary is approximately the size of an erythrocyte. This finding suggests that blood inside the capillary may be considered as an almost linear arrangement of single red blood cells with plasma in between. The BOLD effect is related to the paramagnetic property of deoxyhemoglobin, which is confined to the red blood cells. Thus, the inhomogeneous magnetic field in tissue is a superposition of the magnetic fields around the red blood cells. This finding suggests that the pericapillary field strength is stronger in the near side of capillary segments that contain an erythrocyte than in segments in between that are filled with plasma. This pericapillary magnetic field is obviously more complex than the field around a homogeneous paramagnetic cylinder, as we assumed in our model. However, the determination of this complex field is hampered by several obstacles: the toroidal shape of red blood cells in large vessels changes as these cells enter the capillary, due to mechanical and hydrodynamical interactions of the erythrocyte with the capillary wall and plasma. There is no simple mathematical description for this intracapillary shape of red blood cells, i.e., the magnetic field outside the cell cannot be described by a simple formula. Furthermore, this intracapillary shape of the erythrocyte may be a time-dependent function of mechanical forces, e.g., intramural cyclic pressure variations in myocardium. Due to this complicated situation, it appears that at the present state of knowledge our capillary-tissue model may be a reasonable approach to start with. This model bears the potential to be elaborated for a more realistic, and, hence, complex description of structures in tissue.

Relaxation

We assumed in our analysis a single exponential decay of the relaxation curve. One might argue that in general a multiexponential fit has to be applied. However, at present, the experimental data do only reveal enough information to justify a single exponential approach. Furthermore, our model is not limited to a single exponential fit, but it can be expanded to a multiexponential fit of any order. Since we could determine the Laplace transform (Eq. [30]) of the transverse magnetization decay, the full information of the exact relaxation curve is available. Based on the theory of generalized moment expansion, one of us recently developed an algorithm that allowed a multiexponential approximation of nth order of the relaxation curve from the Laplace transform (15). We had already applied this multiexponential approximation to spin relaxation (17); however, we believe experimental data suggesting a non-single exponential decay should be a prerequisite.

In our study, we only considered the decay of magnetization that is detected by gradient echo sequences, i.e., reversible and irreversible dephasing effects contribute to transverse relaxation. In contrast, in spin-echo sequences, irreversible dephasing effects are detected. In principle, time evolution of magnetization in spin-echo sequences may also be determined according to the *strong collision* model. The operator of time evolution in Eq. [23] has to be replaced by a sequence of this operator and its complex adjoint operator, in which the latter describes the time evolution after the 180° pulse. When multiecho sequences with n echoes is used, this operator sequence has to be repeated n times. Obviously, the mathematical analysis of this relaxation is much more complex and will be one of our future goals.

APPENDIX

Derivation of the Correlation Time

The solution of Eq. [11] requires the determination of a function $f(x) = -(1/\nabla^2)\omega(x)$. This function has to satisfy the inhomogeneous differential equation

$$\nabla^2 f(x) = -\omega(x) \qquad \text{[A1]}$$

Since $\omega(x) = -\delta\omega \cdot R_c^2 \cdot \cos(2\phi)/r^2$ (cylindrical coordinates $x = (r, \phi)$), we make the approach

$$f(x) = g(r) \cdot \cos(2\phi) \qquad \text{[A2]}$$

Application of the operator $\nabla^2 = r^{-1}\partial_r r \partial_r + r^{-2}\partial_\phi^2$ (cylindrical coordinates) on f results in

$$\partial_r^2 g(r) + r^{-1}\partial_r g(r) - 4r^{-2} g(r) = \delta\omega R_c^2 r^{-2} \qquad \text{[A3]}$$

Equation [A3] is solved by

$$g(r) = a \cdot r^2 + b \cdot r^{-2} - \frac{\delta\omega \cdot R_c^2}{4} \qquad \text{[A4]}$$

where the constants a and b are determined so that Eq. [A4] satisfies the boundary conditions of the diffusion process, i.e., $\partial_r g(r) = 0$ when $r = R_c, R_s$. This implies that $a = b = 0$, i.e.,

$$f(x) = -\cos(2\phi) \cdot \frac{\delta\omega R_c^2}{4} \qquad \text{[A5]}$$

Insertion of f in Eq. [11] gives

$$\tau = \frac{1}{K(0)DV} \cdot \int_V dx\ \omega(x) \cdot f(x) \qquad \text{[A6]}$$

$$= \frac{1}{K(0)V} \cdot \int_{R_c}^{R_s} \int_0^{2\pi} dr\ r d\phi \cos^2(2\phi) r^{-2} \cdot \frac{\delta\omega^2 R_c^4}{4D} \qquad \text{[A7]}$$

$$= \frac{1}{K(0)V} \cdot \ln(R_s/R_c) \frac{\pi\delta\omega^2 R_c^4}{4D} \qquad \text{[A8]}$$

with

$$K(0) = \frac{1}{V} \int_V dx\ \omega(x)^2 \qquad \text{[A9]}$$

$$= \frac{1}{V} \int_{R_c}^{R_s} \int_0^{2\pi} dr\ r d\phi (\delta\omega R_c^2 \cdot \cos(2\phi) r^{-2})^2 \qquad \text{[A10]}$$

$$= \frac{1}{V} (R_c^{-2} - R_s^{-2}) \frac{\pi\delta\omega^2 R_c^4}{2} \qquad \text{[A11]}$$

this directly provides the result of Eq. [11].

Derivation of the Laplace transform $\hat{M}_0(s)$

The Laplace transform of the time course of magnetization in the absence of diffusion (static dephasing regime) is

$$\hat{M}_0(s) = \frac{1}{V} \int_V dx \frac{1}{s \cdot \mathbf{id} - i \cdot \omega(x)}$$

$$= \frac{1}{V} \int_{R_c}^{R_s} dr \cdot r \int_0^{2\pi} d\phi \cdot \frac{1}{s \cdot \mathbf{id} - i \cdot (-\delta\omega \cdot R_c^2 \cos(2\phi)/r^2)}$$

$$= \frac{1}{V} \int_{R_c}^{R_s} dr\ r^3 \underbrace{\int_0^{2\pi} d\phi \frac{1}{r^2 s + i\delta\omega R_c^2 \cos 2\phi}}_{= I(r)} \qquad \text{[A12]}$$

Elementary integral transformation and substitution of $e^{i\phi} = z$ provides the integral $I(r)$

$$I(r) = \int_0^{2\pi} d\phi \frac{1}{r^2 s + i\delta\omega R_c^2 \cos 2\phi}$$

$$= \int_0^{2\pi} d\phi \frac{1}{r^2 s + i\delta\omega R_c^2 \cos\phi}$$

$$= \oint_{|z|=1} dz \frac{1}{iz} \cdot \frac{1}{r^2 s + i\delta\omega R_c^2 \frac{1}{2}\left(z + \frac{1}{z}\right)}$$

$$= -\oint_{|z|=1} dz \frac{1}{R_c^2 \delta\omega^{1/2}(z^2 + 1) - isr^2 z}$$

$$= -2\pi i \cdot \operatorname{Res}\left(\frac{1}{R_c^2 \delta\omega^{1/2}(z^2 + 1) - isr^2 z}, |z_p| < 1\right)$$

$$= -2\pi i \cdot \frac{1}{R_c^2 \delta\omega/2} \cdot \frac{1}{z_{p1} - z_{p2}}$$

$$= 2\pi \frac{1}{\sqrt{s^2 r^4 + R_c^4 \delta\omega^2}} \qquad \text{[A13]}$$

where $z_{p2} = i \cdot [sr^2 + \sqrt{(s^2 r^4 + R_c^4 \delta\omega^2)}/(R_c^2 \delta\omega)]$ and $z_{p1} = i \cdot [sr^2 - \sqrt{(s^2 r^4 + R_c^4 \delta\omega^2)}/(R_c^2 \delta\omega)]$ denote the poles of the complex function $(R_c^2 \delta\omega^{(1/2)}(z^2 + 1) - isr^2 z)^{-1}$. The absolute value of the latter is smaller than 1.

Substitution of the right-hand side of Eq. [A13] in Eq. [A12] provides

$$\hat{M}_0(s) = \frac{2\pi}{V} \int_{R_c}^{R_s} dr\ r^3 \frac{1}{\sqrt{s^2 r^4 + R_c^4 \delta\omega^2}}$$

$$= \frac{2\pi}{4Vs^2} \int_{s^2 R_c^4}^{s^2 R_s^4} d\xi \frac{1}{\sqrt{\xi + R_c^4 \delta\omega^2}} = \frac{1}{s^2 \cdot (R_s^2 - R_c^2)}$$

$$\cdot \left(\sqrt{s^2 R_s^4 + \delta\omega^2 R_c^4} - R_c^2 \sqrt{s^2 + \delta\omega^2}\right)$$

$$= \frac{R_c^2 + R_s^2}{\sqrt{s^2 R_s^4 + \delta\omega^2 R_c^4} + R_c^2 \sqrt{s^2 + \delta\omega^2}} \qquad \text{[A14]}$$

REFERENCES

1. Ogawa S, Lee T-M, Nayak AS, Glynn P. Oxygenation-sensitive contrast in magnetic resonance image of the rodent brain at high magnetic fields. Magn Reson Med 1990; 14:68–78.
2. Atalay MK, Forder JR, Chacko VP, Kawamoto S, Zerhouni EA. Oxygenation in the rabbit myocardium: assessment with susceptibility dependent MR imaging. Radiology 1993; 189:759–764.
3. Atalay MK, Reeder SB, Zerhouni EA, Forder JR. Blood oxygenation dependence of T_1 and T_2 in the isolated, perfused rabbit heart at 4.7 T Magn Reson Med 1995; 34:623–627.
4. Li D, Dhawale P, Rubin PJ, Haacke EM, Gropler RJ. Myocardial signal response to dipyridamol and dobutamine: demonstration of the BOLD effect using a double-echo sequence. Magn Reson Med 1996; 36:16–20.

5. Niemi P, Poncelet BP, Kwong KK, Weisskoff RM, Rosen BR, Brady TJ, Kantor HL. Myocardial intensity changes associated with flow stimulation in blood oxygenation sensitive magnetic resonance imaging. Magn Reson Med 1996; 38:78–82.
6. Yablonski DA, Haake EM. Theory of NMR-signal behavior in magnetically inhomogeneous tissues: the static dephasing regime. Magn Reson Med 1994; 32:749–763.
7. Kaul S, Jayaweera AR. Coronary and myocardial blood volumes. Circulation 1997; 96:719–724 [Editorial].
8. Gillis P, Koenig SH. Transverse relaxation of solvent protons induced by magnetized spheres: application to ferritin, erythrocytes, and magnetite. Magn Reson Med 1987; 5:323–345.
9. Torrey HC. Bloch equations with diffusion terms. Phys Rev 1956; 104:563–565.
10. Kennan RP, Zhong J, Gore JC. Intravascular susceptibility contrast mechanisms in tissues. Magn Reson Med 1994; 31:9–21.
11. Bassingwaighte JB, Ypintsol T, Harvey RB. Microvasculature of the dog left ventricular myocardium. Microvasc Res 1974; 7:229–249.
12. Donahue KM, Burstein D, Mannings WJ, Gray ML. Studies of Gd-DTPA relaxivity and proton exchange rates in tissue. Magn Reson Med 1994; 32:66–76.
13. Bauer WR, Schulten K. Theory of contrast agents in magnetic resonance imaging: coupling of spin relaxation and transport. Magn Reson Med 1992; 26:16–39.
14. Jackson DJ. ‘‘Classical Electrodynamics,’’ John Wiley and Sons, New York, 1975.
15. Nadler W, Schulten K. Generalized moment expansion for Brownian relaxation processes. J Chem Phys 1985; 82:151–160.
16. Dattagupta S, Blume M. Stochastic theory of line shape: I. Nonsecular effects in the strong collision model. Phys Rev B 1974; 10:4540–4550.
17. Bauer WR, Schulten K. Nuclear spin dynamics (I = 1/2) under the influence of random perturbation fields in the strong collision approximation. Ber Bunsenges Phys Chem 1992; 96:721–723.
18. Thulborn KR, Waterton JC, Mathews PM, Radda G. Oxygenation dependence of the transverse relaxation time of water protons of whole blood at high fields. Biochim Biophys Acta 1982; 714:265–270.
19. Groth J, Thews G. Die Bedingungen für die Sauerstoffversorgung des Herzmuskelgewebes. Pflügers Arch 1962; 276:142–165.
20. Chrystal GJ, Downey HF, Bashour FA. Small vessel and total coronary blood volume during adenosine infusion. Am J Physiol 1981; 241:H194–H201.
21. Tauchert M, Hilger HH. *in* ‘‘The Pathophysiology of Myocardial Perfusion’’ (W. Shaper, Ed.), p. 141, Elsevier/North Holland Biomedical Press, Amsterdam, 1979.
22. Bing RJ, Hammond MM, Handelsman JC, Powers SR, Spenger FC, Eckenhoff JE, Goodale WT, Hafkenschiel JH, Kety SS. The measurement of coronary blood flow, oxygen consumption, and efficiency of the left ventricle in man. Am Heart J 1949; 38:1.
23. Thews G. Die Sauerstoffdrücke im Herzmuskelgewebe. Pflügers Arch 1962; 276:166–181.
24. Gerdes AM, Callas G, Kasten FH. Differences in regional capillary distribution and myocyte sizes in normal and hypertrophic rat hearts. Am J Anat 1979; 156:523–532.
25. Boxerman JL, Bandettini PA, Kwong KK, Baker JR, Davis TL, Rosen BR, Weisskoff RM. The intravascular contribution to fMRI signal change: Monte Carlo modeling and diffusion weighted studies in vivo. Magn Reson Med 1995; 34:4–10.
26. Bauer WR, Roder F, Hiller K-H, Han H, Fröhlich S, Rommel E, Haase A, Ertl G. The effect of perfusion on T_1 after slice-selective spin inversion in the isolated cardioplegic rat heart: measurement of a lower bound of intracapillary-extravascular water proton exchange. Magn Reson Med 1997; 38:917–923.

Theory of Coherent and Incoherent Nuclear Spin Dephasing in the Heart

Wolfgang R. Bauer,[1,*] Walter Nadler,[2] Michael Bock,[3] Lothar R. Schad,[3] Christian Wacker,[1]
Andreas Hartlep,[2] and Georg Ertl[1]
[1]*II. Medizinische Klinik, Klinikum Mannheim/Universität Heidelberg, Theodor-Kutzer Ufer 1-3, D-68167 Mannheim, Germany*
[2]*HLRZ/NIC c/o Forschungszentrum Jülich, D-52725 Jülich, Germany*
[3]*Department of Biophysics, German Cancer Research Center (DKFZ), D-69120 Heidelberg, Germany*

(Received 30 March 1999)

We present an analytical theory of susceptibility induced nuclear spin dephasing in the capillary network of myocardium. Using a strong collision approach, equations are obtained for the relaxation rate of the free induction and the spin echo decay. Simulation and experimental data are well predicted by the theory. Since paramagnetic deoxyhemoglobin as the origin of nuclear spin dephasing has a higher tissue concentration in myocardium supplied by a stenotic, i.e., significantly narrowed, coronary artery, spin dephasing might serve as a diagnostic tool. Our approach can be modified for capillary networks in other tissues than myocardium and may be applied in material science.

PACS numbers: 87.61.–c, 76.60.Jx

In cardiology, a paramount goal is the detection of significant narrowing, called stenosis, of coronary arteries, and—even more important—the detection of the associated area of the cardiac muscle. There is evidence that this area can be distinguished from normally supplied tissue without contrast agent by NMR imaging from its different transverse spin relaxation time [1]. Water proton spin dephasing is induced by spin-spin interactions and susceptibility differences between different histological substructures such as intra- and extravascular space. In native tissue, this difference is related to the paramagnetic property of deoxygenated hemoglobin which induces perivascular field gradients. Deoxyhemoglobin, which results from intracapillary deoxygenation of almost 100% oxygenated arterial hemoglobin, is predominately located in the capillary and venous system. In the cardiac muscle, this blood oxygen level dependent (BOLD) effect is almost solely due to the magnetic field inhomogeneities around capillaries since they contain more than 90% of intramyocardial blood volume [2]. In myocardium supplied by a stenotic coronary artery, coronary autoregulation tries to maintain sufficient perfusion by compensatory filling of capillaries (recruitment), i.e., deoxyhemoglobin increases in tissue and spin dephasing is accelerated when compared to normally supplied tissue [1]. This difference of spin dephasing can be pronounced by pharmacological coronary dilation since a higher oxygen supply decreases the tissue concentration of deoxyhemoglobin in normal myocardium [3–5], whereas it does not in the poststenotic myocardium [1].

Though the relation between spin dephasing and coronary microcirculation is of great interest for the diagnosis of coronary artery disease, at present there is no satisfying analytical theory that describes the dephasing of diffusing spins in the inhomogeneous magnetic field of the capillary system. There exist theories on spin dephasing for very long and very short correlation times of diffusion induced magnetic field fluctuations. The assumption of static dephasing of spins as proposed by Yablonski *et al.* [6] is not valid in human cardiac NMR imaging systems (field strength less than 2 T) since the diffusion distance l during relaxation (relaxation time $T_2^* >$ 30 ms, $D = 1\ \mu\mathrm{m}^2/\mathrm{ms}$, $l > \sqrt{2T_2^*D} \approx 8\ \mu\mathrm{m}$) has the same magnitude as the intercapillary distance (19 μm). Thus, a single nuclear spin experiences almost the whole pericapillary magnetic field gradient during its relaxation. Kiselev and Posse [7] recently proposed analytical treatments for long and short correlation times. The first extends the static dephasing model by including diffusion. However, only the effect of a *linear* local field gradient on relaxation is considered. Application of this approach would be valid if large vessels would dominate the microvascular architecture of myocardium, which is, however, not the case. The other is a perturbation approach in the local fields. In the cardiac muscle, the motional narrowing condition $\tau\langle\omega^2\rangle^{1/2} \ll 1$ with correlation time τ and variance of fluctuations of the local fields (expressed as frequency) $\langle\omega^2\rangle$ is not fulfilled, though. Approaches which consider spin dephasing for arbitrary correlation times as the Gaussian or Lorentzian phase approximation were not successful since they neither revealed the correct field dependence of the relaxation rate [8] nor the correct fluctuation-dissipation relation [7].

In this paper, an analytical theory is proposed which describes coherent and incoherent spin dephasing in the capillary network of myocardium. It is not an extension of the static dephasing model or a perturbation approach. Instead, it is based on a strong collision approximation which includes both the static dephasing and the motional narrowing regime as two limiting cases.

It has to be emphasized that this approach is not restricted to myocardium, but can be modified for the description of transverse relaxation in capillary networks of other tissues as well. Applications in material science are

0031-9007/99/83(20)/4215(4)$15.00 © 1999 The American Physical Society

possible, too. For example, the effect of complex potentials on spin diffusion, and, hence, on spin dephasing, is exploited to determine the microstructure of spatially or magnetically heterogeneous media [9]. Examples for the former are porous structures, for the latter polymer solutions and liquid crystals in which magnetic heterogeneity is induced by either paramagnetic impurities or an inhomogeneous electrical current. After modifications for the appropriate geometry, the analysis presented below should also be applicable in that field of research.

We will first discuss the *tissue model* employed. The regular parallel architecture of muscle fibers and capillaries in myocardium [10] allows one to reduce considerations from the whole tissue to one tubular capillary (radius R_c) which is concentrically surrounded by its mean cylindrical supply region with radius R_s (Krogh model [11]). Nuclear spin diffusion in the whole tissue is replaced by restricted diffusion in the supply region, i.e., reflectory boundary conditions are introduced at R_s, and, since the capillary wall is nearly impermeable for water on the time scale of spin dephasing [12], also at R_c. We consider only relaxation of extracapillary nuclear spins since in myocardium the relative intracapillary blood fraction $\varsigma = R_c^2/R_s^2$ is less than 10%. The effect of diffusion in field gradients along the capillary axis on spin dephasing is negligible, i.e., it is necessary only to consider two-dimensional diffusion of spins within two concentric circles (R_c, R_s). Basic magnetostatics provides the susceptibility related spin frequency shift around the capillary in cylindrical coordinates as

$$\omega(r, \phi) = -\delta\omega R_c^2 \cos(2\phi)/r^2, \qquad (1)$$

with the characteristic equatorial frequency shift $\delta\omega = 2\pi\gamma\Delta\chi B_0 \cos(\theta)$, where γ is the gyromagnetic ratio, $\Delta\chi$ is the susceptibility difference, and θ is the tilt angle between the capillary axis and the external field which is almost 90° in a clinical scanner. Since $\Delta\chi < 8 \times 10^{-8}$ for blood, the intracapillary magnetization is less than 1 mG for clinical NMR magnets and $\delta\omega \leq 168\ \mathrm{rad\,s^{-1}}$. The contribution of fields of neighboring capillaries is negligible due to the intercapillary distance of 19 μm.

The starting point of our analytical treatment is the free induction decay of the local nuclear transverse magnetization. The time evolution (polar notation: $m = m_x - im_y$) at $x = (r, \phi)$ is determined according to the Bloch Torrey diffusion equations [13] which, written in rotating frame coordinates, are

$$\partial_t m(x,t) = [D\nabla^2 + i\omega(x)]m(x,t), \qquad (2)$$

with diffusion coefficient D. The formal solution of Eq. (2) is $m(x,t) = \exp\{[D\nabla^2 + i\omega(x)]t\}m(x,0)$. Since the spatial resolution of clinical NMR scanners is far above that of capillary dimensions (mm vs μm), the observable is the mean transverse magnetization $M(t)$ within the supply region with volume V:

$$M(t) = V^{-1}\int_V dx \exp\{[D\nabla^2 + i\omega(x)]t\}m(x,0). \qquad (3)$$

The homogeneous water concentration in the cardiac muscle implies a homogeneous initial magnetization distribution $m(x,0)$ which for simplicity is normalized to $m(x,0) = 1$. Since Eq. (2) cannot be solved analytically when the local frequency is given by Eq. (1), a different approach is necessary.

Let us first consider the *fluctuations* of the local magnetic fields, represented by the corresponding local NMR frequencies $\omega(x)$ that a diffusing nuclear spin experiences. Their autocorrelation function $K(t)$ is determined by $K(t) = V^{-1}\int_V dx\, \omega(x) \exp(tD\nabla^2)\omega(x)$, where $\exp(tD\nabla^2)$ is the Green's function of the restricted diffusion. The *correlation time* τ of the field fluctuations is defined as the mean relaxation time [14] of the autocorrelation function, $\tau = \int_0^\infty dt\, K(t)/K(0)$. Using the techniques of Ref. [14], we obtain [15]

$$\tau = (R_c^2/4D)\ln(\varsigma)/(\varsigma - 1). \qquad (4)$$

Inserting realistic values of relative intracapillar blood volume (ς = 5 to 10%), capillary radius (R_c = 2.5 to 2.75 μm), and the diffusion coefficient ($D = 1\ \mu\mathrm{m}^2/\mathrm{ms}$) into Eq. (4) implies that $\tau \leq 6$ ms. Relaxation times of the free induction decay observed using clinical scanners are $T_2^* \geq 30$ ms. Hence, the relaxation time describing the contribution of field inhomogeneities is even longer. This implies that on a time scale in which significant variations of $M(t)$ occur the local field fluctuations are stochastically independent.

This stochastic independence suggests replacing the diffusion operator $D\nabla^2$ in Eq. (2) by a *strong collision operator* [16]. This operator describes the diffusion as a stationary Markov process with a single rate λ that governs the relaxation to the steady state distribution $p(x)$, independent of the initial state. Because of the homogeneity of water in tissue, the steady state distribution is simply $p(x) = 1/V$. The generator $\mathbf{D}$ of the corresponding Markov process is then

$$\mathbf{D} = \lambda(\mathbf{\Pi} - \mathbf{id}), \qquad (5)$$

where $\mathbf{\Pi}$ denotes the projection operator onto the functional space generated by $p(x)$, i.e., the application of this operator on some function $f(x)$ is $\mathbf{\Pi}f(x) = V^{-1}\int_V dx\, f(x)$. The constant λ is determined self-consistently by requiring that $\mathbf{D}$ describes correctly the field fluctuations. This implies $\lambda = \tau^{-1}$ [see Eq. (4)].

Instead of directly solving the time evolution of the magnetization [Eq. (3)] under the strong collision assumption, it is more convenient to consider the Laplace transform:

$$\hat{M}(s) = V^{-1}\int_V dx[s - D\nabla^2 - i\omega(x)]^{-1}m(x,0). \qquad (6)$$

Replacing $D\nabla^2$ by $\mathbf{D}$ and utilizing the operator identity $(A + B)^{-1} = A^{-1} - A^{-1}B(A + B)^{-1}$ we obtain, after some algebra,

$$\begin{aligned}\hat{M}(s) = (1 + \varsigma)\Big[&\sqrt{(s + \tau^{-1})^2 + \delta\omega^2\varsigma^2} \\ &+ \varsigma\sqrt{(s + \tau^{-1})^2 + \delta\omega^2} \\ &- \tau^{-1}(1 + \varsigma)\Big]^{-1}. \qquad (7)\end{aligned}$$

$M(t)$ can be obtained from this result to arbitrary accuracy as a multiexponential function $M(t) \approx \sum_{\nu=1}^{N} f_\nu \exp(-\Gamma_\nu t)$, the parameters determined from (7) using the generalized moment method of [14]. The relaxation time of the free induction process corresponds to the lowest order (mean relaxation time) approximation, which provides the best single-exponential approximation, $M(t) \approx e^{-t/T_2^*}$, by setting $T_2^* = \hat{M}(0)$. Thus,

$$T_2^* = \frac{\tau(1 + \varsigma)}{[\sqrt{1 + (\varsigma\tau\delta\omega)^2} - 1] + \varsigma[\sqrt{1 + (\tau\delta\omega)^2} - 1]}\,. \qquad (8)$$

The free induction decay of magnetization is a result of coherent and incoherent spin dephasing. When instead a *spin echo* experiment is performed, a 180° pulse applied at $t/2$ reflects the spin phase which eliminates the coherent contribution of spin dephasing at the echo time t. Time evolution of the local magnetization before the 180° pulse is that of a free induction decay $m(x, t/2) = \exp\{[D\nabla^2 + i\omega(x)]t/2\}m(x, 0)$. After the phase reflection which is described by the complex adjoint $m(x, t/2) \xrightarrow{180^\circ\,\text{pulse}} m^*(x, t/2)$, there is again a free induction decay, i.e., the global magnetization $M_{\text{SE}}(t)$ after the echo time t is

$$\begin{aligned}M_{\text{SE}}(t) = V^{-1}\int_V dV\, &\exp\{[D\nabla^2 + i\omega(x)]t/2\} \\ &\times \exp\{[D\nabla^2 - i\omega(x)]t/2\}m(x, 0)\,. \qquad (9)\end{aligned}$$

Again replacing $D\nabla^2$ by $\mathbf{D}$, differentiating this relation, and exploiting the structure of the operator $\mathbf{D}$, we obtain a general relation between the contribution of solely incoherent spin dephasing on relaxation (M_{SE}) and that of coherent and incoherent dephasing (M):

$$\partial_t M_{\text{SE}}(t) = \frac{1}{\tau}\,[|M(t/2)|^2 - M_{\text{SE}}(t)]\,, \qquad (10)$$

which is solved by

$$M_{\text{SE}}(t) = \frac{e^{-t/\tau}}{\tau}\left(\tau + \int_0^t d\xi\, e^{\xi/\tau}|M(\xi/2)|^2\right). \qquad (11)$$

For the free induction decay being given by $M(t) \approx \sum_{\nu=1}^{N} f_\nu \exp(-\Gamma_\nu t)$, one obtains

$$M_{\text{SE}}(t) = \sum_{\mu,\nu=1}^{N} \frac{f_\mu f_\nu}{1 - \tau R_{\mu\nu}}\,(e^{-R_{\mu\nu}t} - \tau R_{\mu\nu}e^{-t/\tau})\,, \qquad (12)$$

where $R_{\mu\nu} = (\Gamma_\mu + \Gamma_\nu)/2$.

The determination of the relaxation time T_2 of $M_{\text{SE}}(t)$ depends on the experimental setup. When T_2 is determined from a single echo time t or a multiecho sequence [17] with an interecho time t, then T_2 is usually obtained from

$$T_2 = -\ln[M_{\text{SE}}(t)]/t\,. \qquad (13)$$

However, since $M_{\text{SE}}(t)$ is *not* single exponential already in the simplest case, $N = 1$, the above definition renders T_2 effectively dependent on the echo time t.

When T_2 is determined from several experiments with varying echo times, the best single-exponential approximation, $M_{\text{SE}}(t) \approx e^{-t/T_2}$, is required. Within the mean relaxation time approximation, $T_2 = \int_0^\infty dt\, M_{\text{SE}}(t)/M_{\text{SE}}(0)$, Eq. (12) gives

$$T_2 = T_2^* + \tau\,. \qquad (14)$$

Equations (8) and (14) allow the analysis of various limiting cases. The *motional narrowing* regime is given for $\tau\langle\omega^2\rangle^{1/2} \ll 1$. Then, the relaxation rate of the free induction process is $1/T_2^* = \tau\langle\omega^2(x)\rangle$ with the spatial variance of the spin precession frequency $\langle\omega^2(x)\rangle = \varsigma\delta\omega^2/2$. This relation is the well-known general result for the transverse relaxation rate obtained for the motional narrowing limit.

For very long correlation times, one obtains $1/T_2^* = 2\varsigma\delta\omega$ and $1/T_2 = 0$, i.e., relaxation is due solely to coherent spin dephasing. For very short correlation times, one obtains $T_2^* \approx T_2$, i.e., in this limit the free induction decay is mainly due to incoherent spin dephasing.

Another approximation is possible for small relative intracapillary blood volumes ($\varsigma \ll 1$) and in the regime $\tau\delta\omega \leq 1$, which is realistic in cardiac tissue. Equation (8) then provides $1/T_2^* = \varsigma\tau^{-1}(\sqrt{1 + (\tau\delta\omega)^2} - 1)$, i.e., the rate of the free induction decay is proportional to the intracapillary volume.

Kennan and Gore [8] determined relaxation rates from *Monte Carlo simulations* of transverse polarized spins as a function of the diffusion coefficient. In Figs. 1 and 2, their results are compared to our theoretical predictions from Eqs. (8), (12), and (13), using their tissue parameters and $N = 1$, which proved to be a sufficient approximation. They demonstrate a close similarity of analytically obtained T_2^* vs D and T_2 vs D curves, and those of simulations. The correct asymptotic behavior for very long and short correlation times, as derived above, is evident in both figures. Also the location of the maximum of the T_2 vs D curves is congruent. Figure 1 demonstrates, furthermore, that the dependence of T_2 on the echo time is described correctly. Figure 2 exhibits the correct dependence on the capillary radius.

We recently performed T_2^* mapping in hearts of volunteers [5] before and after application of the coronary dilator dipyridamol, which increases coronary flow by a factor of about 5 without affecting oxygen consumption. This

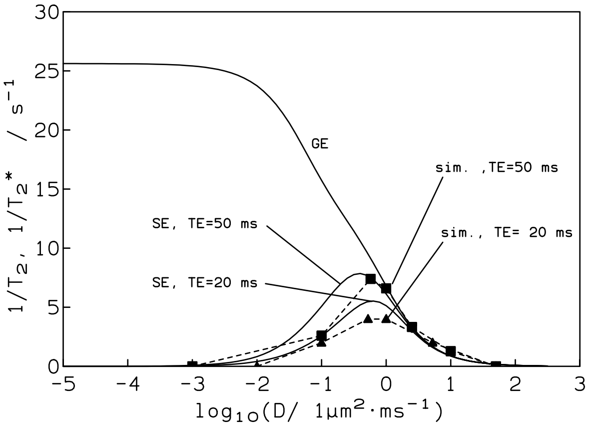

FIG. 1. Relaxation rates of the free induction decay of a gradient echo ($1/T_2^*$, GE) and spin echo experiment ($1/T_2$, SE) as function of the diffusion coefficient. For comparison with simulation date (sim.), the tissue parameters were obtained from Ref. [8] as relative intracapillary blood volume $\varsigma = 5\%$, capillary radius $R_c = 2.5$ μm, intracapillary magnetization of 1.6 mG ($\delta\omega = 269$ rad s^{-1}). The theoretical results (solid lines) were obtained from Eq. (8) for the free induction decay, and from Eqs. (12) and (13) for the spin echo. Two echo (TE) times were analyzed.

decreases the deoxyhemoglobin content and one observes an increase of $T_2^* \approx 36$ ms by 17%. The theory presented above predicts an increase of 13% to 18%, which is in good agreement with the experimental data.

In summary, we developed an analytical theory for the description of spin dephasing in the inhomogeneous magnetic field of the capillary network of myocardium. The underlying strong collision approach is justified in the cardiac muscle and, most probably, albeit with modifications according to different vascular architectures, for many other tissues as well. Note that this approach is not only valid when spin dephasing occurs on a much longer time scale than the local field fluctuations, which is the basis for the strong collision approximation, but also in the static dephasing time.

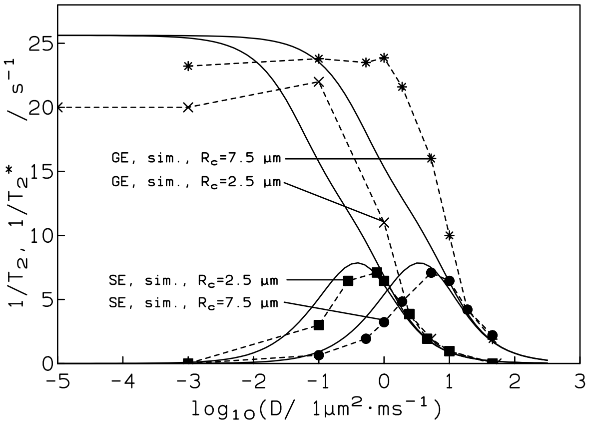

FIG. 2. Relaxation rates of free induction decay ($1/T_2^*$, GE) and spin echo experiments ($1/T_2$, echo time = 50 ms, SE). Simulation (sim.) and theoretical (solid lines) results are compared for a capillary radius of 2.5 and 7.5 μm. Other parameters are as in Fig. 1.

In our applications, we considered only the single-exponential (mean relaxation time) approximation of the full relaxation curve $M(t)$, which proved sufficient for the parameter regime in question. However, in particular for short spin echo times, it can be important to describe the short time behavior of $M(t)$, e.g., $\frac{d}{dt} M(t)|_{t=0} = 0$, in more detail. This is readily possible using the multiexponential approximation for $M(t)$ (see also [18]).

This work was supported by the Deutsche Gesellschaft für Kardiologie, Forschungsfonds des Klinikum Mannheim/Heidelberg Projekt 42, Grant Sonderforschungsbereich 355 “Pathophysiologie der Herzinsuffizienz,” and Graduiertenkolleg “NMR” HA 1232/8-1.

---

*Corresponding author.
Present address: Medizinische Universitäts Klinik, Josef Schneider Strasse 2, 97080 Würzburg, Germany.

[1] C. M. Wacker *et al.,* MAGMA **8**, 48 (1999).
[2] S. Kaul and A. R. Jayaweera, Circulation **96**, 719 (1997).
[3] D. Li *et al.,* Magn. Reson. Med. **36**, 16 (1996).
[4] P. Niemi *et al.,* Magn. Reson. Med. **38**, 78 (1996).
[5] C. M. Wacker *et al.,* Magn. Reson. Med. **41**, 686 (1999).
[6] D. A. Yablonski and E. M. Haake, Magn. Reson. Med. **32**, 749 (1994).
[7] V. G. Kiselev and S. Posse, Phys. Rev. Lett. **81**, 5696 (1998).
[8] R. P. Kennan, J. Zhong, and J. C. Gore, Magn. Reson. Med. **31**, 9 (1994).
[9] P. T. Callaghan, *Principles of Nuclear Magnetic Resonance Microscopy* (Clarendon, Oxford, 1991), p. 371; P. T. Callaghan and J. Stepisnik, Phys. Rev. Lett. **75**, 4532 (1995).
[10] J. B. Bassingthwaighte, T. Yipintsol, and R. B. Harvey, Microvasc. Res. **7**, 229 (1974).
[11] A. Krogh, J. Phys. (London) **52**, 409 (1918).
[12] K. M. Donahue *et al.,* Magn. Reson. Med. **32**, 66 (1994).
[13] H. C. Torrey, Phys. Rev. **104**, 563 (1956).
[14] W. Nadler and K. Schulten, J. Chem. Phys. **82**, 151 (1985).
[15] W. R. Bauer *et al.,* Magn. Reson. Med. **41**, 51 (1999).
[16] S. Dattagupta and M. Blume, Phys. Rev. **10**, 4540 (1974).
[17] S. Meiboom and G. Gill, Rev. Sci. Instrum. **29**, 688 (1958).
[18] W. R. Bauer *et al.,* Magn. Reson. Med. (to be published).

Magnetic Resonance in Medicine 42:1004–1010 (1999)

The Relationship Between the BOLD-Induced T_2 and T_2^*: A Theoretical Approach for the Vasculature of Myocardium

Wolfgang R. Bauer,[1]* Walter Nadler,[2] Michael Bock, Lothar R. Schad,[3] Christian Wacker,[3] Andreas Hartlep,[3] and Georg Ertl[1]

Recently the blood oxygenation level–dependent (BOLD)-related T_2^* of myocardium was derived as an analytical function of intracapillary blood volume, blood oxygenation, and nuclear spin diffusion. The basis of this approach was to approximate the diffusion-induced field fluctuations a nuclear spin is subjected to by strong collision dynamics, i.e., the field fluctuations are uncorrelated. The same analysis is now performed for spin echo experiments that gives myocardial T_2 as a function of the parameters above and the echotime. An analytical relationship between T_2 and T_2^* relaxation is derived. The dependence of T_2 on diffusion, echo time, and blood oxygenation is congruent with simulation and experimental data. Magn Reson Med 42: 1004–1010, 1999. © 1999 Wiley-Liss, Inc.

Key words: BOLD; myocardial imaging; heart; T_2^*

We recently presented an analytical approach in which the blood oxygenation level–dependent (BOLD)-related transverse relaxation time T_2^* of a free induction decay (FID) was derived as a function of tissue parameters as relative intracapillary blood volume and intracapillary blood oxygenation (1). The vascular architecture analyzed was that of myocardium. The basis for this approach was the strong collision approximation of the dynamics of field fluctuations a nuclear spin is subjected to while diffusing in the inhomogeneous pericapillary magnetic field. We could demonstrate (1) that the model predicts data of simulations well (2), experiments in animals (3), and measurements in humans (4,5). In this paper we extend our model to spin echo experiments, i.e., the transverse relaxation time T_2 is derived as a function of tissue parameters and echo time. The analysis is performed for a single and a biexponential approximation of the FID. The results are compared with simulation experiments of Kennan et al. (2) and experimental data of Atalay et al. (3). Finally, a general relation between T_2^* and T_2 is derived.

TISSUE MODEL

The type of tissue model we used for our analysis was recently introduced by us (1). The only vessel type considered are capillaries, because of their dominating volume contribution [>90% vessel volume (6)] in myocardium. Capillaries are considered as parallel cylinders (radius R_c) with a regular intercapillary spacing. Instead of taking spin diffusion in the whole tissue into account, we only consider one capillary with its concentric supply area (radius R_s), which implies that the relative intracapillary volume fraction is $RBV = (R_c/R_s)^2$. This Krogh model implies the introduction of reflectory diffusive boundary conditions at R_s. Because the capillary wall is almost impermeable on the time scale of transverse spin relaxation (7) one assumes reflectory boundary conditions at R_c as well. Due to the length of the capillaries (>400 μm) spin diffusion in the magnetic field gradient parallel to the capillary axis does not contribute much to spin relaxation. Hence, it is sufficient to consider 2D spin diffusion between two concentric cylinders with radius R_c and R_s. We only consider the extravascular fraction of spins due to its dominating contribution [>90% (8)]. The percapillary magnetic field is induced by paramagnetic intracapillary hemoglobin. The precession frequency of this field around the capillary (cylindrical coordinates $x = (r, \phi)$) is determined according to basic magnetostatics as

$$\omega(r, \phi) = -\delta\omega \cdot R_c^2 \cos(2\phi)/r^2, \tag{1}$$

with the characteristic equatorial frequency shift of a magnetized cylinder, $\delta\omega = |\omega(R_c, 0)| = 2\pi\gamma \cdot \Delta M$. The term $\Delta M = \Delta\chi \cdot B_0 \cdot \sin^2(\theta)$ is the difference of extra- and intracapillary magnetization (cgs units), which is induced in an external magnetic field B_0 due to the susceptibility difference $\Delta\chi$. θ is the angle between capillary axis and external field, which is assumed to be 90° throughout this paper.

MATHEMATICAL ANALYSIS

Free Induction Decay in the Strong Collision Approximation

We recently presented a theory (1) in which the BOLD-related FID is derived as a function of microcirculatory parameters in myocardium. The decisive step was to replace the diffusion-induced field fluctuations that influence a precessing nuclear spin, by a strong collision dynamics. This was justified, because the correlation time of these field fluctuations was much shorter than the

---

[1] II. Medizinische Universitätsklinik Mannheim/Heidelberg, Mannheim, Germany.

[2] HLRZ c/o Forschungszentrum Jülich, Jülich, Germany.

[3] Department of Biophysics, German Cancer Research Center, Heidelberg, Germany.

Grant sponsors: Deutsche Gesellschaft für Kardiologie; Forschungsfonds des Klinikum Mannheim/Heidelberg Projekt 42; Grant Sonderforschungsbereich 355 "Pathophysiologie der Herzinsuffizienz"; Graduiertenkolleg "NMR"; Grant number: HA 1232/8-1.

*Correspondence to: Dr. W.R. Bauer, Medizinische Universitätsklinik Würzburg, Josef Schneider Str. 2, 97080 Würzburg, Germany.

Received 27 May 1999; revised 26 August 1999; accepted 15 September 1999.

© 1999 Wiley-Liss, Inc.

BOLD-related relaxation time. In this paper only essentials are repeated.

The time evolution of the local transverse nuclear magnetization (polar notation: $m = m_x - im_y$) is determined by the Bloch-Torrey equation (diffusion coefficient D)

$$\partial_t m(x,\ t) = (D\nabla^2 + i \cdot \omega(x))m(x, t), \qquad [2]$$

which, after formal time integration, provides

$$m(x, t) = \exp\,[(D\nabla^2 + i \cdot \omega(x)) \cdot t]m(x, 0), \qquad [3]$$

and for the mean magnetization in the tissue volume V

$$M(t) = \frac{1}{V}\int_V dx \exp\,[(D\nabla^2 + i \cdot \omega(x)) \cdot t]m(x, 0) \qquad [4]$$

The correlation time of field fluctuations a diffusing nuclear spin is subjected to is (1)

$$\tau = (R_c^2/4D) \cdot |\ln RBV|/(1 - RBV), \qquad [5]$$

for the tissue model considered above. This correlation time is smaller than 6 msec when realistic values for myocardial tissue are inserted ($RBV = 5 - 10\%$, $R_c = 2.75$ μm, $D = 1$ μm^2/msec), i.e., smaller than the myocardial relaxation time $T_2^* > 30$ msec, and, hence, much smaller than the BOLD-related contribution to T_2^*. This implies that on a time scale on which significant alterations of transverse magnetization occur, the magnetic field fluctuations are stochastically independent. Uncorrelated field fluctuations may be considered as a stationary Markov process the generator of which is

$$\mathbf{D} = \lambda(\mathbf{\Pi} - \mathbf{id}), \qquad [6]$$

(9,10) where $\mathbf{\Pi}$ denotes the projection operator onto the functional space generated by the probability density function of the steady state $p(x)$ of this dynamic process [in this case $p(x)$ is identical with the spin density function (1)], i.e., $\mathbf{\Pi}f(x) = p(x) \cdot \int_V dx\, f(x)$ and $\mathbf{id}$ denotes the identity operator. Such an approach is refered to as strong collision approach. The parameter λ is the fluctuation frequency. Self consistency of the strong collision approximation implies that $\lambda = \tau^{-1}$. Replacement of the diffusion operator $D\nabla^2$ in Eqs. [3] and [4] by the strong collision operator $\mathbf{D}$ allows the analytical determination of the Laplace transform $\hat{M}(s) = \int_0^\infty dt\, e^{-st}M(t)$ as

$$\hat{M}(s) = (1 + RBV) \cdot \Big(\sqrt{(s + \tau^{-1})^2 + \delta\omega^2 RBV^2} + RBV\sqrt{(s + \tau^{-1})^2 + \delta\omega^2} - \tau^{-1}(1 + RBV)\Big)^{-1} \qquad [7]$$

The relaxation time of the free induction process is determined according to the mean relaxation time approximation [11] as $T_2^* = \hat{M}(0)$, i.e.,

$$T_2^* = \tau \cdot (1 + RBV) \cdot \Big([\sqrt{1 + (\tau\delta\omega \cdot RBV)^2} - 1] + RBV \cdot [\sqrt{1 + (\tau\delta\omega)^2} - 1]\Big)^{-1}, \qquad [8]$$

Spin Echoes in the Strong Collision Approximation

In this section we will derive the time course of the transverse magnetization, which is subjected to a spin echo sequence. It has to be stressed that the derived relations between reversible and irreversible spin dephasing only depend on the strong collision assumption and do not assume any special form of geometry or form of the inhomogeneous field. A simple spin echo sequence consists of a 90° pulse with a subsequent 180° pulse after $t/2$. The echo is gained after the echo time t.* After each pulse there is a simple free induction relaxation of the transverse magnetization, however, the phase reflection induced by the 180°-pulse refocuses coherent dephasing at t, i.e., the loss of transverse magnetization at t is due to incoherent, i.e., irreversible dephasing.

In the strong collision approximation the time evolution of the local magnetization at $t/2$ before the 180° pulse is given by

$$m(x, t/2) = \exp\,[\mathbf{G}t/2]m(x, 0), \qquad [9]$$

where we introduced the time evolution generator of the FID, $\mathbf{G} = \mathbf{D} + i \cdot \omega(x)$ (Eq. [6]). The 180° pulse induces a reflection of the phase which mathematically leads to a transition of $m(x, t/2)$ to its complex adjoint

$$m(x, t/2) \xrightarrow{180^\circ \text{ pulse}} m^*(x, t/2) = \exp\,[\mathbf{G}^*t/2]m^*(x, 0) \qquad [10]$$

After the 180° pulse time evolution is given by

$$\begin{aligned} m(x, t/2 + \Delta t) &= \exp\,[\mathbf{G}\Delta t]\ m^*(x, t/2) \\ &= \exp\,[\mathbf{G}\Delta t] \exp\,[\mathbf{G}^*t/2]m^*(x, 0) \qquad [11] \end{aligned}$$

and at the echo time t

$$m(x, t) = \exp\,[\mathbf{G}t/2] \exp\,[\mathbf{G}^*t/2]\mathbf{1} \qquad [12]$$

where we exploited that the initial magnetization is homogeneous and normalized to 1, i.e., $m(x, 0) = \mathbf{1}$, with the function $\mathbf{1} \equiv 1$.

---

*We denote the echo time as t instead of the commonly used TE to simplify the editing of the mathematical formulas.

The mean magnetization in the tissue volume V at the echo time is given by

$$M_{SE}(t) = \frac{1}{V}\int_V dV m(x, t)$$

$$= \frac{1}{V}\int_V dV \exp\,[\mathbf{G}t/2]\exp\,[\mathbf{G}^*t/2]\mathbf{1}. \quad [13]$$

Equations [12] and [13] and the structure of the operators **G** and **D** imply that

$$\frac{d}{dt}M_{SE}(t) = \frac{1}{V}\int_V dV \exp\,[\mathbf{G}t/2][\mathbf{G}/2 + \mathbf{G}^*/2]\exp\,[\mathbf{G}^*t/2]\mathbf{1}$$

$$= \frac{1}{V}\int_V dV \exp\,[\mathbf{G}t/2]\mathbf{D}\exp\,[\mathbf{G}^*t/2]\mathbf{1}$$

$$= \frac{1}{V}\int_V dV \exp\,[\mathbf{G}t/2]\frac{1}{\tau}(\mathbf{\Pi} - \mathbf{id})\exp\,[\mathbf{G}^*t/2]\mathbf{1}$$

$$= \frac{1}{\tau}\frac{1}{V}\left(\int_V dV \exp\,[\mathbf{G}t/2]\mathbf{1}\right)\frac{1}{V}\left(\int_V dV \exp\,[\mathbf{G}^*t/2]\mathbf{1}\right)$$

$$- \frac{1}{\tau}\frac{1}{V}\left(\int_V dV \exp\,[\mathbf{G}t/2]\exp\,[\mathbf{G}^*t/2]\mathbf{1}\right)$$

$$= \frac{1}{\tau}M(t/2)\cdot M^*(t/2) - \frac{1}{\tau}M_{SE}(t)$$

$$= \frac{1}{\tau}|M(t/2)|^2 - \frac{1}{\tau}M_{SE}(t), \quad [14]$$

where the function $M(t)$ denotes the time course of magnetization during the free induction decay. Equation [14] is a simple first order differential equation which is solved by

$$M_{SE}(t) = e^{-t/\tau} + e^{-t/\tau}\frac{1}{\tau}\int_0^t d\xi e^{\xi/\tau}|M(\xi/2)|^2 \quad [15]$$

Equation [15] defines the exact time course of magnetization $M_{SE}(t)$ after the echo time t when the strong collision model is assumed. The determination of T_2 from Eq. [15] requires the knowledge of the free induction decay of magnetization $M(t)$. When a single exponential decay of the FID is assumed, i.e., $M(t) \approx e^{-R_2^*t}$, Eq. [15] becomes

$$M_{SE}(t) = e^{-t/\tau} + e^{-t/\tau}\frac{1}{\tau}\int_0^t d\xi e^{\xi/\tau}e^{-R_2^*\xi}$$

$$= e^{-t/\tau} + e^{-t/\tau}\frac{1}{1 - \tau R_2^*}(e^{(1/\tau - R_2^*)t} - 1)$$

$$= \frac{\tau}{1 - \tau R_2^*}(\tau^{-1}e^{-R_2^*t} - R_2^* e^{-t/\tau}) \quad [16]$$

When a biexponential FID is assumed, i.e., $M(t) = f_1e^{-\Gamma_1 t} + f_2e^{-\Gamma_2 t}$ (for the derivation of f_i and Γ_i see Appendix), Eq. [15] provides M_{SE} as

$$M_{SE}(t) = e^{-t/\tau}(1 + C_1 + C_2 + C_3), \quad [17]$$

with

$$C_1 = \frac{f_1^2}{1 - \tau\Gamma_1}(e^{(1/\tau - \Gamma_1)t} - 1) \quad [18]$$

$$C_2 = \frac{f_2^2}{1 - \tau\Gamma_2}(e^{(1/\tau - \Gamma_2)t} - 1) \quad [19]$$

$$C_3 = \frac{2f_1f_2}{1 - \tau\Gamma}(e^{(1/\tau - \Gamma)t} - 1), \quad [20]$$

where $\Gamma = (\Gamma_1 + \Gamma_2)/2$.

APPLICATIONS

Relaxation Rate and Echo Time

When T_2 or the corresponding rate R_2 is determined from a spin echo (multiecho) experiment one assumes a single exponential decay of the magnetization $M_{SE} \approx e^{-t\,R_2}$ at the echo time (or between two echoes at the interechotime) t, which leads to (see Eq. [15])

$$R_2 = \frac{-\ln M_{SE}(t)}{t} \quad [21]$$

Figure 1 demonstrates for different diffusion coefficients the relaxation rate R_2 determined from Eq. [21] as a function of the echo time. A single exponential and a biexponential approximation of the FID in Eq. [15] is analyzed (Eqs. [16] and [17]). One obtains that with increasing echo time the relaxation rate becomes independent from echo time and that this asymptotic value is the same for the single and biexponential FID approximation. Increasing the diffusion coefficient makes this relation evident for shorter echo times. At short echo times the rates are considerably smaller when a biexponential FID is assumed and these data agree better with simulation experiments.

The explanation is given in Fig. 2, where the magnetization decay (Eq. [15]) at the echo time was determined either for a bi- or a single exponential FID approximation in Eq. [15] for two diffusion regimes. For long echo times the magnetization-echo time curves are almost identical for both approximations. However, when short echo times or interecho times are considered there is a considerable difference (Fig. 2b). In the short echo time range ($1 - M_{SE}(t) \ll 1$) the relaxation rate determined from Eq. [21] may be approximated as $R_2 = -\ln\, M_{SE}(t)/t \approx (1 - M_{SE}(t))/t$, i.e., Fig. 2b demonstrates that R_2 obtained from a single or a biexponential FID differs by more than 100%. This and the comparison with simulation data (Fig. 1) implies that the determination of the transverse relaxation rate requires a biexponential approximation of the FID when short (inter-) echo times are considered.

Comparison With Simulations of Kennan et al.

Kennan et al. (2) determined R_2^* and R_2 from simulations of spins diffusing within a quadratic box containing a vessel inside, which was filled with a paramagnetic contrast agent. The orientation of the vessel axis was perpendicular to the external field ($\theta = 90°$) and the length of the box was that of the intercapillary distance. The rate R_2^* was determined from a FID and R_2 from spin echo (multi echo) experiments with varying echo time. We could recently demonstrate that our analytical model (1) predicted well the R_2^* data of FID simulations. In this section we will compare the predictions of our model with the simulations of spin echo experiments.

In one part of his study, Kennan et al. considered R_2 and R_2^* as a function of the diffusion coefficient. When $M_{SE}(t)$ is determined according to Eq. [16], i.e., we assume a single exponential decay of the FID ($M(t)$), the calculated data of R_2 (Eq. [21]) are in close congruence with the simulation data (Fig. 3). The dependence of R_2 on the echotime is also well reflected. The simulation data and our results demonstrate similar characteristic features of the dependence of R_2 on the diffusion coefficient.

- there is a single maximum
- with increasing diffusion coefficient (small correlation times) R_2 becomes independent from the echo time
- $R_2 \approx R_2^*$ when the diffusion coefficient increases. This is the the motional narrowing limit ($\tau \rightarrow 0$), i.e., $R_2 \approx R_2^* \approx \tau \cdot RBV \cdot \delta\omega^2/2$ (Eq. [8], Fig. 3 and Ref. 1).

In another set of simulations Kennan et al. considered the dependence $R_2(D)$ for different vessel sizes (Fig. 4). When R_2 is determined according to Eq. [21] there is again a close congruence between data obtained from simulations and those predicted by our model. The increase of the vessel size leads to a shift of the $R_2(D)$ curve to the right, which is explained by the increase of the correlation time (Eq. [5]).

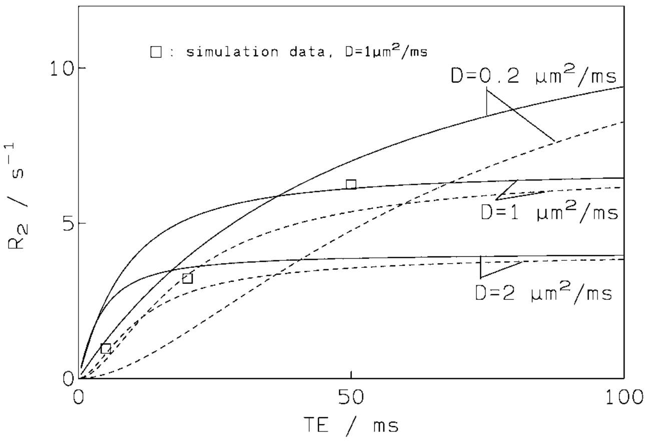

FIG. 1. Transverse relaxation rate R_2 as a function the echo time TE obtained from Eq. [21] and Eqs. [15], [16], and [17]. The difference between intra- and extracapillary magnetization ($=\Delta\chi \cdot B_0$) was assumed to be 1.6 mgauss, which is the valid for deoxygenated blood ($\Delta\chi = 8 \cdot 10^{-8}$ for hematocrit = 40%) in an external field of B_0 = 2T. A single (solid line) and a biexponential (dashed line) approximation of the FID is inserted in Eq. [15]. Three different diffusion regimes (coefficient D) are considered for a relative intracapillary blood volume RBV = 5% and a capillary radius R_c = 2.5 μm. The squares denote relaxation rates of simulated spin-echo experiments (D = 1 μm²/ms, RBV = 5%) for different echotimes (TE = 50, 20, 5 msec) and are taken from Ref. 2. Note that for short echo times, the predictions of the model are closer to simulation data when a biexponential decay of the FID is assumed.

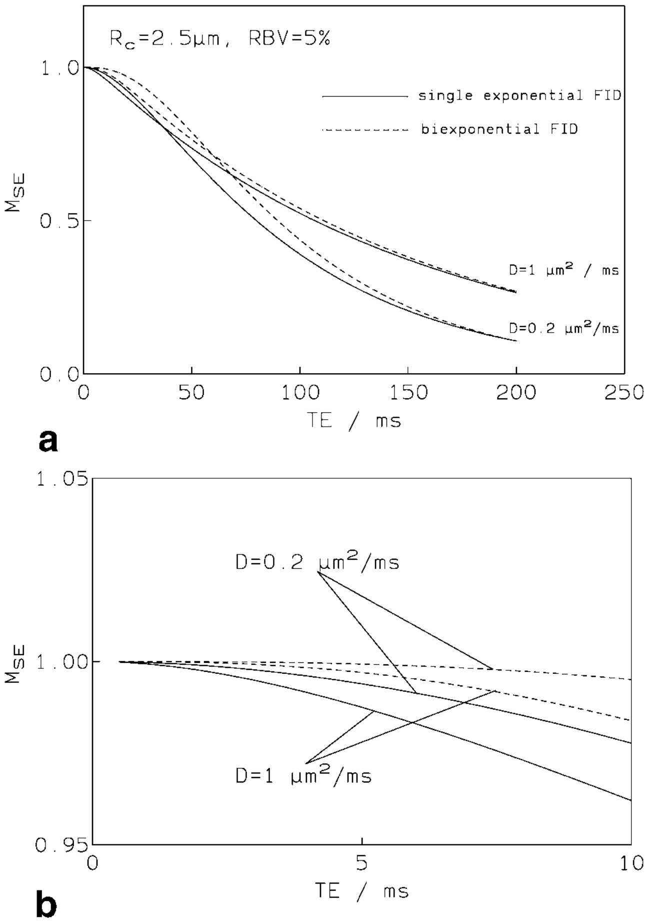

FIG. 2. **a**, **b:** Magnetization M_{SE} as a function of the echo time TE according to Eq. [15] for two different diffusion regimes. As in Fig. 1 a single (solid line) and a biexponential (dashed line) FID approximation is inserted in Eq. [15]. **b**: a magnification of **a** for the range of short echo times.

Comparison With Experimental Data

Atalay et al. determined T_2^* (12) and T_2 (3) in isolated rabbit hearts that were perfused with a red cell suspension at various oxygenation levels. Because experiments were performed under cardioplegic conditions and after maximal vasodilation the oxygenation gradient along the capillary axis was negligible as was recently estimated by us (1). This implies that the intracapillary oxygenation of hemoglobin is almost that of the perfusate. The authors found empirical equations for the dependence of R_2^* and R_2 on the relative oxygen saturation of hemoglobin Y as demonstrated in Fig. 5. The experimental setup of the horizontal imaging system and the heart preparation (12) suggests an almost perpendicular intersection of the capillary axis and the external field. For comparison with our theory we determined R_2^* from Eq. [8] and R_2 from Eq. [21]. The equatorial frequency shift $\delta\omega$ (Eqs. [1] and [8]) was deter-

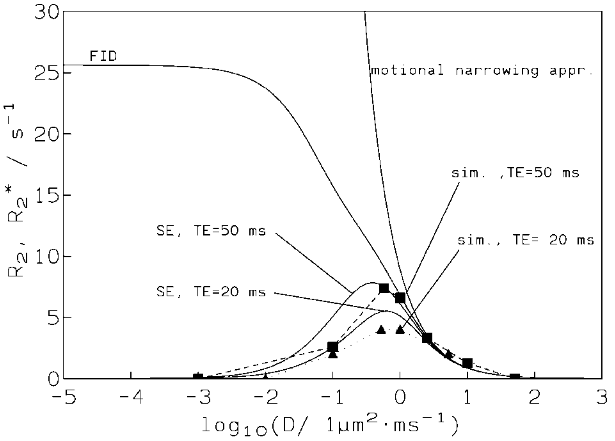

FIG. 3. Relaxation rate as function of the diffusion coefficient *D* for a free induction decay (R_2^*, FID) and spin-echo experiments (R_2, SE). For comparison with simulation data, the tissue parameters were taken from Ref. 2 as: relative intracapillary blood volume *RBV* = 5%, capillary radius R_c = 2.5 µm, intracapillary magnetization of 1.6 mG ($\delta\omega$ = 269 rad · sec^{-1}). The data from the model (solid lines) were obtained from Eq. [8] (FID) and Eqs. [16] and [21] (spin echo). Two echo times were analyzed and compared with simulation curves (square/triangle: spin-echo simulation data for an echo time of 50/20 msec). Note that with increasing diffusion coefficient (decreasing correlation time) both, the relaxation rate of the FID and those of the spin-echo experiments approach the motional narrowing limit, i.e., $R_2 \approx R_2^* \approx \tau \cdot RBV \cdot \delta\omega^2/2$.

mined as $\delta\omega = 2\pi\gamma \cdot \Delta\chi_0(1 - Y) \cdot B_0$ where γ denotes the gyromagnetic ratio, $\Delta\chi_0 = 8 \cdot 10^{-8}$ is the susceptibility difference for complete deoxygenated blood ($Y = 0$), and $B_0 = 4.7$ T is the external magnetic field. Because the authors state that the relaxation rate R_2 was independent from echotime (range: 18–1000 msec) when determined according to Eq. [21] it is justified to describe the magnetization decay $M_{SE}(t)$ by Eq. [16] (Fig. 1). Because Atalay et al. only gave the range of echotimes they used in their experiments we assumed an echotime of 23 msec that appears to be reasonable to detect also fast relaxation in the presence of low blood oxygenation. The relative intracapillary blood volume (RBV) was assumed to be 10%, which is a realistic value for a dilated microvascular system (8). Because our theory describes the BOLD-related part of transverse relaxation, the offset of the empirical curves at 100% oxygen saturation ($R_2^*(Y = 1)$, $R_2(Y = 1)$) was added to our theoretical curves. As the empirical curves, the $R_2^*(Y)$ and $R_2(Y)$ curves obtained from our model almost run parallel (Fig. 5), and there is evident similarity between the empirical and analytical function.

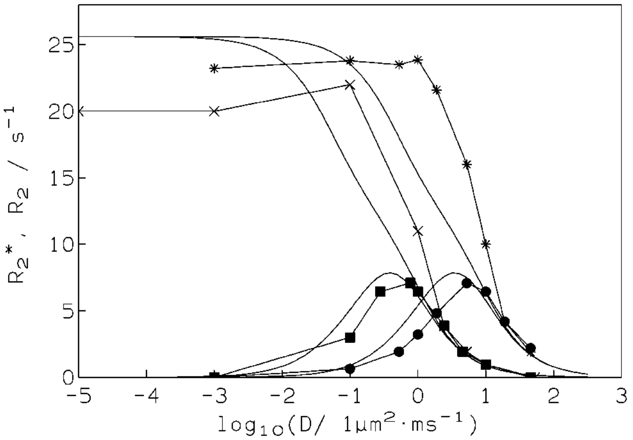

FIG. 4. Relaxation rates of free induction decay (R_2^*) and spin-echo experiments (R_2, echo time TE = 50 msec). The capillary radius is 2.5 µm (X, gradient echo; square, spin-echo simulation data) and 7.5 µm (*, gradient echo; circle, spin-echo simulation data). Solid lines are obtained from the model.

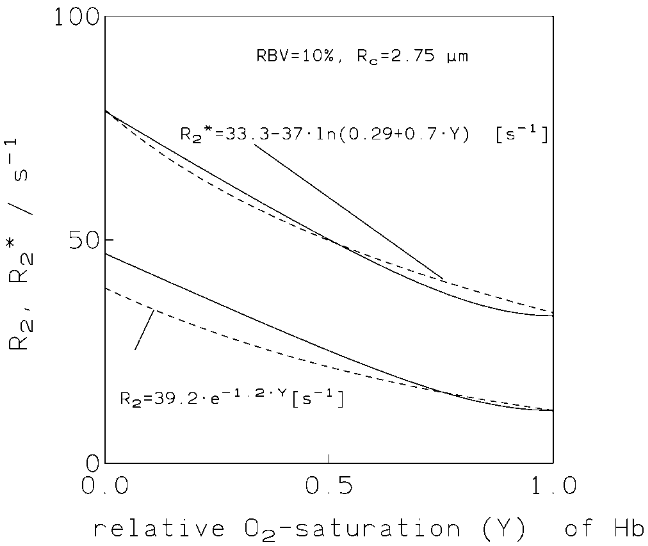

FIG. 5. Myocardial R_2^* and R_2 as a function of the relative oxygen saturation of hemoglobin *Y*. The dashed curves were obtained from empirical equations that Atalay et al. (3) found in red cell–perfused rabbit hearts at 4.7 T from gradient-echo and spin-echo experiments. The solid curves were obtained from Eq. [8] ($R_2^*(Y)$) and Eqs. [16] and [21] ($R_2(Y)$). The relative intracapillary blood volume was assumed to be 10%, which is reasonable for a dilated microvascular system (8), and the capillary radius was assumed to be 2 75 µm, which is a realistic value for a capillary in myocardium (13). Note the congruence between the empirical curves and those obtained from the model.

General Relation Between Irreversible and Reversible Spin Dephasing and Correlation Time

In this section we will derive a general relation between T_2 and T_2^* when the strong collision approach is applied. In this section above the relaxation time (rate) was determined from a single echo time *t* or interecho time when a multiecho sequence is applied. From a more theoretical point of view T_2 should be obtained from a signal echo time curve, i.e., many single spin-echo experiments with different echotimes are required. In this case one cannot apply Eq. [21] for determination of the transverse relaxation time (rate). Instead the best single exponential approximation of magnetization decay is required $M_{SE}(t) \approx e^{-t/T_2}$, which according to the mean relaxation time approximation (11) is

$$T_2 = \int_0^\infty dt\, M_{SE}(t), \qquad [22]$$

Insertion of $M_{SE}(t)$ from Eq. [15] gives

$$\mathrm{T}_2 = \int_0^\infty dt\, e^{-t/\tau} + \int_0^\infty dt e^{-t/\tau} \left(\frac{1}{\tau} \int_0^t d\xi e^{\xi/\tau} |M(\xi/2)|^2 \right)$$

$$= \tau + 2 \cdot |\hat{M}|^2(0), \qquad [23]$$

where we applied the integration, translation, and similarity theorem of Laplace transforms. The further evaluation depends on the approximation of the FID, i.e., $M(t)$. When we assume a single exponential decay, i.e., $M(t) \approx e^{-t/\mathrm{T}_2*}$ we obtain

$$\mathrm{T}_2 \approx \tau + \mathrm{T}_2^*, \qquad [24]$$

that reveals a very simple relationship between T_2 and T_2^*. It has to be stated the derivation of the relation 24 is based on the single exponential form of the FID of tranverse magnetization M. This appears to be a reasonable assumption as long as the T_2 relaxation is obtained from long echotimes. However, when T_2 is obtained from measurements at short echotimes a more precise description of the FID is necessary.

The relation 24 reveals some fundamental properties between T_2 and T_2^*. In the limit of very long correlation times $\tau \rightarrow \infty$ (static dephasing regime) one obtains

$$\mathrm{T}_2 \gg \mathrm{T}_2^* \qquad [25]$$

which reflects the fact that in this limit there is only a minor portion of irreversible dephasing of transversal polarized spins. In the opposite case, i.e., $\tau \rightarrow 0$ (motional narrowing limit) the relation 24 becomes

$$\mathrm{T}_2 \approx \mathrm{T}_2^* \qquad [26]$$

i.e., the most part of dephasing is irreversible.

DISCUSSION

In this paper we demonstrated that our analysis of BOLD-related transverse relaxation can be extended from the free induction decay to spin-echo experiments. A general relation between irreversible and reversible spin dephasing was obtained.

Strong Collision Approach

The base of our analysis is the strong collision approach of the dynamics of the BOLD-related field fluctuations, which is justified according to the relation of correlation and relaxation time ($\tau \ll \mathrm{T}_{2,\mathrm{BOLD}}*$) in myocardium. The interval of correlation times, which satisfy the strong collision condition contains that for which the motional narrowing condition $\tau \cdot \sqrt{\langle \Delta\omega^2 \rangle} \ll 1$ is valid ($\langle \Delta\omega^2 \rangle$ = variance of field fluctuations) because in this limit $\mathrm{R}_2^* = \tau \cdot \langle \Delta\omega^2 \rangle$, i.e. $\mathrm{R}_2^* \tau \ll 1$. The opposite, however, is not true as was recently demonstrated (1).

Furthermore the model presented here also contains the static dephasing regime of spin relaxation as a special case, because static dephasing is the asymptotic state of both dynamics, the diffusion and the strong collision generated field fluctuations. This implies that the strong collision approach represents a two side approximation of spin relaxation. It interpolates relaxation rates coming from very long (static dephasing regime) and short ($\tau \ll \mathrm{T}_{2,\mathrm{BOLD}}$) correlation times.

Kiselev and Posse (14,15) recently presented analytical models to describe transverse relaxation for very long and short correlation times. The first extends the static dephasing regime by consideration of spin diffusion within a local linear field gradient (14,15). The other model, which is used for the description of the fast motion regime, is a perturbation approach in the local magnetic fields (14). The data provided by these models are very close to simulation data of Boxerman et al. (16). The vascular network Kiselev and Posse focused on was that of the brain. This implies that the BOLD effect around larger vessels (veins) has to be considered, i.e., approximations near the static dephasing regime are important. In myocardium, however, the relative volume of the venous system is negligible (6). On the other hand, we have recently shown (1) that the motional narrowing condition is not fulfilled in the capillary system of myocardium which hampers the application of perturbation approaches. One of our future goals is to apply our model to a cerebrovascular network and to compare our analytical results with those of Kiselev and Posse.

Determination of Relaxation Time

We could derive simple relations for the relaxation time or rate as a function of the echo time. It could be demonstrated that for very short echo times (interecho times) a biexponential approximation of the FID leads to rates, which are closer to simulation data.

A general relation between T_2 and T_2^* was obtained under the assumption that T_2 is obtained from a signal (magnetization) echo time curve. It has to be stressed that the simple relation 24 is only valid for the BOLD-related part of transverse relaxation, i.e., relaxation is induced by field fluctuations with a single correlation time. However, in tissue spin dephasing is induced by field fluctations, the dynamics of which is a result of a complex superposition of single processes having their own correlation times.

APPENDIX: BIEXPONENTIAL APPROXIMATION OF THE T_2^* RELAXATION

The generalized moment expansion represents an algorithm to approximate a relaxation time curve $M(t)$ by a sum of exponentials (10,11), $M(t) \approx \Sigma_{\nu=1}^{N} f_\nu \cdot \exp(-\ t\Gamma_\nu)$. The function and its approximation have the same statistical moments. High-frequency moments describe the short time behavior and are the jets of the Taylor expansion of $M(t)$, i.e., $\mu_n = M^{(n)}(0)$. Low frequency moments describe the long time evolution of $M(t)$ and are $\mu_{-n} = 1/(n-1)! \int_0^\infty dt\, t^{n-1} M(t)$, i.e., $\mu_{-n} = (-1)^{n-1}/(n-1)!\ \hat{M}^{(n-1)}(0)$, where $\hat{M}(s)$ denotes the Laplace transform of $M(t)$. When a biexponential approximation $M(t) \approx f_1 \exp(-t\Gamma_1) + f_2 \exp(-t\Gamma_2)$ is applied which reproduces 2 high- and 2 low-frequency moments the coefficients and rates are determined from $f_1\Gamma_1^m + f_2\Gamma_2^m = \mu_m$ with $-2 \le m \le 1$. These moments are

$$\mu_1 = 0, \qquad [27]$$

$$\mu_0 = 1, \qquad [28]$$

$$\mu_{-1} = \frac{(1 + RBV)\tau}{\sqrt{1 + (\tau\delta\omega RBV)^2} - 1 + RBV\left(\sqrt{1 + (\tau\delta\omega)^2} - 1\right)}, \qquad [29]$$

$$\mu_{-2} = \mu_{-1}^2 \cdot (1 - \kappa), \qquad [30]$$

with $\kappa = 1 - (1 + \mathrm{RBV})^{-1} \cdot ([1 + (\tau\delta\omega\mathrm{RBV})^2]^{-1/2} + \mathrm{RBV}\,[1 + (\tau\delta\omega)^2]^{-1/2})$. Equation [27] follows from Eqs. [3] and [4], Eq. [28] from normalization of magnetization ($M(0) = 1$). The parameters of the bi-exponential approximation are then obtained as

$$\Gamma_{1,2} = \frac{\mu_{-1} \pm \sqrt{\mu_{-1}^2 - 4\mu_{-1}^2\kappa}}{2\mu_{-1}^2\kappa} = \mu_{-1}^{-1}\,\frac{1 \pm \sqrt{1 - 4\kappa}}{2\kappa} \qquad [31]$$

$$f_{1,2} = \pm\Gamma_{2,1} \cdot (-\mu_{-1})\,\frac{\kappa}{\sqrt{1 - 4\kappa}} = \frac{1}{2}\left(1 \mp \frac{1}{\sqrt{1 - 4\kappa}}\right) \qquad [32]$$

REFERENCES

1. Bauer WR, Nadler W, Bock M, Schad LR, Wacker C, Hartlep A, Ertl G. Theory of the BOLD effect in the capillary region: an analytical approach for the determination of T_2* in the capillary network of myocardium. Magn Res Med 1999;41:51–62.
2. Kennan RP, Zhong J, Gore JC. Intravascular susceptibility contrast mechanisms in tissues. Magn Res Med 1994;31:9–21.
3. Atalay MK, Reeder SB, Zerhouni EA, Forder JR. Blood oxygenation dependence of T_1 and T_2 in the isolated, perfused rabbit heart at 4.7 T. Magn Res Med 1995;34:623–627.
4. Li D, Dhawale P, Rubin PJ, Haacke EM, Gropler RJ. Myocardial signal response to dipyridamol and dobutamin: demonstration of the BOLD effect using a double-echo sequence. Magn Res Med 1996;36:16–20.
5. Wacker CM, Bock M, Hartlep AW, Beck G, van Kaick G, Ertl G, Bauer WR, Schad LR. Changes in myocardial oxygenation and perfusion under pharmacological stress with dipyridaomole: assessment using T_2* and T_1 measurements. Magn Reson Med 1999;41:686–695.
6. Kaul S, Jayaweera AR. Coronary and myocardial blood volumes (editorial). Circulation 1997;96:719–724.
7. Donahue KM, Burstein D, Mannings WJ, Gray ML. Studies of Gd-DTPA relaxivity and proton exchange rates in tissue. Magn Res Med 1994;32: 66–76.
8. Chrystal GJ, Downey HF, Bashour FA. Small vessel and total coronary blood volume during adenosine infusion. Am J Physiol 1981;241 (Heart. Circ. Physiol. 10):H194–H201.
9. Dattagupta S, Blume M. Stochastic theory of line shape I. Nonsecular effects in the strong collision model. Phys Rev B 1974;10:4540–4550.
10. Bauer WR, Schulten K. Nuclear spin dynamics (I = ½) under the influence of random perturbation fields in the strong collision approximation. Ber Bunsenges Phys Chem 1992;96:721–723.
11. Nadler W, Schulten K. Generalized moment expansion for Brownian relaxation processes. J Chem Phys 1985;82:151–160.
12. Atalay MK, Forder JR, Chacko VP, Kawamoto S, Zerhouni EA. Oxygenation in the rabbit myocardium: assessment with susceptibility dependent MR imaging. Radiology 1993;189:759–764.
13. Bassingwaighte JB, Ypintsol T, Harvey RB. Microvasculature of the dog left ventricular myocadium. Microvascular Res 1974;7:229–249.
14. Kiselev VG, Posse S. Analytical theory of susceptibility induced NMR signal dephasing in a cerebrovascular network. Phys Rev Lett 1998; 81(25):5696–5699.
15. Kiselev VG, Posse S. Analytical model of susceptibility induced MR signal dephasing: effect of diffusion in a microvascular network. Magn Res Med 1999;41(3):499–501.
16. Boxerman JL, Hamberg LM, Rosen BB, Weisskoff RM. MR contrast due to intravascular magnetic susceptibility perturbations. Magn Res Med 1995;34:555–566.

PHYSICAL REVIEW E, VOLUME 65, 066123

Spin dephasing in the extended strong collision approximation

Wolfgang R. Bauer[1,]* and Walter Nadler[2]
[1]*Medizinische Universitätsklinik, Universität Würzburg, Josef Schneider Strasse 3, D-97080 Würzburg, Germany*
[2]*Fakultät für Physik, Bergische Universität, Gauß Strasse 20, D-42097 Wuppertal, Germany*
and NIC c/o Forschungszentrum Jülich, D-52725 Jülich, Germany

(Received 2 October 2001; published 25 June 2002)

For Markovian dynamics of field fluctuations we present here an extended strong collision approximation, thereby putting our previous strong collision approach [Phys. Rev. Lett. **83**, 4215 (1999)] into a systematic framework. Our approach provides expressions for the free induction and spin-echo magnetization decays that may be solved analytically or at least numerically. It is tested for the generic cases of dephasing due to an Anderson-Weiss process and due to restricted diffusion in a linear field gradient.

DOI: 10.1103/PhysRevE.65.066123 PACS number(s): 87.61.−c, 76.60.Jx

I. INTRODUCTION

The understanding of spin dephasing is of paramount interest in all fields of nuclear magnetic resonance (NMR) sciences. In NMR spectroscopy it determines the line shape, in NMR imaging it is—besides longitudinal relaxation—the major mechanism determining the contrast and contains morphological as well as functional information.

The processes contributing to spin dephasing are related to the spin environment. In biological tissues, for example, spin dephasing may result from dipole-dipole interaction of water proton spins with paramagnetic ions such as Fe^{2+}. Another cause is diffusion within inhomogeneous magnetic fields generated by native or contrast agent induced susceptibility differences that are related to tissue composition and/or cellular and subcellular compartments. In magnetic resonance imaging, spin dephasing in external gradient fields is exploited to get information about diffusion within biological systems. These diffusion sensitive imaging techniques are applied to study tissue anisotropy and restrictions of diffusion that are given by membranes of cells and subcellular structures.

Essential for dephasing of spins are the field fluctuations that induce the phase modulations. It is important to note that in biological tissues the relevant processes cover almost the whole range of time scales. For example, the dynamics of interactions of water proton spins with paramagnetic macromolecules such as ferritin is so fast that it can be considered to be within the motional narrowing regime. On the other hand, dephasing of spins in magnetic field gradients around larger vessels is almost coherent, i.e., it is in the static dephasing regime [2]. Hence, for biological applications it is important to obtain results from theory that are valid over the whole motion regime. However, in most cases this is not possible analytically.

Therefore, most efforts have focused on limiting cases. The *motional narrowing limit* is well investigated and a number of analytical results were obtained for it [1]. The characteristic of this limit is that the mean phase shift induced by a field realization is much smaller than 1, i.e., $|\delta\varphi| = \tau\langle\Delta\omega^2\rangle^{1/2} \ll 1$, where the correlation time τ gives the mean duration of some field realization, and $\langle\Delta\omega^2\rangle$ is the variance of the inhomogeneous field. The relaxation time is then obtained as $1/T_2 = \tau\langle\Delta\omega^2\rangle$. In the other limiting case, i.e., the *static dephasing regime* ($\tau\langle\Delta\omega^2\rangle^{1/2} \gg 1$), Yablonski and Haake [2] derived analytical expressions for coherent dephasing of spins in inhomogeneous fields around magnetic centers such as cylinders or spheres. Kiselev and Posse [3] extended Yablonski and Haake's static dephasing approach by considering diffusion of spins within local linear gradients. However, this approach requires that the diffusion length l during dephasing is within the linear approximation of the inhomogeneous fields $\omega(x_0 + l) \approx \omega(x_0) + \partial_x\omega(x_0)l$. Note that expansion around the limiting cases by perturbation approaches leads to divergences in the other respective limits. Therefore, the intermediate motion regime, i.e., almost everything between the static dephasing and motional narrowing limit, was in most situations accessible by simulations only [5].

Recently, we used a strong collision (SC) approach to characterize spin dephasing in a particular situation: An inhomogeneous field around regularly arranged parallel cylinders filled with a paramagnetic substance [4], a model reflecting the capillary network of the cardiac muscle. The results agreed well with simulations [5] over the whole dynamic range and with experimental data [6,7].

The basic idea behind the SC approach is to replace the original generator of the Markov process by a simpler one, the SC generator, which conserves particular features of the original process. In particular, by an appropriate choice of its parameter the SC process reproduces the correlation time of the field fluctuations induced by the original Markov process. There are several advantages of the SC approximation. First, it is correct both in the motional narrowing and the static dephasing limits; thereby also the error in the intermediate regime is reduced considerably, when compared to perturbation approaches. And second, it provides a simple expression for the magnetization decay, which may be solved analytically or at least numerically.

However, the drawback of the SC approach was—up to now—that it is not part of a systematic approximation to or an expansion of the original generator. Therefore, it was unclear how results could be improved beyond the SC approxi-

---

*Corresponding author.

©2002 The American Physical Society

mation. The aim of this paper is to extend the SC approach and provide a framework for a systematic approximation.

In the following section we will present a formal description of spin dephasing that will be the basis for our analytical analysis. In Sec. III we will introduce the extended strong collision (ESC) approximation proper and show how it is used to describe free induction and spin-echo decay. In Sec. IV we will apply it to two generic cases: spin dephasing induced by an Anderson-Weiss process [8] and by restricted diffusion in a linear field gradient. We will close the paper with a summary and a discussion of our results.

II. FORMAL DESCRIPTION OF SPIN DEPHASING

We assume that dephasing of transversely polarized nuclear spins exposed to an external field is induced by randomly fluctuating magnetic perturbation fields with frequency ω_i, where i is a discrete or continuous variable. The transition dynamics between two distinct states i and j is that of a stationary continuous time Markov process described by rates r_{ji} for the transition $i \rightarrow j$. The matrix $\mathbf{R}=(r_{ji})$ as the generator of the Markov process conserves the probability to find a spin within one state, i.e., $r_{ii}=-\Sigma_{j\neq i} r_{ji}$. The eigenvalues l of $\mathbf{R}$ fulfill the condition $l \leqslant 0$ where $l=0$ corresponds to the equilibrium probability distribution. To simplify the notation we denote the normalized left and right eigenvectors of $\mathbf{R}$ as $\langle l|$ and $|l\rangle$, respectively, with $\langle l'|l\rangle=\delta_{l'l}$.

The time evolution between t and $t+dt$ of the transverse magnetization of spins in the state j (in polar notation $m_j = m_{jx} - i m_{jy}$) results from the linear superposition of the transition and the precession dynamics, i.e., $\partial_t m_j(t) = \Sigma_i r_{ji} m_i(t) + i\omega_j m_j(t)$. The precession within the external field was omitted since it only induces a constant offset of the frequency which may be gauged to zero. With the diagonal frequency, matrix $\mathbf{\Omega}=(\delta_{ji}\omega_i)$ one obtains for the magnetization $|m\rangle=(m_j)$,

$$\partial_t |m(t)\rangle = (\mathbf{R}+i\mathbf{\Omega})|m(t)\rangle, \tag{1}$$

which is a generalization of the Bloch-Torrey equation [9] originally formulated for diffusing spins, i.e., $\mathbf{R}\sim\nabla^2$. In most cases it is reasonable to assume that the initial magnetization $|m(0)\rangle$ is proportional to the equilibrium probability distribution $|0\rangle$, e.g., when free diffusion is considered this would imply a homogeneous transverse magnetization. Equation (1) then provides the time evolution of the transverse magnetization (free induction decay) as

$$|m(t)\rangle = \exp[(\mathbf{R}+i\mathbf{\Omega})t]|0\rangle, \tag{2}$$

where the initial magnetization was normalized to 1. The overall magnetization is then determined as

$$M(t)=\langle 0|m(t)\rangle = \langle 0|\exp[(\mathbf{R}+\mathrm{i}\mathbf{\Omega})t]|0\rangle. \tag{3}$$

The free induction decay as determined by Eqs. (2) and (3) results from coherent and incoherent spin dephasing. The incoherent contribution is determined from spin-echo experiments. In-plane polarized spins are rotated by 180° (π-pulse) after a time $t/2$. This pulse transforms the original magnetization $|m(t/2)\rangle$ to its complex adjoint $|m^*(t/2)\rangle=\exp[(\mathbf{R}-i\mathbf{\Omega})t/2]|0\rangle$. This procedure cancels the coherent spin dephasing after the time t (echo time), i.e. the decay of magnetization at t is solely due to incoherent spin dephasing. The time course of the magnetization after the pulse, i.e., for times $t'>t/2$, is determined by

$$|m(t')\rangle = \exp[(\mathbf{R}+i\mathbf{\Omega})(t'-t/2)]\exp[(\mathbf{R}-i\mathbf{\Omega})t/2]|0\rangle, \tag{4}$$

i.e., the overall spin-echo magnetization at the echo time t is

$$\begin{aligned} M_{SE}(t) &= \langle 0|\exp[(\mathbf{R}+i\mathbf{\Omega})t/2]\exp[(\mathbf{R}-i\mathbf{\Omega})t/2]|0\rangle \\ &= \langle m(t/2)|m^*(t/2)\rangle. \end{aligned} \tag{5}$$

Equation (5) relates the overall spin-echo magnetization to the magnetization of the free induction decay.

III. THE STRONG COLLISION APPROXIMATION AND ITS EXTENSION

The analytical determination of the free induction decay according to Eqs. (3) is restricted to very few cases, e.g., free diffusion in a linear gradient or stochastic fluctuations between two precession frequencies. The idea of the strong collision approach and its extension is to replace the generator of the Markov process $\mathbf{R}$ by a more simple generator $\mathbf{D}$ that conserves specific features of the original dynamics.

A. Strong collision approximation

In many cases the stochastic fluctuations of the perturbation fields occur on a much shorter time scale than spin dephasing, i.e., the correlation time τ of field fluctuations is much shorter than the relaxation time of the magnetization. For ergodic Markov processes one can estimate that after some value of τ a spin has visited almost all relevant states with the equilibrium probability. On the other hand, there is only little change of the magnetization during this time interval. Therefore, spin dephasing in this situation can be described equivalently by a process in which the transition rate between two states $i \rightarrow j$ is independent of the initial state. Consequently, the transition rate for $i \rightarrow j$ is proportional to the equilibrium probability of the final state, $p_{0,j}$. Such a dynamics is referred to as *strong collision dynamics*.

The generator $\mathbf{D}$ of this process has the form

$$\mathbf{D} = -\lambda(\mathbf{id}-\mathbf{\Pi}_0), \tag{6}$$

where $\mathbf{\Pi}_0=|0\rangle\langle 0|$ is the projection operator onto the eigenspace generated by the the equilibrium eigenvector of $\mathbf{R}$, and **id** is the identity operator. The factor λ has to be determined self-consistently.

Since the starting point of the strong collision approximation is the observation that—in many cases of interest—the correlation of the stochastic field fluctuations appear on a shorter time scale than that of changes of the magnetization, only the long-time behavior of the field fluctuations is of importance. This long-time behavior is characterized by the correlation time of the two-point autocorrelation function of the field fluctuations (see also Appendix A),

$$C_2(t)=\langle\omega(t)\omega(0)\rangle=\langle 0|\mathbf{\Omega}\exp(\mathbf{R}t)\mathbf{\Omega}|0\rangle, \tag{7}$$

which is defined as

$$\tau_2=\int_0^\infty dt\frac{C_2(t)-C_2(\infty)}{C_2(0)-C_2(\infty)}=\frac{\langle 0|\mathbf{\Omega}[\exp(\mathbf{R}t)-\mathbf{\Pi}_0]\mathbf{\Omega}|0\rangle}{\langle 0|\mathbf{\Omega}^2|0\rangle-\langle 0|\mathbf{\Omega}|0\rangle^2}. \tag{8}$$

Stochastic field fluctuations determined by the SC process should have the same correlation time as the original process, leading to the self-consistency condition

$$\tau_2^{(\mathrm{SC})}(\lambda)=\tau_2. \tag{9}$$

It is easy to determine that the correlation time for the strong collision approximation is $\tau_2^{(\mathrm{SC})}(\lambda)=\lambda^{-1}$, see Eq. (C2), leading to

$$\lambda=\tau_2^{-1}. \tag{10}$$

B. Extended strong collision approximation

The extension of the strong collision approximation is based on a comparison with the spectral expansion of the original operator,

$$\mathbf{R}=\sum_{j=0}^{\infty} l_j\mathbf{\Pi}_j, \tag{11}$$

where $l_0=0>l_1>\cdots$ are the ordered eigenvalues of $\mathbf{R}$ and $\mathbf{\Pi}_j=|j\rangle\langle j|$ is the projection operator onto the eigenspace corresponding to l_j. Since the time evolution operator is $\exp(\mathbf{R}t)=\Sigma_{j=0}^{\infty}e^{l_j t}\mathbf{\Pi}_j$, it is clear that the low order eigenvalues determine the long-time behavior, while higher orders dominate shorter and shorter time scales. A comparison with a rewriting of Eq. (6),

$$\mathbf{D}=l_0\mathbf{\Pi}_0-\lambda(\mathbf{id}-\mathbf{\Pi}_0) \tag{12}$$

(note that $l_0=0$), shows that in the strong collision approximation, just the lowest order term of Eq. (11) is taken into account explicitly, while the contribution of the higher eigenvalues is approximated by the self-consistently determined parameter λ.

A natural extension, therefore, would be to take into account more low order eigenvalues explicitly, thereby increasing the accuracy of the description of the long-time behavior:

$$\mathbf{D}_n'=\sum_{j=1}^{n} l_j\mathbf{\Pi}_j-\lambda(\mathbf{id}-\mathbf{\Pi}). \tag{13}$$

with $\mathbf{\Pi}=\Sigma_{j=0}^{n}\mathbf{\Pi}_j$. A stochastic process generated by an operator $\mathbf{D}_n'$ in Eq. (13) will be referred to as a simplified extended strong collision (ESC_n') approximation of order *n*. As before, the contribution of the higher eigenvalues is approximated by the parameter λ, which is determined again self-consistently from condition (9). Here it leads to

$$\lambda=\frac{c_2(0)-\sum_{j=1}^{n}|\omega_{0i}|^2}{c_2(0)\tau_2+\sum_{j=1}^{n}l_j^{-1}|\omega_{0i}|^2}, \tag{14}$$

with $\omega_{0i}=\langle 0|\mathbf{\Omega}|i\rangle$ and $c_2(0)=\langle 0|\mathbf{\Omega}^2|0\rangle-\omega_{00}^2$. Note that for $n\to 0$ this equation becomes Eq. (10) again.

However, there are several problems involved with an approximation based on Eqs. (13) and (14). Practically, an exact determination of the low order eigenvalues and eigenvectors is possible only in special cases. Therefore, one has to deal with the problem that the eigenvalues and eigenvectors are known either only approximately or not at all. Furthermore, even with eigenvalues and eigenfunctions known, it turns out that the ESC′ approximation may be not applicable at all in certain situations: If the autocorrelation function of the field fluctuations is determined fully by the eigenfunctions included in $\mathbf{D}'$, Eq. (14) is undetermined. In that case additional self-consistency requirements would be necessary for a better description of the intermediate time regime.

Nevertheless, the above approach can be readily adapted to these situations. Equation (13) can be viewed as an optimized reduced description of the relaxation in various subspaces of the original operator $\mathbf{R}$. Such a optimized description should also be possible for subspaces that are not eigenvectors of $\mathbf{R}$. We can, therefore, set

$$\mathbf{D}_n=-\sum_{j=1}^{n}\lambda_j\mathbf{\Pi}_j-\lambda(\mathbf{id}-\mathbf{\Pi}). \tag{15}$$

However, now the rates λ_j, $j=1,\ldots,n$ are not eigenvalues anymore, but have to be determined by additional self-consistency requirements, see below. Moreover, the $\mathbf{\Pi}_j$ are not projectors onto the eigenspace of a particular eigenvalue, but onto the spaces defined by arbitrarily chosen mutually orthogonal functions $|f_j\rangle$, $j=1,\ldots,n$, with $\langle f_i|f_j\rangle=\delta_{ij}$ and $\langle f_j|0\rangle=0$; i.e., the projectors have the form $\mathbf{\Pi}_j=|f_j\rangle\langle f_j|$ and $\mathbf{\Pi}=\mathbf{\Pi}_0+\Sigma_{j=1}^{n}\mathbf{\Pi}_j$. Naturally, one would try to choose the functions $|f_j\rangle$ close to the eigenfunctions $|j\rangle$, although it is not required for the extension to work. Another natural function space, for example, is based on polynomials in the frequency operator $\mathbf{\Omega}$, i.e.,

$$|f_i\rangle=p_i(\mathbf{\Omega})|0\rangle, \tag{16}$$

where p_i is some polynomial of degree *i*, the coefficients of which are chosen in such a way that the orthonormal relations are fulfilled. In the following we will refer to this base of functions as the Ω base.

In analogy to Eq. (13) a stochastic process generated by an operator $\mathbf{D}_n$ in Eq. (15) will be referred to as an extended strong collision (ESC_n) approximation of order *n*. It is evident that the ESC_0 approximation refers to the strong collision approximation.

We mentioned already that the rates λ_j, $j=1,\ldots,n$ in Eq. (15) have to be determined now by additional self-consistency requirements. As it was with the SC approximation, the aim of the ESC_n approximation is to approximate more closely the correlation of field fluctuations. This is achieved by considering also higher order correlation functions

$$C_m(t_{m-1},\dots,t_1)=\left\langle \omega\left(\sum_{j=1}^{m-1} t_j\right)\dots\omega(t_2+t_1)\omega(t_1)\omega(0)\right\rangle$$
$$=\langle 0|\mathbf{\Omega}\exp(\mathbf{R}t_{m-1})\mathbf{\Omega}\cdots\exp(\mathbf{R}t_1)\mathbf{\Omega}|0\rangle. \tag{17}$$

Following the same arguments as for the strong collision approximation, the long-time behavior of the C_m is of interest. In the same way as for the strong collision approximation this should be characterized by some first order statistical moment, which is obtained by integration of the correlation function over $t_{m-1},\dots,t_1$. However, direct usage of C_m is hampered by its nonvanishing asymptotic behavior: It is easily seen that from the relation $\lim_{t_\nu\to\infty}\exp(\mathbf{R}t_\nu)=\mathbf{\Pi}_0$ follows

$$\lim_{t_\nu\to\infty} C_m(t_{m-1},\dots,t_1)=C_{m-\nu}(t_{m-1},\dots,t_{\nu+1})$$
$$\times C_\nu(t_{\nu-1},\dots,t_1), \tag{18}$$

which does not necessarily vanish. In the strong collision approximation we avoided this problem by considering the operator $[\exp(\mathbf{R}t)-\mathbf{\Pi}_0]$ instead of $\exp(\mathbf{R}t)$ in Eq. (8), i.e., we considered only the relaxational part of the stochastic process. When we perform the same replacement in Eq. (17) we obtain modified correlation functions $c_m(t_{m-1},\dots,t_1)$ that we will call *quasicumulants* (see Appendix A). They vanish asymptotically for all t_ν. We now require that the generalized correlation times derived from these quasicumulants,

$$\tau_m^{m-1}=\int_0^\infty \Pi_{i=1}^{m-1} dt_i \frac{c_m(t_{m-1},\dots,t_1)}{c_m(0,\dots,0)}, \tag{19}$$

are equal for the exact process and for the extended strong collision description. The relaxation rates are, therefore, determined by

$$\tau_m^{(\mathrm{ESC}_n)}(\lambda,\lambda_1,\dots,\lambda_n)=\tau_m,\quad m=2,4,\dots,2n+2, \tag{20}$$

which replace the single self-consistency condition (9). Note that in many systems the correlation functions $c_m(t_{m-1},\dots,t_1)$ vanish for odd values of *m* due to symmetry. Therefore, we require the equivalence of relaxation times in Eq. (20) for even values of *m* only. Otherwise one has to determine the correlation times of the first $n+1$ nonvanishing correlation functions.

It is important to emphasize some properties of the ESC approximation. First of all, it usually does not reduce to the ESC′ approximation when eigenfunctions are used for the projection operator; i.e., the $\lambda_1,\dots,\lambda_n$ do not take on the numerical values of the corresponding eigenvalues, although they usually do approximate them. In the light of the problems with the ESC′ approximations mentioned above, it will turn out that this is an advantage: the self-consistent determination of the relaxation parameters λ and $\lambda_1,\dots,\lambda_n$ according to Eq. (20) is more balanced than when only Eq. (9) is used, and gives rise to an improved approximation. Moreover, the self-consistency conditions (20) imply that both processes, the ESC process and the original Markov process, have the same motional narrowing expansion of the transverse relaxation, as it is shown in Eq. (B7).

C. Transverse spin relaxation in the extended strong collision approximation

In this section we will exploit the simple structure of the generator $\mathbf{D}_n$ to determine the time course of magnetization. We will consider both: the free induction decay, i.e., the superposition of coherent and incoherent spin dephasing, and the spin-echo decay, i.e., pure incoherent spin dephasing.

1. Free induction decay

In the extended strong collision approximation the generator $\mathbf{R}$ of the free induction decay in the generalized Bloch-Torrey equation (1) is replaced by the generator $\mathbf{D}_n$ of Eq. (15). Instead of solving the propagator $\mathbf{U}(t)=\exp[(\mathbf{D}_n+i\mathbf{\Omega})t]$ it is more convenient to solve its Laplace transform $\hat{\mathbf{U}}(s)=(s-\mathbf{D}_n-i\mathbf{\Omega})^{-1}$, which may be expanded as

$$\hat{\mathbf{U}}(s)=\hat{\mathbf{U}}_0(s+\lambda)+\hat{\mathbf{U}}_0(s+\lambda)\mathbf{\Lambda}\hat{\mathbf{U}}(s). \tag{21}$$

where $\hat{\mathbf{U}}_0(s)=(s-i\mathbf{\Omega})^{-1}$ is the Laplace transform in the static dephasing limit ($\mathbf{D}_n=\mathbf{0}$), and the operator $\mathbf{\Lambda}$ is defined as

$$\mathbf{\Lambda}=\sum_{j=0}^{n}(\lambda-\lambda_j)\mathbf{\Pi}_j, \tag{22}$$

where we set $\lambda_0=0$. We will now confine the operators in Eq. (21) onto the subspace defined by the projection operator $\mathbf{\Pi}=\Sigma_{j=0}^{n}\mathbf{\Pi}_j$. Using the abbreviation $\mathbf{O}^{\Pi}\coloneqq\mathbf{\Pi}\mathbf{O}\mathbf{\Pi}$ for denoting any operator $\mathbf{O}$ confined to that subspace, we obtain

$$\hat{\mathbf{U}}^{\Pi}(s)=\hat{\mathbf{U}}_0^{\Pi}(s+\lambda)+\hat{\mathbf{U}}_0^{\Pi}(s+\lambda)\mathbf{\Lambda}^{\Pi}\hat{\mathbf{U}}^{\Pi}(s), \tag{23}$$

where we exploited the fact that $\mathbf{\Lambda}=\mathbf{\Pi}\mathbf{\Lambda}\mathbf{\Pi}$ and the idempotency of projection operators, i.e., $\mathbf{\Pi}=\mathbf{\Pi}^2$. Equation (23) is of fundamental importance. It demonstrates that the relation (21) between the ESC approximation and the static dephasing is also valid in the subspace $[|0\rangle,|f_1\rangle,\dots,|f_n\rangle]$. This simplifies determination of spin relaxation considerably, since one only has to determine the $(n+1)\times(n+1)$ matrices[1] of the static dephasing limit $\hat{\mathbf{U}}_0^{\Pi}$ and $\mathbf{\Lambda}$, i.e.,

$$\hat{\mathbf{U}}^{\Pi}(s)=[\mathbf{\Pi}-\hat{\mathbf{U}}_0^{\Pi}(s+\lambda)\mathbf{\Lambda}^{\Pi}]^{-1}\hat{\mathbf{U}}_0^{\Pi}(s+\lambda). \tag{24}$$

---

[1] In case of degeneracy of the eigenvalues the matrix dimension is the sum of the dimensions of the eigenspaces plus 1.

The Laplace transform of the overall magnetization decay $\hat{M}_{[n]}(s)$ in the extended strong collision approximation has the form

$$\hat{M}_{[n]}(s)=\langle 0|\hat{\mathbf{U}}^{\Pi}(s)|0\rangle. \tag{25}$$

For the special case of the strong collision approximation, ESC$_0$, Eqs. (24) and (25) result in

$$\hat{M}_{[0]}(s)=\frac{\hat{M}_{sd}(s+\lambda)}{1-\hat{M}_{sd}(s+\lambda)\lambda}, \tag{26}$$

with $\hat{M}_{sd}(s)=\langle 0|\hat{\mathbf{U}}_0(s+\lambda)|0\rangle$ as the Laplace transform of the overall magnetization in the static dephasing regime. The time evolution $M(t)$ can be obtained from Eqs. (24) and (25) either by the numerical inverse Laplace transform by or using the generalized moment approach [4,10], which allows a multiexponential approximation.

2. Spin-echo decay

The spin-echo decay is obtained by inserting the generator $\mathbf{D}_n$ into Eq. (5), i.e.,

$$\begin{aligned}\partial_t M_{SE,[n]}(t)&=-\lambda M_{SE,[n]}(t)+\langle m(t/2)|\mathbf{\Lambda}|m^*(t/2)\rangle\\&=-\lambda M_{SE,[n]}(t)+\langle 0|\mathbf{U}(t/2)\mathbf{\Lambda}\mathbf{U}^*(t/2)|0\rangle\\&=-\lambda M_{SE,[n]}(t)+\langle 0|\mathbf{U}^{\Pi}(t/2)\mathbf{\Lambda}\mathbf{U}^{*\Pi}(t/2)|0\rangle,\end{aligned} \tag{27}$$

i.e., the spin-echo decay is expressed as a function of the spin-echo amplitude M_{SE}, and the projection of the free induction decay onto the subspace $[|0\rangle,|f_1\rangle,\ldots,|f_n\rangle]$, i.e., $\mathbf{U}^{\Pi}(t)|0\rangle$. This projection of the free induction decay is obtained from Eq. (24) by inverse Laplace transform, i.e., $\mathbf{U}^{\Pi}(t)|0\rangle=\mathcal{L}^{-1}(\hat{\mathbf{U}}^{\Pi}(s)|0\rangle)$. The solution of Eq. (27) is

$$M_{SE,[n]}(t)=e^{-\lambda t}\left[1+2\int_0^{t/2}d\xi e^{2\lambda\xi}\langle 0|\mathbf{U}^{\Pi}(\xi)\mathbf{\Lambda}\mathbf{U}^{*\Pi}(\xi)|0\rangle\right] \tag{28}$$

3. Time constants of transverse relaxation

The free induction and the spin-echo decay are usually described by the time constants T_2^* and T_2. However, there is no unique definition of these parameters. One definition of the relaxation times is

$$\begin{aligned}1/T_2^*&=-\ln[M(t)]/t,\\1/T_2&=-\ln(M_{SE})/t.\end{aligned} \tag{29}$$

For the ESC decay one has to replace M by $M_{[n]}$ and M_{SE} by $M_{SE,[n]}$. This definition implies a dependence of relaxation times on t, except for single exponential decay.

Another definition of relaxation times is based on the assumption that these constants provide the best single exponential approximation of magnetization decays, i.e., $M(t)\approx e^{-t/T_2^*}, M_{SE}\approx e^{-t/T_2}$. According to the mean relaxation time approximation the relaxation times are then the first long-time moments of the decays [10], i.e.,

$$\begin{aligned}T_2^*&:=\mu_{-1}(M)=\int_0^{\infty}dt\,M(t),\\T_2&:=\mu_{-1}(M_{SE})=\int_0^{\infty}dt\,M_{SE}(t).\end{aligned} \tag{30}$$

For a single exponential the mean relaxation time definition and the definitions (29) give the same results. According to definition (30) the relaxation times of the ESC decays can be related to their Laplace transforms as

$$\begin{aligned}T_2^*&=\hat{M}_{[n]}(0),\\T_2&=\hat{M}_{SE,[n]}(0).\end{aligned} \tag{31}$$

The term $\hat{M}_{[n]}(0)$, which provides T_2^*, is obtained from Eq. (25). Applying some rules of Laplace transforms, the term $\hat{M}_{SE,[n]}(0)$ giving T_2 is obtained from Eq. (27) as

$$T_2=\lambda^{-1}+2\sum_{i=0}^{n}(1-\lambda_i/\lambda)\Theta_i, \tag{32}$$

where

$$\begin{aligned}\Theta_0&=\int_0^{\infty}dt|\langle 0|\mathbf{U}^{\Pi}(t)|0\rangle|^2\\&=\frac{1}{2\pi i}\int_{-i\infty}^{i\infty}dz\langle 0|\hat{\mathbf{U}}^{\Pi}(z)|0\rangle\langle 0|\hat{\mathbf{U}}^{*\Pi}(-z)|0\rangle\end{aligned} \tag{33}$$

is the mean relaxation time of the absolute squared overall free induction magnetization $|M_{[n]}(t)|^2=|\langle 0|\mathbf{U}(t)^{\Pi}|0\rangle|^2$, and for $i\geqslant 1$,

$$\begin{aligned}\Theta_i&=\int_0^{\infty}dt\langle 0|\mathbf{U}^{\Pi}(t)|f_i\rangle\langle f_i|\mathbf{U}^{*\Pi}|0\rangle(t)\rangle\\&=\frac{1}{2\pi i}\int_{-i\infty}^{i\infty}dz\langle 0|\hat{\mathbf{U}}^{\Pi}(z)|f_i\rangle\langle f_i|\hat{\mathbf{U}}^{*\Pi}(-z)|0\rangle\end{aligned} \tag{34}$$

are transit times describing the transient occurrence of the nonequilibrium components of the free induction decay $\mathbf{U}(t)|f_i\rangle$. Equation (32) relates T_2, which describes the incoherent, i.e., irreversible, component of spin dephasing to the stochastic field dynamics (λ,λ_i) and time constants of the free induction decay (Θ_i), i.e., Eq. (32) is a dissipation-fluctuation-coherence relation. Note that the Eqs. (33) and (34) directly relate the time constants Θ_i to the Laplace transform of the free induction decay $\hat{\mathbf{U}}^{\Pi}(s)$ given by the fundamental equation (23).

From Eq. (32) one can derive asymptotic relations for very fast and slow stochastic field fluctuations. Let ϵ be some scaling parameter of $\mathbf{D}_n$, i.e., $\lambda,\lambda_i\sim\epsilon$, then Eq. (32) reads in the static dephasing limit $(\epsilon\rightarrow 0)$

$$T_2 \approx \lambda^{-1}, \tag{35}$$

where we exploited that $\Theta_i(\epsilon)$ approaches its finite static dephasing limit. For very fast fluctuations i.e., in the motional narrowing limit ($\epsilon \to \infty$) one exploits that $\langle f_i|\hat{\mathbf{U}}(s)|0\rangle/\langle 0|\hat{\mathbf{U}}(s)|0\rangle \sim \epsilon^{-1}$, as a power expansion demonstrates, i.e., one obtains

$$T_2 \approx 2\Theta_0. \tag{36}$$

This implies that the spin-echo relaxation time is almost identical with the relaxation time of the absolute squared magnetization of the free induction decay, or vice versa that the free induction decay is almost irreversible.

The dissipation-fluctuation-coherence relation (32) takes a very simple form in the strong collision approximation, when we assume that the overall magnetization decay is well approximated by a single exponential, i.e., $M_{[0]}(t) \approx e^{-t/T2^*}$. Since $\lambda = \tau_2^{-1}$, see Eq. (10), Eq. (32) reads

$$T_2 = \tau_2 + 2\Theta_0 \approx \tau_2 + T_2^*. \tag{37}$$

From Eqs. (37) follows that in the motional narrowing limit $T_2 \approx T_2^*$ holds whereas in the static dephasing limit of the strong collision approximation the relation $T_2 \approx \tau_2$ holds.

IV. APPLICATIONS

A. Anderson-Weiss model

The Anderson-Weiss model [8] is one of the rare approaches—besides the ESC approximation—which describes spin dephasing over the whole dynamic range of stochastic field fluctuations. The approach is suitable, for example, when dephasing is induced by spin interaction with a great number of independently fluctuating perturbation fields in the spin environment. Then analytical results are obtained for the free induction and the spin-echo magnetization decay as

$$M(t) = \exp\left[-\int_0^t (t-\xi) c_2(\xi) d\xi\right], \tag{38}$$

$$M_{SE}(t) = \exp\left[-4\int_0^{t/2} (t/2-\xi) c_2(\xi) d\xi + \int_0^t (t-\xi) c_2(\xi) d\xi\right], \tag{39}$$

where c_2 is the modified two-point correlation function (see Appendix A). In this section we will first characterize the class of Markovian processes which fulfills the conditions of the Anderson-Weiss model. This leads to a generalized Bloch-Torrey equation according to Eq. (1), which is solved. Finally we compare the Anderson-Weiss model with its ESC_0 and ESC_1 approximation.

1. Markovian and Anderson-Weiss dynamics

The Anderson-Weiss approach is based on a Gaussian distribution of perturbation field frequencies ω. Even more important is the *additional* assumption that the stochastic phase accumulation of a spin $\phi = \int_0^t d\xi \omega(\xi)$ also exhibits a Gaussian distribution. This latter condition implies that the Green's function $G(\omega_j, \omega_i, t)$, i.e., the probability that a spin initially precessing with frequency ω_i precesses at t with ω_j, is also a Gaussian function in ω_j, ω_i with the condition $G(\omega_j, \omega_i, 0) = \delta(\omega_j - \omega_i)$. This implies that only nearest neighbor transitions rates are nonvanishing. Markovian processes in a continuous variable ω with this property are described equivalently by a Fokker-Planck equation [11], i.e., the probability density $p(\omega)$ satisfies

$$\partial_t p(\omega,t) = \mathbf{R} p(\omega,t) = \partial_\omega D(\omega)[\partial_\omega - F(\omega)] p(\omega,t), \tag{40}$$

where $D(\omega)$ is a—possibly ω dependent—diffusion coefficient and $F(\omega)$ is some driving force. Since the equilibrium probability density is a Gaussian function one obtains $F(\omega) = -c\omega$ with $c > 0$. The generalized Bloch-Torrey equation (1), which determines the dynamics of magnetization as a superposition of precession and stochastic transitions, then reads

$$\partial_t m(\omega,t) = [\partial_\omega D(\omega)(\partial_\omega + c\omega) + \mathrm{i}\omega] m(\omega,t). \tag{41}$$

The derivation of the Eqs. (40) and (41) is of fundamental importance, since it states that a Markovian dynamics of a variable ω, which satisfies the Anderson-Weiss conditions, is equivalent to a diffusion process in this variable within a harmonic potential $c\omega^2/2$ and vice versa. Transformation of variables $\omega \to c^{1/2}\omega$ and $t \to c^{-1/2} t$ simplifies Eq. (41) to

$$\partial_t m(\omega,t) = [\partial_\omega \beta(\omega)(\partial_\omega + \omega) + \mathrm{i}\omega] m(\omega,t), \tag{42}$$

where we continue to denote also the transformed variables as ω and t and $\beta = c^{3/2} D$ is the transformed diffusion coefficient. In the following we will restrict consideration to the case of a constant diffusion coefficient β. The left and right sided eigenfunctions of the transition operator $\mathbf{R} = \beta\partial_\omega(\partial_\omega + \omega)$ are the Hermite functions, i.e.,

$$|n\rangle \sim \exp(-\omega^2/2) H_n(\omega),$$
$$\langle n| \sim H_n(\omega) \tag{43}$$

with eigenvalues

$$l_n = -n\beta. \tag{44}$$

From the definition of the Hermite functions and the operator intertwining relation $[\partial_\omega, (\partial_\omega + \omega)] = 1$ follow the recursive equations

$$|n+1\rangle = -\frac{1}{n+1}\partial_\omega |n\rangle, \quad |n-1\rangle = (\partial_\omega + \omega)|n\rangle,$$
$$\langle n+1| = \langle n|(\partial_\omega + \omega), \quad \langle n-1| = -\frac{1}{n}\langle n|\partial_\omega, \tag{45}$$

which also provide the normalization of eigenfunctions. The advantage of the Markovian formulation of the Anderson-

Weiss model is that it does not only provide global parameters but also local ones, e.g., the time course of the magnetization with frequency ω. Straightforward application of Eqs. (45) and some operator algebra provides the solution of Eq. (42) as

$$\begin{aligned} m(\omega,t) &= \exp[\beta\partial_\omega(\partial_\omega+\omega)+\mathrm{i}\omega]|0\rangle \\ &= \exp[-\beta^{-1}t+\beta^{-2}(1-e^{-\beta t})](2\pi)^{-1/2} \\ &\quad\times\exp[-1/2\{\omega-\mathrm{i}\beta^{-1}(e^{\beta t}-1)\}]. \end{aligned} \tag{46}$$

Integration over ω just gives the free induction decay of the overall magnetization

$$M(t)=\exp[-\beta^{-1}t+\beta^{-2}(1-e^{-\beta t})], \tag{47}$$

which is just equivalent to the result of Eq. (38), since the two-point correlation function of Eq. (42) is $c_2(t)=e^{-\beta t}$ [see Eq. (E1)]. Insertion of this two-point correlation function into Eq. (39) provides the spin-echo decay as

$$M_{SE}(t)=M(t/2)^2\exp[\beta^{-2}(e^{-\beta t/2}-1)^2]. \tag{48}$$

Relaxation times of the free induction and spin-echo decay were determined according to Eqs. (30).

2. ESC approximation

The ESC propagator is determined from the propagator in the static dephasing limit $\mathbf{U}_0=\exp(\mathrm{i}\mathbf{\Omega}t)=[\exp(\mathrm{i}\omega t)]$, and the $\mathbf{\Lambda}$ matrix of Eq. (22), both restricted either to the function space $[|0\rangle]$ for the ESC$_0$ or $[|0\rangle,|f_1\rangle]$ for the ESC$_1$ approximation Eq. (24). The special structure of the transition rate operator of the Anderson-Weiss model implies that the base of eigenfunctions, Eqs. (43), is identical with the Ω base, Eq. (16), i.e., $p_n(\mathbf{\Omega})|0\rangle=|n\rangle$. Hence, we will set in the following $|f_1\rangle=p_1(\mathbf{\Omega})=|1\rangle$.

ESC$_0$ approximation. The matrix element of the Laplace transformed propagator in the static dephasing limit required for the ESC$_0$ approximation is

$$\langle 0|\hat{\mathbf{U}}_0(s)|0\rangle=\sqrt{\pi/2}e^{s^2/2}\,\mathrm{erfc}(s/\sqrt{2}), \tag{49}$$

where $\mathrm{erfc}(z)=1-\mathrm{erf}(z)$ is the complementary error function. The coefficient λ, which guarantees the self-consistency condition Eq. (9), is determined form the Eqs. (C2) and (E2) as

$$\lambda=\beta. \tag{50}$$

ESC$_1$ approximation. The matrix elements of the Laplace transformed propagator in the static dephasing limit required for the ESC$_1$ approximation in the Ω base are that of Eq. (49) and

$$\begin{aligned} \langle 0|\hat{\mathbf{U}}_0(s)|1\rangle &= N\mathcal{L}[\langle 0|\exp(\mathrm{i}\mathbf{\Omega}t)\mathbf{\Omega}|0\rangle] \\ &= N(-\mathrm{i})\mathcal{L}[\partial_t\langle 0|\exp(\mathrm{i}\mathbf{\Omega}t)|0\rangle] \\ &= N\mathrm{i}[1-s\langle 0|\hat{U}_0(s)|0\rangle], \end{aligned} \tag{51}$$

where the factor N generally is some normalization factor with $N^2=\langle 0|\mathbf{\Omega}^2|0\rangle$, i.e., in the case of the Anderson-Weiss model it is simply $N=1$. Consequently, using some elementary rules of Laplace transforms, one derives the other matrix elements as

$$\begin{aligned} \langle 1|\hat{\mathbf{U}}_0(s)|0\rangle &= \langle 0|\hat{\mathbf{U}}_0(s)|1\rangle, \\ \langle 1|\hat{\mathbf{U}}_0(s)|1\rangle &= N^2 s[1-s\langle 0|\hat{\mathbf{U}}_0(s)|0\rangle], \end{aligned} \tag{52}$$

It has to be stressed that the Eqs. (51) and (52) are generally valid for all ESC$_1$ approximations in the Ω base.

The coefficients λ,λ_1 guaranteeing the self-consistency condition Eq. (20) are obtained from Eqs. (D4),(E2) and (D7),(E4)

$$\begin{aligned} \lambda_1 &= \beta, \\ \lambda &= 2\beta. \end{aligned} \tag{53}$$

Relaxation in the ESC$_0$ and ESC$_1$ approximation. The matrix $\hat{\mathbf{U}}_0^{\Pi}(s)$ and the coefficients λ and λ_1 determine the Laplace transformed ESC propagator $\hat{\mathbf{U}}^{\Pi}(s)$ in Eq. (24), which itself is the base for all other calculations. It directly provides T_2^* when defined as the first moment, Eq. (31), of the free induction decay Eq. (25). Insertion of $\hat{\mathbf{U}}^{\Pi}(s)$ into Eqs. (33) and (34) provides according to Eq. (32) the relaxation time of the spin-echo decay when defined as its first long-time moment Eq. (31). Inverse Laplace transformation of $\hat{\mathbf{U}}^{\Pi}(s)$ gives the ESC propagator $\mathbf{U}^{\Pi}(t)$, which itself allows determination of the spin-echo decay Eq. (28).

The relaxation time $T_2^* := \mu_{-1}(M)$ of the Anderson-Weiss process is well approximated by the ESC$_0$ and ESC$_1$ approximation over the whole dynamic range of stochastic field fluctuations (Fig. 1). In the static dephasing regime all curves approach $\lim_{\beta\to 0}\mu_{-1}^{-1}=\sqrt{2/\pi}$. The successive approximation of the spin-echo relaxation by the ESC approximation is seen from the magnetization decay curves (Fig. 2) and the curves showing the dependence of T_2 obtained by either definition [Eqs. (29) and (30)] on the diffusion coefficient β as Fig. 3 demonstrates. The latter curves all run parallel in the motional narrowing regime $[\tau_2(\langle 0|\mathbf{\Omega}^2|0\rangle)^{1/2}=\beta^{-1}\ll 1]$ and exhibit a similar location of the maximum relaxation rate. Towards the static dephasing regime $(\beta\to 0)$ the rate of the Anderson-Weiss process declines less than the rates of the ESC processes.

B. Spin dephasing by restricted diffusion in a linear gradient field

1. The exact process

Whereas dephasing of free diffusing spins in a linear gradient field can be treated analytically, only numerical solutions exists for the restricted diffusion case [12]. On the one hand restricted diffusion in a linear gradient field provides a simple model to study principle features of spin dephasing by diffusion. On the other hand treatment of this problem is not only of academic interest as already mentioned in the

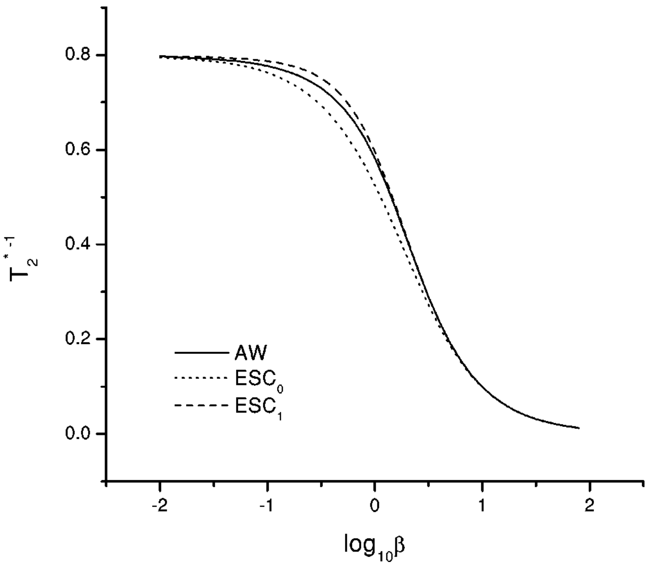

FIG. 1. Relaxation time T_2^* (defined as the first long-time moment μ_{-1}) of the free induction decay in the Anderson-Weiss model (AW) and its ESC_0 and ESC_1 approximation as a function of the diffusion coefficient β.

Introduction. We will approximate the free induction and spin-echo decay of the global magnetization for the case of restricted diffusion by the strong collision approximation (ESC_0) and its first extension (ESC_1). The ESC_1 approximation will be performed for both, in the Ω-polynomial base, i.e., $|f_1\rangle \sim \mathbf{\Omega}|0\rangle$, and in the eigenfunction base, i.e., $|f_1\rangle = |1\rangle$.

We assume that the spins diffuse within an interval of size L in a linear gradient field $\omega(x) = gx$. Reflecting boundary conditions at $x = \pm L/2$ imply that $\partial_x m(\pm L/2, t) \equiv 0$. With D as the diffusion coefficient and $\mathbf{R} = D[\partial_x^2]$ the Bloch-Torrey equation (1) has the form $\partial_t m(x,t) = (D[\partial_x^2] + igx)m(x,t)$, where the brackets [ ] denote that the application of the operator ∂_x^2 is restricted to functions which fulfill the reflecting boundary conditions. Transformation of variables $x \rightarrow x/L$ and $t \rightarrow tgL$ results in

$$\partial_t m(x,t) = (\beta[\partial_x^2] + ix)m(x,t), \tag{54}$$

and vanishing derivatives at the edges of the unit interval

$$\partial_x m(\pm 1/2, t) \equiv 0, \tag{55}$$

with the diffusion coefficient $\beta = D/(gL^3)$. We continue to denote also the transformed variables as x and t to reduce the number of symbols. When the initial magnetization is proportional to the equilibrium probability, i.e., $m(x,0) \equiv 1$, the Laplace transform $\hat{m}(x,s)$ of the local magnetization decay satisfies

$$(\beta[\partial_x^2] + ix)\hat{m}(x,s) = -1. \tag{56}$$

Equation (54) was solved numerically. Integration of the result over the unit interval provided the free induction decay of the overall magnetization, and application of Eq. (5) on the result gave the spin-echo decay. When the spin-echo relaxation time was defined as the first statistical moment of the magnetization decay Eq. (30) was applied. For determination of T_2^*, defined as the first moment of the free induction decay, Eq. (56) was solved numerically, and integration $\int_{-1/2}^{1/2} dx \hat{m}(x,s) = \hat{M}(s)$ gave $T_2^* = \hat{M}(0) = \mu_{-1}(M)$.

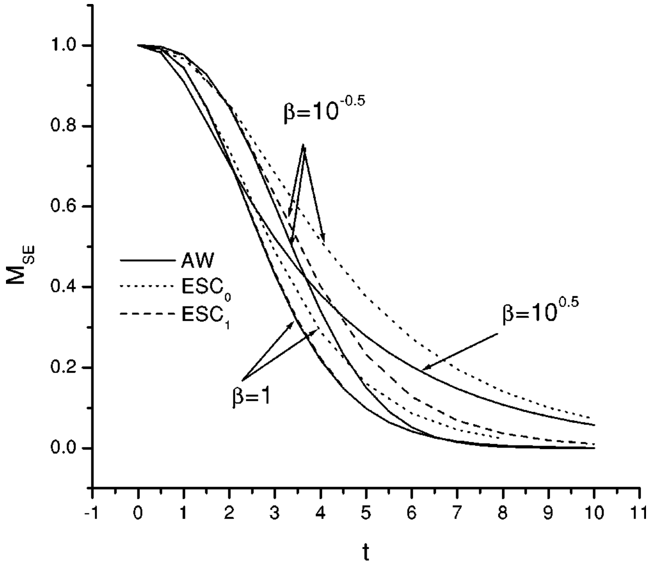

FIG. 2. Spin-echo magnetization decay in the Anderson-Weiss model (AW) and its ESC_0 and ESC_1 approximations for three different diffusion coefficients β. Note: for the diffusion coefficient close to the motional narrowing regime ($\beta = 10^{0.5}$) the Anderson-Weiss and the ESC curves almost run parallel. Therefore for the clearness of the figure, only the Anderson-Weiss curve is shown. In the intermediate motion regime $\beta = 1$ the original and the ESC_1 curve still run parallel, whereas the ESC_0 approximation already shows a moderate deviation. Towards the static dephasing regime ($\beta = 10^{-0.5}$) the successive improved approximation of the Anderson-Weiss curve by the ESC curves is evident.

2. ESC approximation

The determination of the ESC_0 and ESC_1 approximation is completely analogous to that for the Anderson-Weiss model, except that the Ω polynomial and the eigenfunction base are not identical.

ESC_0 approximation. The equilibrium function for the restricted diffusion within the unit interval is

$$|0\rangle = 1, \tag{57}$$

i.e., one obtains

$$\langle 0|\hat{\mathbf{U}}_0(s)|0\rangle = i \ln\left(\frac{s - i/2}{s + i/2}\right). \tag{58}$$

The self-consistency condition for the strong collision approximation (9) determines the parameter λ as [see Eqs. (C2) and (E11)]

$$\lambda = 10\beta. \tag{59}$$

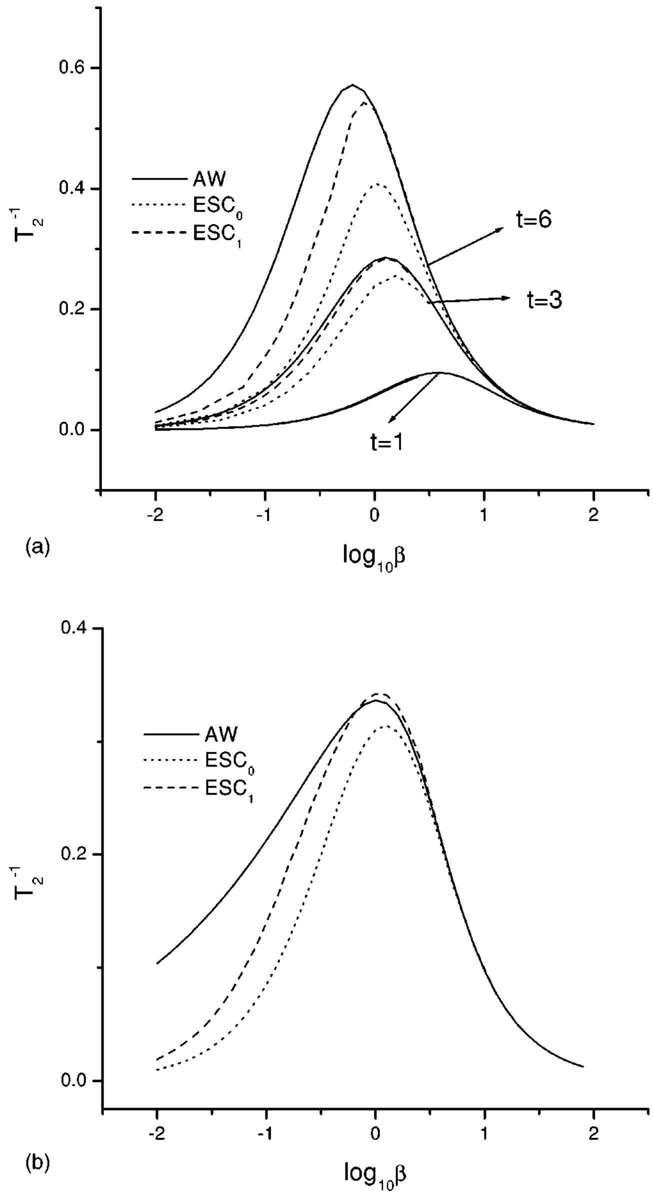

FIG. 3. Dependence of the spin-echo relaxation time T_2 on the diffusion coefficient β for the Anderson-Weiss model (AW) and its ESC$_0$ and ESC$_1$ approximation: (a) The relaxation time was defined according to Eq. (29) by the echo time t, and (b) as the first long-time moment μ_{-1} of spin-echo magnetization decay according to Eq. (30). The Anderson-Weiss curves and the corresponding approximations converge as β approaches the motional narrowing regime $\tau_2(\langle 0|\mathbf{\Omega}^2|0\rangle)^{1/2}=\beta^{-1}\ll 1$. When defined by the echo time (a) the T_2 curves of the Anderson-Weiss model and its approximations all run parallel for the short echo time $(t=1)$. With increasing echo time $(t=3,6)$ the successive ESC approximation becomes evident.

Insertion of the results of Eqs. (58) and (59) into Eq. (24) determines the Laplace transformed propagator in the ESC$_0$ approximation $\langle 0|\hat{\mathbf{U}}(s)|0\rangle$ from which T_2^*, T_2, and spinecho decay curves are obtained.

ESC$_1$ approximation in the Ω-polynomial base. The lowest order function besides the equilibrium state in the Ω-polynomial base has the form

$$|f_1\rangle=\langle 0|\mathbf{\Omega}^2|0\rangle^{-1/2}\mathbf{\Omega}|0\rangle=2\sqrt{3}x. \tag{60}$$

The matrix element (58) and the Eqs. (51) and (52) then directly provide the static dephasing operator $\hat{\mathbf{U}}_0(s)=(s-ix)^{-1}$ in the $[|0\rangle,|f_1\rangle]$ base. The parameters λ_1,λ of the ESC$_1$ approximation are determined from the self-consistency condition (20), i.e., with Eqs. (D4), (E11) and Eqs. (D7),(E17), one obtains

$$\lambda_1=10\beta,$$

$$\lambda=\frac{443\,520}{8900}\beta,$$

$$\approx 49.83\beta. \tag{61}$$

Development in the eigenfunction space. The normalized nonequilibrium eigenfunctions of the restricted diffusion operator are

$$|\nu\rangle=\sqrt{2}\sin(\nu\pi x) \quad \text{for } \nu=1,3,\ldots$$

$$=\sqrt{2}\cos(\nu\pi x) \quad \text{for } \nu=2,4,\ldots. \tag{62}$$

Since $[\partial_x^2]$ is a symmetric operator, left and right sided eigenfunctions are identical. With $|f_1\rangle=|1\rangle$ and $z=\pi(1/2+is)$ one obtains

$$\langle 0|\hat{\mathbf{U}}_0(s)|1\rangle=\sqrt{2}[\sinh(\pi s)\mathrm{Ci}(\xi) + i\cosh(\pi s)\mathrm{Si}(\xi)]\Big|_{\xi=-z^*}^{\xi=z},$$

$$\langle 1|\hat{\mathbf{U}}_0(s)|1\rangle=-2\arctan(2s)-[i\cosh(2\pi s)\mathrm{Ci}(\xi) + \sinh(2\pi s)\mathrm{Si}(\xi)]\Big|_{\xi=-2z^*}^{\xi=2z}, \tag{63}$$

where Ci and Si denote the integral cosine and integral sinus function, respectively. The parameters λ_1, λ in the eigenfunction base are determined similarly as in the Ω base (see Appendixes D and E) and one obtains

$$\lambda_1\approx 9.89\beta,$$

$$\lambda\approx 41.6\beta. \tag{64}$$

Relaxation in the ESC$_0$ and ESC$_1$ approximation. Figure 4 demonstrates the first long-time moment of the free induction decay, that of the strong collision approximation, and its first extension for both bases as a function of the diffusion coefficient β. All curves show the same asymptotic behavior in the static dephasing $(\beta\rightarrow 0)$ and in the motional narrowing limit $[\tau_2(\langle 0|x^2|0\rangle)^{1/2}=1/(20\sqrt{3})\beta^{-1}\ll 1]$. Furthermore, the better approximation by the ESC$_1$ curves compared to the ESC$_0$ curve in the intermediate motion regime is evident. There is no significant difference between the ESC$_1$ approximation in the eigenfunction and in the Ω-polynomial base.

The spin-echo magnetization decay is shown in Fig. 5. Especially in the long-time behavior near the static dephasing regime, the ESC$_1$ curves either in the eigenfunction space or in the Ω space demonstrate a better approximation

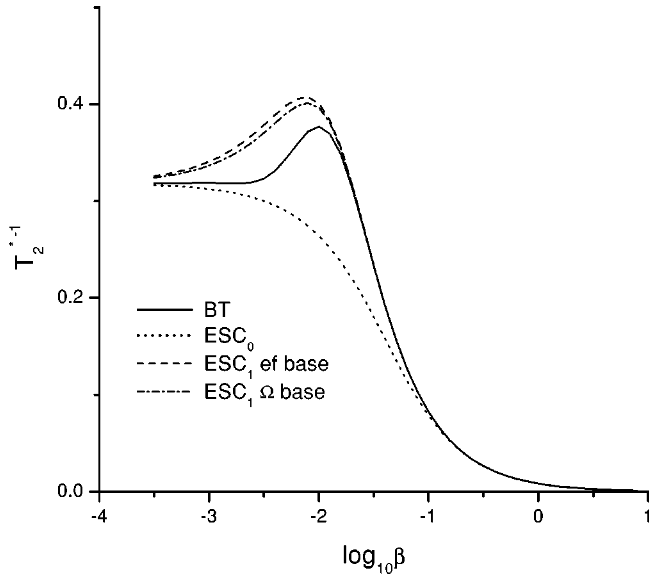

FIG. 4. Relaxation time of the free induction decay T_2^* of spins diffusing within a linear field gradient in the unit interval as a function of the diffusion coefficient β. T_2^* is defined as the first long-time moment μ_{-1} and obtained from the Bloch-Torrey (BT) equation (54). The ESC approximations are shown. The ESC$_1$ approximation was determined for the eigenfunction (ef) and the Ω base.

than the ESC$_0$ curve. This is also reflected by the dependence of spin-echo relaxation rate $1/T_2$ on the diffusion coefficient (Figs. 6 and 7). When defined by the echo time [Eq. (29)] the ESC$_0$ and ESC$_1$ curves run parallel with the curve obtained for restricted diffusion dynamics for short echo times. For longer echo times and decreasing diffusion coefficients the ESC$_1$ curve provides a better approximation. Again as for the free induction decay there is no significant difference between ESC$_1$ approximations in the eigenfunction and that in the Ω base.

V. SUMMARY AND DISCUSSION

Analytical results on transverse spin relaxation due to stochastic phase modulation exist mainly for limiting cases, such as the motional narrowing and the static regime. Perturbation approaches are only valid close to their respective limits, and they diverge as one tries to extend them towards the opposite motion regime. Particularly the intermediate motion regime cannot be described reliably by such a treatment.

We choose a different approach. Our aim was to approximate the dynamics, assumed to be Markovian, by a more simple one that conserves specific features of the original. The starting point was the strong collision approximation [4] that assumes the transition probability between two states being independent from the initial state, an approximation that holds when spin dephasing occurs on a time scale significantly longer than the stochastic phase modulations. Hence, all states perpendicular to the equilibrium state relax with the same exponential factor that is determined self-consistently by comparison with the field fluctuations.

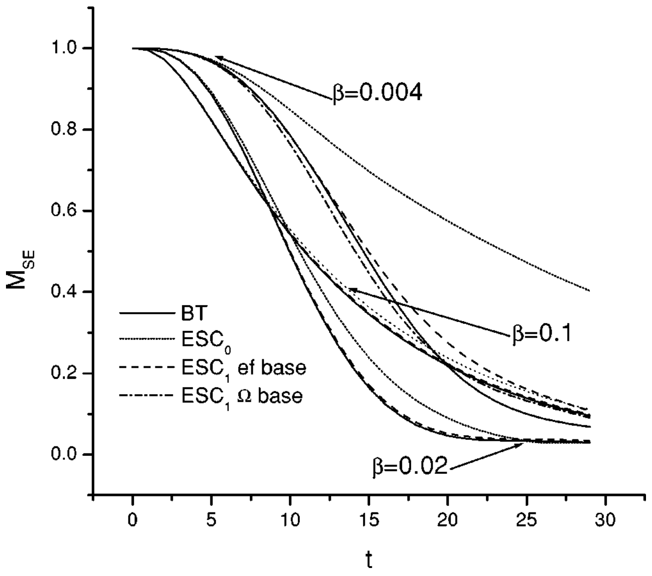

FIG. 5. Spin-echo magnetization decay for restricted diffusion within a linear field gradient in the unit interval as obtained from the Bloch Torrey (BT) equation (54). Three diffusion coefficients β are considered. The ESC approximations in the different diffusion regimes are demonstrated. The ESC$_1$ approximation was obtained for the eigenfunction (ef) and the Ω base.

Note that the motional narrowing limit as well as the static dephasing regime are described correctly by this approximation. Consequently, the error in the intermediate motion regime is already less than it would be by perturbation approaches of a comparable low order. Nevertheless, there is still room for improvement. Also, one would like to have higher order approximations that can be used to check the quality of low order descriptions.

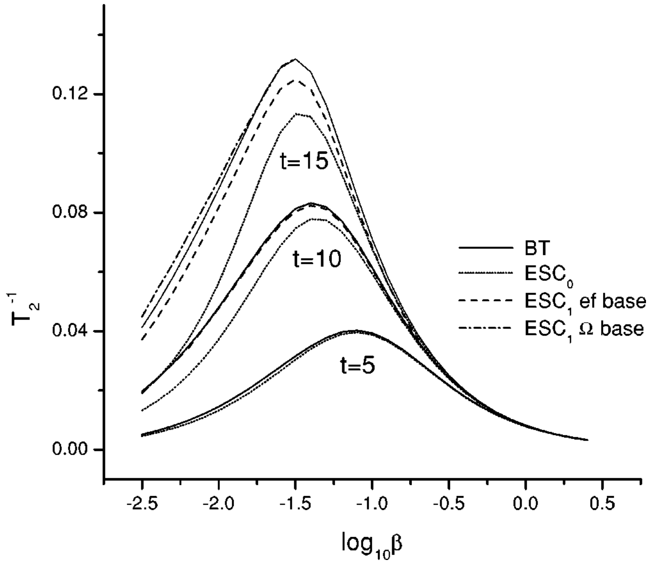

FIG. 6. Spin-echo relaxation time T_2 as a function of the diffusion coefficient β for restricted diffusion in the unit interval and the corresponding ESC approximations. The labeling of the curves is as in Fig. 4. The relaxation time was defined by the echo time t according to Eq. (29).

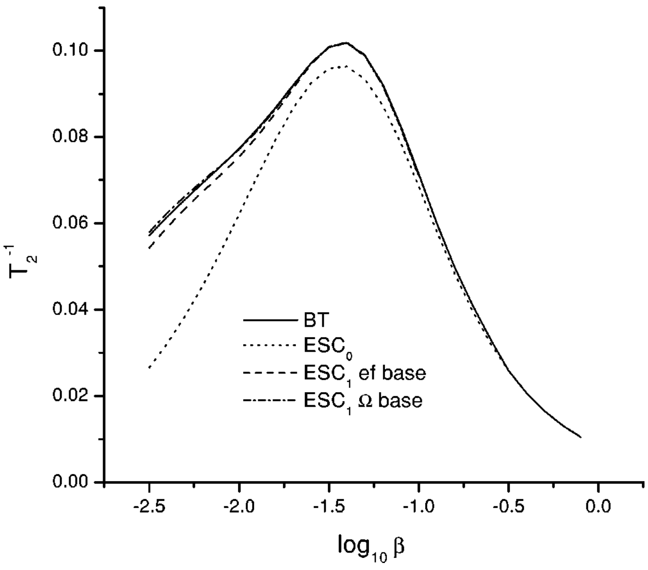

FIG. 7. Spin-echo relaxation time T_2 as a function of the diffusion coefficient β for restricted diffusion in the unit interval and the ESC approximations. Labeling is as in Fig. 4. The relaxation time is defined as the first long-time moment μ_{-1} of the spin-echo decay Eq. (30).

A systematic extension of the strong collision ansatz is to include the relaxation of states of an appropriate finite function base explicitly. We require that correlation times of original and approximate dynamics are identical to a certain order. This self-consistency condition assures that both dynamics have the same motional narrowing expansion of spin dephasing. As it was already in the strong collision ansatz, spin dephasing is asymptotically identical for both dynamics in the limit of the static motion regime.

The finite function base of the ESC$_n$ approximation may be given by the first n ordered eigenfunctions of the generator of the original phase modulations. Obviously, then the ESC generator directly reflects the dynamics of the original generator up to a time scale corresponding to the nth eigenvalue. For practical applications the ESC approach within an eigenfunction space may be a safe way to approximate spin dephasing. However, when the determination of the eigenfunctions is tedious, the application of the Ω base $[|0\rangle,|f_1\rangle \sim \mathbf{\Omega}|0\rangle,|f_2\rangle\sim\mathbf{\Omega}^2|0\rangle, \ldots]$ may be more appropriate, at least for the ESC$_1$ approximation. Within the Ω base the determination of the two- and four-point correlation times (see Appendix D) and the propagator in the static motion regime, Eq. (52), is considerably simplified.

The mechanism by which the ESC$_1$ approach in the Ω base works becomes evident by the following consideration: terms of the motional narrowing expansion Eq. (B1) may be interpreted as repetitive interactions of the spin system with the inhomogeneous field $\mathbf{\Omega}$ and intermediate evolution with the free propagator $\exp(\mathbf{R}t_i)$. In the motional narrowing limit, one obtains from Eq. (B7),

$$1/T_2=\hat{c}_2(0)=\int_0^\infty dt\langle 0|\mathbf{\Omega}\exp(\mathbf{R}t)\mathbf{\Omega}|0\rangle$$

$$=\langle 0|\mathbf{\Omega}^2|0\rangle\int_0^\infty dt\langle f_1|\exp(\mathbf{R}t)|f_1\rangle, \qquad (65)$$

where the factor $\langle 0|\mathbf{\Omega}^2|0\rangle$ is due to the normalization of $|f_1\rangle$, $\langle f_1|f_1\rangle=1$. Equation (65) implies that in the motional narrowing limit, the long-time behavior of spin dephasing solely depends on the free propagator related relaxation of the state $|f_1\rangle$, i.e., this state remains the only relevant one. Hence, it is obvious that in the intermediate motion regime an ESC$_1$ approximation including the state $|f_1\rangle$ in its generator is superior to the ESC$_0$ approximation.

Within the function base the propagator of spin dephasing is directly related to the propagator of spin dephasing in the absence of stochastic phase modulations. This specific feature of the ESC dynamics tremendously facilitates the actual determination of spin dephasing for the following reasons: (i) in many cases the propagator in the static motion regime (which is an average phase factor) may be determined analytically or at least numerically; (ii) the determination of the propagator from that in the static motion regime is self-contained within the base, i.e., it is obtained from a combination of finite dimensional matrices.

The two lowest order ESC approximations were applied to two generic models: spin dephasing in the Anderson-Weiss model, i.e., Gaussian frequency distribution and Gaussian transition dynamics, and dephasing by restricted diffusion in a linear frequency gradient. The reason for this choice was that—besides their generic character—these models allow either an analytical (Anderson-Weiss) or, at least, a simple numerical treatment (linear gradient) of magnetization decay. These features are helpful to prove the ESC approach. For the Anderson-Weiss model we determined the corresponding Markov generator of the phase modulations, which—to our knowledge—was done here for the first time.

For both generic models the subsequent improvement by ESC$_n$ approximations of dephasing parameters and magnetization decays could be demonstrated. One of our next aims will be the application of the ESC approach to more realistic scenarios.

In closing, we would like to emphasize that the ESC approach is actually not limited to spin dephasing only. It can be applied, in principle, in any situation where the time behavior of complicated observables of stochastic processes is of interest. In each case, however, an appropriate function base has to be chosen, corresponding to the Ω base for spin dephasing.

ACKNOWLEDGMENTS

We thank P. Grassberger for a critical reading of the manuscript. This work was supported by the Deutsche Forschungsgesellschaft: Sonderforschungsbereich 355 "Pathophysiologie der Herzinsuffizienz," SFB 237 "Unordnung und grosse Fluktuationen," and Graduiertenkolleg "NMR" HA 1232/8-1.

APPENDIX A: AUTOCORRELATION FUNCTIONS AND QUASICUMULANTS

The general n-point autocorrelation function of stochastically fluctuating fields ω_j is defined as

$$C_n(t_{n-1},\dots,t_1) := \sum_{j_{n-1},\dots,j_0} p\left(\omega_{j_{n-1}},\sum_{i=1}^{n-1} t_i;\dots;\omega_{j_1},t_1;\omega_{j_0},0\right)\prod_{\nu=0}^{n-1}\omega_{j_\nu}, \tag{A1}$$

where $p(\omega_{j_{n-1}},\Sigma_{i=1}^{n-1}t_i;\dots;\omega_{j_1},t_1;\omega_{j_0},0)$ is the probability to find at $t=0$ the frequency ω_{j_0}, at $t=t_1$ the value $\omega_{j_1},\dots,$ and at $t=\Sigma_{i=1}^{n-1}t_i$ the frequency $\omega_{j_{n-1}}$.When the stochastic dynamics is determined by a Markov process, this probability can be factored into transition probabilities between sequential states $i\rightarrow i+1$ after the interval t_{i+1} and the initial $(t=0)$ probability distribution, i.e.,

$$p\left(\omega_{j_{n-1}},\sum_{i=1}^{n-1} t_i;\dots;\omega_{j_0},0\right) = \prod_{i=1}^{n-1} p(\omega_{j_i}\leftarrow\omega_{j_{i-1}},t_{j_i})p(\omega_{j_0},0). \tag{A2}$$

The transition probabilities after the interval t_i are the matrix elements of evolution operator $\exp(\mathbf{R}t_i)$. Since the dynamics is assumed to be stationary the initial probability $p(\omega_{j_0},0)$ is the equilibrium state probability distribution, i.e., we can rewrite Eq. (A1),

$$C_n=\langle 0|\mathbf{\Omega}\exp(\mathbf{R}t_{n-1})\mathbf{\Omega}\cdots\exp(\mathbf{R}t_1)\mathbf{\Omega}|0\rangle, \tag{A3}$$

where $\mathbf{\Omega}=(\omega_j\delta_{j,k})$ is the diagonal frequency matrix. A modification of the correlation functions occurs if one exchanges the evolution operator $\exp(\mathbf{R}t)$ with the operator $\exp(\mathbf{R}t)-\mathbf{\Pi}_0$, where $\mathbf{\Pi}_0=|0\rangle\langle 0|$ is the projection operator onto the equilibrium state space. This modified evolution operator describes the relaxation of observables minus their equilibrium state values. The modified autocorrelation functions will be denoted as quasicumulants and they are then defined as

$$c_n=\langle 0|\mathbf{\Omega}[\exp(\mathbf{R}t_{n-1})-\mathbf{\Pi}_0]\mathbf{\Omega}\cdots[\exp(\mathbf{R}t_1)-\mathbf{\Pi}_0]\mathbf{\Omega}|0\rangle. \tag{A4}$$

The Laplace transform of the correlation function in Eq. (A4) has the form

$$\hat{c}_n(s_{n-1},\dots,s_1)=\langle 0|\mathbf{\Omega}\left[\frac{1}{s_{n-1}-\mathbf{R}}-\frac{1}{s_{n-1}}\mathbf{\Pi}_0\right]\times\mathbf{\Omega}\cdots\left[\frac{1}{s_1-\mathbf{R}}-\frac{1}{s_1}\mathbf{\Pi}_0\right]\mathbf{\Omega}|0\rangle. \tag{A5}$$

This Laplace transform allows the determination of temporal moments of the normalized autocorrelation function $c_n(t_{n-1},\dots,t_1)/c_n(0,\dots,0)$ as the generalized correlation times

$$\tau_n^{n-1}=\hat{c}_n(0,\dots,0)/c_n(0,\dots,0). \tag{A6}$$

APPENDIX B: MOTIONAL NARROWING EXPANSION

The motional narrowing expansion is a perturbation approach to determine the overall magnetization $M(t)$—or its Laplace transform $\hat{M}(s)$—in terms of powers of the fluctuating fields $\mathbf{\Omega}$. It is based on the assumption that the stochastic fluctuations are more rapid than the precession frequencies of the perturbation fields (motional narrowing limit). We will present a general relation between the relaxation of the magnetization and the correlation of the field fluctuations that contains the motional narrowing limit as a limit case. The first step is to expand the Laplace transform of the overall magnetization, Eq. (3), in $\mathbf{\Omega}$, i.e.,

$$\begin{aligned}\hat{M}(s)&=\left\langle 0\left|\frac{1}{s-\mathbf{R}-i\mathbf{\Omega}}\right|0\right\rangle\\&=\langle 0|(s-\mathbf{R})^{-1}+i(s-\mathbf{R})^{-1}\mathbf{\Omega}(s-\mathbf{R})^{-1}\\&\quad+i^2(s-\mathbf{R})^{-1}\mathbf{\Omega}(s-\mathbf{R})^{-1}\mathbf{\Omega}(s-\mathbf{R})^{-1}+\cdots|0\rangle\\&=s^{-1}+s^{-2}i\langle 0|\mathbf{\Omega}|0\rangle+s^{-2}i^2\langle 0|\mathbf{\Omega}(s-\mathbf{R})^{-1}\mathbf{\Omega}\rangle+\cdots\\&=s^{-1}\left(1+s^{-1}\sum_{\nu=1}^{\infty}i^{\nu}\hat{C}_{\nu}(\underbrace{s,s,\dots,s}_{(\nu-1)\times})\right),\end{aligned} \tag{B1}$$

where $\hat{C}_\nu$ are the Laplace transformed *n*-point correlation functions of Eq. (A3). To avoid singularities at $s=0$ it is better to consider $\hat{M}^{-1}(s)$. When we set $q=s^{-1}\Sigma_{\nu=1}^{\infty}i^{\nu}\hat{C}_{\nu}(\underbrace{s,s,\dots,s}_{(\nu-1)\times})$, one obtains

$$\begin{aligned}\hat{M}^{-1}(s)&=s\left(1+\sum_{\rho=1}^{\infty}(-1)^{\rho}q^{\rho}\right)\\&=s-\sum_{\nu=1}^{\infty}i^{\nu}\hat{C}_{\nu}+s^{-1}\sum_{\nu_1,\nu_2=1}^{\infty}i^{\nu_1+\nu_2}\hat{C}_{\nu_1}\hat{C}_{\nu_2}\\&\quad+\cdots+(-1)^{\rho}s^{-(\rho-1)}\sum_{\nu_1,\dots,\nu_\rho=1}^{\infty}i^{\nu_1+\nu_\rho}\\&\quad\times\prod_{m=1}^{\rho}\hat{C}_{\nu_m}+\cdots.\end{aligned} \tag{B2}$$

Rearrangement of terms of equal order in $\mathbf{\Omega}$ provides

$$\hat{M}^{-1}(s)=s-\sum_{j=1}^{\infty}i^{j}K_j, \tag{B3}$$

where the coefficients K_j have the form

$$\begin{aligned}K_j&=\hat{C}_j-s^{-1}\sum_{\nu_1+\nu_2=j}\hat{C}_{\nu_1}\hat{C}_{\nu_2}+\cdots+(-s)^{1-\rho}\\&\quad\times\sum_{\nu_1+\cdots+\nu_\rho=j}\prod_{m=1}^{\rho}\hat{C}_{\nu_m}+\cdots+(-s)^{1-j}\hat{C}_1^{j}.\end{aligned} \tag{B4}$$

A comparison of this sum with the modified correlation functions c_j, Eqs. (A4) and (A5), shows that

$$K_j=\hat{c}_j(\underbrace{s,\ldots,s}_{(j-1)\times}), \tag{B5}$$

i.e., one obtains

$$\hat{M}^{-1}(s)=s-\sum_{j=1}^{\infty} i^j\hat{c}_j(\underbrace{s,s,\ldots,s}_{(j-1)\times}). \tag{B6}$$

Equation (B6) expands the relaxation of the magnetization in terms of correlation functions to an arbitrary order. The long-time behavior of $M(t)$ is determined by the Laplace transform in the limit of small s, i.e., in this range the relation

$$\hat{M}^{-1}(0)=-\sum_{j=1}^{\infty} i^j\hat{c}_j(0,0,\ldots,0) \tag{B7}$$

is valid; see also Eq. (A6). The series in Eq. (B7) contains terms of magnitude $\leqslant\langle 0|\mathbf{\Omega}^{\nu}|0\rangle/l^{\nu}$, where l denotes nonvanishing eigenvalues of $\mathbf{R}$. The latter determine the fluctuation frequency. In the motional narrowing limit these fluctuations are much higher than the precessing frequencies $\langle 0|\mathbf{\Omega}^{\nu}|0\rangle/l^{\nu}\ll 1$, i.e., after normalization of the average perturbation field $\langle 0|\mathbf{\Omega}|0\rangle$ to zero, i.e., $c_1=0$, $M(t)$ is given a single exponential decay with the well known result for the transverse relaxation rate as $1/T_2=\hat{c}_2(0)=\tau_2\langle 0|\mathbf{\Omega}^2|0\rangle$.

APPENDIX C: QUASICUMULANTS IN THE STRONG COLLISION APPROXIMATION

In the strong collision (ESC$_0$) approximation the quasicumulants take a very simple form. Insertion of the generator $\mathbf{D}=-\lambda(\mathbf{id}-\mathbf{\Pi}_0)$ into Eq. (A5) results in

$$\hat{c}_n^{(\mathrm{ESC}_0)}(s_{n-1},\ldots,s_1)=\prod_{i=1}^{n-1}\frac{1}{s_i+\lambda}c_{n-1}(0,\ldots,0), \tag{C1}$$

i.e., the quasicumulant is a product of single exponential functions $e^{-\lambda t_i}$ and the generalized correlation times, Eq. (A6), are all identical, namely,

$$\tau_n^{(SC)}=\lambda^{-1}\ . \tag{C2}$$

APPENDIX D: QUASICUMULANTS IN THE EXTENDED STRONG COLLISION APPROXIMATION

We restrict ourselves here to the ESC$_1$ approximation and determine the correlation functions and generalized relaxation times for the Ω-polynomial base only in order to show the principle. Extensions to higher order approximations and to other function bases are straightforward, although they may be more tedious to calculate.

For ESC$_1$ the generator of the stochastic field fluctuations has the form $\mathbf{D}=-\lambda_1\mathbf{\Pi}_1-\lambda(\mathbf{id}-\mathbf{\Pi}_0-\mathbf{\Pi}_1)$. We will determine only the Laplace transforms of the two- and four-point correlation functions, since the three-point correlation functions vanishes in the models we consider. According to Eq. (A5) the determination of the correlation functions requires the operator

$$\frac{1}{s-\mathbf{D}}-\frac{1}{s}\mathbf{\Pi}_0=\frac{1}{s+\lambda_1}\mathbf{\Pi}_1+\frac{1}{s+\lambda}(\mathbf{id}-\mathbf{\Pi}_0-\mathbf{\Pi}_1). \tag{D1}$$

Assuming that the average frequency vanishes, i.e., $\langle\mathbf{\Omega}\rangle=\langle 0|\mathbf{\Omega}|0\rangle=0$, which can always be achieved by normalization, $|f_1\rangle\sim\mathbf{\Omega}|0\rangle$. Hence, the projector $\mathbf{\Pi}_1=|f_1\rangle\langle f_1|$ takes the form

$$\mathbf{\Pi}_1=\frac{\mathbf{\Omega}|0\rangle\langle 0|\mathbf{\Omega}}{\langle 0|\mathbf{\Omega}^2|0\rangle}\ . \tag{D2}$$

For the Laplace transformed two-point correlation function one obtains then

$$\hat{c}_2^{(\mathrm{ESC}_1)}(s)=(\lambda_1+s)^{-1}\langle 0|\mathbf{\Omega}^2|0\rangle, \tag{D3}$$

i.e., the two-point correlation function exhibits a single exponential decay with relaxation rate

$$\tau_2^{(\mathrm{ESC}_1)}=\lambda_1^{-1}. \tag{D4}$$

The four-point correlation function is

$$\begin{aligned}\hat{c}_4^{(\mathrm{ESC}_1)}(s_3,s_2,s_1)=&\frac{1}{(s_3+\lambda_1)(s_1+\lambda_1)}\\&\times\left(\frac{1}{s_2+\lambda_1}-\frac{1}{s_2+\lambda}\right)\frac{\langle 0|\mathbf{\Omega}^3|0\rangle^2}{\langle 0|\mathbf{\Omega}^2|0\rangle}\\&+\frac{1}{(s_3+\lambda_1)(s_2+\lambda)(s_1+\lambda_1)}\\&\times(\langle 0|\mathbf{\Omega}^4|0\rangle-\langle 0|\mathbf{\Omega}^2|0\rangle^2).\end{aligned} \tag{D5}$$

The four-point correlation time is then determined as

$$\begin{aligned}\tau_4^{(\mathrm{ESC}_1)}=&[\hat{c}_4^{(\mathrm{ESC}_1)}(0)/c_4^{(\mathrm{ESC}_1)}(0)]^{1/3}\\=&\left[\frac{1}{\lambda_1^2}\left(\frac{1}{\lambda_1}-\frac{1}{\lambda}\right)\frac{\langle 0|\mathbf{\Omega}^3|0\rangle^2}{\langle 0|\mathbf{\Omega}^2|0\rangle(\langle 0|\mathbf{\Omega}^4|0\rangle-\langle 0|\mathbf{\Omega}^2|0\rangle^2)}\right.\\&\left.+\frac{1}{\lambda_1^2\lambda}\right]^{1/3}.\end{aligned} \tag{D6}$$

In the case of the Anderson-Weiss model and for the restricted diffusion linear gradient, one has $\langle 0|\mathbf{\Omega}^3|0\rangle=0$, i.e., Eq. (D6) simplifies to

$$\tau_4^{(\mathrm{ESC}_1)}=\sqrt[3]{\frac{1}{\lambda_1^2\lambda}}\ . \tag{D7}$$

APPENDIX E: RELAXATION TIMES OF CORRELATION FUNCTIONS IN THE MODELS

In this final appendix we will determine the generalized relaxation times of stochastic field fluctuations up to the fourth order for the generic models we discuss in the main text.

1. Diffusion in a harmonic potential

When field fluctuations result from diffusion in a harmonic potential according to Eq. (40) and spin dephasing is described by Eq. (42), the corresponding Laplace transformed two-point correlation function, Eq. (A5), is

$$\begin{aligned}\hat{c}_2(s)&=\left\langle 0\left|\omega\frac{1}{s-\beta\partial_\omega(\partial_\omega+\omega)}\omega\right|0\right\rangle\\&=\left\langle 1\left|\frac{1}{s-\beta\partial_\omega(\partial_\omega+\omega)}\right|1\right\rangle\\&=\frac{1}{s+\beta},\end{aligned}\tag{E1}$$

where we applied the operator properties of $\partial_\omega,(\partial\omega+\omega)$ according to Eqs. (45). This result shows that the two-point correlation function exhibits a single exponential decay. Since $c_2(0)=\langle 0|\omega^2|0\rangle=1$, one obtains

$$\tau_2=\beta^{-1}\ .\tag{E2}$$

Since $c_3(t)$ vanishes, the next relevant correlation function is $c_4(t)$. Similarly, one obtains for its Laplace transform

$$\hat{c}_4(s_3,s_2,s_1)=\frac{2}{(s_3+\beta)(s_2+2\beta)(s_1+\beta)}\ .\tag{E3}$$

And since $c_4(0)=\langle 0|\omega^4|0\rangle=2$ the corresponding correlation time is

$$\tau_4=\sqrt[3]{\frac{1}{2}}\beta^{-1}\ .\tag{E4}$$

2. Restricted diffusion in a linear gradient field

In this section we will determine the correlation times τ_n of Eq. (A6) for $n=2,4$ for the one-dimensional restricted diffusion of spins in a unit box in which they are affected by a linear gradient field. In dimensionless parameters one obtains for the generator $\mathbf{R}=\beta[\partial_x^2]$, where β is the dimensionless diffusion coefficient. The brackets denote that the application of the operator ∂_x^2 is restricted to functions with a vanishing derivative at $x=\pm 1/2$ (reflecting boundary conditions). The frequency operator is $\mathbf{\Omega}=x$ and the equilibrium state eigenfunction is $|0\rangle\equiv 1$.

The determination of correlation times τ_n requires the calculation of the Laplace transformed quasicumulants $\hat{c}_n(0,\ldots,0)$, Eq. (A6). The definition of these quasicumulants according to Eq. (A5) shows the need of recurrent determination of terms of the form

$$f=\lim_{s\to 0}[-(s-\mathbf{R})^{-1}+s^{-1}\mathbf{\Pi}_0]g,\tag{E5}$$

with some function g, i.e., f fulfills

$$\mathbf{R}f=(1-\mathbf{\Pi}_0)g,\tag{E6}$$

i.e., with $\mathbf{R}=\beta[\partial_x^2]$ Eq. (E6) becomes a second order differential equation. The application of the inverse second order differential operator leaves, in general two integration constants. One may be determined from the reflective symmetric boundary conditions; however, a further condition is needed to get the second constant. A spectral decomposition $\mathbf{R}$ in Eq. (E5) shows $\Pi_0 f\equiv 0$, i.e., we obtain as a further condition

$$\int_{-1/2}^{1/2}dx\, f(x)=0.\tag{E7}$$

Two-point correlation time. We define

$$f_1(x)=\lim_{s\to 0}[-(s-\mathbf{R})^{-1}+s^{-1}\mathbf{\Pi}_0]x|0\rangle=\beta^{-1}(x^3/6-x/8),\tag{E8}$$

which obviously fulfills the reflecting boundary condition at $x=\pm 1/2$ and Eq. (E7). Hence, the two-point Laplace transformed quasicumulant is

$$\begin{aligned}\hat{c}_2(0)&=-\langle 0|x\lim_{s\to 0}[-(s-\mathbf{R})^{-1}+s^{-1}\mathbf{\Pi}_0]x|0\rangle\\&=\int_{-1/2}^{1/2}dx\, x\, f_1(x)=\beta^{-1}\frac{1}{120}\ ,\end{aligned}\tag{E9}$$

and with

$$c_2(0)=\langle 0|x^2|0\rangle=\int_{-1/2}^{1/2}dx\, x^2=1/12,\tag{E10}$$

one obtains

$$\tau_2=\frac{1}{10}\beta^{-1}\ .\tag{E11}$$

Four-point correlation time. Iterative application of Eq. (E5) defines

$$f_2(x)=\lim_{s\to 0}[-(s-\mathbf{R})^{-1}+s^{-1}\mathbf{\Pi}_0]xf_1(x),\tag{E12}$$

which, according to Eq. (E6), fulfills

$$\begin{aligned}\beta[\partial_x^2] f_2(x) &= (1-\mathbf{\Pi}_0) x f_1(x)\\ &= x f_1(x) - \int_{-1/2}^{1/2} dx\, x f_1(x)\\ &= x f_1(x) + \frac{1}{120}\beta^{-1}\ . \end{aligned} \tag{E13}$$

Insertion of f_1, Eq. (E8), and considering the reflective boundary conditions and the condition (E7) yields

$$f_2(x) = \beta^{-2}\left(\frac{x^6}{180} - \frac{x^4}{96} + \frac{x^2}{240} - \frac{37}{161280}\right). \tag{E14}$$

Similarly to the procedure above we could determine a function $f_3(x)$, but instead we use a different approach which exploits the symmetry of eigenfunctions of the operator $\mathbf{R} = \beta[\partial_x^2]$. The Laplace transformed four-point quasicumulant is

$$\begin{aligned}\hat{c}_4(0,0,0) &= -\left\langle 0 \left| \overbrace{x \lim_{s_3\to 0}\left[-\frac{1}{s_3-\mathbf{R}} + \frac{1}{s_3}\mathbf{\Pi}_0\right] x}^{=f_1(x)} \right.\right.\\ &\quad \times \lim_{s_2\to 0}\left[-\frac{1}{s_2-\mathbf{R}} + \frac{1}{s_2}\mathbf{\Pi}_0\right] x\\ &\quad \left.\left. \times \lim_{s_1\to 0}\left[-\frac{1}{s_1-\mathbf{R}} + \frac{1}{s_1}\mathbf{\Pi}_0\right] x \right| 0 \right\rangle\\ &= -\int_{-1/2}^{1/2} dx\, f_1(x) x f_2(x)\\ &= \beta^{-3}\frac{89}{79\,833\,600}, \end{aligned} \tag{E15}$$

and with

$$c_4(0,0,0) = \langle 0|x^4|0\rangle - \langle 0|x^2|0\rangle^2 = \frac{1}{180}, \tag{E16}$$

we finally have

$$\tau_4 = \sqrt[3]{\frac{89}{443\,520}}\,\beta^{-1}. \tag{E17}$$

---

[1] A. Abragham, *The Principles of Nuclear Magnetism* (Oxford University Press, New York, 1961).

[2] D. A. Yablonski and E. M. Haake, Magn. Reson. Med. **32**, 749 (1994).

[3] V. G. Kiselev and S. Posse, Phys. Rev. Lett. **81**, 5696 (1998).

[4] W. R. Bauer *et al.*, Phys. Rev. Lett. **83**, 4215 (1999).

[5] R. P. Kennan, J. Zhong, and J. C. Gore, Magn. Reson. Med. **31**, 9 (1994).

[6] C. M. Wacker *et al.*, Magn. Reson. Med. **41**, 686 (1999).

[7] C. M. Wacker *et al.*, MAGMA **8**, 48 (1999).

[8] P. W. Anderson and P. R. Weiss, Rev. Mod. Phys. **25**, 269 (1953).

[9] H. C. Torrey, Phys. Rev. **104**, 563 (1956).

[10] W. Nadler and K. Schulten, J. Chem. Phys. **82**, 151 (1985).

[11] C. W. Gardiner, *Handbook of Stochastic Methods* (Springer, Berlin, 1983).

[12] A. Duh, A. Mohorič, and J. Stepišnik, in *Proceedings of the 15th European Experimental NMR Conference* (University of Leipzig, Leipzig, 2000), p. 1.

Magnetic Resonance in Medicine 41:686–695 (1999)

Changes in Myocardial Oxygenation and Perfusion Under Pharmacological Stress With Dipyridamole: Assessment Using T_2^* and T_1 Measurements

Christian M. Wacker,[1,2] Michael Bock,[3] Andreas W. Hartlep,[1,2] Gabriele Beck,[1]
Gerhard van Kaick,[1] Georg Ertl,[2] Wolfgang R. Bauer,[2] and Lothar R. Schad[1]*

The aim of this pilot-study was to evaluate changes in myocardial oxygenation and perfusion under pharmacological stress with dipyridamole (DIP) by means of MRI. Twenty healthy volunteers were examined using a multi-echo gradient-echo sequence. The differential myocardial signal response due to the blood oxygen level dependent (BOLD) effect was studied under variable conditions of myocardial oxygen supply caused by the vasodilator DIP. Unlike contrast agents (CA) methods, which require at least two injections of CA and DIP, the presented methods require only a single infusion of DIP. To assess changes in myocardial perfusion, a saturation recovery TurboFLASH (SRTFL) sequence with centric reordering for T_1 measurements was used with global and slice-selective spin-preparation (five volunteers). The signal response was measured at baseline conditions and when myocardial blood flow was increased during pharmacological stress with DIP. Administration of DIP induced a 17 ± 9% increase in T_2^*. Enhanced perfusion resulted in a 15 ± 5% decrease of T_1 after slice-selective spin preparation and a calculated increase in absolute perfusion of about 5.1 ml/(g × min), which reflects coronary reserve.

The study shows that DIP-induced alterations in the relationship between myocardial oxygen supply and demand are detectable in healthy volunteers using T_2^* and T_1 measurements. A combination of T_2^* and T_1 examinations could become a useful diagnostic tool for the non-invasive assessment of myocardial oxygenation and perfusion in patients with coronary artery disease (CAD). Magn Reson Med 41:686–695, 1999. © 1999 Wiley-Liss, Inc.

Key words: magnetic resonance imaging; myocardial perfusion; myocardial oxygenation; blood oxygen level dependent (BOLD); heart physiology; dipyridamole pharmacology; stress test

Diagnosis and treatment of coronary artery disease (CAD) require information on myocardial oxygenation and perfusion. Methods currently used for the measurements of myocardial perfusion in clinical routine are either invasive or not quantitative or both. Recently, fast and ultrafast MRI has been applied to assess coronary circulation and myocardial perfusion. The two major approaches for myocardial perfusion imaging use exogenous or endogenous contrast agents (CA). Several studies during the last decade report on the application of exogenous CA and first pass dynamics for this purpose (1–7).

Tissue oxygenation and perfusion can be studied without the use of MR CA by changes in the apparent transverse relaxation time T_2^* in correlation with the oxygenation state of hemoglobin [BOLD effect (8,9)] and changes of the apparent T_1, which depend on the tissue perfusion.

Experiments which quantify tissue perfusion without CA, utilize water as an endogenous CA or explore the paramagnetic effect of deoxyhemoglobin to detect tissue oxygenation from T_2^*-sensitive MRI techniques. The BOLD contrast is particular useful for myocardial imaging, since tissue blood volume and flow as well as oxygen consumption result in T_2 and T_2^* modulations owing to local alterations of the deoxyhemoglobin concentration. The transition of diamagnetic oxyhemoglobin to paramagnetic deoxyhemoglobin produces changes of local magnetic fields resulting in signal loss in T_2^*-weighted images. This BOLD effect has recently been applied to humans to assess myocardial blood oxygenation. Li et al. described an increase of T_2^* by 46 ± 22% after coronary vasodilatation following administration of dipyridamole (DIP) using a segmented, interleaved, double-gradient pulse sequence (10).

Arterial spin labeling is a simple, noninvasive technique that avoids the use of CA, but at the expense of a low signal-to-noise ratio. Williams and Koretsky estimated myocardial perfusion in the isolated rat heart (11). Bauer et al. proposed slice selective spin inversion in the isolated cardioplegic rat heart to measure T_1 with the advantage of applying this method to the in situ heart (12). They demonstrated that variations of perfusion directly reflect changes of the apparent spin-lattice relaxation time T_1. To separate inflow-related and stationary T_1 effects, they performed T_1 measurements with global and slice-selective spin preparation. The same group recently applied this method to rat myocardium in vivo (13). However, this technique has not yet been applied to humans so far.

In this work, we first used a multi-gradient echo pulse sequence to assess T_2^*. Then a saturation recovery technique was applied to evaluate the apparent T_1 under global and slice-selective spin preparation. Measurements were performed before, during, and after pharmacological stress induced by DIP to observe changes in myocardial oxygenation and perfusion.

DIP, adenosine and dobutamine are the major agents used for pharmacologic stress testing. Clinical trials show

---

[1]Research program "Radiological Diagnostics and Therapy," Deutsches Krebsforschungszentrum (DKFZ), Heidelberg, Germany. [2]II. Med. Univ. Klinik Mannheim/Heidelberg, Mannheim, Germany. [3]Tumorzentrum Heidelberg/Mannheim, Heidelberg, Germany.

Parts of this work were presented at the Sixth Scientific Meeting of the International Society for Magnetic Resonance in Medicine (Sydney 1998) and at the Annual Meeting of the German Society of Cardiology (Mannheim 1998).

Grant sponsor: Deutsche Gesellschaft für Kardiologie; Grant sponsor: Forschungsfonds der Universitätsklinik Mannheim/Heidelberg; Grant number: 42.

*Correspondence to: Prof. Dr. Lothar Schad, Research program "Radiological Diagnostics and Therapy," Deutsches Krebsforschungszentrum (DKFZ) Heidelberg, Im Neuenheimer Feld 280, 69120 Heidelberg, Germany.
E-mail: l.schad@dkfz-heidelberg.de

Received 3 February 1998; revised 18 September 1998; accepted 29 October 1998.

© 1999 Wiley-Liss, Inc.

that all three drugs can be used safely and effectively in patients with symptoms of CAD. DIP and adenosine mediate coronary artery vasodilatation. DIP, the only agent with approved labeling for use in stress testing, inhibits adenosine indirectly, in contrast to adenosine, a direct agonist with a rapid onset and short duration of action. DIP acts through the accumulation of adenosine, which reduces sympathetic tone in vasomotor nuclei of the brain stem and inhibits norepinephrine release in noradrenergic neurons but activates arterial chemoreceptors. Therefore DIP produces enhanced coronary vasodilatation without increasing heart work in contrast to dobutamine, which increases cardiac output and heart rate as well as promoting coronary artery vasodilatation (14). The side effect profile of DIP is relatively benign and the agent's extremely short half-life makes most adverse reactions like headache and dizziness clinically insignificant.

MATERIALS AND METHODS

Pulse sequences were implemented on a 1.5 T whole body scanner (SIEMENS Vision, Erlangen, Germany) with gradient overdrive using the integrated body coil for radiofrequency (rf) excitation and a four-element phased-array coil for signal reception. Fast, non-ECG-triggered scout images (FLASH) were used to position the double-oblique short-axis plane of the heart between the valve system and papillary muscle. ECG-gated T_1 and T_2^* amplitude images were obtained within a single breathhold in the diastole, when the ventricle's cross section is at its maximum. To verify that all T_1 images were acquired at the same time during diastole, all images were displayed in a fast cine-loop. Images showing an obvious movement of the heart were rejected. For slice-selective T_1 measurements the imaging plane was positioned within the saturation volume (Fig. 1).

T_2^* Measurements

For T_2^* measurements a segmented gradient echo pulse sequence was used, which acquired 10 successive gradient echoes per rf excitation. The echo times TE of the 10 images ranged from 6 to 54 msec at an echo separation $\Delta TE = 5.4$ msec. First-order motion compensation was included in slice-selection direction. During each cardiac cycle, five phase-encoding lines were acquired with incremented flip angles between 20° and 90° to maintain a constant myocardial signal (15). Data were acquired during mid-diastole in a sampling window of 300 msec. An inplane resolution of 1.61×1.17 mm^2 at a slice thickness $SL = 6$ mm was achieved at a matrix size of 140×256 and a field of view (FOV) of 225×300 mm^2. The acquisition time for a single scan was $140/5 \times 0.8 \approx 22$ sec assuming an average RR-interval of 800 msec. A non-selective 180° hyperbolic secans rf-pulse inverted the magnetization at the beginning of the heart cycle to suppress the ventricular signal from flowing blood. Slice-selective re-inversion directly followed, which resulted in an approximate nulling of the longitudinal magnetization of inflowing blood during data acquisition (black blood).

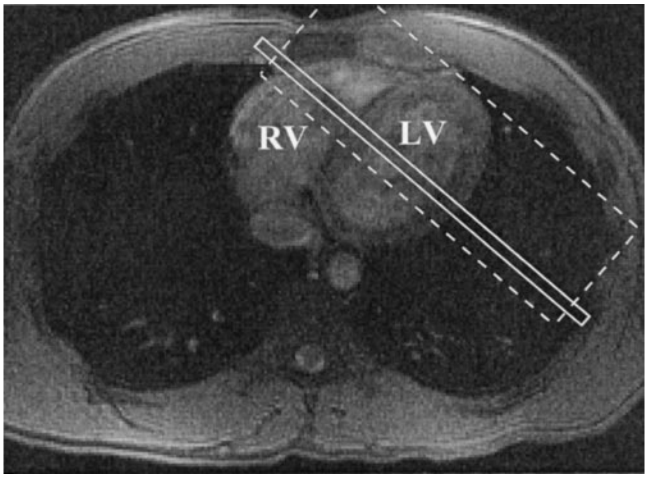

FIG. 1. Position of the measurement slice (solid box) and the saturation volume (dashed line) used in slice-selective T_1 measurements. LV, left ventricle; RV, right ventricle.

T_1 Measurements

A saturation-recovery TurboFLASH pulse sequence (SRTFL) was used to determine the apparent T_1 of myocardium after global and slice-selective spin preparation, as proposed recently (16,17). Nine images at nine different saturation recovery times TS = 100, 200, 300, 400, 600, 800, 1000, 1200 and 1400 msec were acquired. An ECG-trigger delay TD was adjusted for each TS to acquire data at the same phase of the cardiac cycle (mid-diastole), i.e., $TD + TS = 400$ msec $+ 72 \times RR$-interval with $n = 0$ or 1 (Fig. 2). A composite saturation pulse consisting of five 90°-pulses separated by spoiler gradients eliminated the longitudinal magnetization after the trigger delay TD. The saturation slab compromised the readout slice for slice-selective experiments, while non-selective 90°-pulses were used for global spin preparation. After the saturation recovery time TS, data were acquired using a fast FLASH readout scheme with partial centric reordering to maintain the T_1 contrast for the central Fourier lines. The first 39 of 80 phase-encoding lines were centric reordered, while the remaining 41 lines sampled one side of k-space linearly to provide sufficient spatial resolution. The other imaging parameters were: ($TR/TE/\alpha$/FOV/matrix/SL) = (2.5 msec/1.1 msec/8°/225 $\times$ 300 mm^2/80 $\times$ 128/10 mm). The calculated in-plane resolution was 2.81×2.34 mm^2. The results of T_1 measurements in phantoms using the SRTFL sequence were validated against an established TurboFLASH T_1-measurement technique (18) and showed no systematic deviations.

Volunteers and Protocols

Twenty volunteers (20 to 59 years of age, mean 31 ± 10, five female) without history of cardiovascular disease were studied. Sixteen volunteers underwent 22 T_2^* examinations, five volunteers were measured with the SRTFL sequence. One volunteer underwent T_2^* and T_1 measurements within one exam. Volunteers were informed about possible side effects of the drug such as headaches, nausea and general feelings of warmth. In all volunteers, MR examinations were performed after informed consent had been obtained. The volunteers avoided the consumption of tea and coffee as well as medication containing aminophyl-

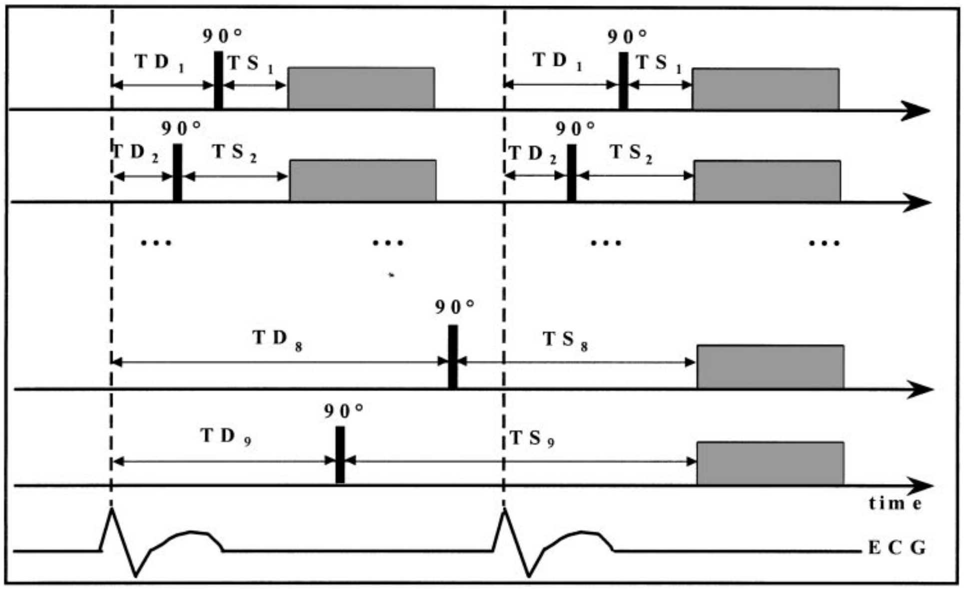

FIG. 2. Schematic diagram of the SRTFL pulse sequence: after a 90° (selective or global) spin preparation nine images are obtained using nine different saturation recovery times *TS*. Trigger delay *TD* was chosen to ensure data acquisition at the same time in diastole. One image was acquired per heartbeat for $TD + TS < RR$-interval. If $TD + TS > RR$-interval spin preparation was in the first and signal reception was in the second heartbeat.

line and cardiovascular activants at least 12 hr before the DIP test protocol. Heart rate was continuously monitored and blood pressure was measured before and after the examinations. Images were acquired repeatedly at rest and under DIP-induced stress (Persantin, Dr. Karl Thomae GmbH, Germany; rate: 0.56 mg/kg, infused over 4 min via an antecubital vein). If the heart rate did not increase within 4 min, a high-dose regime was used with additional 0.28 mg/kg over 2 min. Infusion was controlled by an infusion system (CAI 626P, DOLTRON AG, Switzerland), which allowed precise adjustment of infusion rate and duration to the volunteer's weight. All scans were acquired in an end-expiratory breathhold to eliminate respiratory motion artifacts. To verify that all images were acquired at the same time during diastole, all images were displayed in a fast cine-loop. T_2* and SRTFL-T_1 measurements were repeated at least 20 to 30 times to obtain both values under baseline conditions and during maximum drug effect. The whole procedure was finished when the heart rate returned to baseline values (or +10%, in most cases about 20–25 min after DIP infusion). T_1 examinations after global and slice-selective preparation were performed alternating for about 45 min in one volunteer. If possible with the chosen FOV, T_2^* and T_1 values of skeletal muscle tissue (volunteers back) were also assessed in the same slices as for myocardium.

Data Evaluation

For data evaluation, the individual MR images were transferred to an offline-workstation and processed using our own software package. The region of interest (ROI) was the complete myocardium in short-axis view. In order to obtain representative results, ROIs were segmented manually three to five times and compared by the same observer. ROIs were selected in the first amplitude image and then copied to the other images. Final T_2^* and T_1 values represent the average of these three to five evaluations. T_2^* and T_1 were determined by averaging the single-pixel T_2^* and T_1 values for the whole area of the short-axis view. To avoid fit errors from regions of low signal, an individually selected intensity threshold (typically two to three times the mean noise amplitude) was defined in the first image, which was used to mask individual pixels. From the 10 images of the T_2^* echo series a T_2^*-map was calculated by applying a linear fit to the natural logarithm of the signal intensities.

T_1 was obtained by the fit of the theoretical relaxation curve

$$S(TS, S_0, \beta, T_1) = S_0 \times (1 - [1 - \cos\beta] \times e^{-TS/T_1}) \quad [1]$$

to the image series using a nonlinear Marquard-Levenberg algorithm (19). Here, S_0 represents the signal amplitude without spin preparation ($TS \to \infty$), and β is the effective flip angle of the preparation pulse.

Assessment of Relative Perfusion Changes and Absolute Perfusion

The relative variations of perfusion ΔP were estimated from the T_1 values under slice selective spin preparation (T_{1s}) (12,13) using the relation

$$\Delta P = \Delta\left(\frac{1}{T_{1S}}\right) \times \lambda, \quad [2]$$

where the partition coefficient λ is the quotient of the relative water content of tissue and perfusate, which is nearly one. Assuming a two-compartment model for tissue and fast water exchange between intracapillary space and extravascular tissue, the perfusion *P* can be calculated from two T_1 maps [one with a slice-selective saturation pulse (T_{1s}) and one with global saturation (T_{1g})]. Absolute perfusion *P* [ml/(*g* × min)] (12,13) can be obtained according to

$$P = \frac{1}{T_{1blood}} \times \left(\frac{T_{1g}}{T_{1S}} - 1\right) \times \lambda, \quad [3]$$

where $T_{1\text{blood}}$ is measured in heart chambers in nonselective T_1 maps.

Statistical Analysis

Two data sets of measured T_2^* or T_1 values were analyzed to show whether the infusion of DIP produces a real and significant difference in T_2^* or T_1 (Fig. 8b). The first data set (*d1*) includes T_2^* or T_1 values obtained before the heart rate increased. A second data set (*d2*) includes T_2^* or T_1 values acquired during increased heart rate until the baseline heart rate was reestablished (or baseline values plus 10%, if initial heart rate was not reestablished at the end of exam). The significance P of the difference of means was calculated by Student's t test. Values were given as mean ± standard deviation (SD) of the mean.

RESULTS

T_2^* Measurements

Figure 3 shows representative T_2^*-weighted amplitude images in a short-axis view of a healthy volunteer. The myocardium is distinguished from the blood-filled heart chambers. However, in most cases susceptibility artifacts occurred in phrenicomediastinal recess which superimposed posterolateral and lateral sections of myocardium (Fig. 3, last echoes). Figure 4 shows T_2^* maps of the manually segmented left ventricular myocardium before (Fig. 4a) and after (Fig. 4b) infusion of DIP with corresponding relaxation curves of T_2^* (Fig. 4c,d). Mean T_2^* values in the myocardium of four volunteers are plotted as a function of time after DIP infusion (Fig. 5a–d). The different shapes reflect the variability of T_2^* as a function of time after infusion of DIP. Measurements were performed in 1-min repetitions over a period of approximately 25 min. T_2^* increased by 17 ± 10% (from 35 ± 3 to 42 ± 5 msec) when regarding the mean of maximum responses of all volunteers. Mean increase in T_2^* during the interval of increased heart rate (data set *d2*) was 10 ± 5% (from 35 ± 3 to 39 ± 4 msec, $P = 0.05$, all volunteers). A significance of 0.01 was achieved when disregarding the data of one volunteer who showed no effect after DIP administration. SD of T_2^* fit was below 3%. T_2^* increased 4 ± 2 min after the onset of DIP-infusion (Table 1). The mean duration of the observed DIP-effect was 9 ± 6 min when regarding the time period of increased heart rate. Heart rate increased from 63 ± 9 to 85 ± 11 bpm, i.e. total breathhold time for T_2^* measurements was 20–27 sec (140/5 × RR-interval).

The feasibility of T_2^* assessment in skeletal muscle of volunteer's back was depending on the chosen FOV. Changes of T_2^* in skeletal muscle ($n = 11$) were $<3\%$ ($P = 0.52$) with absolute values: $T_2^* = 31 \pm 2$ msec.

T_1 Measurements

Figure 6 shows SRTFL-amplitude images after global (Fig. 6a) spin preparation with the corresponding T_1 maps (Fig. 6b). Apparent T_1 as a function of time after slice-selective saturation is given in Figure 7. In this case, the DIP-induced T_1 reduction of 19% started 5 min after beginning of DIP-infusion and persisted for 11 min. Figure 8a shows the data of a volunteer who underwent T_2^* and T_1 measurements within a single examination. Here, T_2^* increase started 2 min after onset of DIP-infusion and the total increase was about 17% (35 to 41 msec). T_1 decreased by about 8% and heart rate increased from 60 to 76 bpm. Absolute values of apparent T_1 were evaluated (Table 2) yielding a 17 ± 4% lower value in myocardium before DIP injection when comparing global to slice-selective satura-

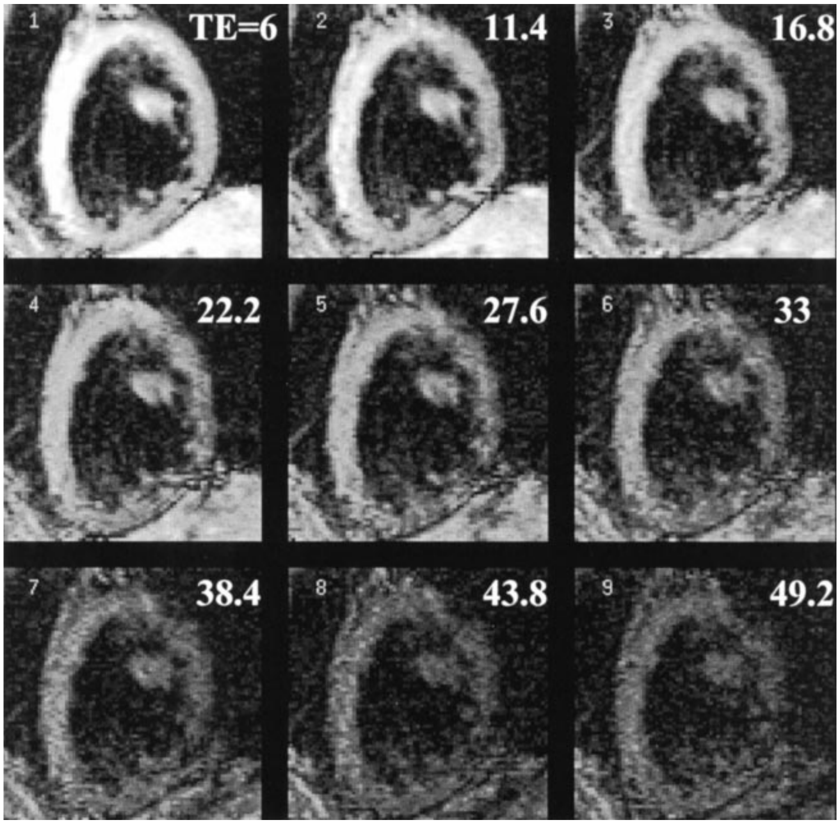

FIG. 3. Amplitude images (T_2^*) in a midventricular short-axis view of a healthy volunteer. Note different echo times *TE* from 6 to 49.2 msec (the 10th image with $TE = 54$ msec is not shown).

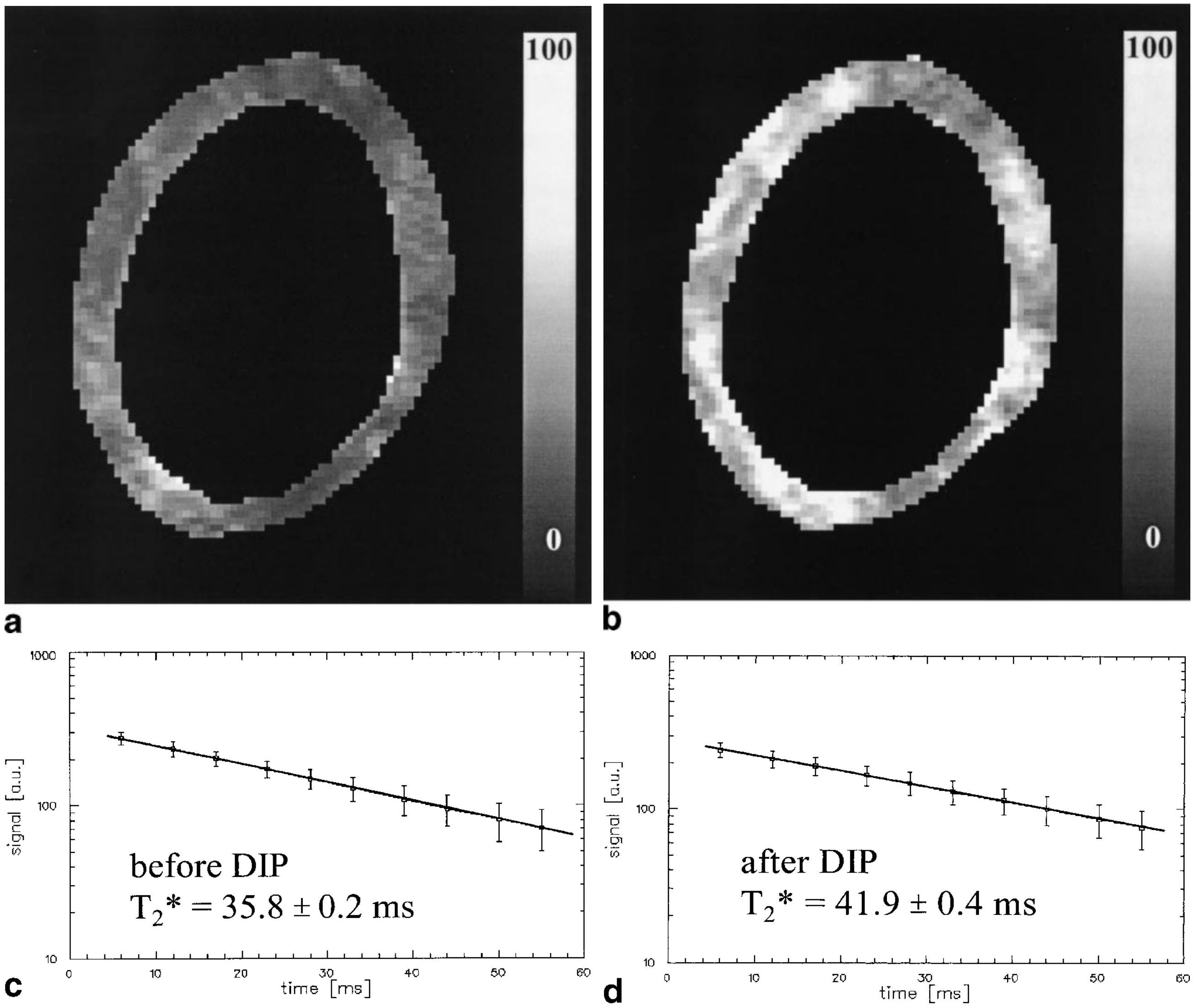

FIG. 4. T_2^* maps of the manually segmented myocardium (left ventricle) before (**a**) and 10 min after (**b**) onset of DIP infusion in a 28-year-old healthy volunteer. Colorbars from black to white reflect T_2^* values from 0 to 100 msec. Corresponding relaxation curves of T_2^* in logarithmic scaling (**c,d**), where error bars are given by the mean of the noise. Note the 17% increase of T_2^* from 35.8 ± 0.2 msec to 41.9 ± 0.4 msec, which was accompanied by a change in heart rate from 60 to 93 bpm (+55%).

tion. This value decreased by 10 ± 12% after DIP (15 ± 5% when disregarding the data of one volunteer, who showed an increase in T_1) with $P = 0.06$ (Table 2). Onset and duration of DIP-induced T_1 decrease were comparable with onset and duration of T_2^* increase. The mean increase in heart rate was from 73 ± 11 to 92 ± 10 bpm, i.e. total breathhold time for T_1 measurements was 9–15 sec. In myocardium, no significant change of T_1 was observed after global spin saturation before and after DIP-infusion (decrease was 2%, $P = 0.44$).

Spin-lattice relaxation time T_1 was also assessed in the reference tissues skeletal muscle and fat tissue. T_1 of skeletal muscle ($n = 5$) showed a decrease less than 5% for global compared to slice-selective preparation (SD of T_1 fit $<3\%$). In skeletal muscle, the administration of DIP caused no further statistically significant changes in apparent T_1 ($<1\%$, $P = 0.61$) after both methods of spin preparation. T_1 estimated in fat tissue (back of volunteers) did not change after both types of spin preparations before and after DIP (SD of T_1 fit $<3\%$). Absolute T_1 of skeletal muscle and fat correlated well with the typical T_1 of these tissues of about 1000 msec and 330 msec.

Assessment of Relative Perfusion Changes and Absolute Perfusion

Using Eq. 2, measured T_1 yield an increase of relative perfusion by 6.4 ml/(g × min). Absolute perfusion [Eq. (3)] increased from 8.5 to 13.6 ml/(g × min), using $T_{1\text{blood}} = 1516 \pm 21$ msec.

Side Effects of DIP

All subjects were able to hold their breath for the same length of time following DIP as under control conditions. Sixteen of all 26 examinations (62%) were performed at a high-dose DIP regime, i.e. 14 of 22 T_2^* measurements (64%) and two of five T_1 examinations (40%). Eleven volunteers

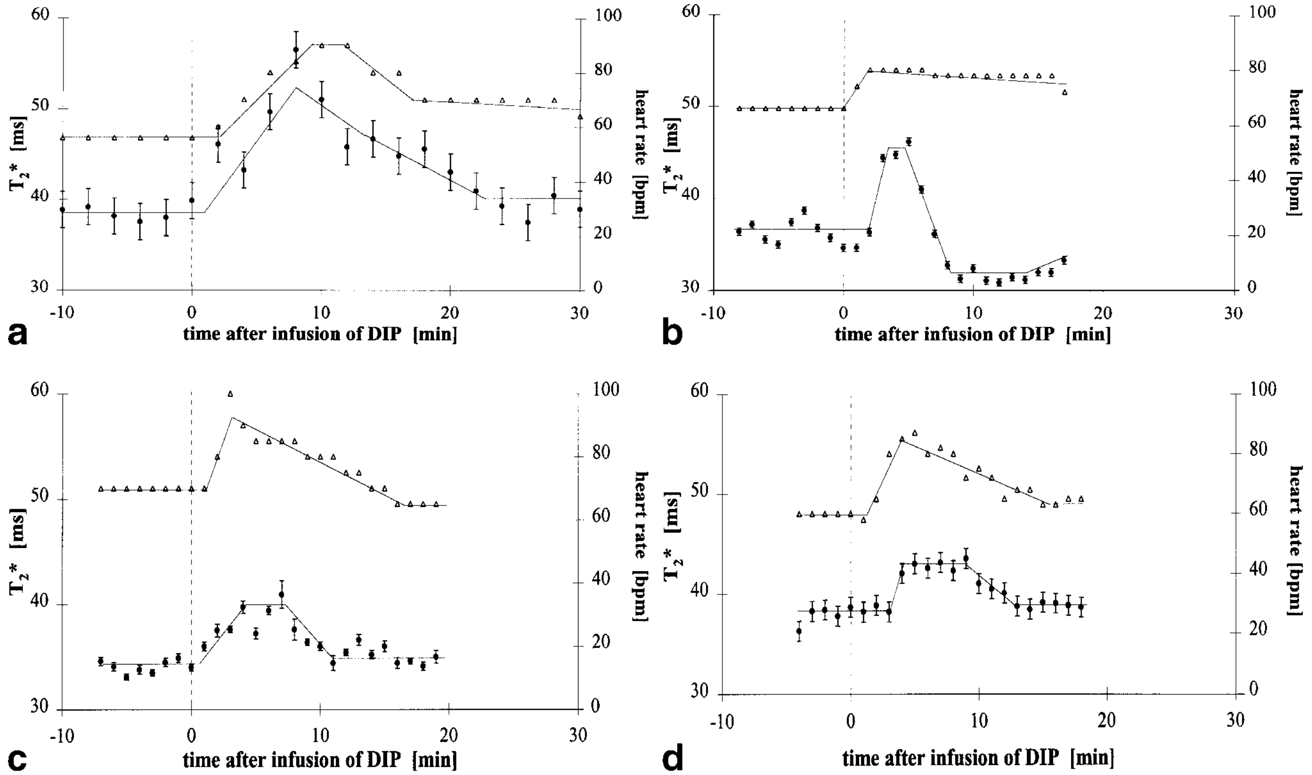

FIG. 5. Examples of different T_2^* time courses [four healthy volunteers, aged 36 years (**a**), 59 years (**b**), 23 years (**c**) and 22 years (**d**)]. T_2^* values (●) and heart rate (△) are shown before and after infusion of DIP. Note different shapes of T_2^* curves (also curves of heart rate) from peak-like to more plateau-like (a to d). Increase in heart rate (right ordinate) corresponds to onset of T_2^* increase (left ordinate). An undershoot for T_2^* as shown in panel b from min 8 to the end of the experiment was not observed in general. Solid lines are drawn to guide the eye and the dashed line marks the onset of DIP-infusion. Error bars: *SD* of T_2^* fits.

(39% of all examinations, 45% of all high-dose examinations) experienced side effects as mild headache (n = 6, one high-dose), general feelings of warmth (n = 4, three high-dose) and dizziness (n = 1, high-dose) after administration of DIP. The symptoms were promptly relieved without aminophylline and it was not necessary to interrupt the DIP-infusion in any case. During T_2^* examinations, the heart rate increased from 63 ± 9 to 85 ± 11 bpm (35 ± 15%, Table 1). Increase during T_1 examinations was 73 ± 11 to 92 ± 10 bpm (27 ± 9%, Table 2). Values for blood pressure before and after completion of MR examination were essentially unchanged. Breath holding of up to 30 sec is not likely to have a different effect on deoxyhemoglobin when the heart is stressed compared to control conditions.

DISCUSSION

In this study, significant changes in myocardial oxygenation and perfusion upon pharmacological stress with DIP could be observed. T_2^* and T_1 were measured in single breathholds within 9–27 sec and a rapid repetition of measurements was achieved. With a scanning time of 30 to 40 min, the examination lasted altogether about 1 hr, including volunteer preparation (i.e. ECG, intravenous line and location of the midventricular short-axis view of the left ventricle).

DIP increases coronary blood flow from $P_{\text{rest}} \approx 0.8$ ml/(g × min) to $P_{\text{DIP}} \approx 4$ ml/(g × min) with negligible effect on oxygen consumption (20). Therefore, the capillary deoxyhemoglobin concentration should decrease, while the BOLD

Table 1
T_2^* Values Before and After DIP (16 volunteers, 22 measurements)

	Onset (min)	Duration (min)	T_2^*			Increase		*P*
			Baseline (msec)	Max_1 (msec)	Max_2 (msec)	Max_1 (%)	Max_2 (%)	
Mean_{myo} ± SD	4 ± 2	9 ± 6	35 ± 3	39 ± 4	42 ± 5	10 ± 5	17 ± 10	0.05
Mean_{sm} ± SD			31 ± 2			change < 3		0.52

For evaluation the whole myocardium (midventricular short-axis view) was segmented manually. T_2^* increased by 10 ± 5% (comparing baseline values to values during increased heart rate) and 17 ± 10% (comparing baseline values to mean of the maximum values). The observed difference in T_2^* values was significant (P=0.05 for all volunteers). A significance of P = 0.01 was obtained when disregarding one volunteer who showed no effect after DIP administration, T_2^* obtained in skeletal muscle did not change significantly. Heart rate increased from 63 ± 9 to 85 ± 11 bpm (35 ± 15%).

myo, myocardium; sm, skeletal muscle; Max_1, mean of increased T_2^* values during increased heart rate; Max_2, mean of maximum values.

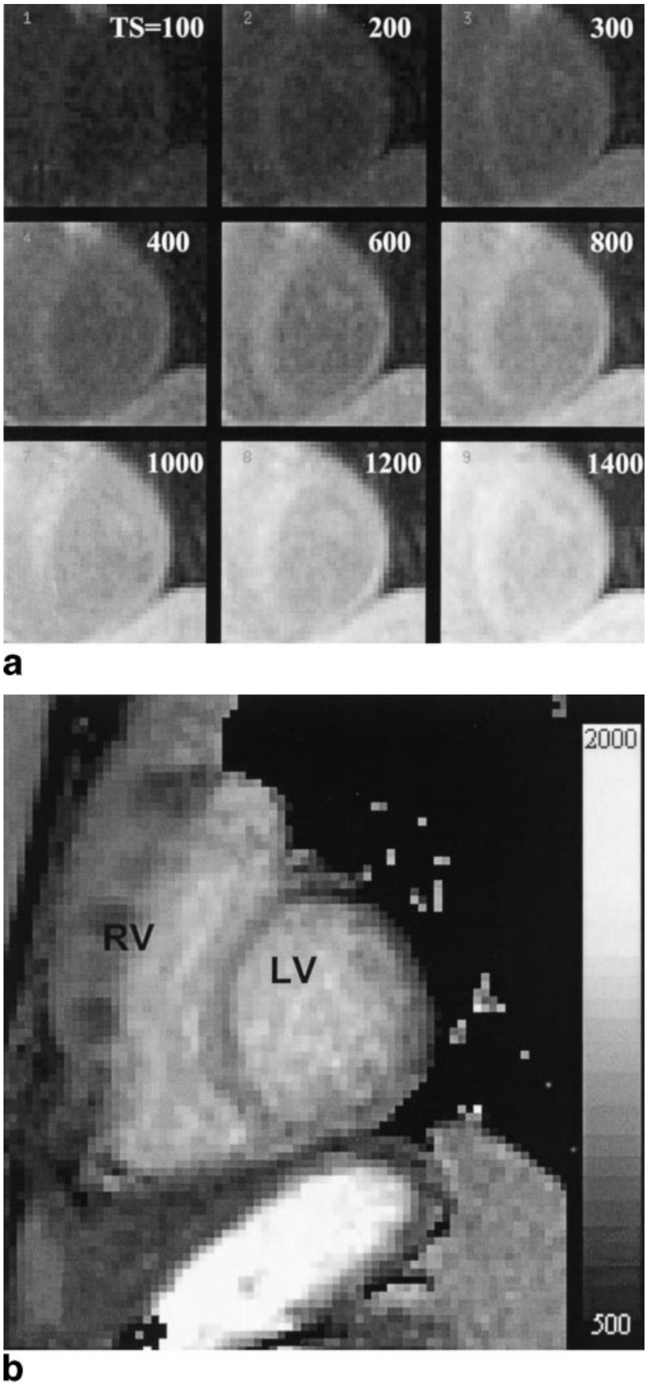

FIG. 6. Amplitude images (SRTFL) after global saturation (**a**). Saturation times *TS* of the nine images were 100, 200, 300, 400, 600, 800, 1000, 1200 and 1400 msec. Corresponding T_1-map in the T_1 range of 500 (black) to 2000 msec (white) is shown in panel **b.** RV, right ventricle; LV, left ventricle.

effect should arise. Under resting conditions the oxygen pressure in the venous coronary system is about 17 Torr (21), i.e. the oxygenation of hemoglobin is about $Y_v \approx 25\%$. Arterial oxygenation is about $Y_a \approx 100\%$ and the myocardial oxygen consumption $M\dot{V}O_2$ is proportional to coronary blood flow and the arteriovenous difference of oxygenation $\Delta Y_{rest} = Y_a - Y_v$, i.e. $M\dot{V}O_2 \approx \dot{P} \times \Delta Y$. Since DIP does not alter the oxygen consumption $M\dot{V}O_2$, administration of this drug reduces the arteriovenous difference to $\Delta Y_{DIP} = P_{rest}/P_{DIP} \times \Delta Y_{rest} = 15\%$.

T_2^* Measurements

A short-axis view was chosen, because of the topology of capillaries in myocardium, which are arranged parallel to the muscle fibers. Concerning the myocardial blood volume, the dominating vessels are the capillaries with a volume fraction of more than 90% of the intramyocardial blood volume; hence, the fraction of the venous compartment is less than 10% (22). This implies that in myocardium the volume contribution of the capillaries to the BOLD effect is clearly dominating.

The observed overall increase in T_2^* of about 17% (maximum) and 10% (mean) after DIP administration correlates well with findings of Niemi et al. (23). This result is also in good agreement with an analytical approach of our group to determine T_2^*, based on the strong collision approximation for a capillary model which is derived from capillary geometry in myocardium. The description of this approach is given in detail elsewhere (24). In short, we determined the transverse relaxation rate as a function of the relative capillary volume fraction, the capillary radius, the intracapillary BOLD-related magnetization and the diffusion coefficient. In contrast to the motional narrowing approximation, the strong collision approximation is not based on any assumption of the relation of local field strength and correlation time. Its application therefore is justified if the local field fluctuations are rapid compared to relaxation processes.

The T_2^* increase reflects a decrease in myocardial venous deoxyhemoglobin concentration and an increase in oxyhemoglobin concentration as described by Li et al. (10). A mean increase of up to 50% as measured in a previous study was not found. Variations in numbers of echoes (10 vs. 2) and signal-to-noise ratio (S/N) may have resulted in differences in image quality and accuracy of T_2^* estimation between our and a previous study (10). In the present

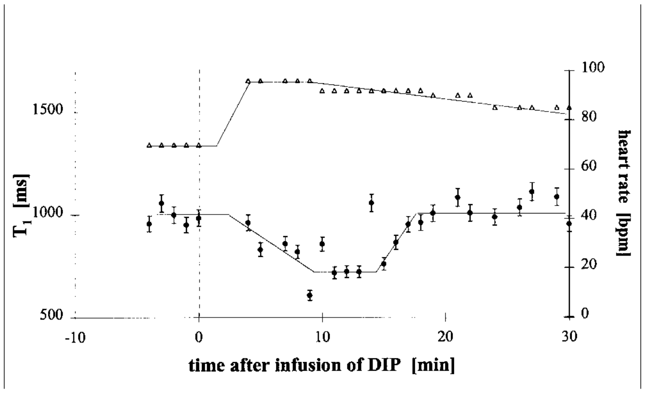

FIG. 7. Values of apparent T_1 in myocardium (●) after slice-selective saturation and heart rate (△) before and after infusion of DIP (healthy volunteer aged 36 years). Onset of apparent T_1 decrease appeared 5 min after beginning of DIP-infusion and remained for about 11 min. Apparent T_1 decreased by 19% after administration of DIP. Note increase in heart frequency (right ordinate) corresponding to decreased T_1 values (left ordinate). Solid lines are drawn to guide the eye and the dashed line marks the onset of DIP-infusion. Error bars: *SD* of T_1 fit.

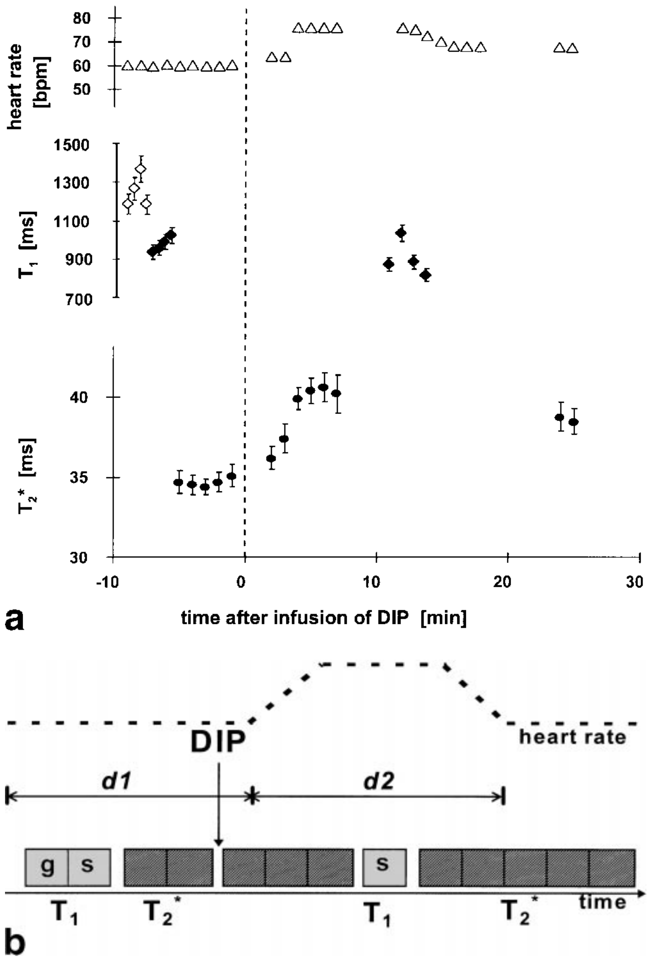

FIG. 8. **a:** Example of a volunteer who underwent T_2^* (●, bottom) and T_1 measurements (◇ global saturation, ◆ slice-selective preparation, middle) within a single exam (△ heart rate, top). T_2^* examination were repeated before, during and after administration of dipyridamole (DIP). T_1 measurements were done before (global and slice-selective saturation) and after DIP (slice-selective saturation) when heart rate was increased. Afterwards T_2^* measurements were repeated. The whole exam was finished when heart rate was returning to baseline values. Error bars: *SD* of T_2^* and T_1 fit. **b:** Proposed examination protocol derived from the presented results: T_1 measurements [global (g) and slice-selective (s) preparation] before DIP and repetition of slice-selective preparation when heart rate is increased. T_2^* examination repeated before, during and after administration of DIP. Finish of the whole exam when initial heart rate is reestablished. Data are collected in two sets (*d1* and *d2*) for statistical analysis.

study, the last echoes with echo times of about 50 msec showed worse S/N, but a T_2^* fit out of the remaining echoes could be done with high precision (SD of fit $<3\%$). A difference in the selected ROIs [whole cross-sectional area in the current study vs. parts of the interventricular septum in (10)] is another possible reason for different results (see next section on susceptibility artifacts). Nevertheless, both studies demonstrate significant increase in T_2^* during DIP-induced hyperemia.

Onset of T_2^* change and the absolute T_2^* increase were highly variable as shown in Table 1. The time course of T_2^* values showed either a peak or a plateau and a variable shape of increase and decrease. T_2^* values returned to baseline after a time period corresponding well to the pharmacological data of DIP. In most cases, the effect of DIP on T_2^* and heart rate vanished completely after 25–30 min; however, this interval was variable and unpredictable. A complete recovery of T_2^* to baseline values was therefore not documented in all cases. A correlation of onset and duration of T_2^* increase with age or dosage of DIP could not be found. Correlation of T_2^* shapes with other biological variables obtained by independent methods would be necessary for an adequate description of the pharmacological dynamics of DIP.

Susceptibility Artifacts Along the Infero-apical Border of the Heart in T_2^* Measurements

In the present study, however, in most cases reproducible susceptibility artifacts occurred in phrenicomediastinal recess which superimposed posterolateral and lateral sections of myocardium and resulted in a systematic underestimation of overall T_2^*. In our opinion, there are two possible explanations for these susceptibility artifacts:

Through-plane field pertubations caused by magnetic susceptibility differences between venous blood in the posterior vein of the left ventricle (PVLV) and myocardium may contribute to T_2^* enhancement and severe focal signal loss in cardiac images. In a study of Reeder et al. (25), regions of severe signal loss were consistently found adjacent to the PVLV in echo-planar images. A large off-resonance shift was seen at the same location in all field maps. To overcome this problem, they proposed data acquisition within the first few ms after rf excitation to prevent signal loss from focal regions around the PVLV.

Atalay et al. (26,27) noted, that in vivo porcine studies and studies in humans at 1.5 *T* and higher fields demonstrate a reproducible susceptibility artifact along the infero-

Table 2
T_1 Values Obtained After Global and Slice-Selective Preparation Before and After DIP (five volunteers, five examinations)

	T_1			Decrease		P
	Global (msec)	Sel_1 (msec)	Sel_2 (msec)	Global/sel_1 (%)	$\text{Sel}_1/\text{sel}_2$ (%)	
$\text{Mean}_{\text{myo}} \pm \text{SD}$	1219 ± 72	1004 ± 45	907 ± 110	17 ± 4	10 ± 12	0.06
$\text{Mean}_{\text{sm}} \pm \text{SD}$	1047 ± 20	997 ± 42	996 ± 28	<5	change < 1	0.61

For evaluation the whole myocardium (midventricular short-axis view) was segmented manually. In apparent T_1, a mean decrease of $17 \pm 4\%$ was observed when comparing global to slice-selective saturation ($P=0.06$), decrease was $10 \pm 12\%$ when comparing slice-selective preparation before and after DIP. Disregarding one volunteer, who showed an increase in T_1 after DIP, decrease was $15 \pm 5\%$. After global saturation, T_1 of myocardium and skeletal muscle did not change significantly upon DIP stress (2%, $P=0.44$ and $<1\%$, $P=0.46$). Heart rate increased from about 73 ± 11 to 92 ± 10 bpm ($27 \pm 9\%$).

myo, myocardium; sm, skeletal muscle; Sel_1, slice-selective saturation before DIP; Sel_2, slice-selective saturation after DIP during increased heart rate.

apical border of the heart. They performed in vivo porcine studies at 3 T to explore the source of this artifact. They found that the artifact was absent when the lungs were retracted and the heart was surrounded by free air. Under the same conditions, variations of the apex-diaphragm distance appeared to have a minimal effect on the signal of the myocardium. Also, when adenosine was administered, and coronary venous Hb saturation rose from 30–40% to 70–80%, no change was found in the appearance of the artifact. They concluded that the primary cause of the cardiac susceptibility artifact is due to the heart-lung interface along the apical and inferior segments of the heart. Since free air in the same geometry did not duplicate the artifact, it is likely that packing of air into alveoli and small bronchial airways is the major source of the artifact.

In our opinion, both arguments contribute to the observed susceptibility artifact. A compromise has to be found between rapid data acquisition and the number of echoes to obtain a stable and reproducible fit. We found that in humans the artifacts could be reduced, if measurements were performed in end-expiratory breathhold when phrenicomediastinal recess diminished. Nevertheless, an exact evaluation of the inferior border of the heart might become difficult, e.g. in patients with altered myocardium in these regions owing to a stenosis of circumflex branch of left coronary artery.

T_1 Measurements

Our data show that changes in myocardial perfusion under DIP-induced stress are detectable using the presented T_1 examinations. As predicted by theory, changes in the apparent T_1 measured following global spin preparation were different from those measured following slice selective spin preparation. A further significant DIP-induced change in T_1 should only occur with slice-selective preparation due to the inflow of non-saturated spins. This hypothesis was substantiated by our study, showing a decrease in myocardial T_1, whereas T_1 of skeletal muscle did not change after DIP. As predicted, our results also reflect the fact that the SRTFL-sequence presented here detects changes in T_1 corresponding to altered perfusion. In one volunteer, even a T_1 increase after DIP was observed. This phenomenon of an assumed decrease in perfusion under DIP-stress will be evaluated by additional examinations.

The total number of T_1 examinations is certainly too small for a final conclusion. However, data could indicate a trend according to perfusion changes.

Assessment of Relative Perfusion Changes and Absolute Perfusion

The calculated increase in the relative perfusion change ΔP of about 6 ml/(g × min) is comparable, although higher than reported values (20). Using Eq. (2), the estimation of ΔP depends only on the parameter T_{1s}, obtained before and after DIP. A possible reason for the calculated higher ΔP could be an overestimation of the true DIP-induced difference in T_1 owing to measurement inaccuracy. In contrast to ΔP, the calculation of absolute perfusion P [Eq. (3)] is not only influenced by the parameter T_{1s}, but also by T_{1g} and $T_{1\text{blood}}$, which have to be determined by different measurements. Therefore, inaccuracies in T_{1s}, T_{1g}, and $T_{1\text{blood}}$ estimations could lead to the difference in perfusion values P (20). Moreover, this could also be responsible for the difference in calculated perfusion changes ΔP of 6.4 ml/(g × min) [calculated with Eq. (2)] and 5.1 ml/(g × min) [using Eq. (3)].

In our study, $T_{1\text{blood}}$ measured in heart chambers after non-selective preparation (12,13) agreed with reference values (28–30). Janick et al. (28) observed that $T_{1\text{blood}}$ varies from 2170 to 1100 msec, if hematocrit X varies from 0.2 to 0.6. They calculated $T_{1\text{blood}}$ by the relation $R_1 = 0.23 + 1.14 \times X\ \text{sec}^{-1}$ (at 1.5 T) (28). Assuming a mean hematocrit of 0.4, $T_{1\text{blood}} = 1460$ msec, which correlates well with $T_{1\text{blood}} = 1516 \pm 21$ msec from our measurements. However, exact determination of $T_{1\text{blood}}$ in the heart chambers remains difficult owing to disturbed flow and turbulences.

The problem of inaccuracies of T_1 estimation can be handled by improving precision and reproducibility of the measurement, e.g. by acquiring a second data set with saturation times of 4 to 5 × T_1, which could stabilize the T_1 fit, and by increasing the number of acquisitions (NEX). However, these data can not be obtained in a single breathhold. Also, longer acquisition times, e.g. by using navigator techniques, will exclude the detection of rapid T_1 changes. As usual in time-resolved MR studies, a compromise has to be found between short acquisition time and high S/N.

About 60% of the examinations were performed with a high-dose DIP-regime. The effect of different DIP doses on the signal curves has to be evaluated in future studies. In principle, the application of these techniques is not limited to the vasodilator DIP, myocardial studies with other drugs will also be possible.

Unlike CA methods, which require at least two injections of CA and DIP, the presented methods require only a single infusion of DIP. First-pass perfusion techniques are very robust and therefore appropriate for clinical implementation, but are limited by the transient nature of the first-pass effect, which evolves in times in the order of myocardial transit times (3). As most of the MR CA are more or less nephrotoxic, repeated examinations are not possible. Moreover, the process of quantification of absolute perfusion is quite high in such studies, e.g. since the data have to be folded with an arterial input function. One advantage of the CA techniques is the possibility of fast visualization of a CA enhancement at S/N, which provides a more qualitative measure of tissue perfusion. S/N of the individual T_2^* or T_1 measurements is low compared to contrast-enhanced imaging techniques; nonetheless, it was sufficient in this study to measure these parameters in the chosen large ROI (whole cross section) at a precision of about 5%. In future studies, a combination of both approaches (with and without CA) will provide a deeper understanding of myocardial perfusion and oxygenation.

The presented techniques are only applied to a single short-axis slice. Future developments will be directed towards extending these techniques so that several slices can be scanned in parallel. This will allow scans of the whole myocardium in a reasonable short time. Recently, the total post-processing time could be reduced significantly by calculating T_2^* parameter maps immediately after data acquisition during the image reconstruction process.

Online-generated T_2^* maps showing myocardial regions with altered oxygenation will provide rapid diagnostic information to the investigator.

CONCLUSION

In this study DIP-induced changes in myocardial oxygenation and perfusion could be monitored using T_2^* and T_1 examinations. The time-dependence of T_2^* and apparent T_1 was observed by a series of rapid measurements within 30–40 min. For the first time, absolute perfusion in the human heart could be calculated in vivo and allowed us to estimate coronary reserve from T_1 measurements. This approach could be a promising supplement and an useful alternative to first-pass techniques currently used in clinical cardiac MRI.

The combination of T_2^* and T_1 examinations provides not only physiological information in vivo non-invasively, when one parameter is known, it also can be used to predict the other parameter and to compare this prediction with the experimental measurements.

ACKNOWLEDGMENTS

The authors thank Peter Bachert, Ph.D. for extensive discussion throughout the project and for comments on the manuscript. Thanks to Nils Dannenberg and Timen Brakebusch for their technical assistance in the performance of the experiments and Sabine Muller for the editorial help. Supported by Deutsche Gesellschaft für Kardiologie (CM Wacker) and Forschungsfonds der Universitätsklinik Mannheim/Heidelberg Projektnummer 42 (AW Hartlep).

REFERENCES

1. Judd RM, Reeder SB, Atalar E, McVeigh ER, Zerhouni EA. A magnetization-driven gradient echo pulse sequence for the study of myocardial perfusion. Magn Reson Med 1995;34:276–282.
2. Wilke N, Simm C, Zhang J, Ellermann J, Ya X, Merkle H, Path G, Ludemann H, Bache RJ, Ugurbil K. Contrast-enhanced first pass myocardial perfusion imaging: correlation between myocardial blood flow in dogs at rest and during hyperemia. Magn Reson Med 1993;29:485–497.
3. Wilke N, Jerosch-Herold M, Stillman AE, Kroll K, Tsekos N, Merkle H, Parish T, Hu X, Wang Y, Bassingthwaighte J, Bache RJ, Ugurbil K. Concepts of myocardial perfusion imaging in magnetic resonance imaging. Magn Reson Q 1994;10:249–286.
4. Wilke N, Kroll K, Merkle H, Wang Y, Ishibashi Y, Xu Y, Zhang J, Jerosch-Herold M, Muhler A, Stillman AE, et al. Regional myocardial blood volume and flow: first-pass MR imaging with polylysine-Gd-DTPA. J Magn Reson Imaging 1995;5:227–237.
5. Judd RM, Atalay MK, Rottman GA, Zerhouni EA. Effects of myocardial water exchange on T_1 enhancement during bolus administration of MR contrast agents. Magn Reson Med 1995;33:215–223.
6. Saeed M, Wendland MF, Higgins CB. The developing role of magnetic resonance contrast media in the detection of ischemic heart disease. Proc Soc Exp Biol Med 1995;208:238–254.
7. Edelmann RR, Li W. Contrast-enhanced echo-planar MR imaging of myocardial perfusion: preliminary study in humans. Radiology 1994; 190:771–777.
8. Ogawa S, Lee TM, Kay AR, Tank DW. Brain magnetic resonance imaging with contrast dependent on blood oxygenation. Proc Natl Acad Sci USA 1990;87:9868–9872.
9. Ogawa S, Tank DW, Menon R, Ellerman JM, Kim S-G, Merkle H, Urgubil K. Intrinsic signal changes accompanying sensory stimulation: functional brain mapping with magnetic resonance imaging. Proc Natl Acad Sci USA 1992;89:5951–5955.
10. Li D, Dhawale P, Rubin PJ, Haacke EM, Gropler RJ. Myocardial signal response to dipyridamole and dobutamine: demonstration of the BOLD effect using a double-echo gradient-echo sequence. Magn Reson Med 1996;36:16–20.
11. Williams DS, Grandis DJ, Zhang W, Koretsky AP. Magnetic resonance imaging of perfusion in the isolated rat heart using spin inversion of arterial water. Magn Reson Med 1993;30:361–365.
12. Bauer WR, Roder F, Hiller KH, Han H, Fröhlich S, Rommel E, Haase A, Ertl G. The effect of perfusion on T_1 after slice selective spin inversion in the isolated cardioplegique rat heart. Magn Reson Med 1997;38:917–923.
13. Kahler E, Belle V, Waller C, Rommel E, Hiller KH, Voll S, Bauer WR, Haase A. Quantitative determination of perfusion and regional blood volume in rat myocardium in vivo. ESMRMB, 14th Annual Meeting, Bruessel, Book of Abstracts, 1997. p 91–92.
14. McGuinness ME, Talbert RL. Pharmacological stress testing: experience with dipyridamole, adenosine and dobutamine. Am J Hosp Pharm 1994;51:328–346.
15. Atkinson D, Brant Zawadzki M, Gillan G, Purdy D, Laub G. Improved MR angiography: magnetization transfer suppression with variable flip angle excitation and increased resolution. Radiology 1994;190:890–894.
16. Bock M, Schad LR, Bauer WR, Knopp MV, Lorenz WJ. A segmented saturation recovery turboFLASH (SSRTF) sequence for in vivo T_1-measurements in the heart. Fourth Scientific Meeting of the ISMRM, New York, 1996. p 653.
17. Bock M, Bauer WR, Hillenbrand H, Schad LR. T_1-maps of the human heart acquired in a single breathhold. Fifth Scientific Meeting of the ISMRM, Vancouver, 1997. p 2057.
18. Blueml S, Schad LR, Stepanow B, Lorenz WJ. Spin-lattice relaxation time measurement by means of a TurboFLASH technique. Magn Reson Med 1993;30:289–295.
19. Press WH, Flannery BP, Teukolsky SA, Vetterling WT. Numerical recipes: the art of scientific computing. Cambridge University Press; 1986.
20. Tauchert M, Hilger HH. In: Schaper W, editor. The pathophysiology of myocardial perfusion. Elsevier/North Holland; Amsterdam, 1979. p 141.
21. Bing RJ, Hammond MM, Handelsman JC, Powers SR, Spenger FC, Eckenhoff JE, Goodale WT, Hafkenschiel JH, Kety SS. The measurement of coronary blood flow, oxygen consumption, and efficiency of the left ventricle in man. Am Heart J 1949;38:1.
22. Kaul S, Jayaweera AR. Coronary and myocardial blood volumes. Circulation 1997;96:719–724.
23. Niemi P, Poncelet BP, Kwong KK, Weisskoff RM, Rosen BR, Brady TJ, Kantor HL. Myocardial intensity changes associated with flow stimulation in blood oxygenation sensitive magnetic resonance imaging. Magn Reson Med 1996;36:78–82.
24. Bauer WR, Nadler W, Bock M, Schad LR, Wacker CM, Haase A, Ertl G. Theory of the BOLD effect in the capillary region: an analytical approach for the determination of T_2^* in the capillary network of myocardium. Magn Reson Med 1999;41:51–62.
25. Reeder SB, Faranesh AZ, McVeigh ER. In vivo measurement of T_2^* and field inhomogeneity: implications for cardiac EPI. Sixth Scientific Meeting of the ISMRM, Sydney, 1998. p 797.
26. Atalay MK, Poncelet BP, Kantor HL, Brady TJ, Weisskoff RM. Susceptibility artifact at the cardiac apex of porcine hearts at 3T is primarily due to the heart-lung interface. Sixth Scientific Meeting of the ISMRM, Sydney, 1998. p 130.
27. Atalay MK, Reeder SB, Zerhouni EA, Forder JR. Blood oxygenation dependence of T_1 and T_2 in the isolated, perfused rabbit heart at 4.7 T. Magn Reson Med 1995;34:623–627.
28. Janick PA, Hackeney DB, Grossmann RI, Asakura T. MR imaging of various oxidation states of intracellular and extracellular hemoglobin. AJNR 1991;12:891–897.
29. Gomori JM, Grossman RI, Yu-Ip C, Asakura T. NMR relaxation times of blood: dependence on field strength, oxidation state, and cell integrity. J Comput Assist Tomogr 1987;11:684–690.
30. Bryant RG, Marill K, Blackmore C, Francis C. Magnetic relaxation in blood and blood clots. Magn Reson Med 1990;13:133–144.

ELSEVIER Magnetic Resonance Materials in Physics, Biology and Medicine 8 (1999) 48–54

MAGMA
Magnetic Resonance Materials in Physics, Biology and Medicine

BOLD-MRI in ten patients with coronary artery disease: evidence for imaging of capillary recruitment in myocardium supplied by the stenotic artery☆

Christian M. Wacker [a,b], Michael Bock [c], Andreas W. Hartlep [a], Wolfgang R. Bauer [b], Gerhard van Kaick [a], Stefan Pfleger [b], Georg Ertl [b], Lothar R. Schad [a,*]

[a] *Forschungsschwerpunkt Radiologische Diagnostik und Therapie, Deutsches Krebsforschungszentrum (DKFZ), 69120 Heidelberg, Germany*
[b] *II. Med. Univ. Klinik Mannheim/Heidelberg, 68135 Mannheim, Germany*
[c] *Tumorzentrum Heidelberg/Mannheim, 69120 Heidelberg, Germany*

Received 1 October 1998; accepted 18 November 1998

Abstract

Changes of myocardial oxygenation can be studied by measurements of the apparent transverse relaxation time T_2^*, which is correlated with the oxygenation state of hemoglobin. In this study, ten patients with coronary artery disease (CAD) underwent blood oxygenation level dependent (BOLD) T_2^* measurements using a segmented gradient echo pulse sequence with ten echoes. T_2^* measurements were performed in a single short-axis slice of the heart at rest and under pharmacological stress with dipyridamole (DIP), which increases myocardial blood flow. For comparison, all patients underwent X-ray angiography and stress-echocardiography within 4 days after the MR exam. In one patient, MR examination was repeated 10 weeks after percutaneous transluminal coronary angioplasty (PTA). In the differential T_2^* maps, expected ischemic areas of myocardium were identified in six patients. In these regions, T_2^* values (30 ± 8 ms) were significantly reduced when compared to the remaining myocardium (48 ± 9 ms, $P < 0.01$). In four patients, the myocardial region of interest could not be assessed owing to severe susceptibility artifacts in the ischemic region. The success of the PTA treatment could be visualized from a more homogeneous DIP induced increase in T_2^* within the ischemic myocardium (from 26 ± 1 to 29 ± 1 ms before PTA versus 26 ± 1 to 31 ± 4 ms after PTA, $P < 0.001$). © 1999 Elsevier Science B.V. All rights reserved.

Keywords: MRI; Myocardial oxygenation; BOLD; Dipyridamole; Stress test; Coronary artery disease; Percutaneous transluminal angioplasty

---

1. Introduction

At present, the method of choice for the diagnosis of coronary artery disease (CAD) is X-ray coronary arteriography. Although this technique is well established in the diagnosis of the CAD, the functional significance of an arteriographic lesion often cannot be determined from arteriograms alone. This is because there may be a lack of correlation between coronary luminal narrowing and myocardial perfusion and contraction. In addition, stress echocardiography and myocardial scintigraphy are important clinical examinations to as-

---

☆ This work was presented in part at the 15th Annual Meeting of the European Society for Magnetic Resonance in Medicine and Biology (Geneva 1998), at the 6th Scientific Meeting of the International Society for Magnetic Resonance in Medicine (Sydney 1998, Book of Abstracts, p. 897), and at the Annual Meeting of the German Society of Cardiology (Mannheim 1998).

* Corresponding author. Tel.: +49-6221-422569; fax: +49-6221-422572.

E-mail address: l.schad@dkfz-heidelberg.de (L.R. Schad)

1352-8661/99/$ - see front matter © 1999 Elsevier Science B.V. All rights reserved.
PII: S1352-8661(99)00004-6

sess the physiological significance of coronary artery lesions.

In recent years, MRI of ischemic heart disease has become an increasingly important diagnostic tool. Coronary MRI investigations allow the clinician to assess the physiologic significance of an obstructive lesion and the functional capacity of collateral vessels. The effect of pharmaceutical treatment or surgical procedures such as coronary bypass or percutaneous transluminal coronary angioplasty (PTA) can be monitored with high sensitivity and with reduced observer bias. Consequently, moderately invasive MRI techniques are discussed as potentially cost-effective diagnosis and monitoring strategies for patients with CAD and acute ischemia. To be clinically useful, MR techniques must be able to differentiate between normal and abnormal myocardial function. Furthermore, they should detect disturbances of myocardial function at an earlier stage than any other comparable imaging modality.

The magnetic properties of oxygenated and deoxygenated hemoglobin can be used to visualize tissue oxygenation (BOLD effect [1,2]). The transition of diamagnetic oxyhemoglobin to paramagnetic deoxyhemoglobin causes changes in the local magnetic field inhomogeneity [15,16], which can be monitored as signal changes in T_2^*-weighted images. The BOLD contrast has been primarily exploited in neuro-functional MRI to localize areas of neuronal activity. In myocardial imaging, BOLD MRI detects modulations of the deoxyhemoglobin concentration caused by local changes in myocardial blood volume and flow as well as oxygen consumption. In humans, the myocardial BOLD effect has been investigated recently [3]. To assess changes in myocardial oxygenation and perfusion under pharmacological stress with dipyridamole (DIP), we studied healthy volunteers using T_2^* and T_1 measurements [4,5].

DIP mediates coronary artery vasodilatation. It inhibits adenosine indirectly and it acts through the accumulation of adenosine, which activates arterial chemoreceptors. Therefore DIP produces enhanced coronary vasodilatation without increasing heart work in contrast to dobutamine, which increases cardiac output and heart rate as well as promoting coronary artery vasodilatation [10–14]. The DIP induced vasodilatation causes an increase in diamagnetic oxyhemoglobin. Hence, the magnetic field gets more homogeneous and T_2^* increases. In the ischemic myocardium, the vessels are already dilated and DIP cannot produce further vasodilatation. As a consequence, T_2^* should not increase so much in ischemic regions.

In this study, T_2^* measurements were performed in patients with CAD to differentiate between normal and ischemic myocardium. T_2^* measurements were acquired in a single breathhold before, during and after infusion of DIP.

2. Materials and methods

2.1. Patients

Ten patients with expected CAD were examined (44–69 years of age, mean 59 ± 7, two female). All patients had no history of myocardial infarction, but suffered from stress-induced stenocardia. One patient suffered from angina even under resting conditions. Patients underwent X-ray angiography, stress echocardiography and MR examination within 4 ± 2 days. One patient was reinvestigated 10 weeks after PTA with stent implantation of the proximal left anterior descending artery (LAD).

2.2. X-ray angiography

Cardiac catheterization was done after inguinal puncture of the right femoral artery with a size 5 French catheter. Coronary arteries were assessed in the typical left anterior oblique (LAO) and right anterior oblique (RAO) projections.

2.3. Stress echocardiography

Echocardiography was done at rest and after administration of DIP (rate: 0.56 mg kg^{-1} body weight over 4 min) and atropine (0.75 mg). After the examination patients were antagonised with 200 mg aminophylline.

2.4. MR examination

MR exams were performed on a 1.5 T whole body scanner (SIEMENS Vision, Erlangen, Germany) with gradient overdrive using the integrated body coil for radiofrequency (rf) excitation and a 4-element phased-array coil for signal reception. Fast, non-ECG-triggered scout images (FLASH) were used to position the imaging slice at the short-axis plane of the heart between the valve system and papillary muscle.

For T_2^* measurements a segmented gradient echo pulse sequence was used, which acquired ten successive gradient echoes per rf excitation. The echo-times TE of the ten images ranged from 6 to 54 ms at an echo separation $\Delta TE = 5.4$ ms. First-order motion compensation was included in the slice-selection direction. During each cardiac cycle, five phase-encoding lines were acquired with flip angles incremented between 20 and 90° to maintain a constant myocardial signal [6]. Data were acquired during mid-diastole in a sampling window of 300 ms. An in-plane resolution of 1.61×1.17 mm^2 with a slice thickness $SL = 6$ mm was achieved with a matrix size of 140×256 and a field of view (FOV) of 225×300 mm^2. The acquisition time for a single scan was $140/5 \times 0.8 \approx 22$ s assuming an average RR-interval of 800 ms. A non-selective 180° hyperbolic secant rf-pulse inverted the magnetization at the beginning of the heart cycle to suppress the ventricular signal from flowing blood. Slice-selective re-inversion directly followed, which resulted in an approximate nulling of the longitudinal magnetization of inflowing blood during data acquisition (black blood). ECG-gated amplitude images were obtained in diastole, when the ventricle's cross section is at its maximum.

Patients were informed about possible side effects of dipyridamole such as headaches, nausea and general feelings of warmth. MR examinations were performed after informed consent had been obtained. The patients avoided the consumption of tea and coffee as well as medication containing aminophylline at least 12 h before the DIP test protocol. The patient's heart rate was continuously monitored and blood pressure was measured before and after the examinations. Images were acquired repeatedly at rest and under DIP-induced stress (rate: 0.84 mg kg^{-1}, infused over 4 min via an antecubital vein). Measurements were done in 1-min-repetitions until the initial heart rate was reestablished. Infusion was controlled by an infusion system (CAI 626P®, DOLTRON AG, Switzerland), which allowed precise adjustment of the infusion rate relative to the patient's weight.

2.5. Data evaluation

For data evaluation, MR images were transferred to an offline-workstation and processed using a home-written software package. In a first step, a region of interest (ROI) was placed around the complete myocardium in the first amplitude image (which was the brightest) of the ten echo image series. In order to minimize the effect of ROI positioning on the final results, the ROI placement was repeated two to three times and compared by the same observer.

Maps of the apparent transverse relaxation time T_2^* were calculated by applying a linear fit to the logarithm of the signal intensities in the ROI. In the late echo images signal intensities often reached the noise level (Fig. 1), which caused systematic errors in the logarithmic fit. To minimize these fit errors, the noise amplitude was first determined in a region outside the body. In the following fitting procedure, only those signal intensities that exceeded the noise amplitude threshold by a factor of 2 to 3, were used.

Furthermore, average T_2^* values of the myocardium were calculated from the mean of the signal intensities in the ROI. To localize myocardial areas with lower T_2^* values, the series of T_2^* maps acquired before, during and after DIP administration was displayed in a fast cine-loop. In this display mode, areas of reduced or no T_2^* increase under DIP were identified visually and ROIs were placed manually. For these expected ischemic regions, average T_2^* values were determined (T_{2i}^*) and compared to the remaining myocardium (T_{2n}^*).

2.6. Statistical analysis

To test the statistical significance of the T_2^* increase under DIP, T_2^* values (i.e. overall T_2^* values, T_{2i}^* and T_{2n}^*) were grouped into two sets. Baseline values of T_2^* were defined from the data acquired before DIP administration and before there was an increase in heart rate. The second data set included all those measurements where the heart rate exceeded the baseline value by 10%. The significance, P, of the difference of means was calculated using Student's t-test.

3. Results

3.1. X-ray angiography

Cardiac catheterization showed extreme stenosis ($>90\%$) of the LAD ($n=7$), the posterior descending artery (RCA, $n=1$), and the circumflex branch of the left coronary artery (LCX, $n=2$, Table 1).

3.2. Stress echocardiography

Echocardiography with DIP and atropine showed hypo- and dyskinesia in myocardial areas ($n=6$) sup-

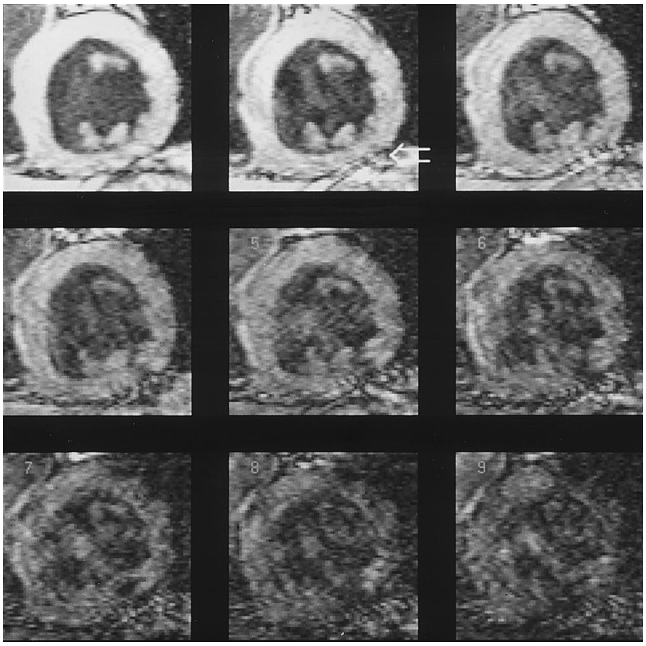

Fig. 1. Amplitude images in a short-axis view (patient no. 4). The myocardium is clearly distinguished from the blood filled heart chambers. Note the signal loss from images 1–9. Susceptibility artifacts occur in the infero-lateral border of the heart (white arrow) and overlay parts of the infero-lateral myocardium.

Table 1
Results from X-ray angiography, stress echocardiography and MR examinations[a,e]

	Angiography	Echo	MR				Ischemia
Patient	Stenosis of	Dyskinesia	Lower T_2^*	Quality	Artifact region	Artifacts, − severity	Detected
1[b]	LAD	sept	sept	+	ant/lat	−−−	+
2	LAD	0	ant/sept	+++	ant/sept	−−	−
3	LAD	[d]	sept	++	inf	−	+
4	LAD	sept	sept	+++	lat	−−	+
5	LAD	sept	ant/sept	++	inf	−−	+
6	RCA[c]	inf	0	+	inf	−−−	−
7	LCX	0	sept	+	lat	−−	−
8_{I}	LAD	sept	ant/sept	++	inf	−−	+
8_{II}	LAD	[d]	ant/sept	++	inf	−−	+
9	LAD	sept	sept	+++	ant/inf	−	+
10	LCX	0	0	++	inf/ant	−−	−

[a] LAD, anterior descending artery; LCX, circumflex branch of left coronary artery; RCA, posterior descending artery; 0, no pathologic findings.

[b] Echocardiography and MR examination were performed without DIP due to stenocardia under resting conditions.

[c] Distal stenosis.

[d] Examination was not performed.

[e] Quality of amplitude images is scaled from + (normal) to +++ (very good). Severity of artifacts is scaled from − (moderate) to −−− (very bad). $8_{I,II}$-patient before and after PTA (Fig. 3).

plied by stenotic coronary arteries. Three patients showed no myocardial dysfunction of the left ventricle, one patient was not stressed owing to stenocardia under resting conditions. Two patients were not examined echocardiographically (Table 1). During the examination, one patient suffered from drug induced stenocardia and dyspnea.

3.3. MR examination

Overall T_2^* increased by $6 \pm 8\%$ (from 34 ± 6 to 37 ± 6 ms) during the interval of increased heart rate ($P = 0.26$). The increase in T_2^* was $9 \pm 7\%$ ($P < 0.1$) when the data of three patients, who showed a small decrease in T_2^* values ($< 1\%$) after DIP administration, was disregarded. Standard deviation (SD) of the T_2^* fit was below 3%. One patient was not stressed with DIP owing to stenocardia under resting conditions. T_2^* increased by 2 ± 1 min after the onset of DIP-infusion. The observed side effects of DIP were severe stenocardia ($n = 3$), dyspnea ($n = 1$) and dizziness ($n = 2$). In three cases the examination had to be interrupted early due to severe stenocardia ($n = 2$) or dyspnea ($n = 1$). One patient was antagonised with intravenous aminophylline (200 mg). The average heart rate increased from 61 ± 6 to 74 ± 7 bpm, i.e. by $22 \pm 7\%$ ($P < 0.001$). The mean duration of the increased heart rate was 15 ± 6 min (18 ± 4 min when disregarding the data of three patients where the examination had to be interrupted early). The maximum heart rate was 81 ± 8 min, i.e. maximum increase was $34 \pm 12\%$. Regions with lower T_2^* values, which corresponded with ischemic areas, as expected from X-ray angiography and echocardiography, were clearly detected in six patients (Table 1, Fig. 2). In four patients, expected ischemic myocardium could not be identified owing to severe susceptibility artifacts, which overlaid the interesting myocardial regions (Fig. 1). When comparing areas with lower T_2^* values to the remaining myocardium under DIP stress, T_{2i}^* increased from 30 ± 8 to 32 ± 6 ms ($P = 0.27$) and T_{2n}^* changed from 48 ± 9 to 48 ± 8

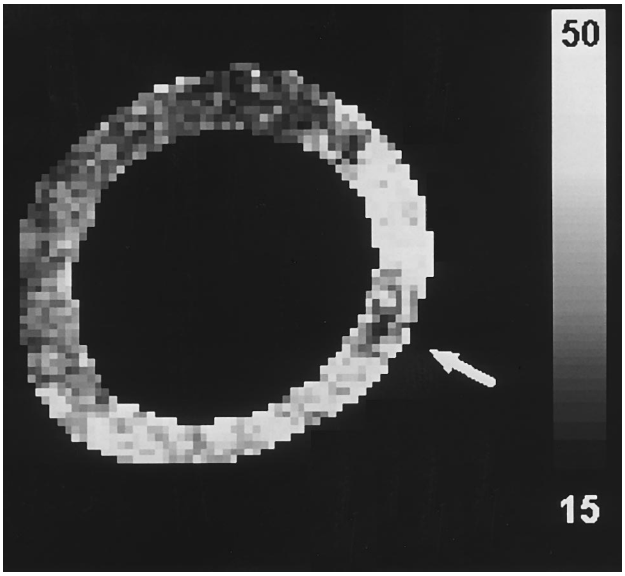

Fig. 2. Calculated T_2^* map of a patient (no. 9) with severe stenosis of the LAD and hypokinetic myocardial septum. The ROI was obtained by outlining the endo- and epicardial orders of the myocardium in the ten amplitude images. The colorbar ranging from black to white reflects T_2^* values from 15 to 50 ms. Areas with lower T_2^* values could be well distinguished in the antero-septal and septal region. The dark section in the lateral part of myocardium (white arrow) results from the susceptibility artifact which was seen in the amplitude images.

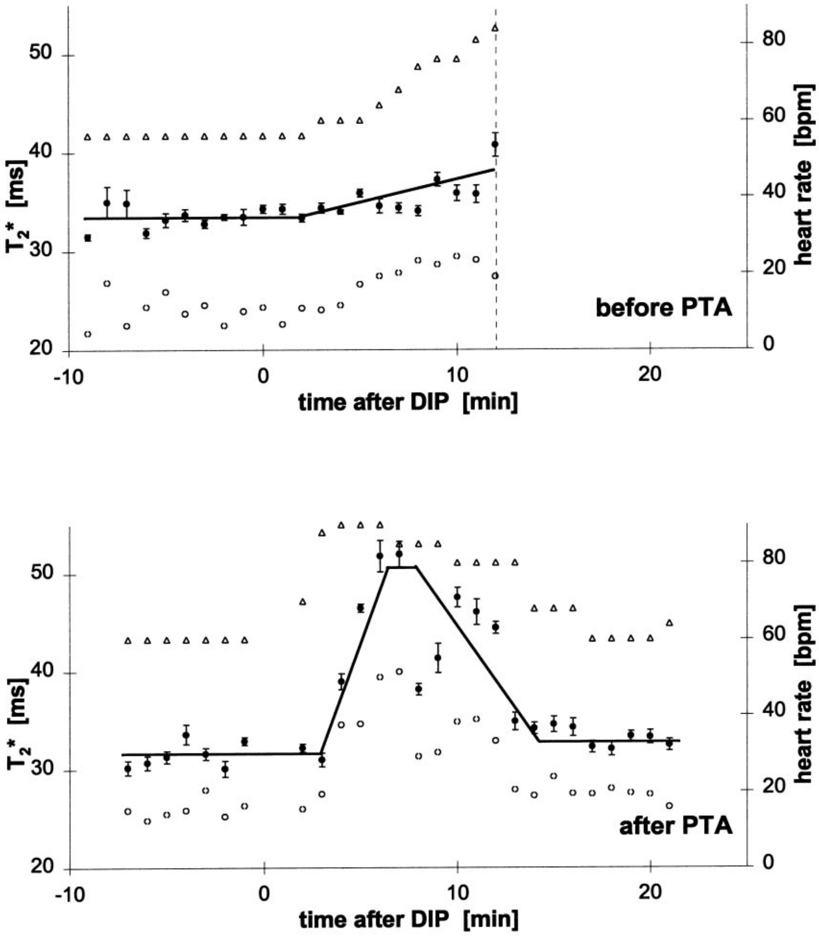

Fig. 3. Patient with stenosis of LAD (patient no. 8). T_2^* values (whole myocardium (●), antero-septal area (○) and heart rate (△) as a function of time. Before PTA the examination was interrupted owing to severe stenocardia of the patient (dashed line), after PTA the MR examination was finished without complications. Solid lines are drawn to guide the eye. Error bars: SD of T_2^* fit (< 3%).

ms ($P = 0.41$). The difference between T_{2i}^* and T_{2n}^* was statistically significant ($P < 0.01$ before DIP, $P = 0.0001$ after DIP).

One patient was reinvestigated 10 weeks after PTA of the LAD. Mean T_2^* values were plotted as a function of time (Fig. 3). Before PTA, T_2^* values of the whole myocardium (antero-septal region) increased from 34 ± 1 (26 ± 1) to 36 ± 2 (29 ± 1) ms. However, the examination had to be interrupted due to severe angina pectoris with a fit of perspiration but stable circulation. The patient was antagonised with intravenous administration of aminophylline (200 mg) and symptoms of cardiac ischemia promptly ceased. After PTA, T_2^* increased from 34 ± 1 (26 ± 1) to 39 ± 5 (31 ± 4) ms and the examination could be finished without complications. When observing the obtained T_2^* maps, differences between regions of expected ischemia and regions of normal myocardium were less pronounced than they were prior to PTA.

4. Discussion

In this study, BOLD-MRI of myocardium in patients with CAD was assessed for the first time. However, there are conspicuous differences in T_2^* values when comparing the present results with findings of healthy volunteers obtained in a former study [4,5]. Recently reported results correlate well with an analytic approach for the determination of T_2^* in the capillary network of the myocardium [7], where we determined the transverse relaxation rate as a function of the relative capillary volume fraction, the capillary radius, the intracapillary BOLD-related magnetization and the diffusion coefficient. In contrast to the motional narrowing approximation, the strong collision approximation is not based on any assumption of the relation of local field strength and correlation time. Its application therefore is justified if the local field fluctuations are rapid compared to relaxation processes. Concerning the myocardial blood volume, the dominating vessels are the capillaries with a volume fraction of more than 90% of the intramyocardial blood volume; hence, the fraction of the venous compartment is less than 10% [14]. This implies that in myocardium the volume contribution of the capillaries to the BOLD effect is clearly dominant. A T_2^* increase reflects a decrease in myocardial venous deoxyhemoglobin concentration and an increase in oxyhemoglobin concentration as described by Li et al. [3]. Therefore, a missing increase in T_2^* under DIP stress shows that there is no adequate increase in myocardial perfusion and oxyhemoglobin concentration owing to the narrowed supplying coronary artery.

A significant difference in T_2^* was observed, when comparing expected ischemic to non-ischemic myocardium ($P < 0.01$ before DIP, $P = 0.0001$ after DIP). However, the differences in T_2^* before and after DIP were not statistically significant in both myocardial areas. Moreover, an expected significant increase in the non-ischemic area as predicted by theory and described recently in healthy volunteers [5] was not observed. To understand these findings, the following facts have to be considered: areas with lower T_2^* values were identified visually and ROIs were placed manually. Of course, most of these areas were associated with the LAD being the supplying coronary artery, so that the remaining (and expected non-ischemic) myocardium was localized in lateral and inferior regions. It was precisely these regions that suffered from severe susceptibility artifacts, which occurred from the infero-lateral border of the heart and overlaid infero-lateral regions of myocardium. Possible reasons for these artifacts were discussed recently. Reeder et al. [8] stated that through-plane field pertubations caused by magnetic susceptibility differences between venous blood in the posterior vein of the left ventricle (PVLV) and myocardium may contribute to T_2^* enhancement and severe focal signal loss in cardiac images. Atalay et al. [9] found that the primary cause of the cardiac susceptibility artifact is due to the heart-lung interface along the apical and inferior segments of the heart. Therefore, an exact evaluation of the inferior border of the heart might be difficult in patients with altered myocardium in these regions resulting from a stenosis of the LCX or RCA. In our study, we tried to exclude regions of the myocardium, which displayed susceptibility artifacts from the evaluation. However, dependent on the extension of the artifact, the area of artifact-free myocardium was reduced. As a consequence, a smaller ROI was chosen and this might be responsible for the inaccuracy of absolute T_2^* values in these areas.

However, there is a significant difference in T_2^* when comparing values of the expected ischemic myocardium (30 ± 8 before vs. 32 ± 6 ms after DIP, increase of $4 \pm 8\%$, $P = 0.27$) with results from healthy volunteers (35 ± 3 before vs. 39 ± 4 ms after DIP, increase of $10 \pm 5\%$, $P = 0.05$, [4,5]). The difference in T_2^* is also significant when comparing values of the expected normal myocardium (48 ± 9 before vs. 48 ± 8 ms after DIP, $P = 0.41$) with results from healthy volunteers. A possible explanation for this phenomenon could be the influence of different drugs on the myocardial metabolism. In our study, all patients took aspirin, nitrate and beta-blocking agent. The influence of these drugs and interaction with DIP could therefore be responsible for the different T_2^* values estimated in regions of myocardium expected to be normal in patients with CAD and in the myocardium of healthy volunteers [4,5].

Another interesting finding is the following: even without DIP, the areas with lower T_2^* values could be clearly distinguished from the remaining myocardium, so that future studies without DIP might allow an easier and completely noninvasive detection of myocardial ischemic regions within a few minutes.

An increase in heart rate occurred earlier (2 vs. 4 min) and remained prolonged (18 vs. 9 min), which could reflect both a change in myocardial metabolism and a difference in pharmacological response to drugs due to ischemia.

Seven patients suffered from stenosis of the LAD. In six of them, areas with lower T_2^* values were detected in septal and anteroseptal myocardium. In one patient, the interesting myocardium was superimposed by susceptibility artifacts, which made an evaluation impossible. In three patients, the altered myocardium supplied by the RCA or LCX could not be detected due to overlapping susceptibility artifacts. Since there are no techniques to reduce the artifacts from the infero-lateral border of the heart, a detection of RCA- and LCX-associated myocardium will remain difficult.

One patient was reinvestigated after PTA of LAD and showed an increase in T_2^* within expected ischemic regions which was higher than before the intervention. This could reflect the improved situation in myocardial oxygenation after PTA. However, this hypothesis has to be substantiated by additional examinations, e.g. myocardial scintigraphy or positron-emission tomography (PET).

In future developments, navigator techniques might by helpful to increase the S/N by permitting a higher number of acquisitions. Non-breathhold examinations will also improve the patient's compliance, particularly in patients with respiratory insufficiency. Multi-slice techniques will be necessary to scan different myocardial planes in a reasonable time. A detection of ischemic myocardium could then be possible even without knowing the results of arteriography.

In conclusion, our preliminary results show that altered myocardium, which is associated with a stenosis of the LAD, is detectable using T_2^* measurements. Areas with significant lower T_2^* values were identified even without the use of DIP. Therefore, future examinations will require only a few minutes. However, the administration of DIP could be important to detect moderate alterations in myocardial oxygenation, if the presented T_2^* measurements become more sensitive and less inaccurate. This depends mainly on reducing the mentioned susceptibility artifacts. The detection of a significant increase in T_2^* in the non-ischemic myocardium as observed in healthy volunteers and predicted by theory should then be possible. In addition, the time dependent response of T_2^* to different drugs which influence myocardial metabolism could also be an interesting field in cardiovascular research.

Acknowledgements

Supported by Deutsche Gesellschaft für Kardiologie (CM Wacker) and Forschungsfonds der Universitätsklinik Mannheim/Heidelberg Projektnummer 42 (AW Hartlep). The authors thank David Saloner, Ph.D. for helpful discussion and for comments on the manuscript and Gabriele Beck, Ph.D. for initial developments of a multi-echo gradient sequence.

References

[1] Ogawa S, Lee TM, Kay AR, Tank DW. Brain magnetic resonance imaging with contrast dependent on blood oxygenation. Proc Natl Acad Sci USA 1990;87:9868–72.

[2] Ogawa S, Tank DW, Menon R, Ellerman JM, Kim SG, Merkle H, Urgubil K. Intrinsic signal changes accompanying sensory stimulation: functional brain mapping with magnetic resonance imaging. Proc Natl Acad Sci USA 1992;89:5951–5.

[3] Li D, Dhawale P, Rubin PJ, Haacke EM, Gropler RJ. Myocardial signal response to dipyridamole and dobutamine: demonstration of the BOLD effect using a double-echo gradient-echo sequence. Magn Reson Med 1996;36:16–20.

[4] Wacker CW, Bock M, Hartlep AW, et al. Oxygenation and perfusion measurements in the human heart under pharmacological stress with dipyridamole. 6th Scientific Meeting of the ISMRM, Sydney, Book of Abstracts, 1998, p. 897.

[5] Wacker CW, Bock M, Hartlep AW, Beck G, van Kaick G, Ertl G, Bauer WR, Schad LR. Changes in myocardial oxygenation and perfusion under pharmacological stress with dipyridamole: assessment using T_2^* and T_1 measurements. Magn Reson Med, 1999 in press.

[6] Atkinson D, Brant Zawadzki M, Gillan G, Purdy D, Laub G. Improved MR angiography: magnetization transfer suppression with variable flip angle excitation and increased resolution. Radiology 1994;190(3):890–4.

[7] Bauer WR, Nadler W, Bock M et al. Theory of the BOLD effect in the capillary region: an analytical approach for the determination of T_2^* in the capillary network of myocardium. Magn Reson Med 1999;41:51–62.

[8] Reeder SB, Faranesh AZ, McVeigh ER. In vivo measurement of T_2^* and field inhomogeneity: implications for cardiac EPI. 6th Scientific Meeting of the ISMRM, Sydney, Book of abstracts, 1998, p. 797.

[9] Atalay MK, Poncelet BP, Kantor HL, Brady TJ, Weisskoff RM, Susceptibility artifact at the cardiac apex of porcine hearts at 3T is primarily due to the heart-lung interface. 6th Scientific Meeting of the ISMRM, Sydney, Book of abstracts, 1998, p. 130.

[10] McGuinness ME, Talbert RL. Pharmacological stress testing: experience with dipyridamole, adenosine and dobutamine. Am J Hosp Pharm 1994;51(3):328–46.

[11] Tauchert M, Hilger HH. In: Schaper W, editor. The pathophysiology of myocardial perfusion. Amsterdam: Elsevier/North Holland Biomedical Press, 1979:141.

[12] Bing RJ, Hammond MM, Handelsman JC, Powers SR, Spenger FC, Eckenhoff JE, Goodale WT, Hafkenschiel JH, Kety SS. The measurement of coronary blood flow, oxygen consumption, and efficiency of the left ventricle in man. Am Heart J 1949;38:1.

[13] Niemi P, Poncelet BP, Kwong KK, et al. Myocardial intensity changes associated with flow stimulation in blood oxygenation sensitive magnetic resonance imaging. Magn Reson Med 1996;36:78–82.

[14] Kaul S, Jayaweera AR. Coronary and myocardial blood volumes. Circulation 1997;96:719–24.

[15] Atalay MK, Reeder SB, Zerhouni EA, Forder JR. Blood oxygenation dependence of T_1 and T_2 in the isolated, perfused rabbit heart at 4.7 T. Magn Reson Med 1995;34:623–7.

[16] Janick PA, Hackeney DB, Grossmann RI, Asakura T. MR imaging of various oxidation states of intracellular and extracellular hemoglobin. AJNR 1991;12:891–7.

Danksagung

Ich möchte mich bei meiner Ehefrau Andrea Bauer und meinen Kindern Alexander und Nicolas bedanken. Viele gute Ideen der theoretischen Arbeit kamen mir, während ich die Zeit mit Ihnen verbrachte. Alle haben mir immer auf ihre Weise geholfen.

Meinen Eltern ein Dankeschön, daß Sie mich immer unterstützt haben.

Von Herrn Dr. Walter Nadler vom Forschungszentrum Jülich habe ich gute Impulse, gerade was physikalisches Denken angeht, erhalten. Viele Ansätze entwickelten sich aus Gesprächen mit ihm. Gleichzeitig hat er mir als Profi auf dem Gebiet der theoretischen Physik immer geholfen, komplizierte Sachverhalte einfach und didaktisch gut darzustellen.

Herrn Prof, A. Haase möchte ich für die immer vorhandene Unterstützung, was NMR-, aber auch organisatorische Probleme angeht, danken. Mit ihm verbindet mich eine langjährige fruchtbare Zusammenarbeit.

Herrn Prof. G. Ertl möchte ich für die stets vorhandene Unterstützung, was organisatorische und verhandlungstechnische Dinge angeht, danken.

Weiterhin gilt mein Dank meiner wissenschaftlichen Arbeitsgruppe, also Herrn Dr. K.-H. Hiller, Frau S. Voll, Frau Y. Vogt, Frau Dr. C. Waller, Herrn Dr. C. Wacker, Herrn Dr. M. Nahrendorf, Herrn Dr. Hanns Hillenbrand, Herrn J. Streif und Herrn S. Köhler, sowie meinen Kooperationspartnern am Deutschen Krebsforschungszentrum Heidelberg in der Arbeitsgruppe von Prof. L. Schad. Durch die Arbeitsgruppe und die Kooperation entstand die experimentelle Basis, die Fragestellungen hervorbrachte, die zu der Promotionsarbeit geführt haben.